NAVAL POSTGRADUATE SCHOOL

MONTEREY, CALIFORNIA

DISSERTATION

COMPUTATIONAL MODELING OF THE SPATIAL
DISTRIBUTION AND TEMPORAL DECAY OF
GEOMAGNETICALLY TRAPPED DEBRIS OF A HIGH
ALTITUDE NUCLEAR DETONATION

by

Christopher Gene Cross, Jr.

June 2007

Dissertation Supervisor: Dennis Hewett

Approved for public release; distribution is unlimited

THIS PAGE INTENTIONALLY LEFT BLANK

REPORT DOCUMENTATION PAGE			*Form Approved OMB No. 0704-0188*
Public reporting burden for this collection of information is estimated to average 1 hour per response, including the time for reviewing instruction, searching existing data sources, gathering and maintaining the data needed, and completing and reviewing the collection of information. Send comments regarding this burden estimate or any other aspect of this collection of information, including suggestions for reducing this burden, to Washington headquarters Services, Directorate for Information Operations and Reports, 1215 Jefferson Davis Highway, Suite 1204, Arlington, VA 22202-4302, and to the Office of Management and Budget, Paperwork Reduction Project (0704-0188) Washington DC 20503.			
1. AGENCY USE ONLY (*Leave blank*)	**2. REPORT DATE** June 2007	**3. REPORT TYPE AND DATES COVERED** Dissertation	
4. TITLE AND SUBTITLE: Computational Modeling of the Spatial Distribution and Temporal Decay of Geomagnetically Trapped Debris of a High Altitude Nuclear Detonation		**5. FUNDING NUMBERS**	
6. AUTHOR(S) Christopher Gene Cross, Jr.			
7. PERFORMING ORGANIZATION NAME(S) AND ADDRESS(ES) Naval Postgraduate School Monterey, CA 93943-5000		**8. PERFORMING ORGANIZATION REPORT NUMBER**	
9. SPONSORING / MONITORING AGENCY NAME(S) AND ADDRESS(ES) N/A		**10. SPONSORING / MONITORING AGENCY REPORT NUMBER**	
11. SUPPLEMENTARY NOTES The views expressed in this thesis are those of the author and do not reflect the official policy or position of the Department of Defense or the U.S. Government.			
12a. DISTRIBUTION / AVAILABILITY STATEMENT Approved for public release; distribution is unlimited		**12b. DISTRIBUTION CODE**	

13. ABSTRACT (maximum 200 words)

With the absence of nuclear weapons testing there has been an increase in the reliance on simulation and modeling for the analysis of nuclear weapons effects. The principal objective of this dissertation was to develop a particle code for modeling the spatial distribution and temporal decay of ionized fission fragments and beta-decay electrons injected into the magnetic field of the earth. No known code existed for this explicit purpose. The code provides a robust, realistic computational capability to predict the persistent radiation environment produced for such an injection (most likely due to a nuclear detonation at high altitudes) into L-shells less than 1.5. The code can also be used to produce a source term for the weapons debris from a nuclear detonation at any high altitude location. Using the model, several of the free parameters are examined and reported to highlight the sensitivity of the persistent environment to the initial conditions fission fragment release. The parameters examined and reported here include the effects of ion release location (longitude, latitude, and altitude), the charge state of the fission fragments, the beta decay half-life, the initial pitch angle of the fission fragments, and the significance of neutral fission fragments. Additionally, the effects of the magnetic bubble on the dispersion and trapping efficiency of the particles is studied and reported.

14. SUBJECT TERMS Trapped Radiation, Belt-Pumping, High Altitude Nuclear Explosion, Fission Fragments, Magnetic Bubble, Nuclear Weapons, Beta Decay	**15. NUMBER OF PAGES** 263
	16. PRICE CODE

17. SECURITY CLASSIFICATION OF REPORT Unclassified	**18. SECURITY CLASSIFICATION OF THIS PAGE** Unclassified	**19. SECURITY CLASSIFICATION OF ABSTRACT** Unclassified	**20. LIMITATION OF ABSTRACT** UL

THIS PAGE INTENTIONALLY LEFT BLANK

COMPUTATIONAL MODELING OF THE SPATIAL DISTRIBUTION AND TEMPORAL DECAY OF GEOMAGNETICALLY TRAPPED DEBRIS OF A HIGH ALTITUDE NUCLEAR DETONATION

Christopher Gene Cross, Jr.
Lieutenant Colonel, United States Army
B.S., Mechanical Engineering, North Carolina State University, 1987
M.S., Applied Physics, University of Washington, 1998

Submitted in partial fulfillment of the requirements for the degree of

DOCTOR OF PHILOSOPHY IN PHYSICS

from the

NAVAL POSTGRADUATE SCHOOL
June 2007

Author: _____
Christopher Gene Cross, Jr.

Approved by:

_____   _____
Dennis Hewett   Craig Smith
Deputy Associate Division Leader   Chair Professor of Lawrence
for Computational Physics   Livermore National Lab
Lawrence Livermore National Lab   Dissertation Committee Chair
Dissertation Supervisor

_____   _____
Tom Thomson   William Colson
Deputy Program Leader   Professor of Physics
Lawrence Livermore National Lab

_____   _____
Richard Olsen   Todd Weatherford
Professor of Physics   Assistant Professor of Electrical
                                                    & Computer Engineering

Approved by: _____
James Luscombe, Chairman, Department of Physics

Approved by: _____
Julie Filizetti, Associate Provost for Academic Affairs

iii

THIS PAGE INTENTIONALLY LEFT BLANK

ABSTRACT

With the absence of nuclear weapons testing there has been an increase in the reliance on simulation and modeling for the analysis of nuclear weapons effects. The principal objective of this dissertation was to develop a particle code for modeling the spatial distribution and temporal decay of ionized fission fragments and beta-decay electrons injected into the magnetic field of the earth. No known code existed for this explicit purpose. The code provides a robust, realistic computational capability to predict the persistent radiation environment produced for such an injection (most likely due to a nuclear detonation at high altitudes) into L-shells less than 1.5. The code can also be used to produce a source term for the weapons debris from a nuclear detonation at any high altitude location. Using the model, several of the free parameters are examined and reported to highlight the sensitivity of the persistent environment to the initial conditions fission fragment release. The parameters examined and reported here include the effects of ion release location (longitude, latitude, and altitude), the charge state of the fission fragments, the beta decay half-life, the initial pitch angle of the fission fragments, and the significance of neutral fission fragments. Additionally, the effects of the magnetic bubble on the dispersion and trapping efficiency of the particles is studied and reported.

THIS PAGE INTENTIONALLY LEFT BLANK

TABLE OF CONTENTS

LIST OF FIGURES

x

xi

THIS PAGE INTENTIONALLY LEFT BLANK

LIST OF TABLES

THIS PAGE INTENTIONALLY LEFT BLANK

ACKNOWLEDGMENTS

The author wishes to thank all who were directly and indirectly responsible for the success of this dissertation. I would like to first thank Dr. Dennis Hewett for his patience, untiring devotion to my professional growth, and his commitment to my development as a physicist. Second, I owe Tom Thomson a few more bottles of Scotch for the many late nights he spent helping me unravel the many mysteries of science and for continually introducing me to new intellectual adventures. I am also quite grateful to Dr. Craig Smith for his efforts and willingness to facilitate my research at Lawrence Livermore National Laboratory. All of the assistance I received from the professionals at Lawrence Livermore National Laboratory and the Naval Postgraduate School made this work possible.

There is no way to fully express my appreciation for the devotion of my wife, Karin, and my two wonderful sons, Blake and Brock. Their love and patience were a constant sources of essential support as we completed this journey in time. I could not have dreamed of a better supporting task, especially when I was away on travel. Karin has always been my biggest fan and her love and devotion make everything possible. Thank you all for allowing me this opportunity.

THIS PAGE INTENTIONALLY LEFT BLANK

PREFACE

The motivation for this research and the dissertation was based on my experience while serving three years as a nuclear effects analyst at USSTRATCOM from June of 2001 until June of 2004. While working at the United States Strategic Command (USSTRATCOM) I was queried on multiple occasions about the effects of a nuclear detonation in space. Some of the scenarios we considered were intentional high-altitude burst, an atmospheric test, and a salvage/contact fused nuclear missile or warhead intercepted by a missile defense network. Most of those familiar with the effects of a high-altitude nuclear explosion (HANE) were aware of the electromagnetic pulse (EMP) generated by a HANE, but very few nuclear planners and weapons effects experts had an appreciation for the effects of a detonation of a nuclear weapon on the space environment. In order to answer the difficult questions about weapons effects posed to me by the leadership of USSTRATCOM, my team of physicists and weapons effects experts initiated an exhaustive search for current modeling capabilities. As we began our research and exploration to understand the effects of a high altitude nuclear detonation, one of the obvious and potentially devastating realizations was the significant threat of the degradation of space-based systems caused by trapped radiation resulting from a nuclear event in space.

As we pursued our effort to characterize the current state of modeling capabilities, I was amazed with the lack of understanding of the trapped radiation environment and our capability to model the phenomena resulting from dispersion of debris from a nuclear device. Both analytical and numerical models existed for prompt radiation and EMP, but no useful model was available, for the full range of possible and most probable altitudes for a possible nuclear detonation, to adequately predict the distribution of the debris in the magnetic belts, to include the energetic electrons from beta decay of the fission fragments. I can declare the lack of a useful model because I "stood on the high ground" and reached out to the Department of Defense (DoD) and the Department of Energy (DoE) communities for help on this problem without success.

As suggested, one of the most important phenomena to be considered is trapped radiation. The colloquial term for trapped radiation is "belt pumping" implying an increase in the quantity of energetic electrons trapped in the magnetic belts of the earth's magnetic field. Additionally, the debris ions can become trapped in the earth's magnetic field and cannot be ignored. Clearly, an increase in the high-energy electrons and ions could present a significant threat to the satellites in orbit around the world. However, as my experience indicated, the DoD and DoE experts were unable to model the "trapped radiation" environment and the effects of that environment on satellites at most detonation altitudes of interest. The models that did exist were capable of reproducing the data from a limited number of US high altitude nuclear tests, but were not effective in predicting the belt-pumping from weapons at different yields and lower altitudes.[1] The fidelity of the existing models was classified as low by a "blue ribbon panel" of experts as part of an examination of the existing database and belt pumping predictive capability with an uncertainty of at least an order of magnitude.[2]

The existing models are generally large scale diffusion models that do not include much of the critical physics introduced in this dissertation. Almost all of the modeling of HANE effects was funded during the Cold War when a nuclear exchange was expected to involve thousands of multi-kiloton warheads. High fidelity models were not necessarily practical or essential.

Today, we find ourselves in a new and different strategic environment. We must now be able to provide higher fidelity answers about the effects of single and much lower yield nuclear weapons at many different altitudes. The conclusion of our study and research at USSTRATCOM was that a modeling capability was needed that would include the detailed physics necessary to track the weapons debris and beta electrons as the particles interacted with the atmosphere and the magnetic field perturbations caused

---

[1] E.M. Jakes, K.J. Daul, and R. Greaves, "PL-TR-1056: Exo-atmospheric Nuclear Radiation Environments Prediction and Shielding Codes, Final Report, "Report for Phillips Laboratory, Advance Weapons and Survivability Directorate, Air Force Material Command, Kirtland Air Force Base, NM, March 1993, 33-34.

[2] C. Allen, B. Roth, "Final Report Summarizing Blue Ribbon Panel and Support Work Assessing the Status of the High Altitude Nuclear Explosion (HANE) Trapped Radiation Belt Database," final report to Air Force Research Laboratory, June 2006.

by the nuclear explosion at multiple altitudes and weapons yields. Without such a capability a significant gap would continue to exist in our nuclear effects modeling capability.

We realize that the probability of failure (and the time to failure) of a satellite from a single nuclear detonation depends on the yield of the weapon, the height of burst (HOB), the longitude and latitude of the detonation, the vulnerability and shielding of the satellite, the accumulated dose to each satellite, and other factors related to the space-radiation environment. The Defense Threat Reduction Agency (DTRA) estimated that many, if not all, low-earth orbit (LEO) satellites could significantly degrade in performance or catastrophically fail in several months following a nuclear detonation in space.[3] This estimate was based on the sparse knowledge from our atmospheric tests and a scientific estimate from DoD experts. The estimate came with a lot of uncertainty and no analytical model to support the conclusions of the study. Certainly catastrophic failure of all satellites was an answer, but not necessarily the correct answer to the question of the effects of a nuclear detonation on space systems. A better understanding of the space environment following a nuclear detonation was clearly necessary in order to increase confidence in predictions and reduce the uncertainties of the estimates. All too often, while assigned as a nuclear effect analyst, I was unable to provide adequate answers to the leadership of USSTRATCOM on the effects of a nuclear detonation on the nation's satellites. As a consequence, the primary objective of my dissertation is to advance our modeling and predictive capability to address such issues.

As I started my work as a student at the Naval Postgraduate School I was able to take advantage of the capability and experience of the National Laboratories. Lawrence Livermore National Laboratory (LLNL) currently has well-established codes to model the output of weapons out to around one meter from the burst. LLNL is also investigating the applicability of fluid codes with "plasma collisionality" in order to track the weapon's debris from a distance of one meter out to five kilometers. Additionally, LLNL is verifying and validating the geometry between existing codes in the kinetic ion regime

---

[3] R.C. Webb, "The Effects of a Nuclear Detonation in Space (with an Emphasis on Low Earth Orbit Satellites)," (6 July 1998): Briefing to Defense Science Research Meeting, Electronics Technology Division, Defense Special Weapons Agency.

and is looking at the effect of the charge state of the weapon's debris. There was, as indicated, a recognized gap in the particle-tracking codes needed to determine where the ionized debris and energetic betas go and the effects of the charged particles on the space environment. This particle tracking gap became the starting point for my journey.

With the bridging of this gap in our ability to model weapons effects, future weapons effects analysts will have the capability to provide our nation's leadership with improved answers about "belt pumping" and the effects of the radiation environment on satellites. Let me be clear that the objective of this study was not to encourage or advocate the use of nuclear weapons in space. The results of this study not only improve our understanding of the space-radiation environment caused by a nuclear weapon, but further discourage the use of nuclear weapons in space.

I.   INTRODUCTION

Since the beginning of the nuclear age, simulation and modeling have been developed in parallel with nuclear weapons testing. The first modern, electronic, reprogrammable digital computer, ENIAC, designed and developed to calculate artillery firing tables, was used to assist in the computational modeling of the first hydrogen bomb.[4] Computational verification of weapon designs became a cornerstone of weapons programs and synonymous with the development and design of nuclear weapons. During the period of US nuclear testing (1945 – 1992) models were also developed as a basis for understanding the physics of nuclear weapons effects. During the period of nuclear testing results of tests were compared to the predictions of the models, and the computational capability was able to iteratively evolve with the subsequent collection of additional data.

Recently, with the curtailment of nuclear weapons testing, there has been a dramatic increase in the reliance on simulation and modeling for analyzing nuclear weapons effects. One of the areas in nuclear effects modeling that is particularly rich in physics and yet void in current modeling capability is that of high altitude nuclear explosions. Specifically absent is the capability to predict the persistent environment caused by a nuclear detonation in space and to model the effects of the weapons debris environment on space-based systems. Therefore, the primary focus of this dissertation is to fill the gap in our ability to model the location and behavior of charged particles resulting from a nuclear explosion as they become trapped in the magnetic field of the earth.

This dissertation builds and applies software that enables effective analysis of the persistent radiation environment caused by a nuclear detonation in space. The strategy was to develop an understanding of the underlying physics and then construct a computational model necessary to include the essential physics. The flow of the dissertation follows this strategy and is shown below:

---

[4] R. Rhodes, *The Making of the Atomic Bomb*, (New York: Simon and Schuster, 1986), 771.

1. Establish the essential physics of charged particles trapped in a dipole magnetic field.

2. Develop computational techniques to solve for the trajectories of the charged particles trapped in the dipole field.

3. Validate the models against the analytical solutions of charged particles in a vacuum and dipole field.

4. Establish the physics of particle scattering, energy loss, and other non-ideal effects that affect the trapped radiation environment.

5. Develop a more accurate understanding of the magnetic field of the earth and introduce a simple model to account for the tilted and shifted dipole field of the earth.

6. Develop computational techniques to model the trapped particles as they scatter and lose energy due to collisions with the atmosphere.

7. Integrate the fission spectrum beta decay into the model as a source for the trapped electrons.

8. Review and examine the existing data from high altitude nuclear testing.

9. Study the effect of the different initial conditions possible for the release of the fission fragments into the earth's magnetic field.

10. Study the effects of the magnetic bubble and magnetic perturbations on the dispersion and trapping of the weapon's debris and energetic electrons.

11. Provide a predictive model and software path for the trapped radiation environment caused by a nuclear detonation.

The model derived in this work addresses most of the essential physics of trapped radiation at altitudes of the low-earth orbit satellites. The results of the model have immediate application across the spectrum of weapons effects studies of DoD and DoE. Additionally, with the software path in place, improvements to the physics can and should be added in the future.

In order to understand the nature of the electromagnetic environment caused by charged particles trapped in the earth's magnetic field, this dissertation began a study to model the behavior of electrons and ions trapped in a dipole field similar to the magnetic field of the earth. Starting the Lorentz force, equation 1, using SI units, (where F is the force on a particle, q is the charge of a particle, E is the electric field, v is the velocity of the particle, and B is the magnetic field) two time integration techniques, Euler-Cromer and a Boris push, were developed and used to track the charged particles trapped in the earth's magnetic field.

(1.1) $\vec{F} = q(\vec{E} + \vec{v} \times \vec{B})$

Both of these integration schemes were developed and tested and ultimately the Boris push was selected as the preferred computational method because the Boris push it was capable of producing the same results as the Euler-Cromer in much less time.

A guiding center approach was also developed and applied in order to approximate the location of the particles and further reduce the computational requirements of the simulation. Comparisons were made between the results using the guiding center approximation and the results using the more detailed Boris push and Euler-Cromer methods. All computational results were compared to analytical solutions of particle motion in a perfect vacuum magnetic dipole field. After establishing confidence that all models accurately matched the known analytical results, a more realistic description of the earth's magnetic field and the effects of atmosphere were added to the codes.

During the initial model analysis and validation using numerical simulations and guiding center approximations the following simplifying assumptions were made: (a) the earth's magnetic field was a perfect dipole with a dipole moment of 8.05 x 10^{22} A-m^2; (b) there was no electric field; (c) there was no energy loss of the particles; (d) the electrons were relativistic; (e) there is no tilt or offset of the earth's magnetic axis with respect to the geographical axis; and (f) there is no effect of the interplanetary magnetic field (IMF) on the particle (Parks claims this is a valid assumption out to about r = 5Re where Re is defined as the radius of the earth[5] (6,375,000 m). After the computer code was validated for a charged particle trapped in the Earth's "perfect" dipole field the above assumptions were adjusted to account for physics that must be included in order to properly model charged particles trapped in the earth's magnetic field.

Eventually a source term of fission fragments from an unclassified model of a nuclear weapon was applied to the model and the results are reported. The weapon debris fission fragments were tracked as they dispersed into the local environment. After the "magnetic bubble" caused by the nuclear detonation collapsed, the positively charged

---

[5] George K. Parks, *Physics of Space Plasmas: An Introduction*, 2nd ed. (Bolder, Co: Westview Press, 2004), 56.

fission fragments interacted with the earth's dipole magnetic field and generally followed the magnetic lines (often referred to as the lines of force) as determined by the Lorentz force. Many of the fission fragments experienced collisions within the atmosphere causing pitch-angle diffusion, radial scattering, and ionization energy losses. Other fragments became trapped in the earth's field with minimal interaction with the atmosphere. Many of the fission fragments beta decayed, some as many as eight times, injecting high-energy electrons into the magnetic field. Both the fission fragments and beta decay electrons were tracked as they drifted around the earth causing an environment that was potentially hazardous to satellites.

The balance of the dissertation consists of a discussion of the background physics required to effectively analyze the subject phenomena (Chapter II); two chapters describing the model development effort, the first (Chapter III) presenting the basic model that is amenable to comparison to exact analytical solutions, and the second (Chapter IV) describing the addition of features needed to address additional phenomenology necessary to accurately analyze the complexities of the real world; a chapter describing key elements related to the potential source term (Chapter V); a chapter (Chapter VI) summarizing the complete integrated model featuring the characteristics and source term information previously described; and finally a chapter that presents the results of the application of the model to a variety of important problems (Chapter VII).

II.   THEORETICAL BACKGROUND

2.1.   THE DYNAMICS OF CHARGED PARTICLES IN A MAGNETIC FIELD

The general shape of the dipole field of the earth is shown in Figure 2.1.1. The
north (N) and south (S) markings on the sphere represent the geographical poles and not
the magnetic poles. The magnetic poles are currently in the reverse sense of the
geographical poles.
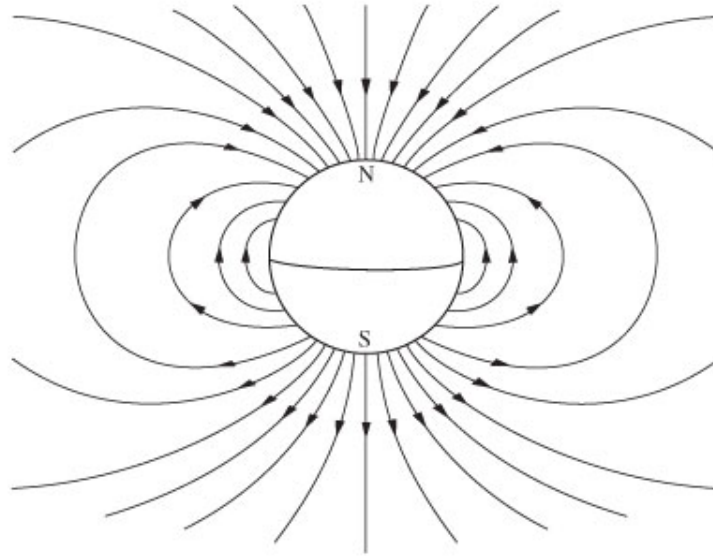
**Figure 2.1.1: The magnetic dipole of the earth with a dipole moment of 8.05 x 10^{22}
A-m^{2}.**

Following the description in Parks, the relevant Maxwell's equations are:

(2.1.1) $\nabla \bullet \vec{B} = 0$

(2.1.2) $\nabla \times \dfrac{\vec{B}}{\mu_0} = \vec{J} + \dfrac{\partial \vec{D}}{\partial t}.$

By allowing the current density $(\vec{J})$ to vanish in the vacuum of space, $\vec{J} = 0$, the
permeability of free space (μ_0) to remain constant, and considering a steady-state

condition where the displacement current $(\vec{D})$ remains static, $\dfrac{\partial \vec{D}}{\partial t} = 0$, equation 2.1.2 can

be written

5

(2.1.3) $\nabla \times \vec{B} = 0$.

In the case where equation 2.1.3 is satisfied, a scalar potential is defined by

(2.1.4) $\vec{B} = \nabla \Psi$.

For the dipole field, the scalar potential is represented by

(2.1.5) $\Psi = -\dfrac{\mu_0}{4\pi} \vec{M} \bullet \nabla \dfrac{1}{r}$

where $\vec{M}$ is the dipole moment of the earth defined as $\vec{M} = -M\hat{z}$. In order to express the magnetic field of the earth in Cartesian units, the radius, r, is defined as the distance from the center of the earth and r_0 is the distance to the surface of the earth ($r_0 = 6375$ km). Figure 2.1.2 represents the coordinate system where the x-axis corresponds to a longitude of 0 degrees.
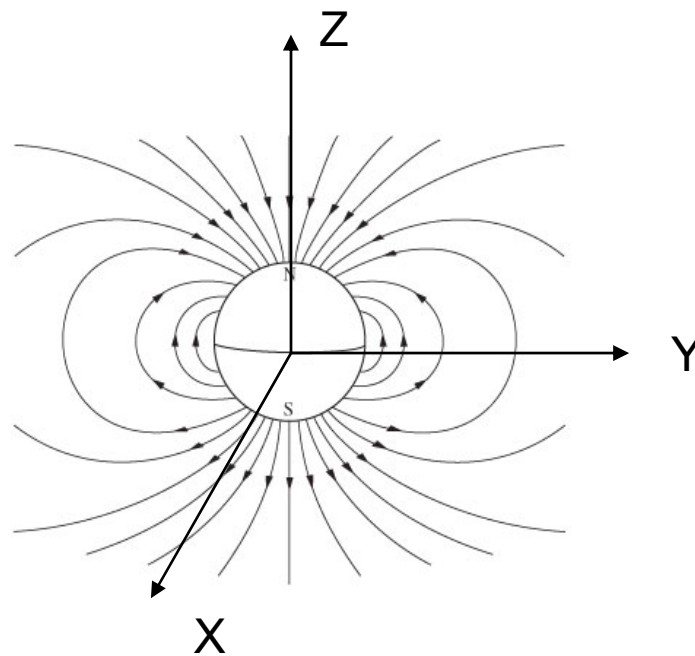
Figure 2.1.2: The coordinate systems used for modeling and calculations.

Using the Cartesian coordinates, the distance from the center of the dipole to the location of interest is

(2.1.6) $r = \sqrt{x^2 + y^2 + z^2}$.

Combining equations 2.1.4, 2.1.5, 2.1.6 yields

$$\Psi = -\frac{\mu_0}{4\pi}\vec{M}\bullet\nabla\frac{1}{\sqrt{x^2+y^2+z^2}}$$

$$\Psi = \frac{\mu_0}{4\pi}M\frac{z}{(x^2+y^2+z^2)^{3/2}}$$

The magnetic field of the dipole is

(2.1.7) $\qquad \vec{B} = \nabla\left[\frac{\mu_0}{4\pi}M\frac{z}{(x^2+y^2+z^2)^{3/2}}\right].$

The x, y, and z components of the earth's magnetic field are

(2.1.8) $\qquad B_x = -\frac{3\mu_0}{4\pi}M\frac{x*y}{(x^2+y^2+z^2)^{5/2}} = -\frac{3\mu_0}{4\pi}M\frac{x*z}{r^5}$

(2.1.9) $\qquad B_y = -\frac{3\mu_0}{4\pi}M\frac{x*y}{(x^2+y^2+z^2)^{5/2}} = -\frac{3\mu_0}{4\pi}M\frac{y*z}{r^5}$

(2.1.10) $\qquad B_z = \frac{\mu_0}{4\pi}M\left[\frac{(x^2+y^2+z^2)-3z^2}{(x^2+y^2+z^2)^{5/2}}\right] = \frac{\mu_0}{4\pi}M\left[\frac{r^2-3z^2}{r^5}\right].$

Figure 2.1.3 represents the dipole magnetic field of the earth.
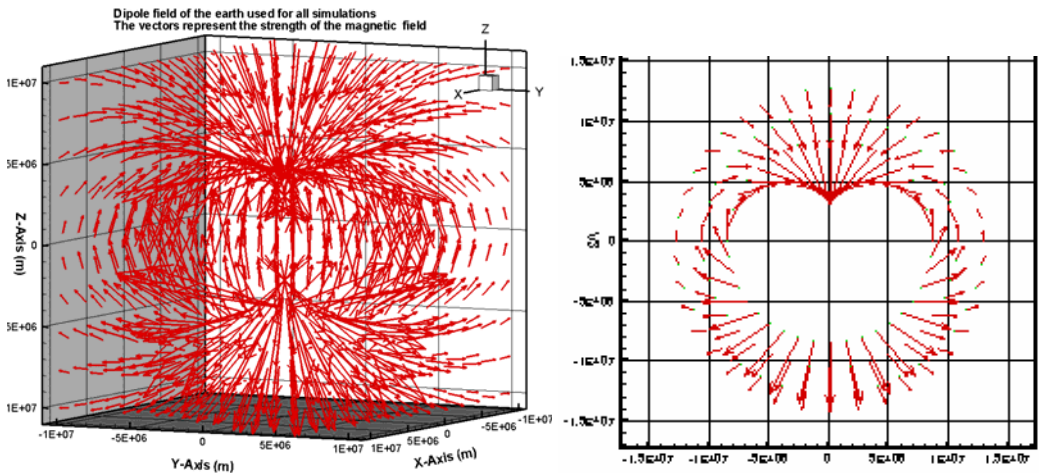
Figure 2.1.3: Earth's dipole magnetic field generated using equations 2.1.8, 2.1.9, and 2.1.10. The diagram on the left is a complete 3-D representation and the diagram on the right is a 2-D representation. The lengths of the vectors represents the magnitude of the magnetic field.

During the first series of simulations carried out in this research to verify the performance of the initial, simplified models, the only force allowed to act on the particle was the force due to the magnetic field. No electric fields were included. The work, W_B, done by the Lorentz force is

(2.1.11) $W_B = q(\vec{v} \times \vec{B}) \bullet \vec{v} = 0$

Similarly, by ignoring the radiation emitted by the charged particles as they spiral around in the magnetic dipole field (shown later to be negligible for the energies of the electrons emitted from beta decay), the kinetic energy of the particle is conserved.

$$m\frac{d\vec{v}}{dt} \bullet \vec{v} = m\vec{v} \bullet \frac{d\vec{v}}{dt} = 0$$

(2.1.12) $m\vec{v} \bullet \frac{d\vec{v}}{dt} = \frac{d}{dt}(\frac{1}{2}mv^2) = 0$

Energy conservation is therefore appropriately correct and is used as one of the checks to establish confidence in the simulations designed to track particles moving in a magnetic field. Maintaining energy conservation with the models was also a way to bound the limit on the size of the time step used in the computations. Once confidence is established using the model representing the magnetic field only, the contribution of an electric field is readily added to the Lorentz force.

The motion of the non-relativistic charged particle with mass (m) and charge (q) in the earth's magnetic field ($\vec{B}$) is described using Lorentz force. The Lorentz force is written as

(2.1.13) $m\vec{a} = q(\vec{v} \times \vec{B})$

(2.1.14) $m\frac{d\vec{v}}{dt} = q(\vec{v} \times \vec{B})$.

Equation 2.1.11 implies that the only force acting on the charged particle is perpendicular to the velocity and the magnetic field.

Next, consider the velocity vector as the vector sum of the velocity perpendicular to the local magnetic field ($\vec{v}_\perp$) and the velocity parallel to the local magnetic field ($\vec{v}_\parallel$). The $\vec{v}_\parallel$ component of the velocity describes the velocity of the particle along the

direction of the magnetic field lines and the $\bar{v}_\perp$ component of the velocity perpendicular to the magnetic field lines and describes a particle circling about the magnetic field lines.

(2.1.15) $\vec{v} = \vec{v}_\perp + \vec{v}_\parallel$

In a uniform magnetic field where $v_\parallel \times \vec{B} = 0$, equation 2.1.14 now becomes

$$\frac{d\vec{v}_\perp}{dt} + \frac{d\vec{v}_\parallel}{dt} = \frac{q}{m}(\vec{v}_\perp \times \vec{B})$$

(2.1.16) $\frac{d\vec{v}_\perp}{dt} = \frac{q}{m}(\vec{v}_\perp \times \vec{B})$.

One may also conclude that in a uniform magnetic field

(2.1.17) $\frac{d\vec{v}_\parallel}{dt} = 0.$

The motion of a particle described by equations 2.1.16 and 2.1.17 is helical with a constant velocity parallel to the magnetic field and a constant speed perpendicular to the magnetic field. For the remainder of the dissertation, the appropriate vector symbols are not included in the description of the parallel and perpendicular components of the velocity. The $v_\parallel$ will always describe component of the velocity in the direction along the magnetic field line and the $v_\perp$ will describe the component of velocity perpendicular to the magnetic field line.

The non-relativistic equations of motion of the spiraling particle are reduced to

(2.1.18) $m\frac{v_\perp^2}{r_c} = qv_\perp B$

(2.1.19) $r_c = m\frac{v_\perp}{qB}$

(2.1.20) $\omega_c = \frac{v_\perp}{r_c} = \frac{qB}{m}$

where r_c is the Larmor radius (also called the gyro-radius or cyclotron radius) and ω_c is the Larmor frequency (also called the gyro-frequency or cyclotron frequency). In order to apply equations 2.1.18, 2.1.19, 2.1.20 to relativistic particles, the relativistic Lorentz factor, (γ), is introduced into the equations to account for an effective mass of the particle common in the study of relativistic particles. The Lorentz factor is defined by

9

$$\gamma = \frac{1}{\sqrt{1 - v^2/c^2}}.$$

The relativistic mass, often called the effective mass, is the rest mass multiplied by Lorentz factor

$$m_{eff} = \gamma m_{rest}.$$

A 2-MeV electron has a value of $\gamma = 3.9$ and a speed around 2.9×10^8 m/s. The magnetic field at the magnetic equator of the earth at an altitude of 400 km is on the order of 3×10^{-5} T and q/m for an electron is -1.76×10^{11} C/kg. Using the relativistic expressions of equations 2.1.19 and 2.1.20 where the mass becomes an effective mass, the Larmor radius is on the order of 200 m and the angular frequency is approximately 1.3×10^6 rad/s. The implication is that the electron makes a "complete" orbit around the field line in about 6 μs.

For a non-relativistic particle the kinetic energy (T) is given by

$$(2.1.21) \qquad T = \frac{1}{2} m (v_\perp^2 + v_\parallel^2).$$

The $v_\perp$ describes the electron's orbital speed perpendicular to the magnetic field as the electron spirals around the magnetic field lines. The rotation of a charged particle around a loop produces a situation similar to a circular current loop or "ring current" described by in detail by Jackson.[6] The current (I) can be defined as,

$$(2.1.22) \qquad I = \frac{q v_\perp}{2\pi r_c} = \frac{q \omega_c}{2\pi} = \frac{q^2 B}{2\pi m}.$$

The magnetic dipole moment[7] (μ) of a current carrying loop is

$$\vec{\mu} = I \int d\vec{a} = I\vec{a}.$$

where $\vec{a}$ is the surface area of the loop with a direction normal to the surface. The magnitude of the magnetic dipole moment of the circular current loop is

$$(2.1.23) \qquad \mu = I(\text{Area of loop}) = I\pi r_c^2$$

[6] J. D. Jackson, *Classical Electrodynamics*, 3rd ed. (Hoboken, NJ: John Wiley and Sons, Inc., 1998), 181.

[7] D. J. Griffiths, *Introduction to Electrodynamics*, 2nd ed. (Englewood Cliffs, NJ: Prentice Hall, 1989), 244.

Using equation 2.1.22 and 2.1.23, the magnetic dipole moment is written

$$\mu = \frac{qv_\perp r_c}{2}.$$

The direction of μ is in the opposite direction of the magnetic field. Another useful characteristic of the magnetic moment in a uniform/adiabatic magnetic field is that, without collisions or dispersion, the magnetic moment is conserved. The conservation of the magnetic moment is presented in detail in Section 2.3.1.

The magnetic flux, Φ_m, is a description of the magnetic field "lines of force" that pass through an area. The magnetic flux through a loop is expressed as

$$\Phi_m = \int \vec{B} \bullet d\vec{a}$$

(2.1.24) $\Phi_m = B\pi r_c^2.$

This magnetic flux is related to the magnetic field in an interesting way: the field points along the magnetic flux lines and its magnitude is proportional to how tightly those flux lines are packed together. Where the flux lines are closely spaced, as they are near the poles of a magnetic dipole in Figure 2.1.1, the magnetic field is strong. Where the lines of force are farther apart, the magnetic field is relatively weak.[8] The magnetic flux through the current loop remains constant (this will be proven later in section 2.3) as the electron moves in the slowly changing magnetic dipole field. In order to maintain a constant flux as the magnetic field changes, the orbital radius and perpendicular velocity of the charged particle are adjusted to maintain the constant magnetic flux. As $v_\perp$ changes to maintain the constant flux, conservation of energy requires that $v_\parallel$ also changes.

In order to develop an expression for the potential energy of a current carrying loop in a magnetic field, Jackson[9] develops an expression for the total force exerted by the magnetic field on the loop,

(2.1.25) $\vec{F} = \nabla(\vec{\mu} \bullet \vec{B})$

Recalling that the potential energy, U, is defined as

---

[8] L. A. Bloomfield, *How Things Work: The Physics of Everyday Life*, (New York: John Wiley and Sons, 1997), 425.

[9] Jackson, 189.

$$U = -\int \vec{F} \bullet d\vec{x}$$

then the potential energy becomes

(2.1.26) $U = -\int \nabla(\vec{\mu} \bullet \vec{B}) \bullet d\vec{x}.$

Therefore, the potential energy stored in the magnetic field of a circular current loop, ε_μ, due to the magnetic moment of the loop in the magnetic field is

(2.1.27) $\varepsilon_\mu = -\vec{\mu} \bullet \vec{B} = \mu B$ (the direction of μ is the opposite direction of B)

The potential energy of equation 2.1.27 is equal to the perpendicular kinetic energy, $T_\perp$, of the charged particle. Therefore, for non-relativistic speeds

$$\varepsilon_\mu = T_\perp = \varepsilon_\perp$$

so

(2.1.28) $\mu B = \dfrac{1}{2} m v_\perp^2.$

If the magnetic moment is constant, then as the magnetic field increases so does the perpendicular component of the velocity. If the magnetic field decreases then the perpendicular component of the velocity decreases. The increase in $v_\perp$ causes the current to increase and the area of the loop to decrease. Therefore, the area of the current loop is largest when the magnetic field is the least (at the earth's magnetic equator) and the area of the current loop is smallest when the magnetic field is the largest (at the conjugate or mirror points.) The total kinetic energy of a particle trapped in a magnetic field (equation 2.1.21) can be written as

(2.1.29) $T = \dfrac{1}{2} m(v_\parallel^2) + \mu B$

By combining equations 2.1.24 and 2.1.19 the enclosed magnetic flux, Φ_m, is

$$\Phi_m = \dfrac{\pi m^2 v_\perp^2}{q^2 B}.$$

If the enclosed magnetic flux through the current loop is constant, using $\varepsilon_\perp = \mu B$ the magnetic flux can also be written

(2.1.30) $\Phi_m = \left(\dfrac{2\pi m}{q^2}\right)\dfrac{\varepsilon_\perp}{B} = const.$

12

Recall that $\varepsilon_\perp = \dfrac{mv_\perp^2}{2} = \mu B$ so the enclosed flux is

$$\Phi_m = \left(\frac{2\pi m}{q^2}\right)\mu = \text{constant.}$$

Therefore, the magnetic dipole moment is also constant.

(2.1.31) $\mu = \text{constant.}$

Another important parameter is the pitch angle. The pitch angle (α) is defined as the angle between the velocity vector of the particle and the magnetic field. The pitch angle at the magnetic equator is designated α_0. In general the pitch angle is calculated using

(2.1.32) $\alpha = \text{Tan}^{-1}(\dfrac{v_\perp}{v_\parallel})$

The components of the velocity are determined using

(2.1.33) $v_\parallel = v\text{Cos}(\alpha)$ (v is the magnitude of the full velocity vector)

(2.1.34) $v_\perp = v\text{Sin}(\alpha)$

The pitch angle can have values between 0 and 180 degrees. The pitch angle is a simple way to describe the charged particle's velocity with respect to the magnetic field.

In order to understand how the pitch angle is related to the trapping of a charged particle in the earth's magnetic field equation 2.1.30 can be expressed as

$$\frac{\varepsilon_\perp}{B} = \text{constant} = \frac{mv_\perp^2}{2B} = \left(\frac{mv^2}{2}\right)\frac{\text{Sin}^2(\alpha)}{B}$$

where $\dfrac{1}{2}mv^2$ is the total kinetic energy and is assumed to remain constant. Therefore, the knowledge of the pitch angle and magnetic field at any location along the particle's trajectory is useful in determining the pitch angle and magnetic field at another location along the trajectory.

(2.1.35) $\dfrac{\text{Sin}^2(\alpha_1)}{B_1} = \dfrac{\text{Sin}^2(\alpha_2)}{B_2}$ (the subscripts 1 and 2 represent different

locations)

As the particle travels along the direction of the field lines and eventually approaches a location closer to the earth, the magnetic field increases and the magnitude of the pitch angle approaches 90 degrees. At this point, called the mirror point (or turning point), all of the kinetic energy is due to the $v_\perp$ component of the velocity. At the mirror point the $v_\parallel$ component is zero so the particle is no longer moving in the direction of the magnetic field lines and the direction of $v_\parallel$ reverses. The particle turns around and travels back down the magnetic field line toward another location where the magnetic field has the same magnitude as the mirror point and the magnitude of the pitch angle again becomes 90 degrees. This point is called the conjugate point of the original mirror point. The magnetic field at the mirror point (B_{mirror}) is

(2.1.36) $B_{mirror} = \dfrac{B_0}{Sin^2(\alpha_0)}$ (B_0 is the magnetic field at the magnetic equator)

The mirroring (often referred to as magnetic trapping) is caused by the converging magnetic field lines at the magnetic north and south poles of the earth. The process of mirroring can be understood physically by studying the field geometry.[10] Figure 2.1.4 shows a converging geometry of a magnetic field. A particle at point 1 moving in this field at the instant shown has a velocity vector into the page such that $\vec{v} = -v_x$. (All directions are based on the axis shown on Figure 2.1.4 where vectors with directions parallel to the y axis are considered parallel components and vectors with directions parallel to the x and z axes are considered perpendicular components of the vector.) At point 1 a negatively charged particle experiences a force $F_y = qv_x B_z$ that accelerates the particle in the positive y-direction and is parallel to the magnetic field of line 2. The force in the F_y-direction acts to slow the particle in the parallel direction when approaching the converging field or increase the speed of the particle in the parallel direction as the particle moves away from the converging field. This same force, F_y, causes the particle, after stopping in the negative y-direction, to turn around and accelerate off toward the conjugate point. The particle also experiences a force in the negative z-direction where $F_z = -qv_x B_y$. This force defines the value for the centripetal force and is considered

<hr>

[10] W. N. Hess, *Introduction to Space Science*, (New York: Gordon and Breach Science Publishers, 1965), 29.

perpendicular to the magnetic field of line 2. At the turning point (mirror point) the particle has no velocity in the y-direction and all of the velocity is perpendicular to magnetic field line 2. If the field did not converge then the B_z component would be zero and the force parallel to line 2 would equal zero. The particle in the non-converging field would feel no force in the parallel direction of the B field and the particle would continue to follow the lines of force with a spiraling motion with a gyro-radius defined by

$$r_c = \frac{mv_\perp}{qB_y} \text{ where } v_\perp = \sqrt{v_x^2 + v_z^2} = \text{const.}$$ In the case of a non-converging magnetic field,

the y component (or parallel component) of the velocity would remain constant. Converging magnetic field lines are essential elements of magnetic traps or magnetic bottles.
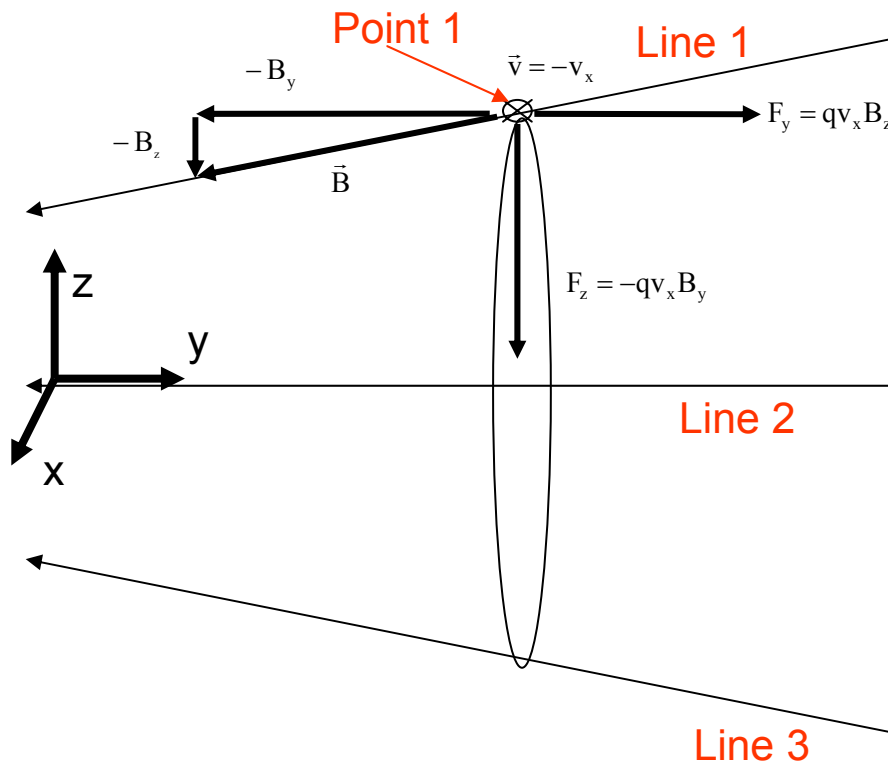
Figure 2.1.4: Sketch of a particle gyrating in a converging magnetic field. The particle is subject to two forces, one that produces the circular motion due to $B_{\parallel}$ and another that pushes the particle away from the stronger field region due to $B_\perp$.

2.2. GUIDING CENTER APPROXIMATION

From studying the trajectory of the electron in the dipole field, one notes that the electron spirals around the magnetic field lines while traveling along the same general direction as the magnetic field. The particle's velocity vector was shown at point 1 on Figure 2.1.4 to have a parallel component and perpendicular component to field line 2. If the electron was viewed by an observer moving along the field lines with the parallel component of the electron's velocity then the observer would record an electron spinning around in a loop that would have the largest radius at the equator and the smallest radius at the mirror points. The perpendicular speed of the electron, in the frame of the observer, would be least at the equator and greatest at the turning point. The reference frame of this observation such that an observer is moving with the parallel component of velocity leads to a guiding center approximation. The guiding center is used to describe the trajectory the particle as if it were moving along at the center of the gyro-orbit of the particle with only the parallel component of the velocity. This approach simplifies the trajectory of a charged particle moving in a magnetic field by neglecting the gyro-motion of the particle.

It will be shown that the guiding center approximation trajectories match the full time integration techniques of the Lorentz force, and that the number of time steps required for the guiding center numerical simulation is significantly reduced. Note that the bounce period (defined as twice the time required for a particle to travel from one conjugate point to another) of a 2-MeV electron at 400 km above the equator is on the order of 0.1 s. The relatively short bounce period, among other things, imposes a definite limit to the maximum size of the time step if the particles are tracked individually using the guiding center computational techniques. The maximum size of the time step is some fraction of the bounce period.

16

The concept of the guiding center is developed in several plasma and space physics texts.[11,12,13] In general location of the guiding center (r_{gc}) for the dipole field is defined as

(2.2.1) $\vec{r}_{gc} = \vec{r} - \vec{r}_c$

where $\vec{r}$ is the position vector of the particle from the center of the earth (center of the dipole) and r_c (the magnitude is the Larmor radius defined by equation 2.1.19) is the position vector of the particle with respect to the center of gyration along the magnetic field lines. The direction of $\vec{r}_c$ is radially inward toward the center of the gyro-radius. Recall the Lorentz force on the spiraling particle is $\vec{F} = q\vec{v} \times \vec{B}$.

The Lorentz force is also written using $\omega_c^2 = \dfrac{v_\perp^2}{r_c^2} = \dfrac{q^2 B^2}{m^2}$.

(2.2.2) $m\omega_c^2 \vec{r}_c = q\vec{v} \times \vec{B}$.

Next by defining the velocity of the charged particle as

$\vec{v} = v_\parallel + v_\perp$

and by substituting equation 2.1.20 into equation 2.2.2

(2.2.3) $mv_\perp = r_c qB$.

From equation 2.2.3, an equation for the perpendicular component of the momentum is developed.

$p_\perp = r_c qB$

By definition, the $\vec{r}_c$ vector is perpendicular to the magnetic field vector, $\vec{B}$, so the perpendicular component of the momentum, $\vec{p}_\perp$, is written

(2.2.4) $\vec{p}_\perp = q\left(\vec{r}_c \times \vec{B}\right)$.

[11] F. F. Chen, *Introduction to Plasma Physics and Controlled Fusion, Volume 1: Plasma Physics*, 2nd ed. (New York: Plenum Press, 1984).

[12] George K. Parks, *Physics of Space Plasmas: An Introduction*, 2nd ed. (Colorado: Westview Press, 2004).

[13] W. N. Hess, *Introduction to Space Science*, (New York: Gordon and Breach Science Publishers, 1965).

Finally, by crossing both sides with $\vec{B}$, an expression for the Larmor radius vector is

(2.2.5) $\qquad \vec{r}_c = -\dfrac{\vec{p}_\perp \times \vec{B}}{qB^2}$.

Now combining equations the guiding center vector from equation 2.2.1 becomes

(2.2.6) $\qquad \vec{r}_{gc} = \vec{r} + \dfrac{\vec{p}_\perp \times \vec{B}}{qB^2}$

By allowing the guiding center to change as the particle moves along the field lines and taking the time derivative of both sides of equation 2.2.6 becomes

(2.2.7) $\qquad \dfrac{d\vec{r}_{gc}}{dt} = \dfrac{d\vec{r}}{dt} + \dfrac{\dfrac{d\vec{p}_\perp}{dt} \times \vec{B}}{qB^2}$.

The development of the guiding center approximation assumes that the force due to the magnetic field plus some other force or forces act on the guiding center. The net force acting on the guiding center of the particle using the guiding center approximation is

$$\vec{F}_{total} = q\vec{v} \times \vec{B} + \sum \vec{F} .$$

$\vec{F}$ is some non-magnetic force or forces acting perpendicular to the magnetic field. In other words,

$$\dfrac{d\vec{p}_\perp}{dt} = \vec{F}_{total-\perp} = q\vec{v} \times \vec{B} + \sum \vec{F}_\perp .$$

The next step is to recall that the simple definition the velocity of the particle is

$$\dfrac{d\vec{r}}{dt} = \vec{v} .$$

Now assume that only one additional force acts on the particle so that equation 2.2.6 becomes

(2.2.7) $\qquad \dfrac{d\vec{r}_{gc}}{dt} = \vec{v} + \dfrac{\left(q\vec{v} \times \vec{B} + \vec{F}\right) \times \vec{B}}{qB^2}$

(2.2.8) $\qquad \dfrac{d\vec{r}_{gc}}{dt} = \vec{v} + \dfrac{\left(q\vec{v} \times \vec{B}\right) \times \vec{B} + \vec{F} \times \vec{B}}{qB^2}$.

18

Using the vector triple product of $\left(q\vec{v}\times\vec{B}\right)\times\vec{B}$ and recalling that $\vec{v}=v_{\perp}+v_{\parallel}$

equation 2.2.8 becomes

$$\frac{d\vec{r}_{gc}}{dt}=\left(v_{\perp}+v_{\parallel}\right)+\frac{\left(q\left(v_{\perp}+v_{\parallel}\right)\times\vec{B}\right)\times\vec{B}+\vec{F}\times\vec{B}}{qB^{2}}$$

$$\frac{d\vec{r}_{gc}}{dt}=\left(v_{\perp}+v_{\parallel}\right)+\frac{\left(qv_{\perp}\times\vec{B}\right)\times\vec{B}+\vec{F}\times\vec{B}}{qB^{2}}=\left(v_{\perp}+v_{\parallel}\right)+\frac{\vec{F}\times\vec{B}-qB^{2}v_{\perp}}{qB^{2}}$$

(2.2.9) $\qquad \frac{d\vec{r}_{gc}}{dt}=v_{\parallel}+\frac{\vec{F}\times\vec{B}}{qB^{2}}$.

Equation 2.2.9 describes the velocity of the guiding center particle in terms of

parallel and perpendicular components of the velocity. The $\dfrac{\vec{F}\times\vec{B}}{qB^{2}}$ component of the

equation actually describes the guiding center velocity perpendicular to the direction of

the magnetic field. The velocity perpendicular to the magnetic field caused by the

force $\vec{F}$ is called the drift velocity of the guiding center. The drift velocity is always

perpendicular to the magnetic field and may cause the particle to drift east-west or in the

$\hat{r}$ -direction. The guiding center velocity parallel to the magnetic field describes the

particle's trajectory along the direction of the magnetic field lines. There are several drift

velocities described in Chen,[14] but the two most important drift velocities for modeling

charged particles trapped in the dipole field are the grad-B drift and the curvature drift.

When electric fields are present there is also an $\vec{E}\times\vec{B}$ force that causes a drift in the radial

direction.

2.2.1. Grad-B Drift

One of the forces that cause the guiding center of the particle to drift east-west in

the earth's dipole field is due to the gradient in the magnetic field. The drift is known as

the grad-B drift, $\vec{W}_{\nabla B}$. One might expect an electron with a velocity perpendicular to a

homogenous magnetic field to circle around the magnetic field lines with a constant

---

[14] Chen, 19 - 43.

radius given by equation 2.1.19. The electron would orbit the magnetic field with a frequency given by equation 2.1.20. If the field were constant and homogeneous then the particle's orbit would continue to repeat without change.

So how does a gradient in the magnetic field, like the gradient of a dipole field, alter the trajectory of a charged particle? To answer the question, consider what happens if an electron is initialized at the magnetic equator of the earth with a velocity vector that is perpendicular to the earth's magnetic field. Does the electron continue to repeat identical orbits? Or does the particle drift in a preferred direction with similar, but non identical orbits? The answer is first demonstrated Figure 2.2.1.1 where an electron is given an initial velocity perpendicular to the magnetic field and the magnetic field has a gradient in the magnetic field equal to that of the earth. The gradient of the magnetic field and magnetic field used in the example of gradient drift shown in Figure 2.2.1.1 is that of the dipole field of the earth at 400 km above the surface of the earth and on the magnetic equator. If the magnetic field did not have a gradient then the particle would continue to repeat the same orbit like that of a particle orbiting a homogeneous magnetic field. The modeled electron does not, however, repeat identical orbits, but instead drifts slowly to the east. Even though the particle's energy is conserved (magnetic fields do no work), the particle does not close on the original orbit and experiences a drift perpendicular to the magnetic field. The drift is caused by a gradient in the magnetic field.
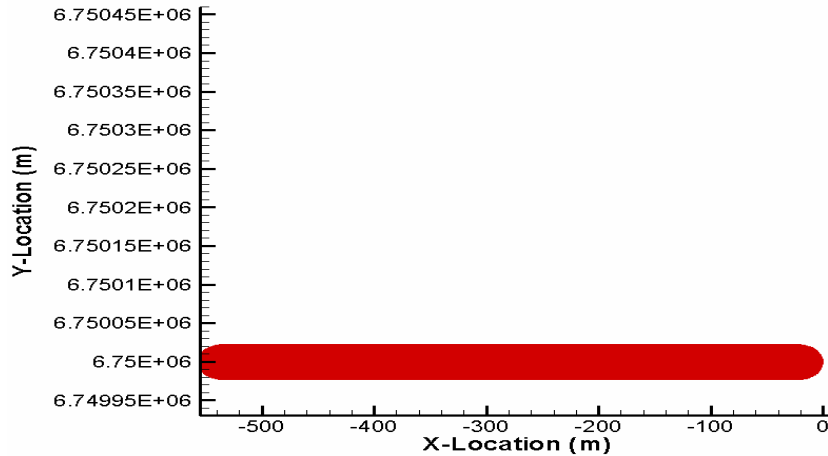
Figure 2.2.1.1: The gradient drift of an electron is shown given the initial conditions: x=0 m, Vx=0 m/s, y=6,750,000 m, Vy=1x108 m/s, z=0 m, Vz=0 and a total simulation time of 1 second. The red area traces the almost path of an electron. The electron is has an initial velocity that is only perpendicular to the field. The electron does not drift in the z direction, but drifts in the negative x-direction (east). The analytical predictions are that the guiding center drift velocity should be -511 m/s and the particle should drift 511 m. By subtracting the radius of orbit from the distance shown on the figure, the guiding center is shown to drift approximately 510 m using the computational methods.

The physical explanation for the gradient drift is that when the electron with a perpendicular component of velocity spirals around the field line, the electron "feels" a larger magnetic field and force when closer to the earth (center of the dipole) and a smaller magnetic field and force on the outside of the orbit around the field line. The result is that from equation 2.1.19 ($r_c = \gamma m \dfrac{v_\perp}{qB}$), r_c is slightly smaller on the inside of the orbit compared to the outside, r_c, of the orbit. This difference between the gyro-radius of curvature as the particle spirals around the field lines causes the guiding center of the particle to drift with each orbit. This is the basis of the guiding center drift.

An exaggerated gradient of the magnetic field is shown in Figure 2.2.1.2.

21
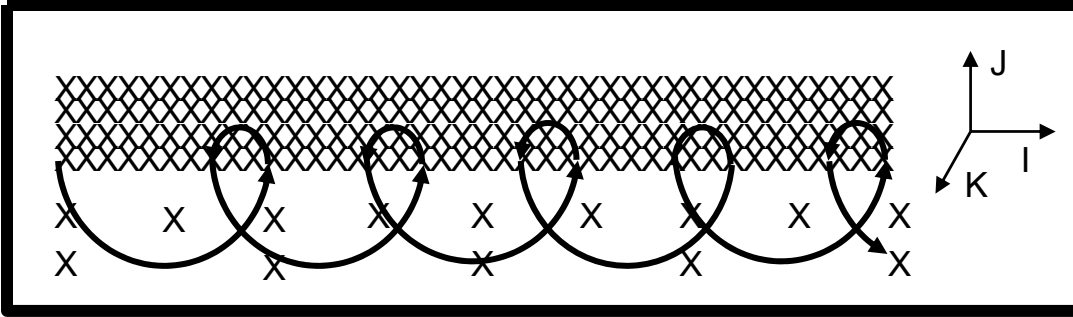
Figure 2.2.1.2: The grad-B drift is demonstrated. The gradient and magnetic field strength is indicated by the density of Xs. The radius of curvature of the positive particle is smaller when the magnetic field is larger as expected from equation 2.2.3. The magnetic gradient causes a drift from left to right. The direction of the magnetic field is in the negative-K direction (into the paper).

The gradient in the field of Figure 2.2.1.2 causes the ion with an initial velocity, $\vec{v}_0 = -v_y \hat{j}$, perpendicular to the magnetic field to drift to the right in the figure instead of repeating a circular orbit. The larger radius of curvature in the region of reduced magnetic field is responsible for the drift. If the particle were an electron then the drift would be in the opposite direction.

In order to determine the analytic expression for the gradient drift one evaluates the Lorentz force, computes the time-average force $< \vec{F} >$, and determines the perpendicular component of the guiding center drift resulting from the magnetic field gradient. In Figure 2.2.1.2 the guiding center of the particle is in the I-direction (toward the right side of the page.) The average Lorentz force in the I-direction is

(2.2.1.1) $< F_i >=< qv_y B_z >$.

However, the time average y-component of the velocity $<v_y> = 0$ because the particle spends as much time moving in the positive J-direction as it spends moving in the negative J-direction. The result is that

(2.2.1.2) $< F_i >= 0$.

The average force in the J-direction (the J-direction is shown on Figure 2.2.1.2) is

(2.2.1.3) $< F_j >=< -qv_x B_z >$.

22

Using the Taylor expansion of the magnetic field about $(i_0 j_0)$, the expression for $<F_j>$ becomes

(2.2.1.4) $F_j \approx -qv_i\left[B_0 + J(\frac{\partial B_k}{\partial J}) + ...\right].$

Equation 2.2.1.4 is valid to second order if $r_c << L$ where r_c is still the cyclotron radius and L is the scale length of the gradient $\frac{\partial B_k}{\partial J}$.[15] By using the zeroth-order solution for v_i

$$v_i = v_\perp \text{Cos}(\omega_c t)$$

and the J location

$$J = r_c \text{Cos}(\omega_c t) = (\frac{v_\perp}{\omega_c})\text{Cos}(\omega_c t)$$

both substituted into equation 2.2.1.4 yields

$$F_j \approx -qv_\perp \text{Cos}(\omega_c t)\left[B_0 + (\frac{v_\perp}{\omega_c})\text{Cos}(\omega_c t)\frac{\partial B_k}{\partial J} + ...\right].$$

The time average of the force, $<F_j>$ becomes

(2.2.1.5) $<F_j> \approx \left[-qv_\perp B_0 <\text{Cos}(\omega_c t)> - \frac{qv_\perp^2}{\omega_c} <\text{Cos}^2(\omega_c t)> \frac{\partial B_k}{\partial J} + ...\right].$

The first term, $qv_\perp B_0 <\text{Cos}(\omega_c t)>$, of equation 2.2.1.5 time-averages to zero and the $<\text{Cos}^2(\omega_c t)>$ of the second term time-averages to $\frac{1}{2}$. The time-average force acting on the particle in the J-direction becomes

(2.2.1.6) $<F_j> = -\frac{qv_\perp^2}{2\omega_c}\frac{\partial B_k}{\partial J}.$

Applying the time average force of equation 2.2.1.6 to the guiding center velocity, $\frac{d\vec{r}_{gc}}{dt} = v_\parallel + \frac{\vec{F} \times \vec{B}}{qB^2}$, yields an expression for the gradient drift velocity, $\vec{W}_{\nabla B}$, of

---

[15] Parks, 104.

(2.2.1.7) $\qquad \vec{W}_{\nabla B} = -\dfrac{v_\perp^2}{2B^2\omega_c}\dfrac{\partial B_k}{\partial J}(\hat{j}\times\vec{B})$

where $\vec{B} = -B_k\hat{k}$.

Equation 2.2.1.7 is developed for the special case of Figure 2.2.1.2 when the magnetic field is directed only in the negative K-direction and the average force is directed in the negative J-direction. In this case the guiding center of the particle drifts in the positive I direction with a velocity of $W_{\nabla B} = \dfrac{v_\perp^2}{2B^2\omega_c}\dfrac{\partial B_k}{\partial J}\hat{i}$. Equation 2.2.1.7 can be written more generally by replacing $\dfrac{\partial B_k}{\partial J}$ with $\vec{\nabla}B$, where B is the magnitude of $\vec{B}$, such that the gradient can be in any direction.

(2.2.1.8) $\qquad \vec{W}_{\nabla B} = \dfrac{v_\perp^2}{2B^2\omega_c}(\vec{B}\times\vec{\nabla}B)$

$$\omega_c = \dfrac{v_\perp}{r_c}$$

(2.2.1.9) $\qquad \vec{W}_{\nabla B} = \dfrac{r_c v_\perp}{2B^2}(\vec{B}\times\vec{\nabla}B).$

Another useful form of equation 2.2.1.9 is written using

(2.2.1.10) $\qquad B\vec{\nabla}B = \dfrac{\vec{\nabla}B^2}{2}$

and

$$r_c = \dfrac{mv_\perp}{qB}.$$

In equation 2.2.1.10, $B^2 = |\vec{B}\bullet\vec{B}|$.

The guiding center drift[16] becomes

(2.2.1.11) $\qquad \vec{W}_{\nabla B} = \dfrac{mv_\perp}{2qB^4}(\vec{B}\times\dfrac{\vec{\nabla}B^2}{2}).$

The components of the gradient of the square of the magnetic dipole field are

---

[16] Chen, 28.

$$\nabla B^2{}_x = -\frac{3M^2 x(x^2 + y^2 + 5z^2)}{(x^2 + y^2 + z^2)^5},$$

$$\nabla B^2{}_y = -\frac{3M^2 y(x^2 + y^2 + 5z^2)}{(x^2 + y^2 + z^2)^5},$$

$$\nabla B^2{}_z = -\frac{12M^2 z^3}{(x^2 + y^2 + z^2)^5}.$$

The grad-B drift is one of the causes of the perpendicular drift of the guiding center in a the earth's dipole field. In order to properly model the trajectory of a charged particle in a magnetic field using the guiding center, one must account for the movement of the charged particle along the magnetic field lines, $v_{||,}$ as well as the movement of the particles perpendicular to the magnetic field, $v_\perp$. The gradient in the magnetic field is one explanation used to model the drift of the particle. The significance of the drift becomes obvious when the Lorentz force is used to model the complete trajectory of the charged particle in the magnetic field and the results are compared to the guiding center approximation. If the gradient drift is included with the guiding center approximation, the modeled guiding center trajectory does not match the complete model using the Lorentz force. Also of important note is that the gradient drift has no dependence on the parallel component of the velocity and the charge dependence of equation 2.2.1.11 provides an analytical explanation of why positive and negative charges drift in opposite directions.

2.2.2. Curvature Drift

Another force causing the particle to drift perpendicular to the magnetic field is the result of the curvature of the magnetic field lines and is known as the curvature drift, $\vec{W}_{curve}$. The curvature drift is only a function of the parallel component of the velocity. When the guiding center particle moves along a curved field line at a distance, r_{curve} (distance from magnetic field lines to the center of the arc of the magnetic field line) the particle, in a non-inertial reference frame, experiences a centrifugal force directed radially away from the center of the arc. The centrifugal force has a magnitude of

$F_{centrifugal} = \dfrac{mv_{||}^2}{r_{curve}}$. The direction of the centrifugal force is radially outward away from the center of the arc. This is not to be confused with a centripetal force that is directed

radially inward toward the center of the arc and is a force used to describe the force acting on a particle in an inertial reference frame. As the particle spirals around the magnetic field line, the centrifugal force is greatest on the inside of the field line when r_{curve} is smaller (closer to the center of the arc of the field line) and is smaller outside the field line (further away from the center of the arc of the field line). When the right-hand-rule and the charge dependence are applied to equation 2.2.9, one observes that centrifugal force acting on the guiding center causes the electron to drift in the same direction as the gradient drift.

Therefore, the force caused by the curvature of the field lines and used in equation 2.2.9, $\dfrac{d\vec{r}_{gc}}{dt} = v_{\parallel} + \dfrac{\vec{F} \times \vec{B}}{qB^2}$ is the centrifugal force[17] written as

$$(2.2.2.1) \qquad \vec{F}_{drift} = \vec{F}_{centrifugal} = mv_{\parallel}^2 \frac{\vec{r}_{curve}}{r_{curve}^2} \ .$$

The curvature drift expression is therefore written

$$(2.2.2.2) \qquad \vec{W}_{curve} = \frac{mv_{\parallel}^2}{qB^2} \frac{\vec{r}_{curve} \times \vec{B}}{r_{curve}^2} \ .$$

The $\vec{r}_{curve}$ vector points to the center curvature of the magnetic field line and is perpendicular to $\vec{B}$. The magnitude of $\vec{r}_{curve}$ has different values for different locations along a magnetic field line because the radius of the arc of the field line in the dipole field is not constant as was shown in Figure 2.1.2.

In order to write the curvature drift equation such that it looks similar to the gradient drift equation, consider now an arc element, $d\vec{s}$, along the direction of $\vec{B}$. The unit vector pointing in the $\vec{B}$ direction is

$$(2.2.2.3) \qquad \hat{e}_1 = \frac{\vec{B}}{B} \ .$$

The unit vector pointing from the center of the arc of path length ds is

$$(2.2.2.4) \qquad \hat{e}_2 = -\frac{\vec{r}_{curve}}{r_{curve}} \ .$$

[17] J.G. Roederer, *Dynamics of Geomagnetically Trapped Radiation*, (Heidelberg: Springer-Verlag Berlin, 1970), 16.

Now let $\hat{e}_3 = \hat{e}_1 \times \hat{e}_2$ and

$$ds = r_{curve}d\phi \quad \text{where}$$
$$\hat{e}_2 d\phi \approx d\hat{e}_1$$
$$\hat{e}_2 ds = r_{curve}d\hat{e}_1$$

and the radius of curvature of the field is defined by

$$\frac{\hat{e}_2}{r_{curve}} = \frac{\partial \hat{e}_1}{\partial s}.$$

The ratio of $-\dfrac{\vec{r}_{gc}}{r_{gc}^2}$ is shown by Parks to be equal to

$$(2.2.2.5) \qquad -\frac{\vec{r}_{gc}}{r_{gc}^2} = \frac{\partial}{\partial s}(\frac{\vec{B}}{B}).$$

By expanding equation 2.2.2.5

$$\frac{\vec{r}_{gc}}{r_{gc}^2} = -\frac{1}{B}\frac{\partial \vec{B}}{\partial s} + \frac{\vec{B}}{B^2}\frac{\partial B}{\partial s} = -\frac{1}{B}\frac{\partial \vec{B}}{\partial s}$$

where

$$\frac{1}{B}\frac{\partial \vec{B}}{\partial s} = \frac{1}{B^2}(\vec{B}\bullet\vec{\nabla})\vec{B}$$

yields

$$(2.2.2.6) \qquad \frac{\vec{r}_{gc}}{r_{gc}^2} = -\frac{1}{B^2}(\vec{B}\bullet\vec{\nabla})\vec{B}.$$

From these equations the curvature drift is expressed as

$$\vec{W}_{curve} = \frac{mv_{\parallel}^2}{qB^2}\vec{B}\times(\vec{B}\bullet\vec{\nabla})\vec{B}$$

$$(2.2.2.7) \qquad \vec{W}_{curve} = \frac{mv_{\parallel}^2}{qB^4}\vec{B}\times\vec{\nabla}\left(\frac{B^2}{2}\right)$$

A quick look at equation 2.2.2.7 reveals that for a given magnetic field curvature, the curvature drift is only a function of the parallel velocity. Like the gradient drift, the

27

charge determines the direction of the curvature drift.[18] This guiding center drift, as suggested by Roederer,[19] is satisfied when there are no currents and $\nabla \times \vec{B} = 0$. The effect of electric fields on the guiding center approximation was not examined or investigated. As a word of caution, if electric fields are included in the analysis and allowed to act on the charged particles then the guiding center approximation derived in this dissertation may no longer remain valid and warrants further study. For all of the work reported in this dissertation, the electric fields are considered small enough to ignore.

The physical nature of the curvature drift was found to be less obvious than that of the gradient drift. Some authors described the force as the centripetal force and others described the force as the centrifugal force. The correct description is the centrifugal force described in the non-inertial reference frame of the particle. In order to demonstrate the predicted curvature drift, the proven Boris Push computational model was used in a nonphysical computational example to show the actual curvature drift of a particle in the absence of a gradient in the magnetic field. Starting with a circular magnetic field in the x-y plane, a particle is initialized with a velocity only in this plane. As the particle winds around this circular magnetic field, it experiences a "curvature drift" in the z direction as shown in the Figure 2.2.2.1 and Figure 2.2.2.2. The magnetic field applied to the electron in Figure 2.2.2.1 and Figure 2.2.2.2 was

$$(2.2.2.8) \qquad \vec{B} = B_0 \left(Sin(\theta)\hat{i} - Cos(\theta)\hat{j} \right)$$

such that $B_{mag} = B_0$ and the gradient of B was equal to zero $\left(\vec{\nabla} B = 0 \right)$. The charge particle drifts slowly in the positive z-direction. The observed drift of the particle was caused by the curvature of the field lines and not a gradient in the magnetic field.

---

[18] Parks, 104.

[19] Roederer, 140.
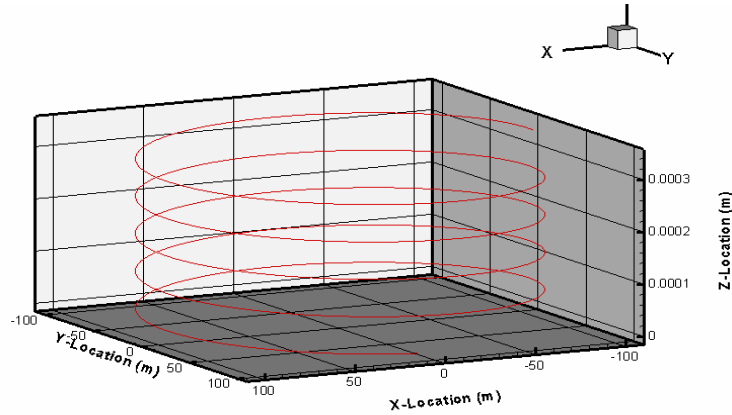
Figure 2.2.2.1: An example of the curvature drift of a very slow electron spiraling around a magnetic field with $\vec{\nabla}B = 0$. A nonphysical magnetic field was used to model the curvature drift of a slow moving electron. The drift in the positive z-direction is small because the electron speed is only 100 m/s, the radius is 100 m, and the run time is only 30 seconds. The field is described bye equation 2.2.2.8. The electron had no initial velocity in the z-direction. The electron's initial velocity was in the plane of the magnetic field. The magnitude of the magnetic field is 5x10-5 T everywhere.
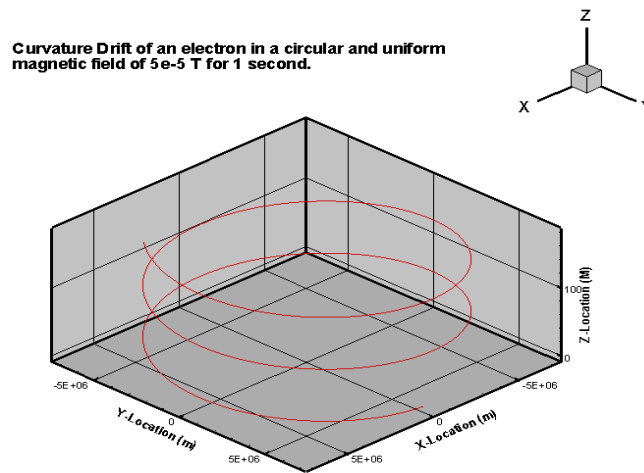
Figure 2.2.2.2: This is another non-physical example (similar to Figure 2.2.2.1) of the curvature drift of a .6 M eV electron moving in a circle with a radius of 6,750,000m (400 km above earth surface) with an equivalent magnitude of the magnetic field of the earth's dipole 400 km above the equator. The electron was initialized with only x and y components of velocity. The field is described by $\vec{B} = B_0\left(Sin(\theta)\hat{i} - Cos(\theta)\hat{j}\right)$. The particle did not have any initial velocity in the z-direction. The magnitude of the magnetic field is 5x10-5 T everywhere. The $\vec{\nabla}B = 0$ so the only drift is caused by the curvature of magnetic field lines. The electron drifts about 150 m in one second. If there were no curvature drift then the orbit of the electron would continue to repeat with no net movement in the z-direction.

29

2.2.3. Guiding Center Drift

A simple comparison between the gradient drift and the curvature drift in the dipole field reveals that both forces cause the particle to drift in the same direction and always perpendicular to the magnetic field. For the dipole field of Figure 2.1.1 the guiding center drift causes the charged particle to drift in an eastward or westward direction depending on the charge of the particle. From Figure 2.2.1.1 one observes that the guiding center of the negatively charged particle drifts about 510 m in the negative x-direction in 1 second due to the grad-B drift (this is identical to the grad-B drift at the magnetic equator of the earth). When an identical particle was modeled to travel in the field of Figure 2.2.2.2 the particle drifted about 150 m in one second and this drift was caused by the curvature of the magnetic field. In both cases the drift was either caused uniquely by only a gradient or a curvature effect. The magnitude of the magnetic field was approximately the same in both cases and was equal to the magnetic field 400 km above the surface on the magnetic equator of the earth where the drift period of a fission fragment with a velocity of ~ 2,000 km/s is on the order of an hour. Clearly both contribute the overall perpendicular drift of the guiding center and are combined to write a general expression for the total drift equation of the guiding center

$$(2.2.3.1) \qquad \vec{W}_{Drift} = \frac{m}{qB^4}\left(v_{\parallel}^2 + \frac{v_{\perp}^2}{2}\right)\vec{B} \times \nabla\left(\frac{B^2}{2}\right).$$

Equation 2.2.3.1 describes the perpendicular (east or west) drift velocity of the guiding center where the perpendicular direction can be found from equation 2.2.9 and the right-hand-rule. The particle also continues to move along the direction of the field line with a parallel velocity. As described earlier, the particle's parallel velocity is greatest at the magnetic equator and is zero at the conjugate points. The magnitude of the drift velocity is therefore also greatest at the magnetic equator and least at the conjugate points. If there is no energy loss then the magnetic moment is constant and the total energy of the particle is constant. By substituting in 2.1.25, $\mu B = \frac{1}{2}mv_{\perp}^2$, equation 2.2.3.1 can also be written

$$(2.2.3.2) \qquad \vec{W}_{\text{Drift}} = \frac{m}{qB^4}\left(v_{\parallel}^2 + \frac{\mu B}{m}\right)\vec{B} \times \nabla\left(\frac{B^2}{2}\right).$$

What is important is that the drift velocity is only in a direction that is perpendicular to the magnetic field and has charge dependence for the direction of the drift. The drift velocity, coupled with the velocity parallel to the magnetic field will serve as the basis for the guiding center approximation used for modeling charged particles.

2.3.   ADIABATIC INVARIANTS

A useful exercise necessary to understand the limits and uses of the guiding center approximation is the development of three adiabatic invariants. In order to use the guiding center approximation without computational corrections, the adiabatic invariants must remain relatively constant. One can prove that, if the change in the physical property is slow (like the gradient of the magnetic field of the earth) compared to the relevant periods of motion and is not related to the periods, the action integrals are invariant.[20] The constancy of the adiabatic invariants presumes conservation of energy. The three adiabatic invariants introduced below are associated with the magnetic flux (adiabatic invariant J_1), bounce period (from conjugate point to conjugate point) (adiabatic invariant J_2), and the drift period of the charged particle around a dipole (adiabatic invariant J_3). The bounce period and drift period of a relativistic electron can range from a fraction of a second to thousands of seconds, depending on the pitch angle and the speed. The bounce period and drift period of a fission fragment can range from seconds to thousands of seconds, also depending of the pitch angle and the speed.

2.3.1.   First Adiabatic Invariant

The first adiabatic invariant is introduced by considering the action integral of the mechanical system where q_i and p_i are the canonical coordinates and the canonical momentum.

$$(2.3.1.1) \qquad J_1 = \oint p_i dq_i$$

---

[20] Jackson, 592.

The integral is over one complete cycle of q_i and the changes in the physical properties of the system are considered slow. For the dipole, the magnetic field varies like $1/r^3$ and the change during electrons gyro-orbit and bounce from conjugate point to conjugate point is slow and adiabatic. Equation 2.3.1.1 is written

(2.3.1.2) $\qquad J_1 = \oint \vec{P}_\perp \bullet d\vec{s}$

where $\vec{P}_\perp$ is the perpendicular component of the momentum with respect to the direction of the magnetic field and $d\vec{s}$ is the differential path along the circular orbit of the electron as it spirals around the magnetic field lines[21].

(2.3.1.3) $\qquad \vec{P}_\perp = \gamma m v_\perp + q\vec{A}$

where $\vec{A}$ is the vector potential. Therefore, the invariant action integral becomes

$$J_1 = \oint (\gamma m v_\perp + q\vec{A}_\perp) \bullet d\vec{s}$$

(2.3.1.4) $\qquad J_1 = \oint \gamma m v_\perp ds + \oint q\vec{A}_\perp \bullet d\vec{s}$

Both the perpendicular component of the velocity and the vector potential are parallel to the path of the electron. By applying Stokes theorem to the right-hand integral of equation 2.3.1.4, the expression is written

$$J_1 = \oint \gamma m v_\perp d\vec{s} + \oint q\vec{A}_\perp \bullet d\vec{s}$$
$$J_1 = \gamma m v_\perp 2\pi r_c + q\oint \vec{B} \bullet d\vec{A}$$

(2.3.1.5) $\qquad J_1 = \gamma m v_\perp 2\pi r_c - qB\pi r_c^2$

Based on the assumption that J_1 is constant and recalling that $v_\perp = \omega_c r_c$ and $qB = \omega_c \gamma m$ then

$$J_1 = 2\pi \gamma m \omega_c r_c^2 - \pi \gamma m \omega_c r_c^2$$
$$J_1 = \pi \gamma m \omega_c r_c^2 = \text{const}$$

(2.3.1.6) $\qquad \gamma m v_\perp r_c = \text{const} .$

---

[21] Jackson, 591.

Combining the expression for the gyro-radius and perpendicular component of the

momentum, $r_c = \dfrac{\gamma m v_\perp}{qB}$ and $p_\perp = \gamma m v_\perp$, leads to a useful expression derived from the

first adiabatic[22]

(2.3.1.7) $\qquad \dfrac{p_\perp^2}{B} = \text{const}.$

Consider again that the magnetic dipole moment is

$$\mu_B = \text{Area} \times \text{Current}$$

$$\mu_B = \pi r_c^2 \dfrac{q v_\perp}{2\pi r_c} = \dfrac{r_c q v_\perp}{2}$$

The $v_\perp$ can be expressed in the form of

(2.3.1.8) $\qquad v_\perp = \dfrac{2\mu_B}{q r_c}.$

From equation 2.3.1.6 $v_\perp$ is written

(2.3.1.9) $\qquad v_\perp = \dfrac{\text{const}}{\gamma m r_c}.$

By setting equation 2.3.1.8 equal to 2.3.1.9 and solving for μ_B

$$\dfrac{\text{const}}{\gamma m r_c} = \dfrac{2\mu_B}{q r_c}$$

$$\mu_B = \dfrac{(\text{const})q}{\gamma m}$$

The result is proof that with slow adiabatic changes and conservation of kinetic energy

then the magnitude of the magnetic dipole moment is constant and conserved.

(2.3.1.9) $\qquad \gamma \mu_B = \text{const}$ (consistent with earlier discussions and assumptions)

Additionally, the magnetic flux through the current loop of the electron must also remain

constant as was assumed (based on $\mu_B = $ constant) in equation 2.1.27 and is now proven

with equation 2.3.1.9.

A closer examination of equation 2.3.1.7 suggests that as the electron approaches

the conjugate point and the magnetic field increases, so does the perpendicular

---

[22] Jackson, 592.

component of the velocity. The increase in $v_\perp$ and the coinciding increase in magnetic field causes r_c to decrease. Eventually, at the mirror point, the parallel component of the momentum approaches zero and all of the momentum is perpendicular to the magnetic field. At the mirror point, all of the energy of the electron is used to generate a magnetic dipole moment required to maintain a constant flux and the constant dipole moment.

Using equation 2.1.26, $\mu_B = \dfrac{mv_\perp^2}{2B}$ where $v_\perp = vSin\alpha$, the value of the magnetic moment is written

(2.3.1.11) $\qquad \mu_B = \dfrac{mv^2 Sin^2\alpha}{2B}.$

Recalling from equation 2.3.1.9 that μ_B is constant, a relationship between the pitch angle, α, and magnetic field at different locations is developed.

(2.3.1.12) $\qquad \dfrac{Sin^2\alpha_1}{B_1} = \dfrac{Sin^2\alpha_2}{B_2}$

The subscripts of equation 2.3.1.12 (associated with α_1, α_2, B_1, and B_2) identify two separate locations along the particles trajectory. Because the pitch angle at the mirror point has a magnitude of 90^0, equation 2.2.1.12 provides a useful relationship used in the simulations.

(2.3.1.13) $\qquad Sin^2\alpha_1 = \dfrac{B_1}{B_{mirror}}$

Equation 2.3.1.12 shows that given the pitch angle and the magnetic field (generally known from the initial conditions of the release of the particle) at any location one can calculate the magnetic field at the mirror point or visa-versa.

Another useful concept and relationship derived from the first adiabatic invariant and equation 2.3.1.13 is the loss cone for trapped particles. Consider that for a particle trapped in the earth's magnetic field there must be some maximum possible value of the magnetic field at the mirror point (B_{max}) due either to a constraint of the magnetic mirror or, in the case of particles trapped in the Earth's dipole field, a minimum altitude below which all of the particle's energy is lost due to collisions with the air. From equation

2.3.1.13 (and the acceptance that a trapped particle has a maximum allowed value of the magnetic field) one derives an expression for the minimum pitch angle of the particle.

(2.3.1.14) $\alpha_{min} = Sin^{-1}(\sqrt{\dfrac{B}{B_{max}}})$

If the particle has a pitch angle less than α_{min} then the particle will not remain trapped and will either collide with the surface of the earth (if no energy loss is assumed) or lose all kinetic energy in the atmosphere (details of ionization energy loss is presented in Chapter V).

The loss cone, as shown in Figure 2.3.1.1 can serve as a screening mechanism and allows one to "ignore" the possibility of trapping of any particles with an initial pitch angle below α_{min}. The problem is slightly complicated when the charged particles continually scatter, change pitch angles, and lose energy in the atmosphere. If the charged particle had changing pitch angles (caused by something like atmospheric scattering), the value of the loss cone angle for screening which particles to track is of limited utility. However, reference to the loss cone is quite common when discussing the cause of early-time losses of particles released into the magnetic fields of the earth.
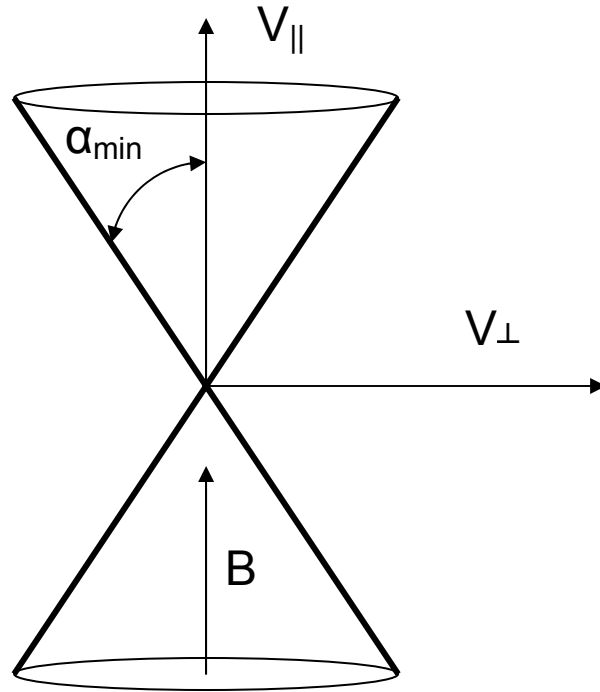
Figure 2.3.1.1: Diagram of the loss cone. Particles inside the loss cone, with a pitch angle less than α_{min}, are not trapped. Particles with a pitch angle greater than α_{min} are trapped in the magnetic bottle.

2.3.2. Second Adiabatic Invariant

The second adiabatic invariant is derived similarly to the first adiabatic invariant.

(2.3.2.1) $\qquad J_2 = \oint \vec{P}_\parallel \bullet d\vec{s}$

where $d\vec{s}$ is the differential of the path length between conjugate point and conjugate point and the momentum vector is parallel to the magnetic field. As the particle moves or "bounces" from mirror point to mirror point, the bounce has an associated bounce frequency. If the second adiabatic invariant is constant in time, dJ_2/dt is equal to zero, then the bounce period is considered constant. If this is constant, then even though the particle drifts to the east or west, the bounce frequency remains constant and is used as a figure of merit for validating the codes and checking the results.

In order to prove that the second adiabatic invariant is constant, Parks[23] uses the following argument. Let

$$\vec{P}_{\|} = \gamma m v_{\|}$$

with a simple substitution for the parallel component of the velocity

$$v_{\|} = \sqrt{V_{total}^2 - v_\perp^2}$$

where non-relativistically

$$v_{total}^2 = \frac{2E_{total}}{m}.$$

Recalling that

$$v_\perp^2 = \frac{2\vec{\mu} \bullet \vec{B}}{m} = \frac{2\mu B}{m} \text{ so that}$$

$$v_{\|} = \sqrt{\frac{2E_{total}}{m} - \frac{2\mu B}{m}} = \sqrt{\frac{2}{m}(E_{total} - \mu B)}$$

and that the total energy is considered a constant. The equation for the second adiabatic invariant has the form

$$(2.3.2.3) \qquad J_2 = \int_a^b \sqrt{\frac{2}{m}(E_{total} - \mu B)} ds .$$

In order for J_2 to be constant the time derivative, dJ_2/dt, must equal zero. The time derivative is written

$$(2.3.2.4) \qquad \frac{dJ_2}{dt} = \frac{\partial J_2}{\partial t} + \left(\frac{\partial J_2}{\partial E}\right)_{s,t} \frac{dE}{dt} + \left(\frac{\partial J_2}{\partial s}\right)_{E,t} \frac{ds}{dt}$$

By expanding and combining equations 2.3.2.3 and 2.3.2.4

---

[23] Parks, 137.

$$\frac{\partial J_2}{\partial t} = \frac{d}{dt}\left(\int_a^b \sqrt{\frac{2}{m}(E_{total} - \mu B)}\,ds\right)$$

$$\frac{\partial J_2}{\partial t} = \left(\int_a^b \frac{1}{\sqrt{\frac{2}{m}(E_{total} - \mu B)}}\left[-\frac{\mu}{m}\frac{\partial B}{\partial t}\right]ds\right) + \left[v_\| \frac{dv_\|}{dt} + \frac{\mu}{m}\frac{\partial B}{\partial t} + \frac{\mu v_\|}{m}\frac{\partial B}{\partial s}\right]*$$

$$\int_a^b \frac{1}{\sqrt{\frac{2}{m}(E_{total} - \mu B)}}\,ds - v_\|\int_a^b \frac{1}{\sqrt{\frac{2}{m}(E_{total} - \mu B)}}\left[\frac{\mu}{m}\frac{\partial B}{\partial s}\right]ds +$$

$$v_\| \frac{1}{\sqrt{\frac{2}{m}(E_{total} - \mu B)}}$$

If the limits of integration are set between the two mirror points (mirror point "a" and mirror point "b") where the $v_\| = 0$ at the mirror points then all terms involving $v_\|$ vanish to zero at the limits of the integration. Additionally, the magnetic field is considered to slowly varying such that $\frac{\partial B}{\partial t} \approx$ constant. The result is

(2.3.2.5) $\qquad \frac{\partial J_2}{\partial t} = -\mu\frac{\partial B}{\partial t}\int_a^b \sqrt{\frac{2}{\gamma m}(E_{total} - \mu B)}\,ds + \mu\frac{\partial B}{\partial t}\int_a^b \sqrt{\frac{2}{\gamma m}(E_{total} - \mu B)}\,ds$.

Therefore the second adiabatic invariant is constant as long as the energy of the particle and $\frac{\partial B}{\partial t}$ both remain constant.[24] The result is then

(2.3.2.6) $\qquad \frac{\partial J_2}{\partial t} = 0$.

As long as equation 2.3.2.6 remains constant then the bounce frequency will remain constant.

The second adiabatic invariance is used to calculate the bounce period, T_b, of charged particle trapped in the Earth's magnetic field. As mentioned, in order for the second adiabatic invariant to remain constant energy must also be conserved. The expression for the bounce period is

[24] T.G. Northrup, *The Adiabatic Motion of Charged Particles*, (New York: Interscience Publishers, 1963), 47.

(2.3.2.7) $\qquad T_b = \int \dfrac{ds}{v_{\parallel}}$

where ds is still the path length from conjugate point to conjugate point and $v_{\parallel}$ is the velocity parallel to the magnetic field.

Recall that, $v_{\parallel} = \sqrt{v^2 - v_{\perp}^2}$ and $v_{\perp}^2 = v^2 \mathrm{Sin}^2\alpha$, so that one can write $v_{\parallel} = \sqrt{v^2(1 - \mathrm{Sin}^2\alpha)}$. Finally by using the expression, $\mathrm{Sin}^2\alpha = \dfrac{B\mathrm{Sin}^2\alpha_0}{B_0}$, the expression for the parrallel component of the velocity becomes

$$v_{\parallel} = v\sqrt{(1 - \dfrac{B\mathrm{Sin}^2\alpha_0}{B_0})}.$$

Using polar coordinates and the dipole field,

(2.3.2.8) $\qquad r = r_0 \mathrm{Sin}^2(\theta)$

and ds, the arc length along the magnetic field line is written

$$ds^2 = dr^2 + r^2 d\theta^2$$

$$ds = \left[\sqrt{\left(\dfrac{dr}{d\theta}\right)^2 + r^2} \right] d\theta$$

$$ds = \sqrt{4r_0^2 \mathrm{Sin}^2(\theta)\mathrm{Cos}^2(\theta) + r_0^2 \mathrm{Sin}^4(\theta)} d\theta$$

(2.3.2.9) $\qquad ds = r_0 \mathrm{Sin}(\theta)\sqrt{(1 + 3\mathrm{Cos}^2(\theta))} d\theta$

The magnetic field can be expressed in polar coordinates using

(2.3.2.10) $\qquad B(r,\theta) = \dfrac{\mu_0 M}{4\pi r^3}\sqrt{1 + 3\mathrm{Cos}^2(\theta)}$

Combining equations 2.3.2.8 and 2.3.2.10

(2.3.2.11) $\qquad \dfrac{B}{B_0} = \dfrac{\sqrt{1 + 3\mathrm{Cos}^2(\theta)}}{\mathrm{Sin}^6(\theta)}$

Equation 2.3.11 is used to is used to establish the expression for the bounce period.[25]

---

[25] Parks, 142.

$$(2.3.2.12) \qquad T_b = 4 \int_{\theta_{max}}^{\pi/2} \frac{r_0 Sin(\theta)\sqrt{(1+3Cos^2(\theta))}d\theta}{v\sqrt{(1-\dfrac{\sqrt{1+3Cos^2(\theta)}}{Sin^6(\theta)}Sin^2\alpha_0)}}$$

The lower of integration, θ_{max}, is found using equations $\dfrac{B_{max}}{B_0} = \dfrac{\sqrt{1+3Cos^2(\theta)}}{Sin^6(\theta)}$ and

$Sin^2\alpha_0 = \dfrac{B_0}{B_{t\,max}}$. The value of θ_{max} is solved using

$$(2.3.2.13) \qquad Sin^6(\theta_{max}) - Sin^2(\alpha_0)\sqrt{1+3Cos^2(\theta_{max})} = 0$$

The solution to the bounce period was first solved by Hamlin et al.[26] The approximate solution for the bounce period is

$$(2.3.2.13) \qquad T_b \approx \frac{4r_0(1.3 - 0.56Sin\alpha_0)}{v}.$$

The equation for the bounce period is useful in validating the computer simulations, but does not represent an exact solution and should be noted as only an approximation. Table 2.3.2.1 lists the bounce period of several different velocities and several different pitch angles.

[26] D.A. Hamlin, R. Karplus, R.C. Vik, K.M. Watson, "Mirror and Azimuthal Drift Frequencies for Geomagnetically Trapped Particles," *J. Geophys. Res., Vol. 66*, 1966: 1.

Speed (m/s)	Pitch Angle (degrees)	Bounce Period (s)
$1.000\times10^{+04}$	15	2990
$1.000\times10^{+04}$	45	2340
$1.000\times10^{+04}$	75	1970
$1.000\times10^{+05}$	15	300.
$1.000\times10^{+05}$	45	234
$1.000\times10^{+05}$	75	196
$1.000\times10^{+06}$	15	29.9
$1.000\times10^{+06}$	45	23.4
$1.000\times10^{+06}$	75	19.6
$1.000\times10^{+08}$	15	0.299
$1.000\times10^{+08}$	45	0.234
$1.000\times10^{+08}$	75	0.197
$2.000\times10^{+08}$	15	0.150
$2.000\times10^{+08}$	45	0.117
$2.000\times10^{+08}$	75	0.098
$2.900\times10^{+08}$	15	0.103
$2.900\times10^{+08}$	45	0.0811
$2.900\times10^{+08}$	75	0.0681

Table 2.3.2.1: The bounce period is shown for different pitch angles at an altitude of 400 km above the equator and different speeds. Equation 2.3.2.13 was used to calculate the bounce periods

While it is obvious that an inelastic collision will change a particle's bounce period, these results also show that the bounce period will change even for elastic collisions if the pitch angle changes. Even if energy is lost, equation 2.3.2.9 might still be used as an approximation for the bounce period.

2.3.3. Third Adiabatic Invariant

The third adiabatic invariant[27] is associated with the drift motion in the azimuthal direction.

(2.3.3.1) $\qquad J_3 = q\Phi_{mag}$

---

[27] M. Schulz, L. J. Lanzerotti, *Particle Diffusion in the Radiation Belts*, (New York: Springer-Verlag, 1974), 12.

In other words, when the third adiabatic invariant is conserved the drift period around the magnetic equator is constant. The procedure for showing that the third adiabatic invariant is conserved is similar to that used for the second invariant.[28,29] Like the first adiabatic invariant where the magnetic flux enclosed by the "current ring" of the electron was constant, one might suspect, with the conservation of energy, that magnetic flux should be conserved by the guiding center gyrating around the equatorial plane of a drift shell. Because the drift period around the earth is on the order of hours and there are often continuous perturbations to the magnetic field, the third adiabatic invariant is often not conserved. However, the drift period of the charged particle is also a useful metric when validating the computational methods in the absence of air, magnetic perturbations, and particle interactions. The charged particle's constant interaction with the atmosphere causes energy loss and scattering. Changes in energy and pitch angle prevent conservation of the third invariant. In general the guiding center east-west drift velocity has been shown to be in the order of 10^4 m/s.

The derivation of the drift period (T_D) is derived by first determining the angular displacement, $\Delta\phi$, for one bounce period.[30] The angular displacement is

$$\Delta\phi = \frac{dS}{r'}$$

(2.3.3.2) $\qquad \Delta\phi = \frac{W_{drift}(\theta)T_b}{rSin(\theta)}.$

Using equation 2.3.2.7 the angular drift that occurs in one bounce is given by the expression

(2.3.3.3) $\qquad \Delta\phi = 4\int_{\theta_{max}}^{\pi/2} \frac{W_{drift}ds}{rSin(\theta)v_{\parallel}}.$

The expression for $\vec{W}_{drift}$ in polar coordinates is written

$$\vec{W}_{Drift} = \frac{m}{qB^4}\left(v_{\parallel}^2 + \frac{v_{\perp}^2}{2}\right)\vec{B}\times\nabla\left(\frac{B^2}{2}\right)$$

---

[28] Roederer, 148.

[29] Northrup.

[30] Parks, 144.

$$(2.3.3.4) \qquad \vec{W}_{\text{Drift}} = \frac{m}{qB^4}\left(v_{\parallel}^2 + \frac{v_{\perp}^2}{2}\right)\left(\frac{3\mu M^3(9\text{Sin}(\theta) + 5\text{Sin}(3\theta))}{256\pi^3 r^{10}}\right)\hat{\phi}.$$

Equation 2.3.3.4 is expanded by rewriting the first term in brackets

$$v_{\parallel}^2 + \frac{v_{\perp}^2}{2} = v^2(1 - \text{Sin}^2(\alpha_0)\frac{B}{B_0}) + v^2\text{Sin}^2(\alpha_0)\frac{B}{2B_0}$$

$$(2.3.3.5) \qquad v_{\parallel}^2 + \frac{v_{\perp}^2}{2} = v^2(1 - \text{Sin}^2(\alpha_0)\frac{B}{2B_0})$$

The magnitude of the drift velocity is shown to have the form of

(2.3.3.6)

$$W_{\text{Drift}} = \frac{3v^2 m\pi r^2}{q\mu_0 M(1 + 3\text{Cos}^2(\theta))^2}\left(1 - \text{Sin}^2(\alpha_0)\frac{\sqrt{1 + 3\text{Cos}^2(\theta)}}{2\text{Sin}^6(\theta)}\right)\left((9\text{Sin}(\theta) + 5\text{Sin}(3\theta))\right).$$

Parks writes equation 2.3.3.6 as

$$(2.3.3.7) \qquad W_{\text{Drift}} = \frac{3v^2(1 + \text{Cos}^2(\theta))\text{Sin}^5(\theta)}{2\omega_0 r_0(1 + 3\text{Cos}^2(\theta))^2}\left(2 - \text{Sin}^2(\alpha_0)\frac{\sqrt{1 + 3\text{Cos}^2(\theta)}}{\text{Sin}^6(\theta)}\right).$$

The expression for equation 2.3.3.2 becomes

$$(2.3.3.8) \qquad \Delta\phi = 4\int_{\theta_{\text{max}}}^{\pi/2}\left[\frac{\frac{3v^2(1 + \text{Cos}^2(\theta))\text{Sin}^3(\theta)}{2\omega_0 r_0(1 + 3\text{Cos}^2(\theta))^{3/2}}\left(2 - \text{Sin}^2(\alpha_0)\frac{\sqrt{1 + 3\text{Cos}^2(\theta)}}{\text{Sin}^6(\theta)}\right)ds}{r_0\text{Sin}^3(\theta)v\sqrt{(1 - \frac{\text{Sin}^2\alpha_0\sqrt{1 + 3\text{Cos}^2(\theta)}}{\text{Sin}^6(\theta)}}}\right].$$

The next step is to set the average drift frequency over one bounce

$$(2.3.3.9) \qquad <\nu_D> = \frac{\Delta\phi}{2\pi T_b}$$

where T_b was defined by equation 2.3.2.12. When Hamlin et al.[31] first solved for the expression of equation 2.3.3.9, they evaluated the integrals numerically for different values of $\text{Sin}^2(\alpha_0)$ and θ_{max} and then developed an expression for the drift period of

$$(2.3.3.10) \qquad T_D \cong \frac{3\gamma mcv^2}{qB_0 r_0}(0.35 + 0.15\text{Sin}(\alpha_0)).$$

---

[31] Hamlin et al., 4.

43

The expression for the drift period, like the bounce period, is only an analytical approximation, but it does compare well to the results from the model using the guiding center approximation and the Boris method. The analytic prediction using equation 2.2.3.10 was useful in helping validate the predictions of the model developed for this dissertation and can be used as a gauge for the for the drift period.

2. 4.   SUMMARY

The intent of Chapter II was to lay the foundation for the modeling of charged particle motion in magnetic fields. The equations of motion of a charged particle in a dipole magnetic field were developed without the effects of particle interaction with air which leads to ionization energy losses, pitch-angle diffusion, and radial dispersion. In addition, a guiding center approximation was developed as a method to model the general equations of motion of a charged particle, without following the true helical motion of the particle. Both approaches have advantages and disadvantages that will be developed in detail in Chapter III where a complete comparison of the two computational methods is presented. Finally, the adiabatic invariants will serve as essential elements in the numerical models. The equations and theory of Chapter II are used as the basis for model development of Chapter III and are now incorporated into computational models designed to efficiently predict and track the trajectories of the charged particles released from a nuclear device.

III.   DEVELOPMENT OF THE NUMERICAL MODELS

Having presented in the previous chapter the background physics important to analysis of persistent exo-atmospheric radiation effects and described the guiding center approximation approach to be used in this research, this chapter presents the development of the modeling approach taken to design and validate the simulations. The selected models need to be capable of tracking thousands and possibly millions of particles for simulated days or weeks as quickly as possible.

This chapter also includes a basic review of the numerical methods for modeling a finite difference equation, beginning with the Euler method. The Euler-Cromer method and the Boris method are then developed and compared to validate the selection of the Boris method as the appropriate full-time integration technique used in for computational modeling. The comparison of the results of the Euler-Cromer method and the Boris push also provide validation and verification of each model against the results of the other model. Finally, the guiding center approximation is developed as a computational model and a comparison of the results of the guiding center and the Boris method are presented. With the appropriate initial conditions, each of the three models is shown to produce results strikingly similar to the other two models and all model results are validated against the analytical approximations for bounce period and drift period (fractions of seconds to thousands of seconds) presented in Chapter II.

3.1.   EULER METHOD

In order to use a numerical simulation to model a charged particle trapped in a magnetic field, the Euler method was applied and tested to establish an initial base-line. A quick summary of the Euler method is presented for those not familiar with numerical integration algorithms.[32] Eventually, the Euler method was found inadequate for tracking particles in a dipole field because it was not able to conserve energy or maintain the correct orbit of the charged particle.

---

[32] N.J. Giordano, *Computational Physics*, (Upper Saddle River, NJ: Prentice Hall, 1997), 347.

The development of the Euler method began with the finite difference form of the derivative of the acceleration and velocity of a charged particle and using the Lorentz force, the velocity and position equations for tracking the charged particle in the dipole field were developed

$$\vec{F} = \frac{d\vec{p}}{dt} = q(\vec{v} \times \vec{B}) \qquad \text{(Lorentz force without the electric field),}$$

$$m\frac{d\vec{v}}{dt} = q(\vec{v} \times \vec{B}),$$

(3.1.1) $\qquad m\dfrac{\vec{v}(i+1) - \vec{v}(i)}{\Delta t} = q(\vec{v} \times \vec{B}) \qquad$ (using the finite difference form of the

derivative),

(3.1.2) $\qquad \vec{v}(i+1) = \vec{v}(i) + \dfrac{q\Delta t}{m}(\vec{v}(i) \times \vec{B}(i)),$

(3.1.3) $\qquad v_x(i+1) = v_x(i) + \dfrac{q\Delta t}{m}(v_y(i)B_z(i) - v_z(i)B_y(i)),$

(3.1.4) $\qquad v_y(i+1) = v_y(i) + \dfrac{q\Delta t}{m}(v_z(i)B_x(i) - v_x(i)B_z(i)),$

(3.1.5) $\qquad v_z(i+1) = v_z(i) + \dfrac{q\Delta t}{m}(v_x(i)B_y(i) - v_y(i)B_x(i)).$

Equations 3.1.3, 3.1.4, and 3.1.5 are the equations for the components of the velocity at time t=t(i+1).

The equations for position were similarly derived.

(3.1.6) $\qquad \vec{v} = \dfrac{d\vec{x}}{dt} = \dfrac{\vec{x}(i+1) - \vec{x}(i)}{\Delta t},$

(3.1.7) $\qquad \vec{x}(i+1) = \vec{x}(i) + \vec{v}(i)\Delta t,$

(3.1.8) $\qquad x(i+1) = x(i) + v_x(i)\Delta t,$

(3.1.9) $\qquad y(i+1) = y(i) + v_y(i)\Delta t,$

(3.1.10) $\qquad z(i+1) = z(i) + v_z(i)\Delta t.$

Equations 3.1.8, 3.1.9, 3.1.10 are the equations for the position at $\vec{x}(i+1)$ established by advancing the positions by $\vec{v}(i)$ multiplied by Δt.

In general, the Euler method uses this technique to calculate the new position based on the old velocity multiplied by the time step, Δt, as shown in equations 3.1.8-3.1.10. The new velocity, $\vec{v}(i+1)$, is then calculated using the old velocity, $\bar{v}(i)$, and the magnetic field at the old position as shown in equations 3.1.3-3.1.5. The iteration is then repeated to continue advancing the position and velocity of the particle in time. For many numerical simulations the Euler method proves adequate for a short time and limited numbers of time steps and can be a very efficient method for computational analysis.

However, when the above equations are applied to a dipole field using the Euler method where the new location at x(i+1) is calculated using the velocity, $v_x(i)$, and then the new velocity, $v_x(i+1)$, is calculated using the magnetic field at the x(i) position, the radius of the orbit slowly increases with time and does not match the expected results presented in Chapter II. Additionally, kinetic energy is not conserved even with painfully small time steps. The Euler method fails when applied to most oscillatory systems (like a charged particle trapped in a dipole field) because the amplitude of the oscillation grows with each time step.[33] As shown in Figure 3.1.1, when using the Euler method, the velocity vector used to advance the particle is always tangential to the direction of motion and never crosses the path of the particle. With each time step, the x(i+1) computed position of the particle is outside of the expected orbit and further away from the center of curvature of the expected path. As time marches on in the simulation the non-physical error increases as the error accumulates. Reducing the size of the time step does not solve the amplitude growth problem, only reduces the error of each time step and prolongs the agony.

As suggested, the velocity vector of equation 3.1.2 is always tangential to the path of motion. Figure 3.1.1 shows the expected circular orbit compared of a particle compared to the Euler method predictions of the orbit. Each time step moves the orbiting particle further away from expected orbit and the center of the circle. Figure 3.1.1 demonstrates in an exaggerated fashion this slow growth of the radius for a particle moving in a circle with no source of added energy. The Euler method does not conserve energy when applied to the trapped particles because, as a result of the limitation of the

---

[33] Giordano, 42.

method, the particle numerically moves away from the expected trajectory as though work were done on the particle. This initial investigation using the Euler method for the numerical integration of a particle orbit has served as a useful and pedagogical introduction to numerical simulation but it is far too inaccurate to be useful in this work.
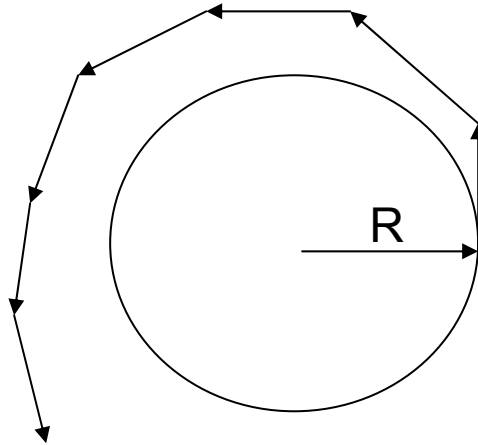
Figure 3.1.1: This represents the error introduced by a numerical simulation using the Euler method of a particle moving with constant speed around a circle of radius, R, and no source of added energy and only a constant magnitude of the centripetal force acting on the particle. The arrows are the exaggerated displacement vectors of each time step using the Euler method. Each successive time step moves the particle farther away from the desired orbit. This figure demonstrates one of the limitations of the Euler method.

3.2. EULER-CROMER METHOD

A potentially suitable solution to the need for an improved approach for trapped electron simulation is the Euler-Cromer method. The Euler-Cromer method is first order accurate[34] and similar to the Euler method, but with subtle changes, has proven appropriate for oscillating systems.[35] The essential difference of the Euler-Cromer method is that the new velocity is computed before advancing the particle to the new

---

[34] Lecture Notes: *Introduction to Finite Differences Methods*: Crowley, Lawrence Livermore Laboratory: provided by Tom Thomson at LLNL.

[35] Lecture Notes: *Introduction to Numerical Modeling,* SE2911, Winter Quarter 2005, Joe Blau, Naval Postgraduate School.

position. The equations used for the new velocity are identical to those of the Euler method (equations 3.1.3, 3.1.4, 3.1.5) using the previous values for velocity and magnetic field. The subtle change is that the new position is calculated using the new velocity, $\bar{v}(i+1)$, components as shown in the equations. This slight change in the order of calculation enables the Euler-Cromer method to, with adequately small time steps, conserve energy and maintain the correct trajectory of the particles in the dipole field because the errors do not accumulate and the trajectory continues to maintain the correct physical conditions.

The Euler-Cromer method equations for position are derived and

$$\vec{v} = \frac{d\vec{x}}{dt} = \frac{\vec{x}(i+1) - \vec{x}(i)}{\Delta t},$$
$$\vec{x}(i+1) = \vec{x}(i) + \vec{v}(i+1)\Delta t,$$

(3.2.1) $x(i+1) = x(i) + v_x(i+1)\Delta t$,

(3.2.2) $y(i+1) = y(i) + v_y(i+1)\Delta t$,

(3.2.3) $z(i+1) = z(i) + v_z(i+1)\Delta t$.

Using equations 3.2.1-3.2.3, the velocity vector used to calculate the new positions is no longer tangential to the path of the particle, but because of the forward advance, now brings the path of the particle across the expected trajectory as shown in Figure 3.2.1. By changing the order of the calculations and using the $\bar{v}(i+1)$ to advance the position of the particle, the Euler-Cromer method does not inherently fail to conserve energy and can be used to model a charged particle trapped in a magnetic field.
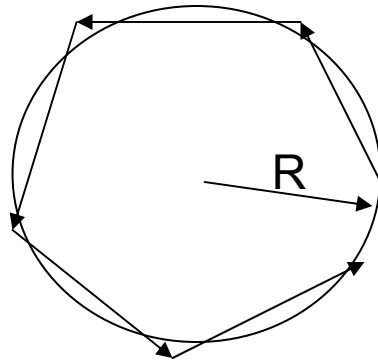
Figure 3.2.1: This represents a numerical simulation using the Euler-Cromer method of a particle moving with constant speed around a circle of radius, R, and no source of added energy. The arrows are the displacement vectors of each time step using the Euler-Cromer method. Each successive time step moves the particle farther across the expected orbit. If the time steps are small enough, the Euler-Cromer method is one approach to modeling particles in dipole magnetic field. This figure demonstrates the advantage of the Euler-Cromer method over the Euler method.

When the Euler-Cromer method was applied to simulate a relativistic electron in the earth's magnetic field, time steps of $1x10^{-9}$ to $1x10^{-10}$ s were needed to maintain strict energy conservation. With time steps of $1x10^{-8}$ s the energy increased rapidly and even with time steps of $1x10^{-9}$ s, the increase of energy was small, but noticeable. For example, given an electron with initial conditions of: $x_0 = 0$, $v_{x0} = 0$, $y_0 = 7375$ km, $v_{y0} = 1x10^8$ m/s, $z_0 = 0$, $v_{z0} = 1x10^8$ m/s (the cyclotron frequency of the electron spiraling along the field lines is $1.3x10^6$ rad/s and the cyclotron radius is about 200 m), and time steps of $1x10^{-8}$ s for 2 real-time seconds (the electron started on the magnetic equator), the electron's kinetic energy increased from 69 kJ to 255 kJ with the Euler-Cromer method. The altitude of the mirror point of the modeled electron continually changed (the mirror point continually moved to a higher altitude and closer to the equator with each bounce) as shown in Figure 3.2.2. The bounce period also continually decreased. The total run time of the simulation was one minute on a on a 2-GHz Pentium.

Using the same initial condition, but decreasing the time steps to $1x10^{-9}$ s, the kinetic energy did increase slowly from 69.6 kJ to 69.7 kJ, but the decreased was small.

The bounce period was constant at 0.25 s and the mirror altitude did not change. Figure 3.2.3 presents the results of this run. The total computer time of the simulation was 10 minutes on a 2 GHz Pentium. In Figure 3.2.2 and Figure 3.2.3 every 10,000 points are plotted (this reduced the size of the data files) and that caused the electron's trajectory to appear distorted, especially around the equator.

The major goal of the dissertation is to build the capability to eventually track thousands and possibly millions of particles for simulated days, weeks, or months. Even with extremely fast and powerful computers, the time required to track the particles using the Euler-Cromer method for long periods quickly becomes unbearably excessive.

There is a factor of 10 increase in run time with each order of magnitude decrease in the size of Δt. When large Δts were used, the kinetic energy would increase until the speed of the electron exceeded the speed of light. When the Euler-Cromer method was applied to non-relativistic electrons with large cyclotron radius and gyro-periods then the method conserved energy (with small enough Δts) and the method proved reliably adequate. However, the non-relativistic electrons are of less interest to the problem of trapped electrons and satellite vulnerability. The conclusion was that the Euler-Cromer method, although adequate for many applications, was not suitable for tracking the many relativistic electrons that would be trapped in the earth's magnetic field in the problems of interest in this research.
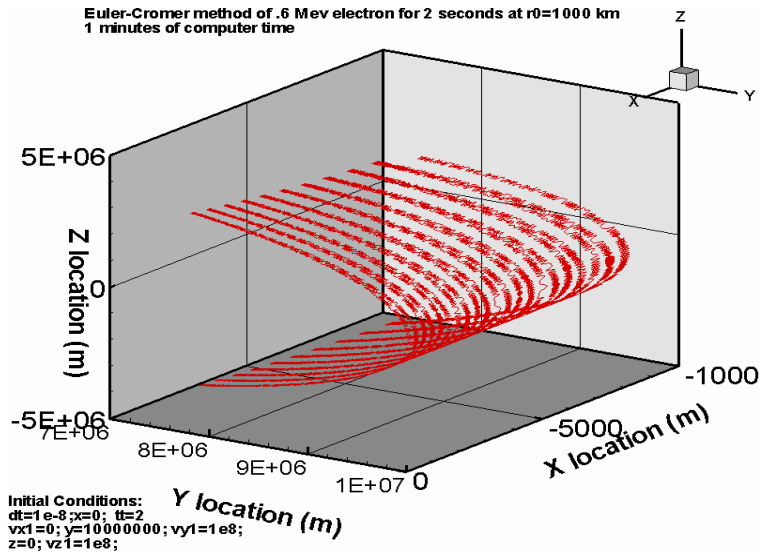
Figure 3.2.2: The Euler-Cromer method applied with a time step of 1x10-8 s for 2 seconds. As the simulation progressed, the total kinetic energy of the electron slowly increased, the turning point increased in altitude and decreased in distance from the equator. The bounce period decreased from 0.24 s to 0.16 s. The results of this run were not consistent with the expected results and as a result are considered to be inadequate.
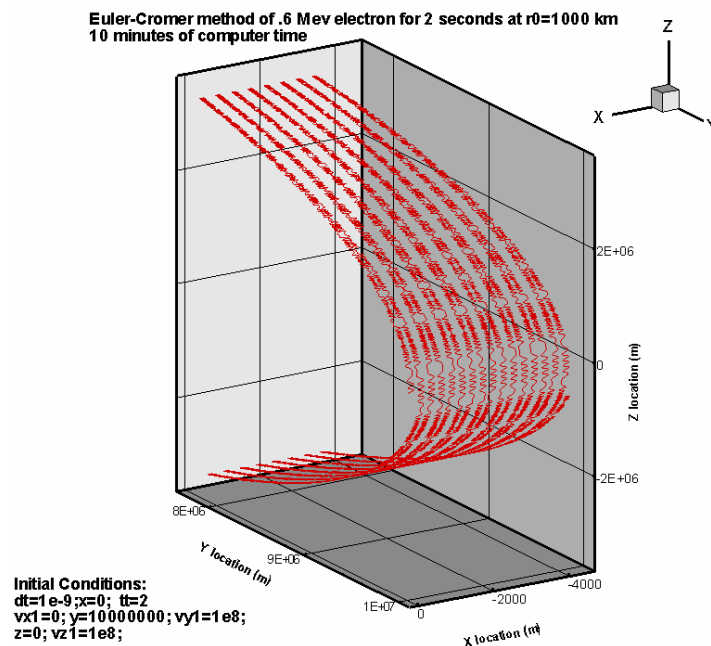
Figure 3.2.3: The Euler-Cromer method was applied with a time step of 1x10-9 s for 2 seconds of real simulation time. The total kinetic energy of the electron increased only slightly and the turning point remained almost constant in altitude. The bounce period was 0.25 s and did not change. The total simulation run time was 10 minutes on a 2-GHz Pentium.

3.3. BORIS PUSH METHOD

Pedagogically, the development and investigation of the Euler-Cromer method was a useful step toward understanding ways to improve computational methods. With small enough time steps, the Euler-Cromer method produced results that matched the analytical solutions, but the method was computationally expensive. In an attempt to find a method at least as good as Euler-Cromer, the Boris-Push method was developed for the dissertation.

The Boris push is a center-differenced, second-order accurate method used as a particle pusher by many physicists at locations like Lawrence Livermore National Laboratory (LLNL)[36]. The derivation begins similarly to the Euler and Euler-Cromer methods. First let

$$\vec{v} = \frac{d\vec{x}}{dt}$$

$$\frac{d\vec{p}}{dt} = q(\vec{v} \times \vec{B})$$

(3.3.1) $\quad \dfrac{d\vec{v}}{dt} = \dfrac{q}{m}(\vec{v} \times \vec{B})$.

By defining omega, Ω, as

(3.3.2) $\quad \vec{\Omega} = \dfrac{q\Delta t}{2m}\vec{B} \quad$ (this is similar to the cyclotron frequency)

(Equation 3.3.2 is written as $\vec{\Omega} = \dfrac{q\Delta t}{2\gamma m}\vec{B}$ for relativistic particles.)

Equation 3.3.1 is written

(3.3.3) $\quad d\vec{v} = (\vec{v} \times \vec{\Omega})$.

The time centered finite difference approximation to equations 3.3.1 and 3.3.3 is

(3.3.4) $\quad \vec{x}^{\,n+1} - \vec{x}^{\,n} = \vec{v}^{\,n+\frac{1}{2}}\Delta t$.

Equation 3.3.3 is now written using n + ½ to represent a one-half of time step

(3.3.5) $\quad \vec{v}^{\,n+\frac{1}{2}} - \vec{v}^{\,n-\frac{1}{2}} = (\vec{v}^{\,n+\frac{1}{2}} + \vec{v}^{\,n-\frac{1}{2}}) \times \vec{\Omega}^{n}$.

---

[36] Dennis Hewett (LLNL), private conversation with author, 18 October 2005.

Both of these equations are second-order accurate and time-reversible, implying that no irreversible numerical diffusion has been inadvertently added. The energy constant $(=|\vec{v}|^2)$ is identical for both difference and differential equations. Additionally, equations 3.3.4 and 3.3.5 are unconditionally stable.[37] Following Hockney and Eastwood and rearranging equation 3.3.5, the two velocity terms the expression for $\vec{v}^n$ becomes

$$(3.3.6) \qquad \vec{v}^n = \vec{v}^{n+\frac{1}{2}} - \left(\vec{v}^{n+\frac{1}{2}} \times \vec{\Omega}^n \right) = \vec{v}^{n-\frac{1}{2}} + \left(\vec{v}^{n-\frac{1}{2}} \times \vec{\Omega}^n \right)$$

where $\vec{v}^n$ is an intermediate velocity. Next add equation 3.3.6 with itself

$$(3.3.7) \qquad 2\vec{v}^n = \vec{v}^{n+\frac{1}{2}} + \vec{v}^{n-\frac{1}{2}} + \left((\vec{v}^{n-\frac{1}{2}} - \vec{v}^{n+\frac{1}{2}}) \times \vec{\Omega}^n \right).$$

Next cross both sides of equation 3.3.7 with $\vec{\Omega}^n$

$$2\vec{v}^n \times \vec{\Omega}^n = \left(\vec{v}^{n+\frac{1}{2}} + \vec{v}^{n-\frac{1}{2}} \right) \times \vec{\Omega}^n + \left[\left(\vec{v}^{n+\frac{1}{2}} - \vec{v}^{n-\frac{1}{2}} \right) \times \vec{\Omega}^n \right] \times \vec{\Omega}^n$$

and use vector identities to get

$$(3.3.8) \qquad 2\vec{v}^n \times \vec{\Omega}^n = \left(\vec{v}^{n+\frac{1}{2}} + \vec{v}^{n-\frac{1}{2}} \right) \times \vec{\Omega}^n + \vec{\Omega}^n \cdot \left(\vec{v}^{n+\frac{1}{2}} - \vec{v}^{n-\frac{1}{2}} \right) \vec{\Omega}^n +$$

$$\Omega^2 \left(\vec{v}^{n+\frac{1}{2}} - \vec{v}^{n-\frac{1}{2}} \right).$$

Note that

$$\vec{\Omega}^n \cdot \left(\vec{v}^{n+\frac{1}{2}} - \vec{v}^{n-\frac{1}{2}} \right) \vec{\Omega}^n = 0 .$$

Using the first part of equation 3.3.6

$$(3.3.9) \qquad \vec{v}^{n+\frac{1}{2}} - \vec{v}^{n-\frac{1}{2}} = \left(\vec{v}^{n+\frac{1}{2}} + \vec{v}^{n-\frac{1}{2}} \right) \times \vec{\Omega}^n ,$$

One can substitute into equation 3.3.8 to get

---

[37] R.W. Hockney, J.W. Eastwood, *Computer Simulation Using Particles*, (Philadelphia: Institute of Physics Publishing, 1988), 112.

$$2\vec{v}^n \times \vec{\Omega}^n = \left(\vec{v}^{n+\frac{1}{2}} - \vec{v}^{n-\frac{1}{2}}\right) + \Omega^2\left(\vec{v}^{n+\frac{1}{2}} - \vec{v}^{n-\frac{1}{2}}\right)\frac{\Delta t}{2} = \left(\vec{v}^{n+\frac{1}{2}} - \vec{v}^{n-\frac{1}{2}}\right)\left(1 + \vec{\Omega}^n\right)$$

which yields

$$(3.3.10)\qquad \vec{v}^{n+\frac{1}{2}} = \vec{v}^{n-\frac{1}{2}} + \frac{2\vec{v}^n \times \vec{\Omega}^n}{1+\Omega^2}.$$

The result is that the charged particle are "pushed" with a time-centered method that is second-order accurate, conserves energy, and is proven to be more stable for larger Δts than the Euler-Cromer method.

For example, an electron with the same initial conditions as applied to the example of the Euler-Cromer method: $x_0 = 0$, $v_{x0} = 0$, $y_0 = 7735$ km, $v_{y0} = 1\times10^8$ m/s, $z_0 = 0$, $v_{z0} = 1\times10^8$ m/s, time steps of 1×10^{-8} s for 2 real-time seconds the change in kinetic energy was less than 0.00001%. The bounce period was 0.25 s and the orbit was extremely stable. The same conditions were run using a time step of 1×10^{-7}s and the kinetic energy decreased by less than 0.02% and even with a time step of 1×10^{-6} s the kinetic energy only decreased by 4%. Figure 3.3.1 and Figure 3.3.2 show the stable electron trajectories of an electron trapped in the earth's magnetic field using the established initial conditions and the Boris method. Only every 10,000 data points were plotted in order to reduce the size of the data files. A time step between 1×10^{-7} s and 1×10^{-8} s was found to be necessary to maintain a stable orbit and conserve energy for the applied conditions during the simulation. This small time step is still a significant constraint if one desires to track multiple particles for long time periods, but at least two orders of magnitude larger time steps are possible for the Boris method when compared to the Euler-Cromer method.

Boris Push of .6 Mev electron for 2 seconds at r0=1000 km
2.7 minutes of computer time

Initial Conditions:
dt=1e-8;x=0; tt=2
vx1=0; y=10000000; vy1=1e8;
z=0; vz1=1e8;
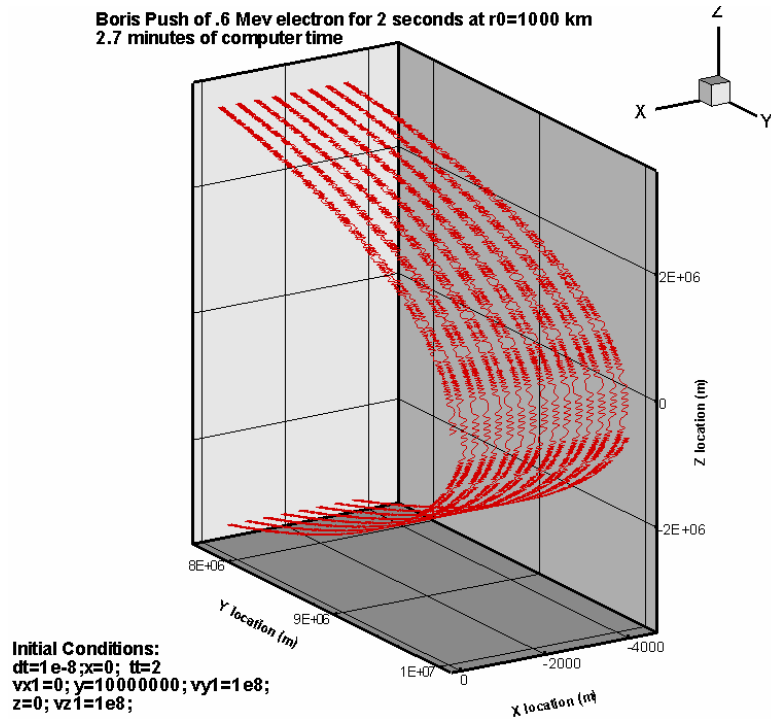
Figure 3.3.1: The Boris push applied method with a time step of 1x10-8 s for 2 seconds. The total kinetic energy of the electron remained constant, the turning point was stable, and the bounce period was constant at 0.25 s.

Boris Push of 1.4 Mev electron for 4 seconds at r0=6775 km
5.6 minutes of computer time

Initial Conditions:
dt=1e-8;x=0; tt=2
vx1=0; y=6775000; vy1=2.6e8;
z=0; vz1=1e8;
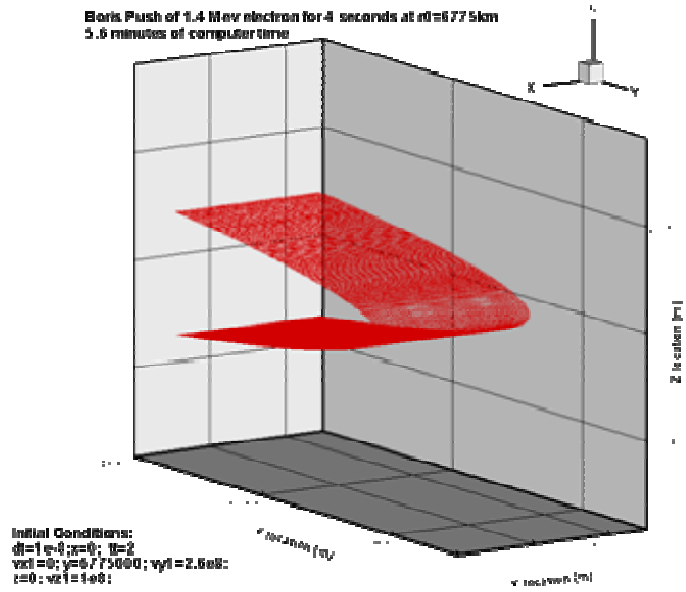
Figure 3.3.2: The Boris push method with a time step of 1x10-8 s for 4 seconds at 400 km above the magnetic equator. The total simulation run time was 5.6 minutes on a 2-GHz processor.

56

3.4.   A COMPARISON BETWEEN THE EULER-CROMER METHOD AND BORIS PUSH

One of the essential underpinnings of the dissertation was to identify and implement an accurate and efficient finite difference method for tracking particles trapped in a magnetic field. To do this several methods were investigated. The Euler-Cromer method was superior to the Euler method, but the Euler-Cromer method required small time steps in order to conserve energy. The intent of comparing different methods was to determine which was best suited for the simulation needed for completion of this dissertation as well as validation of the results of the different methods. The agreement between the results of the Euler-Cromer and Boris methods as well as and a match of the model results to the analytical solutions was critical in the verification and validation of the code. The eventual criteria for selection of the full-time integration method were the technique that minimized computational time and best conserved energy. Although there are certainly higher order schemes (like the Runga-Kutta) that are, perhaps, better at conserving energy, the Euler-Cromer method and the Boris method offered the best hope for meeting all of the criteria, especially to include minimizing computational time. The Euler-Cromer method is one of the principal numerical integration techniques taught and used in the Department of Physics at the Naval Post-Graduate School (NPS) as part of an introductory computational physics course and is a wonderful introduction to computational techniques.

The Boris method is one of the primary techniques used at Lawrence Livermore National Labs for pushing particles and is favored because it is time reversible and the rotation part of the Boris push completely conserves energy. Although the Euler-Cromer method requires less time to run for a given and equal time step, the Boris method was found superior for minimizing computational time and maximizing conservation of energy. Table 3.4.1 shows several runs comparing the two methods for a set of initial conditions. The Boris push conserves energy as well as the Euler-Cromer method with a time step two to three orders of magnitude larger. The result is that the Boris push is one or two orders of magnitude less expensive (in terms of computational time) than the Euler-Cromer for the same results.

Method	Time step (s)	Computer time (s)	Initial to Final bounce period (s)	Change in energy (keV)
Euler-Cromer	1.000×10^{-8}	25	0.251 to 0.2082	68.6 to 123
Boris-Push	1.000×10^{-8}	80	No change	No change
Euler-Cromer	1.000×10^{-9}	294	No change	68.6 to 68.7
Boris-Push	1.000×10^{-7}	8	No change	No change
Boris-Push	1.000×10^{-6}	<1	0.251 to 0.2520	68.6 to 67.5

Table 3.4.1: A comparison of the Euler-Cromer method and the Boris push is presented for the initial conditions: x = 0 m, Vx = 0 m/s, y = 10,000 km, Vy = 1x108 m/s, z = 0 m, Vz= 1x108 m/s. The trajectory of the electron is tracked for 1 second. The Boris method, with a time step of 1x10-7 s, was able to match the energy conservation of Euler-Cromer method that required a time step of 1x10-9 s. To achieve the same level of fidelity and energy conservation, the Boris push required 8 seconds of computer time and the Euler-Cromer method required 292 seconds.

How do the trajectories of the different methods compare? When the two methods were compared using time steps that produced similar energy conservation as shown in Table 3.4.1, the trajectories of the charged particles were in very close agreement and it was difficult to distinguish the two plots of trajectories. Additionally, the two methods predict a bounce period of 0.2058 s compared to the analytical estimate is 0.26 s. The matching of the trajectories of the two methods serves as validation for each method against the other and gave confidence in each integration technique. When the methods were compiled with identical time steps, the trajectories did not match as well because of the lack of energy conservation of the Euler-Cromer method for larger time steps (unless the time steps were 1×10^{-9} s or smaller). Figure 3.4.2 shows the results of the two methods compiled with a time step of 1×10^{-8} s. The lack of energy conservation of the Euler-Cromer method caused the comparisons of the two methods shown in Figure 3.4.2 to be different. Even when the time step of the Boris push is 1,000 times larger than a time step used with the Euler-Cromer method, the Boris push was able to closely match the validated trajectory of the Euler-Cromer method when energy is conserved as shown in Figure 3.4.3.
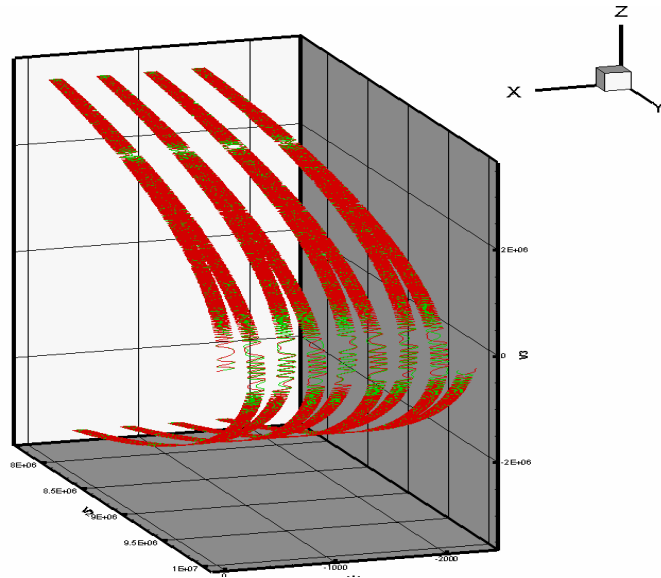
Figure 3.4.1:   The Boris push (green) with a time step of 1x10-8 s and the Euler-Cromer (red) with method with a time step of 1x10-9 s were used to model the trajectory of an electron with an initial condition of: : x = 0 m, Vx = 0 m/s, y = 10,000 km, Vy = 1x108 m/s, z = 0 m, Vz= 1x108 m/s, and a total time of 1 s. The trajectories are shown to be nearly identical. The Boris push required 1.3 minutes of computer time and the Euler-Cromer method required 4.1 minutes of computer time on the same computer system.
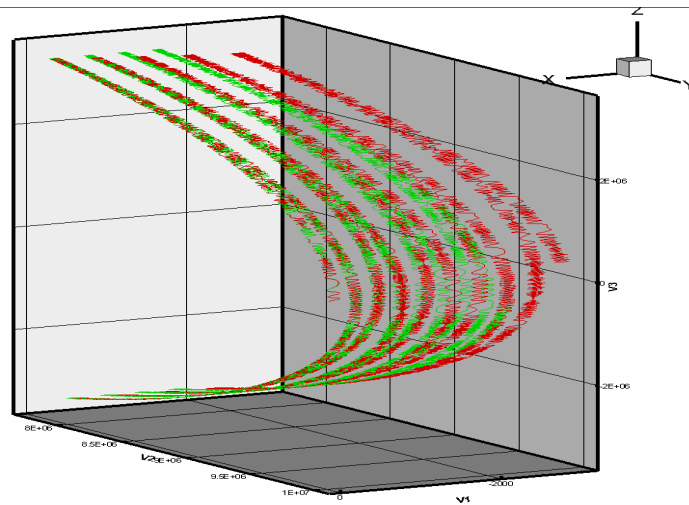
Figure 3.4.2:   Using the same initial conditions as Figure 3.4.1, except that the time step for the Euler-Cromer method was reduced to 1x10-8 s (the same time step as the Boris push), a comparison of the predicted trajectories of Boris (green) and the Euler-Cromer (red) is presented. The Euler-Cromer does not conserve energy (the kinetic energy of the Euler-Cromer doubled in 1 s) and the Euler-Cromer method continually decreased the bounce period. Additionally, the figure shows the conjugate point of the Boris method remaining constant, but the conjugate point of the Euler-Cromer changes.

59
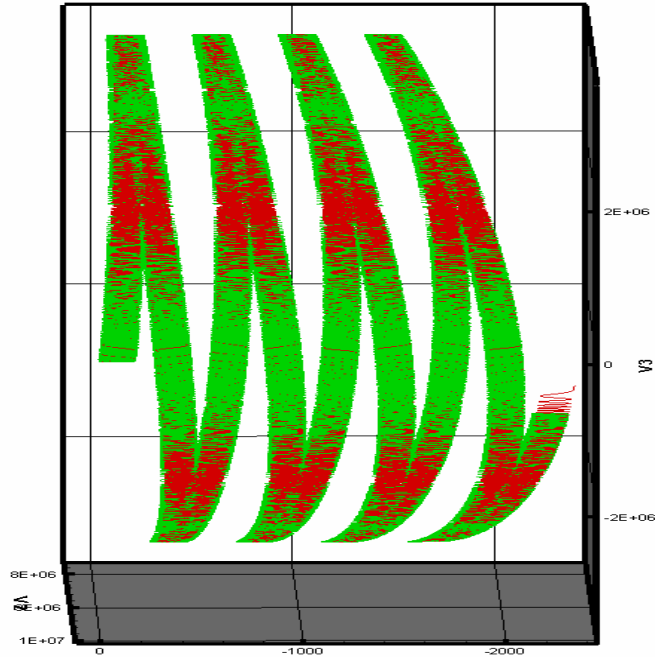
Figure 3.4.3: **This shows the Boris push with a time step of 1x10-6 s compared to the Euler-Cromer method using a time step of 1x10-9 s. The trajectories match closely. The altered Boris trajectory (green) is caused by the large time step used in the simulation. The time step is on the order of the orbit period and the particle overshoots the actual path with each time step, but still follows the general orbit of the Euler-Cromer.**

Many comparisons were made between the two methods and the Boris method always proved superior to the Euler-Cromer method for application in the models developed for this dissertation. Another comparison is presented in Table 3.4.2. The Euler-Cromer method, when the time steps are small enough, matches the trajectory and energy conservation of the Boris method, but is much more costly in computational time. Interestingly when using the Euler-Cromer method with large time steps, the energy of the particle increased and when using the Boris method with large time steps the energy of the particle decreased.

One of the objectives of the dissertation was to investigate and select a computational method that minimizes the computational requirements while providing confidence in the results. If a full time integration is required, then the Boris method is the better computational scheme to be used to track charged particles. However, for an electron, the Boris method still requires a time step of around $1x10^{-7}$ s. This means about

eight seconds of computer time on a 2GHz Pentium computer for every real-time second of the particle tracking. If one were to track 10^8 particles for six real hours, the Boris method would require 4.8 billion hours of computer time on a computer comparable to a 2-GHz Dell Latitude. Although the Boris method was verified as the better method for tracking charged particles, the computational requirement prompted a search for additional alternatives to significantly reduce the computational requirements.

Method	Time step (s)	Computer time (s)	Initial/Final bounce period (s)	% change in energy
Euler-Cromer	1.00×10^{-9}	292	No change	4.00
Euler-Cromer	1.00×10^{-8}	N/A	N/A	see note*
Boris-Push	1.00×10^{-8}	80	No change	No change
Boris-Push	1.00×10^{-7}	8	No change	0.001
Boris-Push	1.00×10^{-6}	<1	No change	1.3

Table 3.4.2:   A comparison of the Euler-Cromer method and the Boris push is presented for the initial conditions: x = 0 m, Vx = 0 m/s, y = 6775 km, Vy = 2.8x108 m/s, z = 0 m, Vz= 1x108 m/s. The trajectory of the electron is tracked for 1 second. The Boris method, with a time step of $1x10^{-6}$ s, was able to match the energy conservation of Euler-Cromer method that required a time step of $1x10^{-9}$ s. Note*: When a time step of $1x10^{-8}$ s was used with the Euler-Cromer method, the electron gained energy and speed until the electron eventually surpassed the speed of light and the simulation failed.

3.5.   INTRODUCTION OF THE GUIDING CENTER APPROXIMATION COMPUTATIONAL TECHNIQUE

As promising as the Boris push is for particles with large gyro-frequencies and large gyro-orbits, it is still very expensive to follow particles that simply bounce back and forth with a small gyro-radius. The guiding center offers truly significant time savings for particles with small gyro-orbit periods. However, to use this approximation with confidence, it was necessary to show that it could be used to match the "true" trajectory of a charged particle with the added bonus of significantly reducing the time required for computation. Recall that in Section 2.2. the guiding center approximation was developed using the perpendicular and parallel components of the velocity. The parallel component, $v_{\parallel}$, describes the motion of the particle along the direction of the magnetic field lines and

the perpendicular component, $v_\perp$, describes the motion of the particle perpendicular to and spiraling around the magnetic field lines. Recall also that, with no energy loss mechanisms, the magnitude of the velocity and energy should remain constant. Once the parallel or perpendicular component of the velocity is determined, and the initial magnitude of the velocity is known, then the orthogonal component of the velocity is easily calculated.

(3.5.1) $\quad \vec{v}^2 = v_\perp^2 + v_\parallel^2$

The second expression useful in the development of the guiding center computational technique is derived from the conservation of the first adiabatic invariant which leads to the expression of equation 2.3.1.7

$$\frac{p_\perp^2}{B} = \text{const}.$$

Given the initial conditions of a charged particle, $(\vec{x}_i, \vec{v}_i)$, the constant of equation 2.3.1.7 is calculated. Once the value of the constant is known and as long as the first adiabatic invariant is conserved, equation 2.3.1.7 is written

(3.5.2) $\qquad \Psi = \dfrac{\gamma^2 m^2 v_{0\perp}^2}{B_0} = \text{const}$

where γ, m, $v_{0\perp}$, and B_0 are determined from the initial conditions. Once the value of Ψ is determined and because it remains constant, a new perpendicular component of the velocity is calculated for any new position of the guiding center.

(3.5.3) $\qquad v_\perp(x, y, z) = \sqrt{\dfrac{\left|\vec{B}(x, y, z)\right|\Psi}{(\gamma m)^2}}$

In other words, as the particle advances to a new location, $\vec{X}_{new}$, and a new value of the magnetic field is calculated, the preservation of the first adiabatic invariant allows one to determine the new components of the velocity using equations 3.5.3 and 3.5.1 at the new location.

In order to advance the guiding center particle to the new position used equation in 3.5.3, the parallel component of the velocity plus the drift velocity from Section 2.2.3

62

$$\vec{W}_{\text{Drift}} = \frac{\gamma m}{qB^2}\left(v_\parallel^2 + \frac{\mu B}{m}\right)\vec{B}\times\nabla\left(\frac{B^2}{2}\right)$$

are combined to develop an expression for the complete guiding center velocity, $\vec{v}_{gc}$.

(3.5.4) $\vec{v}_{gc}(x,y,z) = v_\parallel(x,y,z) + \vec{W}_{\text{Drift}}(x,y,z)$.

The parallel component, $v_\parallel(x,y,z)$, moves the particle along the direction of the

magnetic field and the drift velocity, $\vec{W}_{\text{Drift}}(x,y,z)$, moves the particle perpendicular to

the magnetic field (accounting for the drift.)

The new position of the particle is determined using an expression like the one

developed using the Euler method in Section 3.1.

(3.5.5) $\vec{X}_{new} = \vec{X}_{old} + \vec{v}_{gc}(x,y,z)\Delta t$.

However, similar to the problem identified with the Euler method (not the Euler-Cromer

method), if the velocity vector, $\vec{v}_{gc}$, used in equation 3.5.5 is the velocity vector at the old

position, $\vec{X}_{old}$, then the parallel component of equation 3.5.4 causes the particle to move

slowly outward and away from the expected guiding center trajectory. If a correction to

parallel component of the $\vec{v}_{gc}$ is not made then the method does not work for a particle

trapped in the dipole field.

The solution is quite simple and similar to the modification used in the Euler-

Cromer method. First a new "virtual position" is calculated by allowing a virtual particle

to advance in the parallel direction by one-half of a time step, $\Delta t/2$.

(3.5.6) $\vec{X}_{virtual} = \vec{X}_{old} + v_{\parallel-old}(x,y,z)\dfrac{\Delta t}{2}$

Using equation 3.5.3 and 3.5.1, a new parallel component of the velocity, $v_{\parallel\text{-virtual}}$, is

calculated, , at the virtual particles location. The new equation for advancing the particle

becomes

(3.5.7) $\vec{v}_{gc-new}(x,y,z) = v_{\parallel-virtual}(x_{virtual}, y_{virtual}, z_{virtual}) + \vec{W}_{\text{Drift}}(\vec{X}_{old})$.

The equation for the new guiding center position becomes

(3.5.8) $\vec{X}_{new} = \vec{X}_{old} + \vec{v}_{new}(x,y,z)\Delta t$.

Using the guiding center computational technique described above, the guiding center particle trajectory is calculated and plotted for varying initial conditions (ions and electrons with low and high orbits) and shown in Figures 3.5.1-3.5.5. All of the figures demonstrate the expected bounce and drift trajectories of a charged particle trapped in the earth's dipole field. Each is made using time steps five orders of magnitude larger than would be required to create the data set using the Boris push. The five figures are examples of the capability of the guiding center approximation to properly track the trajectory for relativistic electrons and non-relativistic ions. The details of each figure are provided in the appropriate figure caption.
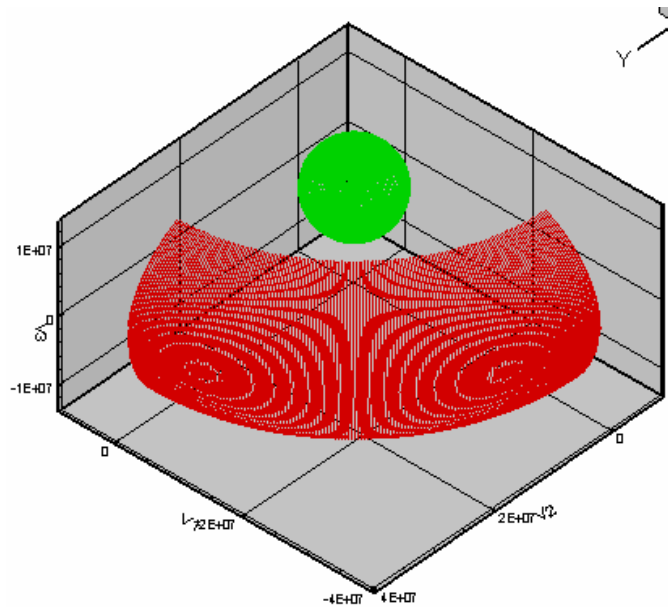
Figure 3.5.1: **Given the initial conditions of: x0=0. m; vx0=0 m/s; y0=38250,000. m (6R$_e$); vy0=2.1e8 m/s; z0=0 m.; vz0=2.1e8 m/s, the plot shows the guiding center trajectory of a 3-MeV electron at L= 6 for one quarter of an orbit. The green sphere represents the earth. The computation required 1.4 seconds of computer time on a 2-GHz Dell.**
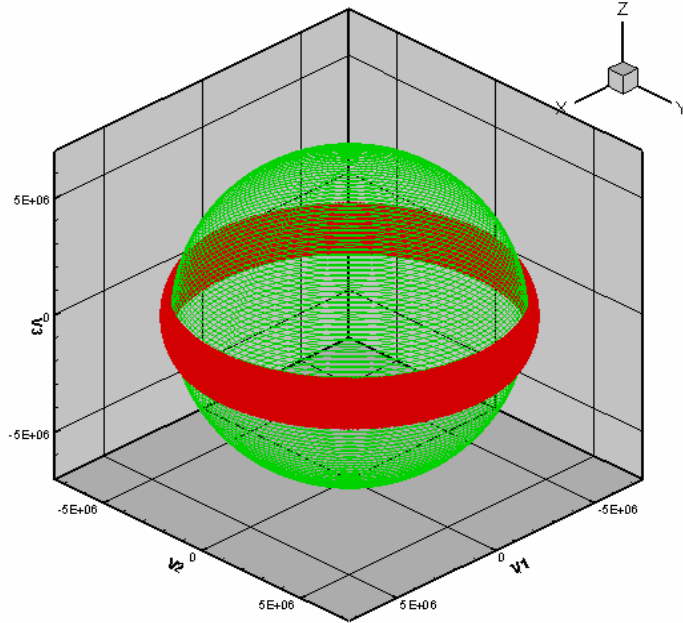
Figure 3.5.2: Given the initial conditions of: x0=0. m; vx0=0 m/s; y0=6750,000. m (1.06R$_e$); vy0=2.82e8 m/s; z0=0 m.; vz0=1e8 m/s, the plot shows the guiding center trajectory of an 8.2-MeV electron at L= 1.05 for a complete orbit. The computation required 45 seconds of computer time to simulate 2400 seconds of real time.
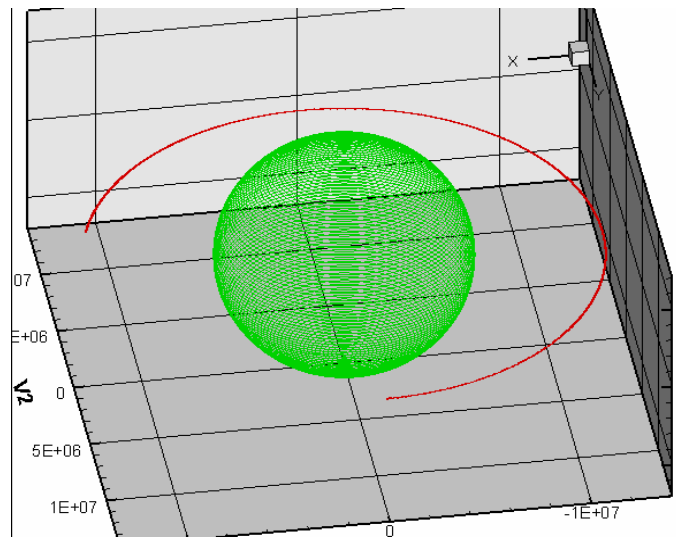
Figure 3.5.3: Given the initial conditions of: x0=0. m; vx0=0 m/s; y0=12750,000. m (2R$_e$); vy0=2.6e8 m/s; z0=0 m.; vz0=0 m/s, the plot shows the guiding center trajectory of a .5-MeV electron at L= 2 for part of an orbit around the earth. The computation required 45 seconds of computer time to simulate 2400 seconds of real time. The orbit also shows the guiding center drift of the particle. The electron's initial velocity was perpendicular to the field and the electron did not move off of the magnetic equator, but drifted to the east.

65
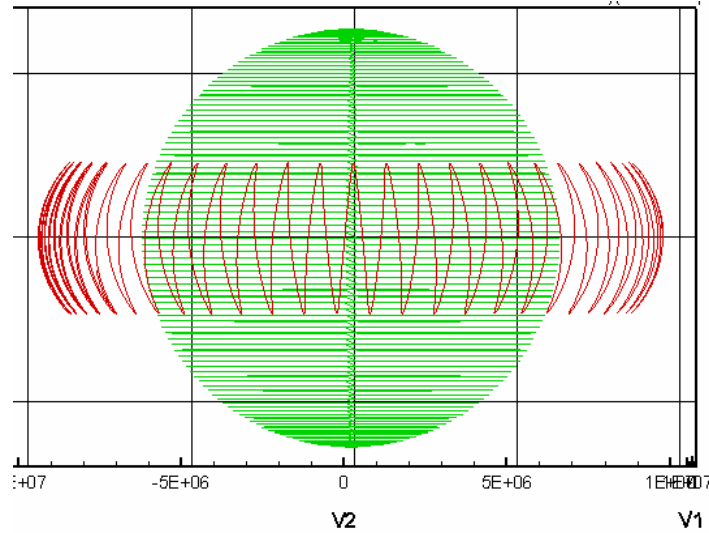
Figure 3.5.4: **Given the initial conditions of a singly charged silver atom: x0=0. m; vx0=0 m/s; y0=9560,000. m (1.5R$_e$); vy0=1.7e6 m/s; z0=0 m.; vz0=1e6 m/s, the plot shows the guiding center trajectory of a 2,000 km/s ion at L= 1.5 for part of an orbit. The computation required 1.3 seconds of computer time to simulate 500 seconds of real time. Because the bounce period of the ion is much longer than the bounce period of an electron, a larger time step (two orders of magnitude) is used as compared the time step used for the electron in the previous figures.**
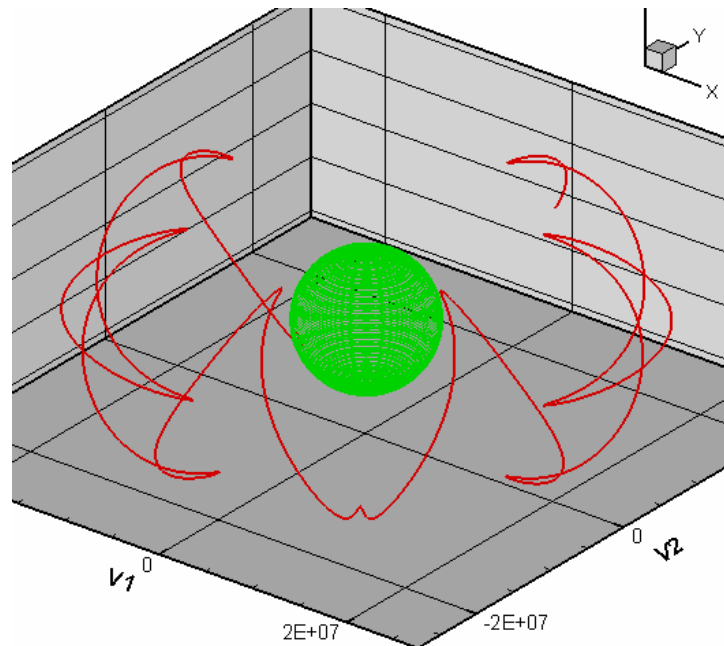
Figure 3.5.5: **Given the initial conditions of a singly charged silver atom: x0=0. m; vx0=0 m/s; y0=25500,000. m (4.02R$_e$); vy0=1.0e6 m/s; z0=0 m.; vz0=1.7e6 m/s, the plot shows the guiding center trajectory of a 2,000 km/s ion at L= 4 for part of an orbit.**

66

The most striking advantage of using the guiding center method is the significant increase in the size of the time step compared to the full time integration techniques. The size of the time step used with the guiding center technique is not constrained by the gyro-period of the particle, but instead, the time step is limited by the bounce period of the particle. Generally, the time step necessary for the guiding center approximation to work well and match the Boris method is no larger than $1/100^{th}$ of the bounce period.

$$(3.5.9) \qquad \Delta t_{max} = \frac{T_{bounce}}{100}$$

For relativistic electrons in the 5 MeV range, the time step is increased to 10^{-3} or 10^{-4} s for the guiding center from 10^{-7} or 10^{-8} s for the Boris push. The increase in the size of the time step decreases the run time for the simulation by four to five orders of magnitude and still the guiding center method used in the simulation matches the expected analytical results. Table 3.5.1 presents a summary of the results of simulations using the guiding center approximation technique. The summary compares the expected values of the bounce period and the drift period to the computed values of the guiding center model. The guiding center computational technique compares very well to the analytical approximation of the bounce period shown in Section 2.3.2 and comes reasonably close to the analytical approximation of the drift period shown in Section 2.3.3.

α_0	Gamma	Ro (km)	L-Shell ~	Analytic Bounce Period (s)	Model Bounce Period (s)	Analytic Drift Period (s)	Model Drift Period (s)
73.3	1.1	38250	6.00	1.12	1.12	13516	13538
16.7	1.1	38250	6.00	1.67	1.65	16974	16926
69.6	3.3	6750	1.06	0.0732	0.0728	3290	3290
70.1	4.9	6750	1.06	0.0711	0.708	2142	2111
70.5	13.8	6750	1.06	0.0697	0.691	727	624
69.6	3.3	7750	1.22	0.0840	0.0835	2875	2860
69.6	3.3	12750	2.00	0.138	0.137	1747	1739
45.0	1.1	12750	2.00	0.0326	0.32	22503	22568
70.5	13.8	12750	2.00	0.132	0.131	384	330
45.0	7.1	38250	6.00	0.466	0.457	272	264

Table 3.5.1:   A comparison is made between the analytical estimate for the values of bounce period and drift period to values of the guiding center model. The bounce period matches analytic approximation very closely and the drift period is close to the analytical approximation. The table demonstrates the utility of the guiding center approximation and provides confidence to the results of the guiding center model.

Although the details of the complete orbit and gyro-motion are lost using the guiding center method, the trajectory of the guiding center is a reasonable approximation for the trajectory of the particle if the Larmor radius is small. For relativistic electrons the guiding center is shown to match the analytical predictions extremely well with relatively large time steps. The reason for development of the guiding center is the minimization of computational time and the guiding center method developed in this dissertation does that very well, at when least compared to the Boris Push or the Euler-Cromer method. Section 3.6 demonstrates how well the guiding center compares with the Boris push. For large gyro-orbits, the guiding center method also matches the analytical predictions of the bounce and drift period, but does not account for the large Larmor radius when predicting the trajectory. The effect of the large gyro-orbit becomes important when atmospheric scattering is introduced. For charged particles in a vacuum, the guiding center approximation works well for large and small gyro-radius particles

Several other computational methods were applied to the guiding center equations in an effort to improve the model presented above. Techniques to improve the model included, but were not limited to a modified Euler-Cromer method, a modified Boris Push, and a straightforward Euler method. None of the techniques were able to match the results of the process described above. The method adopted here is simple and almost exact in matching the expected trajectory and analytical calculations for the description of a particle trapped in the earth's magnetic field.

3.6. COMPARISON OF THE GUIDING CENTER TO THE BORIS PUSH

As suggested in Section 3.5, the guiding center approximation was developed as an alternative to the Boris push because the Boris push is computationally expensive for relativistic electrons since the orbital period can be on the order of 1×10^{-7} s. The time steps used in the Boris push computations should be at least an order of magnitude smaller than the orbit period and a margin of two orders of magnitude is found to be necessary to maintain strict energy conservation. The time step used for relativistic electrons with the guiding center method is between 1×10^{-3} and 1×10^{-4} s. Thus, the

guiding center approximation offers a computational method that significantly reduces the computational time requirements in comparison with the Boris push method without loss of significant trajectory information.

The time step required for the guiding center applied to an electron with an orbit period of 1×10^{-7} s is three to four orders magnitude larger than the orbit period. In other words, calculations using the guiding center approach are around four to five orders of magnitude less computationally expensive than those based on the Boris push method. Considering that there would be at least 10^{20} fission fragments released into the earth's magnetic belts in a nuclear explosion, all efforts to minimize the computer run time are welcomed. The Boris push, however, is most appropriate when complete particle trajectory information is necessary or essential when dealing with a Larmor radius that is large compared to the gradient in the magnetic field or the gradient of the density of the medium. When the Larmor radius of the particle is small compared to these gradients, then the guiding center method can significantly reduce the computational time while still closely matching the particle trajectory.

For example, a 1-MeV electron in a 2.6×10^{-5} T (typical for low L-shell trapped particles) dipole field has a Larmor radius of 110 m and a singly-charged silver atom with a speed of 2,000 km/s has a Larmor radius of 86 km in the same field at the equator. The guiding center approach would be very appropriate for the electron because of the small Larmor radius, but not necessarily appropriate for the silver atom. The guiding center would not only significantly reduce the computational time needed to calculate the trajectory of the electron by at least a factor of 1,000, but would also closely follow the actual trajectory.

Figure 3.6.1 presents a 10 s trajectory of an electron released 400 km above the earth using both the Boris push and the guiding center approximation. The trajectories of each model are shown on the same figure as a comparison of the two models. The two models compare very well and agree on the trajectory. Additionally, Figure 3.6.1 offers magnified sections of the 10 s trajectory in order to demonstrate that the models agree at the beginning, middle, end, and turning points. In Figures 3.6.2 – 3.6.5, the as magnified sections are explained in detail in the figure captions. I compared many trajectories using

the Boris push, the Euler-Cromer, and the guiding center approximation and in every case (when appropriate time steps are used in the models) the agreement between all three models is fantastic—the figures five figures below are representative of many comparisons.
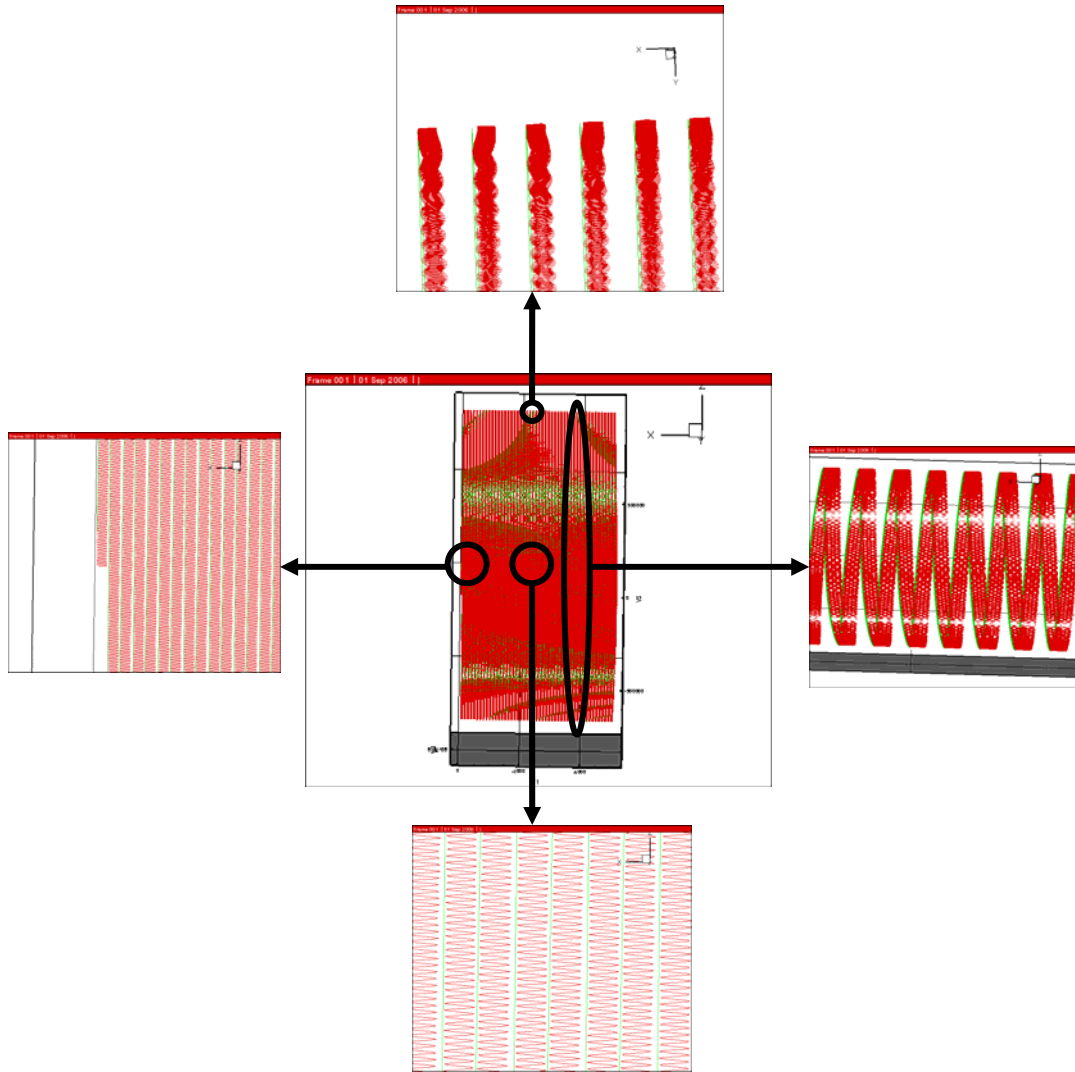
Figure 3.6.1: The initial conditions (for an electron trapped in the earth's dipole) for the computational comparisons between the Boris push (red) and the guiding center (green) were: vx1=0 m, y=6775,000 m, vy1=9.66e07 m/s, z=0 m, vz1=2.6e07 m/s, and a total time real time of 10 s. The time step used in the Boris push as 1x10-8 s and the time step used for the guiding center push as 1x10-4 s. Both computed a bounce period of 0.205 s. The figure shows that the guiding center follows the trajectory of the Boris push almost exactly.
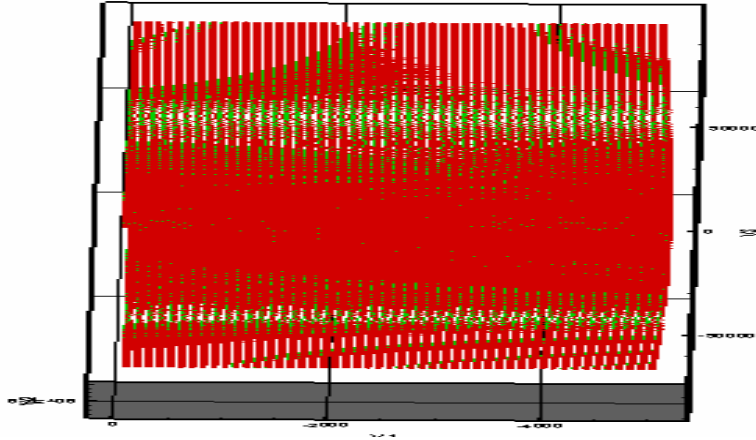
Figure 3.6.2: This is the center figure of Figure 3.6.1 and shows that the guiding center matches the Boris push for the entire trajectory as the green lines (guiding center solution) follow the red trajectory (Boris Push solution).
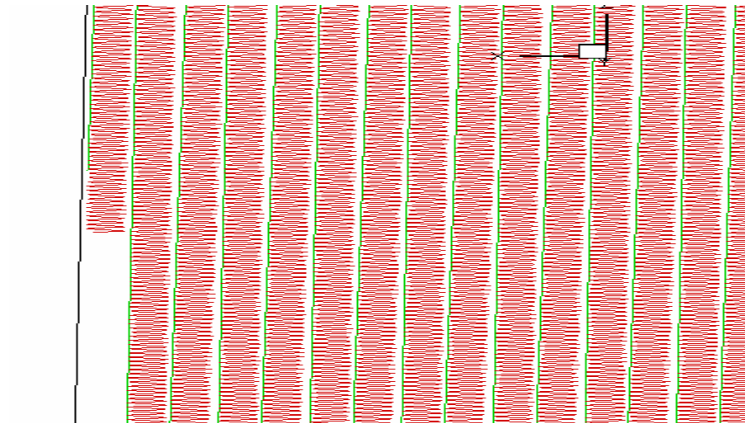
Figure 3.6.3: The left figure of Figure 3.6.1. This shows the early time comparisons of the Boris push and the guiding center. The guiding center solution follows the Boris Push solution.
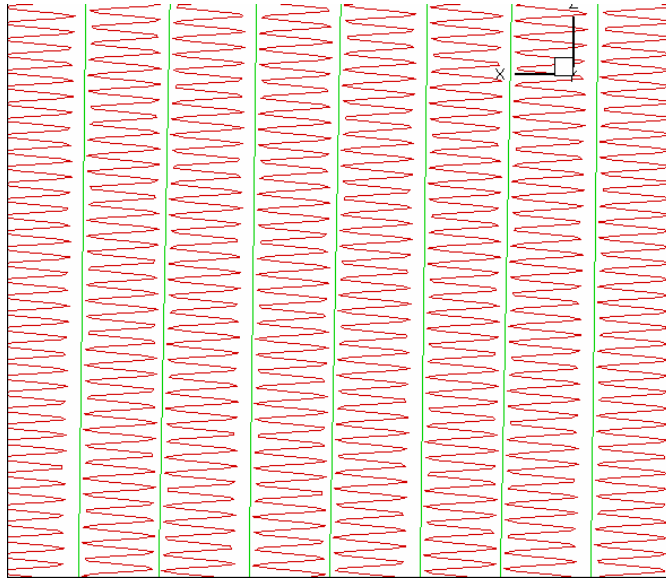
Figure 3.6.4: The bottom figure from Figure 3.6.1. This is the center of the comparisons of the trajectories. Note that the guiding center is always to the left of the Boris trajectory. This is based on the same starting point for each simulation. The electron actually spirals around the field lines and the guiding center ignores the spiral and just follows the general motion of the guiding center.
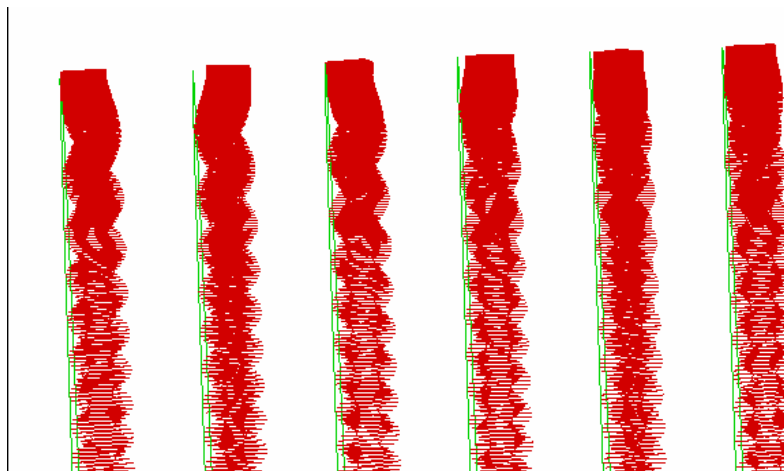
Figure 3.6.5: This is the top figure of Figure 3.6.1. This shows that the turning points of both computational models agree.

Figures 3.6.6 and 3.6.7 offer more comparison of the guiding center and Boris push for relativistic electrons. In every test case for electrons, the Boris push and guiding center were almost identical in terms of modeled trajectory, bounce period, and equatorial

72

drift period with the guiding center offering several orders of magnitude in reduced computational time. Unless the details of the orbit or velocity components are important, the guiding center is used for tracking the electrons.
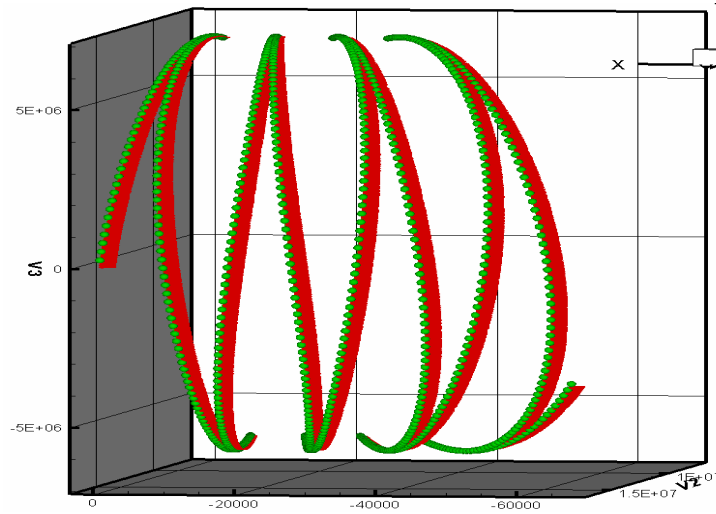
Figure 3.6.6: A comparison between the Boris push and guiding center given the initial conditions: x0=0 m; vx0=0 m/s; y0=16,775,000 m.; vy0=1.0e08 m/s; z0=0 m.; vz0=2.7e08 m/s. The guiding center and Boris push computed a bounce period of 0.2536 s and 0.2538 s. The calculated estimate was 0.2576 s.
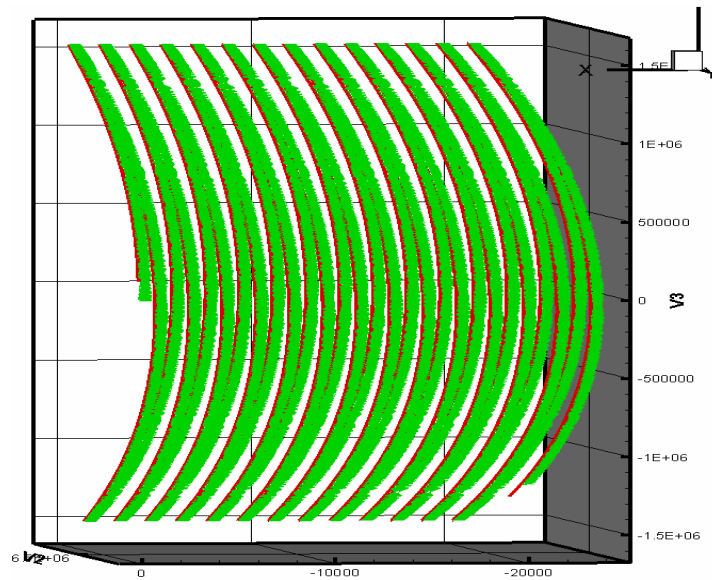
Figure 3.6.7: A comparison between the Boris push and the guiding center of a 4.4 MeV electron with γ=9. The initial conditions were: conditions: x0=0 m; vx0=0 m/s; y0=6775,000 m.; vy0=2.6e08 m/s; z0=0 m.; vz0=1.4e08 m/s. The bounce period of the Boris push was 0.0733 s and the bounce period of the guiding center was 0.0732 s.

Although the guiding center approximation can reduce the time step, Δt, and computational time compared to the Boris push by several orders of magnitude, one needs to demonstrate confidence in the comparison between both models and understand the limitations of each. The trajectory calculated using the guiding center method is shown to match the full trajectory from the Boris push method almost exactly in cases when the Larmor radius is small. When the Larmor radius is large, it may be necessary to use the Boris push if the details of the complete trajectory are important.

For example, a comparative set of calculations was carried out using the initial conditions of an electron; x=0 m, vx1=0 m/s, y=6,775,000 m, vy1=9.66x10^7 m/s, z=0. m; vz1=2.6 x10^7 m/s (this is 400 km above the magnetic equator and a speed of 1 x10^8 m/s and a total time of 10 s.) The bounce period computed from the Boris method was 0.2050 s with a time step of 1x10^{-8} s. The bounce period computed from the guiding center method was 0.2049 s with a time step of 1x10^{-4} s. Using equation 1.3.2.13, the predicted bounce period was 0.2056 s. Recall that equation 1.3.2.13 is not an exact solution but an approximation to the bounce period. The bounce period of the Boris push and the guiding center were close to the estimated value and were almost identical to each other confirming the validity of each method. The Boris push was run with a time step of 1x10^{-8} s and required twenty-seven minutes of computer time. The guiding center was run with a time step of 1x10^{-4} s and required 0.006 minutes of computer time. Table 3.6.1 provides more comparisons of the Boris push and the guiding center given the same set of initial conditions. Even with a time step of 1x10^{-3} s, the guiding center compares very well to the Boris push in terms of trajectory and bounce period of the electron.

Boris Push Computational Values

Time Step (s)	Comp. Time (min)	Bounce Period (s)	Final x (m)	Final y (m)	Final z (m)	Final r_0 (m)
1.00E-08	27.3	0.205	-5020	6620657	-823810	6671715
1.00E-07	12.8	0.206	-5058	6755612	-295545	6762075
1.00E-06	1.3	0.207	-3835	6718438	-502650	6737216

Guiding Center Computation Values

Time Step (s)	Comp. Time (min)	Bounce Period (s)	Final x (m)	Final y (m)	Final z (m)	Final r (m)	% difference in final r_0 from BP
1.00E-03	0.001	0.2039	-5098	6773799	-886420	6831553	2.3397
1.00E-04	0.006	0.2049	-4987	6628334	-803572	6676867	0.0772
1.00E-05	0.032	0.205	-4981	6621524	-821521	6672293	0.0087
1.00E-06	0.29	0.205	-4981	6620819	-823354	6671819	0.0016
1.00E-07	2.92	0.205	-4981	6620722	-823606	6671754	0.0006
1.00E-08	29.3	0.205	-4825	6617306	-832423	6669459	0.0338

Table 3.6.1:   A comparison of the Boris push to the guiding center computational results using the initial conditions: x=0, vx1=0, y=6,775,000 m, vy1=9.66e07 m/s, z=0.; vz1=2.6e07 m/s. The guiding center provides a close approximation to the more accurate Boris push, but saves orders of magnitude in computational time. Note that the bounce period increases slowly when a larger time step is used with the Boris push thus demonstrating a limitation of the Boris push.

The guiding center approximation is not necessarily always a suitable replacement for the Boris push method, but it will provide the correct bounce and drift period for the particle. For the silver atom, the guiding center would only model the guiding center of the trajectory and would not model the actual helical trajectory. Depending on the initial conditions of the ion the importance of the effect of the Larmor radius, this difference between the guiding center trajectory and that of the Boris push could be significant..

Figures 3.6.8, 3.6.9, and 3.6.10 show the comparison between the guiding center trajectories and the Boris push trajectories for the 2,000 km/s, singly charged silver ion given the following conditions: x0=0. m; vx0=0 m/s; y0=7000,000. m; vy0=1.7e6 m/s; z0=0 m.; vz0=1.0e6 m/s; and a total time of the simulation is 25 seconds. Both models predicted a bounce period of 11.5 s compared to the estimate of the bounce period of 11.6

s. Additionally, the figures show that the guiding center follows the same general path of the trajectory, but like the electron, the guiding center does not follow the complete spiral path of the charged particle and there are conditions when we are not particularly interested in the spiral aspect of the path. In terms of an estimate of the trajectory, the guiding center once again proves a great match for the Boris push and analytical predictions.

In Figure 3.6.8 one should note that the red (guiding center) is always on the edge of the green (Boris push) because the particles start at the same location in each model, but the Boris method accounts for the spiral motion of the particle. All of the plots for the ions present the guiding center on the right side of the Boris push trajectory. If the silver atom were negatively charged then it would drift to the right and the guiding center trajectory would be shown on the left side of the Boris trajectory. The figures also show the size of the orbit of the silver atom. The Larmor radius 400 km above and at the magnetic of the equator is around 86 km for the initial conditions. Because the scattering and the ionization energy losses are shown to be directly dependent of the density of the atmosphere, the Boris push is a better method to use with the heavy ions interacting with the atmosphere.

In terms of computing time, the guiding center was run with a time step of 0.1 ($\sim$1/100th of bounce period) seconds and the Boris push was run with a time step of 0.001 s ($\sim$1/100th of gyro-period.) This larger time step for the Boris push, when compared to the electron, is possible because the gyro-period at the magnetic equator of the silver atom in this field is around 0.3 s and the bounce period is 11.5 s. In this case, the large orbital radius, longer gyro-period, and the smaller time step required for the Boris push makes the guiding center less attractive, although the guiding center is still faster. The decision to use the guiding center or Boris push will be based on the significance of the environmental gradients (density and magnetic field) used in the computations.
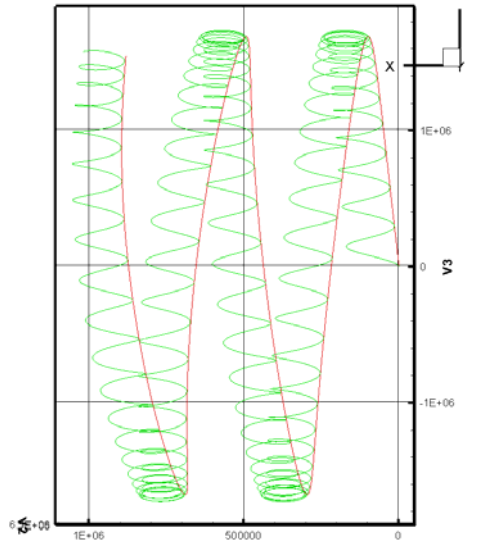
Figure 3.6.8: A comparison of the guiding center and Boris push given the initial conditions of a silver atom of: x0=0. m; vx0=0 m/s; y0=7,000,000. m; vy0=1.7e6 m/s; z0=0 m.; vz0=1.0e6 m/s; and a total time of the simulation is 25 seconds. The radius of the orbit at the equator is 86 km so the guiding center only provides an estimate of the trajectory.
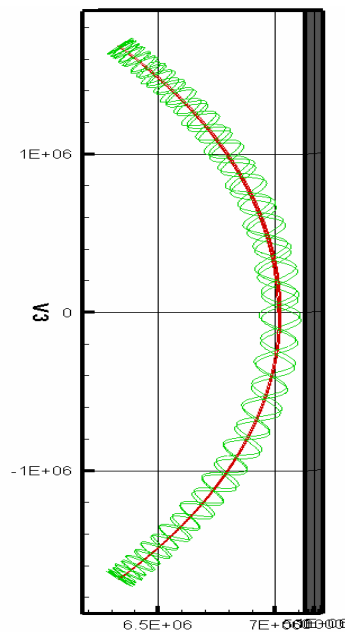
Figure 3.6.9: This is the same initial conditions as in Figure 3.6.8, but looking at the trajectory from the side. The guiding center is shown to approximate the trajectory, but because the Larmor radius is 86 km at the equator, the guiding center is only an approximation.

77
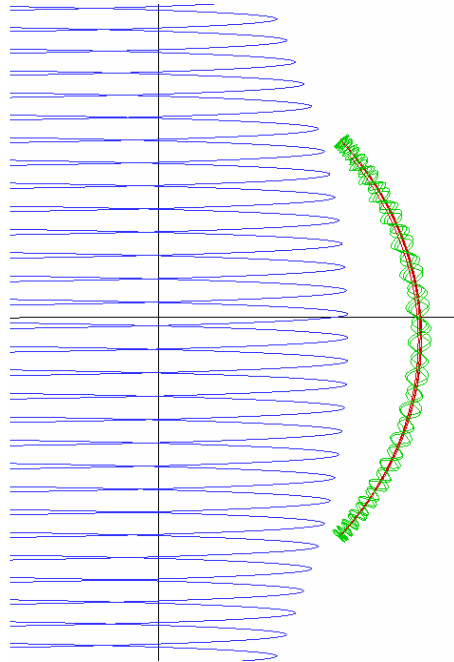
Figure 3.6.10: The earth is in blue in order to provide a sense for the scale of the trajectories of the guiding center (red) and the Boris push (green). In this case, the time steps used in the two simulations are 0.1 s and 0.001 s with a bounce period of 11.5 s. The Larmor orbit at the equator is 86 km.

A final example of the comparison between the Boris Push and the guiding center methods is shown in Figure 3.6.11 where an 11 MeV ($\gamma \approx 22$) electron is released at the magnetic equator with only x and y-components of velocity. Because there is no initial velocity in the z-direction, the particle should not bounce, but only drift around the equator. As expected, the particle is shown to drift around the magnetic equator. The trajectory of the Boris Push is a wonderful match to the trajectory of the guiding center even for this highly relativistic (by trapped radiation standards) electron. Both models predict a drift period of 42 s compared with the analytical estimate of 72 s. As was shown in Table 3.5.1 and derived in Section 2.3.5, the analytical solution is only an estimate to the drift period predicted in the simulation and should be used only as an approximation. The model is capable of providing a more accurate drift period.

78
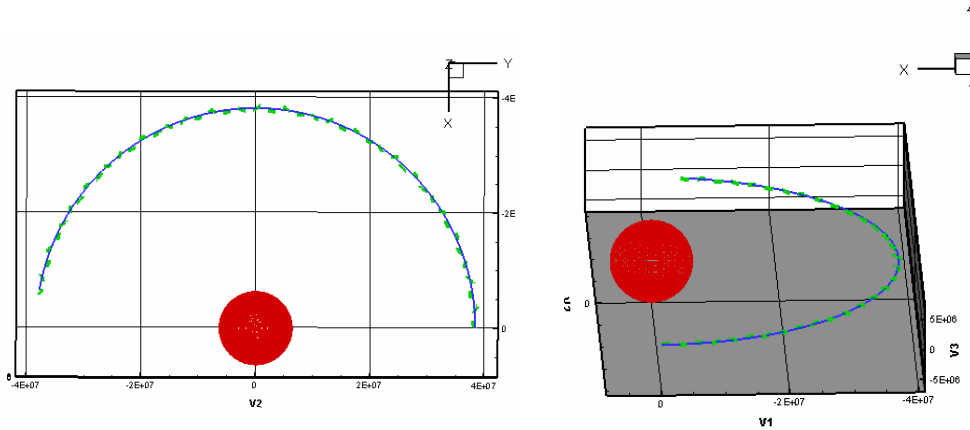
Figure 3.6.11: The above figures are the Boris push compared to the guiding center with an electron with initial conditions: x0= 0 m; vx0=0 m/s; y0=38,250,000 m; vy0=2.997e8 m/s; z0=0 m; vz0=0 m/s; and the total simulation time of 20 s. The drift period from both models is 42 seconds and both models are in complete agreement with each other.

There are clearly initial conditions (relativistic electrons in relatively low L-shells) where the guiding center saves five or so orders of magnitude of computational time and yielding the same results as the Boris push with virtually no loss of information. There are also initial conditions (a large Larmor orbit typical for fission fragment ions) such that the time savings of the guiding center may be less important than the loss of information of the real particle trajectory modeled using the Boris push. The challenge remains to build a computer model capable of injecting at least a million particles into the magnetic field of the earth and tracking all of the injected particles and the electrons resulting from beta decay. The computer code was developed that meets this challenge; as will be shown, the code leverages off the strengths of each model in order to minimize the computational requirement and still provide reasonable results with a high degree of confidence.

What should be clear is that the model and model results presented in Chapter III above provide very close agreement with the theory developed in Chapter II of the motion of charged particles trapped in perfect dipole without any atmospheric interaction. The goal has been make sure that the code could model and match the predictions of the simplest set of conditions. The computational results presented demonstrate a clear ability to match the theoretic predictions of particles trapped in a perfect dipole field. The Boris

79

push offers a high-fidelity method, but requires significant computational assets. When possible the guiding center method allows for a very close approximation to the Boris push with much less computing time. However, the earth's dipole is not perfect and the particles trapped in the earth's field continuously interact with atmospheric constituents. Chapter IV will provide insight into the real physical conditions of the earth's magnetic field, the effect of the atmosphere on the motion of charged particles, and the other physics required to complete the model of the environment caused by a nuclear detonation (or other significant and localized source of charged particles) well above the surface of the earth.

IV.   DEVIATIONS FROM THE IDEAL

Thus far, the theoretical development has centered on simplified (and analytically verifiable) simulations that ignored the effects of the real magnetic field of the earth and the effects of the atmosphere on the charged particles trapped in the magnetic field. The initial computational modeling was developed using a perfect dipole and the assumption of a perfect vacuum in order to establish confidence in the ability to simulate the basic physics and validate output of the code against the analytical solutions. The Boris push and guiding center approximations were both shown to provide a good match to the analytic solutions in these simplified situations. However, in order to provide a useful and comprehensive model for the location of the debris from a nuclear detonation in space, one must include the physics and conditions that represent the reality of the actual environment. It is the purpose of this chapter to extend the simplified model into one that treats these additional complexities.

4.1.   MAGNETIC FIELD OF THE EARTH

An idealized approximation to the earth's geomagnetic field was introduced in Chapter II as a perfect dipole centered on geographic equator of the earth. The true magnetic field of the earth is a bit more complicated due to various sources of magnetism located in the earth as well as the interaction of the interstellar magnetic field with the magnetic field of the earth. Near the surface of the earth, the dipole field is also perturbed by localized concentrations of magnetic ore. Additionally, there are time dependent variations caused by an increase or decrease in solar activity. A complete description of the magnetic field of the earth is a large field of study[38,39] but will not be discussed in great detail and only described within the bounds of the applicability to the low L-shell trapped radiation problem. More comprehensive answers may come with advanced models of the earth's magnetic field, but given the scope of this dissertation, the simplest,

---

[38] United States Air Force, *Handbook of Geophysics*, Rev. ed., United States Air Force, (New York: The Macmillan Co., 1960).

[39] J. B. Cladis et al., *The Trapped Radiation Handbook*, (Palo Alto, CA.: Lockheed Palo Alto Research Laboratory, published by General Electric Company, TEMPO DNA Information and Analysis Center, Santa Barbara, CA, for Defense Nuclear Agency, 1971), 6-61 – 6-65.

and yet accepted, approximation for the earth's magnetic field is developed and utilized in the computer simulation. The primary adjustments to the ideal model of the earth's magnetic field include the tilt of the dipole and the dipole offset from the center of the earth.

Fortunately, the main field affecting the orbits of particles trapped in the low-earth orbits can be represented to an accuracy of about 90 percent by the magnetic field that would result from a tilted dipole field positioned with a slight offset from the center of the earth. The remaining 10 percent of the field near the surface of the earth is due to the concentrations of ore deposits.[40] The interstellar magnetic fields do not normally affect the magnetic field of the earth at altitudes less than five earth radii.[41] Several authors have developed many-termed, spherical-harmonic expansion of the dipole field with appropriate coefficients.[42,43,44] The Trapped Radiation Handbook also offers a basic description of the many-termed, spherical-harmonic expansion. If deemed necessary for higher fidelity results a multi-term expansion may be included for the magnetic field in the computer simulation. For the purpose of the dissertation, the 90 % solution to the magnetic field is more than sufficient. Other models have many more terms from the expansion and, although they may offer better models for detailed analysis of the magnetic field, the multi-term expansions require multiple and costly computer calculations for each time step. Even the 48-term Jensen and Cain model is quite expensive in computer time and will only be added as necessary. However, with the computer code in place, adding the more detailed magnetic field to the code is possible as long as the computer time is available. The addition of a higher fidelity model is a area for future work. For now a reasonable approximation of the magnetic field is applied to the study of trapped radiation.

---

[40] Cladis et al., 2-1.

[41] Parks, 56.

[42] D.C. Jensen and W.A. Whitaker, "A Spherical Harmonic Analysis of the Geomagnetic Field," *J. Geophys. Res.,* Vol. 65, 1960: 2500.

[43] D.C. Jensen and J.C. Cain, "An Interim Magnetic Field," *J. Geophys. Res., Vol. 67*, 1962: 3568-3569.

[44] S. J Hendricsk and J.C. Cain, "Magnetic Field Data for Trapped Particle Evaluations," *J. Geophys. Res.,* Vol. 71, 1963: 346-347.

The magnetic field used in the computer simulation developed as part of this dissertation is a field that would result from dipole displaced by 0.0685 earth radii from the center of the earth toward a direction defined by geographic latitude 15.6° N and longitude 150..4° E. The intersections of the displaced dipole axis with the earth's surface are at 81.0° N, 84.7° W, and at 75.0° S, 120.4° E.[45,46] The same field is used in the Air Force Research Laboratory (AFRL) Satellite Nuclear Radiation Threat Assessment Code System (SNRTACS). SNRTACS is the current DoD standard for modeling nuclear effects on satellites.

The coordinate transformation matrix for the shifted and tilted magnetic field was provided by Bob Greaves, the current program manager of SNRTACS and is described below[47] and shown in Figure 4.1.1 and 4.1.2 (the perfect dipole is shown again in Figure 4.1.3.) The coordinate axis used in the transformation aligns the Y-geographic axis along the zero longitude direction and the X-geographical axis is aligned along the 90^0 west direction.

First the center of the dipole is offset from the geographic center by the translation

$$Tx = (X\text{-geographic} + 367.29) \text{ km,}$$

$$Ty = (Y\text{-geographic} - 204.43) \text{ km,}$$

$$Tz = (Z\text{-geographic} - 117.36) \text{ km.}$$

The rotation of the dipole (the tilt) is calculated with a rotation matrix

$$\begin{bmatrix} X - \text{magnetic} \\ Y - \text{magnetic} \\ Z - \text{magnetic} \end{bmatrix} = \begin{bmatrix} A11 & A12 & A13 \\ A21 & A22 & A23 \\ A31 & A32 & A33 \end{bmatrix} \begin{bmatrix} Tx \\ Ty \\ Tz \end{bmatrix} \text{ where}$$

A11 = 0.97129205, A12 = 0.23641749, A13 = - 0.02642934,
A21 = - 0.22646696, A22 = 0.95294113, A23 = 0.20153391,
A31 = 0.07283175, A32 = - 0.18976292, A33 = 0.97912490.

[45] W.D. Parkinson and J. Cleary, "The Eccentric Geomagnetic Dipole," *J. Geophys. Res.,* Vol. 1, 1962: 346.

[46] Cladis et al., 6-2.

[47] Bob Greaves (Air Force Research Laboratory), private conversation with author, 15 February 2006.

The resulting equations for the conversion from geographic coordinates to magnetic coordinates are

(4.1.1)   X-magnetic = A11*Tx + A12*Ty + A13*Tz,

(4.1.2)   Y-magnetic = A21*Tx + A22*Ty + A23*Tz,
(4.1.3)   Z-magnetic = A31*Tx + A32*Ty + A33*Tz.
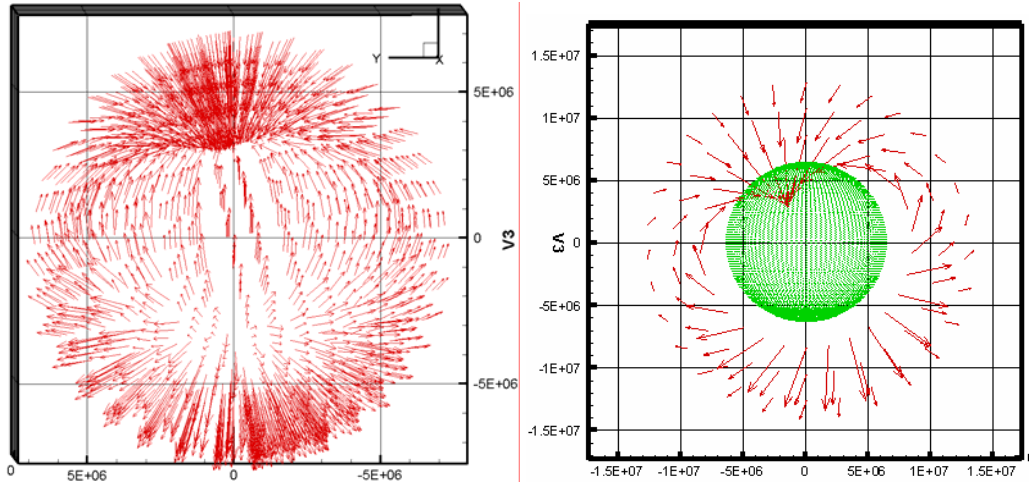
Figure 4.1.1: Plots of the magnetic field of the earth using equations 4.1.1, 4.1.2, and 4.1.3 (shift and tilted dipole.) The plot on the left is a 2-D representation of the modified field shown with the earth in green. The figure on the left is a 3-D representation.
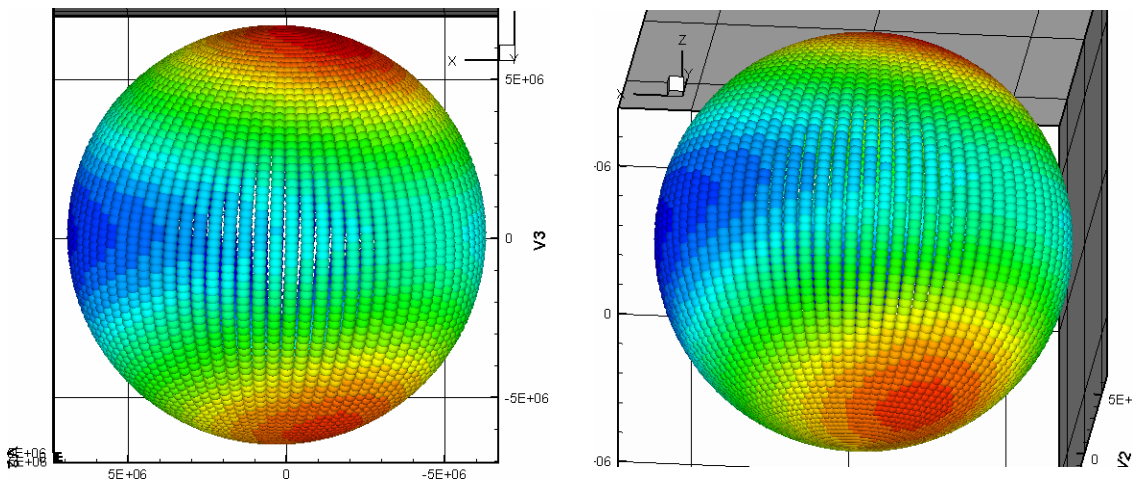
Figure 4.1.2: These contour plots are of the shifted and tilted magnetic field. The blue regions represent areas of lowest field strength on the surface and the red regions represent the areas of largest field strength on the surface. The center of the dark blue region represents the SAA.

The shifted and tilted magnetic dipole causes the magnitude of the field at the surface of the earth to vary for given latitudes. Figure 4.1.3 presents a contour plot of the magnitude of the magnetic field at the surface of the earth for a dipole centered on the geographic center of the earth. The contours are symmetrical about the geographic axis of the earth. This is in contrast to Figure 4.1.4 where the magnetic contours of the shifted and tilted magnetic field are presented for the surface of the earth and are not symmetrical about the geographic axis of the earth. For given latitudes, the magnitude of the earth's surface magnetic field can vary by a factor of 2 as a function of longitude.
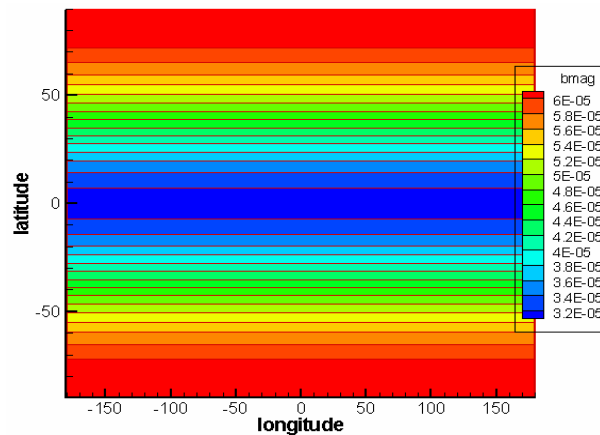
Figure 4.1.3: This is the magnetic contours on the surface of the earth if a perfect dipole was centered at the geographic center of the earth. The values of the magnetic field are in tesla.
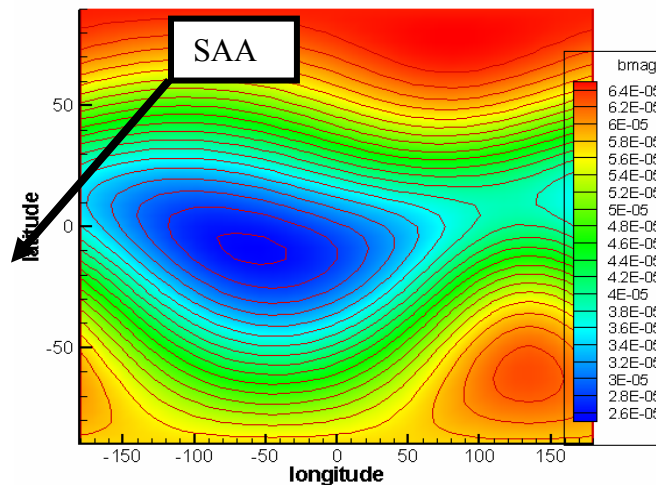
Figure 4.1.4: This is the magnetic contours on the surface with the shifted and tilted dipole as described above. The South Atlantic Anomaly (SAA) used in the simulation is centered on a longitude of 60W and latitude of 10S. The values of the magnetic field are measured in tesla.

85
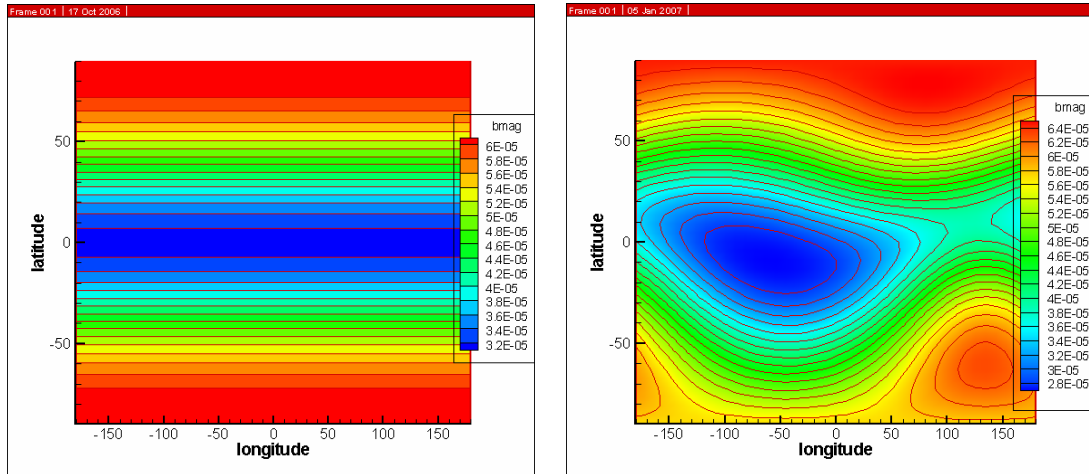
Figure 4.1.5: A side by side comparison of Figures 4.1.3 and 4.1.4.

The South Atlantic Anomaly can significantly affect particles trapped in the earth's magnetic field especially for low L-shell orbits with mirroring altitudes less than 1000 km. The altitude of mirror point may change by more than an order of magnitude as the particle drifts around the earth in a given L-shell. From equation 1.1.36,

$$B_{mirror} = \frac{Sin^2(\alpha_0)}{B_0},$$ recall that unless the pitch angle at the magnetic equator changes, the

magnitude of the magnetic field at the mirror point remains constant as a particle drifts around the dipole field. With the applied magnetic field the altitude of the B_{mirror} changes as the particle drifts due to the shift and tilt of the dipole. The region of the world where the magnetic field is the weakest for a given altitude is often referred to as the South Atlantic Anomaly (SAA) and is centered near Brazil. The effect of the South Atlantic Anomaly is a "scraping-off" effect of the trapped particles. The general location of the South Atlantic Anomaly is shown on Figure 4.1.4. For example, a particle that has a mirror altitude of 1,000 km away from the SAA may mirror as low as 100 km near the SAA. Particles that mirror at 300 km in altitude at a location 180 degrees in longitude away from the South Atlantic Anomaly will have mirror points inside the surface of the earth as the particle approaches the SAA. Obviously, the particle can not mirror inside the earth and it will be shown that the particle would actually lose all kinetic energy in the atmosphere. Figure 4.1.6 shows an electron injected at 400 km above the surface of the

86

earth at a longitude of 0 degrees and latitude of 0 degrees. As the electron drifts around the earth the effects of the air and the surface of the earth are removed in order to demonstrate the required trajectory of the particle. As the particle drifts to the east and as shown in Figures 4.1.6, 4.1.7, 4.1.8, and 4.1.9, depending on the initial conditions, the particle would need to drift through the surface of the earth or deep into the atmosphere in order to maintain the proper drift orbit. The most startling demonstration of this is seen below in Figures 4.1.6 and 4.1.7 where a 1.5 MeV electron is released into the magnetic field at 400 km above the earth on the geographic equator at a longitude of 90E. As the particle drifts to the east, the effect of the shifted and tilted dipole requires that the electron actually mirror inside and pass through the surface of the earth in order to stay on the proper orbit. An electron is not going to pass through the earth as part of the trapped orbit and the electron will not remain trapped as it nears the surface of the earth.
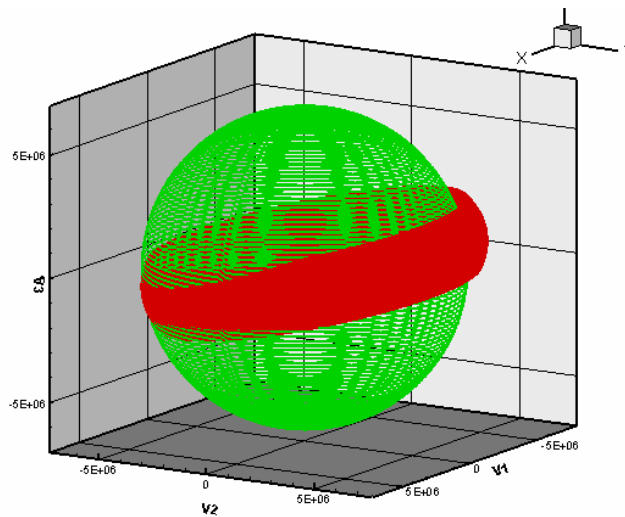
Figure 4.1.6: A 1.5 MeV electron is injected into the magnetic field of the earth at x = 0 m, y = 6775,000 m, and z = 0 m, with Vx = 0, Vy = 2.9x108 m/s, and Vz = -0.75x106 m/s. The particle drifts to the east, but because of the magnetic field of the earth the electrons trajectory passes through the earth. The area where the collision occurs is the vicinity of the South Atlantic Anomaly. Figure 4.1.6 provides a top down view of the trajectory.
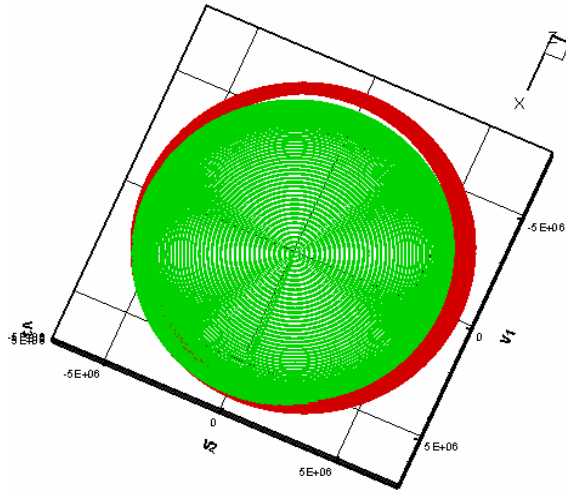
Figure 4.1.7: The trajectory of the1.5 MeV electron from Figure 4.1.6 is looking down on the geographic axis of the earth. The electrons trajectory is shown to pass through the earth.

Figures 4.1.8 and 4.1.9 present another example of the effect of the shifted and tilted dipole. Here a 1.5 MeV electron is released at 1,000 km above the surface of the earth on the magnetic equator and at a longitude of 90E. This electron does not need to pass through the earth to complete its orbit, but near the SAA the electron does mirror deep in the atmosphere and close to the surface of the earth.
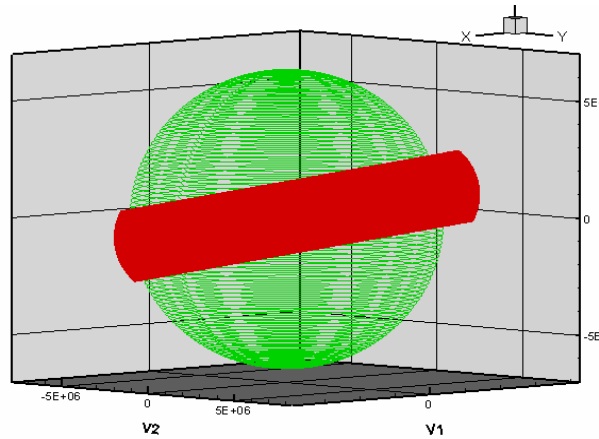
Figure 4.1.8: A 1.5 MeV electron is injected into the magnetic field of the earth at 1,000 km above the surface at x = 0 m, y = 7375,000 m, and z = 0 m, with Vx = 0, Vy = 2.9x108 m/s, and Vz = -0.75x106 m/s. The particle drifts to the east, but because of the magnetic field of the earth the electrons eventually takes the particle deep into the atmosphere of the earth. The area where the collision occurs is the vicinity of the South Atlantic Anomaly. Figure 4.1.9 provides a top down view of the trajectory.
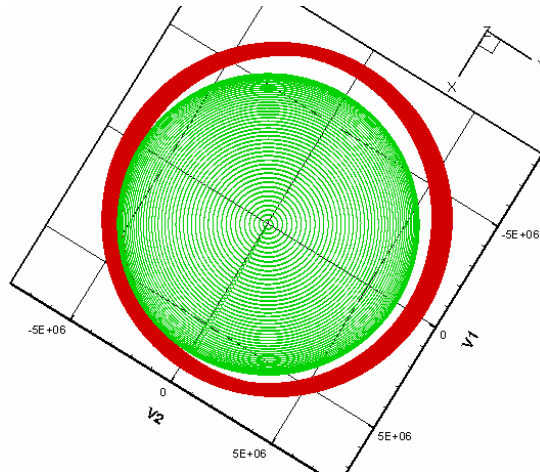
Figure 4.1.9: The trajectory of the 1.5 MeV electron from Figure 4.1.8 is viewed looking down on the geographic axis of the earth. The electrons trajectory is shown to pass deep into the atmosphere of the earth near the South Atlantic Anomaly.

As mentioned the electron does not drift through the surface of the earth and is therefore "scraped" out of orbit due to atmospheric collisions. The actual "scraping" is caused by multiple interactions with the atmosphere where the particle transfers its kinetic energy to the atmosphere and eventually is slowed to the thermal velocity of the atmosphere. The details of the earth's atmosphere are described in section 4.2

The location of injection of the charged particle, therefore, plays an important role in the eventual trapping efficiency of the ions and electrons. A particle injected and trapped near the SAA will move out in altitude as the particle moves on the drift orbit away from the SAA. Generally, for particles released and trapped near the SAA, the lowest mirror point altitude is near the initial trapping longitude and the atmospheric interaction decreases as the particle moves away from the SAA. However a particle that is injected and trapped away from the SAA will mirror at a lower altitude as the particle drifts near the SAA. Generally, the trapping efficiency decreases as the particles mirror at lower altitudes. Figure 4.1.10 shows the results of a 6.3 MeV electron released at 400 km at different longitudes at the geographic equator (the z-coordinate = 0). For the given initial conditions and depending on the longitude of injection, the minimum altitude for the mirror point as the particle drifts around the earth, for many of the particles, is inside the surface of the earth and the particles would no longer be trapped.

89

Lowest Altitude of Mirror Point for 6.3 Mev Electron Released Radially (Vz = 0) at 400 km and at the Geographic Equator at Different Longitudes
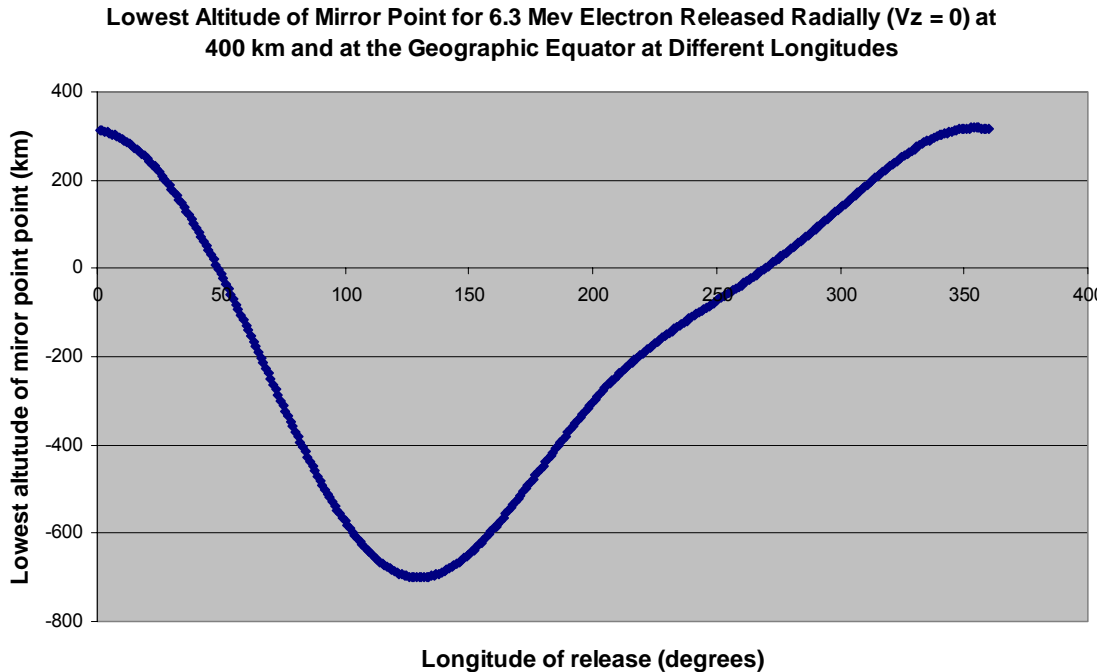
Figure 4.1.10: Electrons were injected at the geographic equator with identical velocities of 2.99x108 m/s directed radially outward. The minimum altitude of the mirror point is shown as a function of the longitude of release. Many of the particles with a mirror altitude less than 100 km are lost due to interactions with the atmosphere. The shape of the figure is a result of the different initial pitch angles of the electrons due to the shift and tilt of the dipole field. The trapping efficiency of electrons in the lower L-shells is strongly dependent on the latitude and longitude of release.

An observant reader might note that at two points of injection in Figure 4.1.10, the particle's velocity would be perpendicular to the magnetic field. One would expect the electron with a velocity strictly perpendicular to the magnetic field to only spiral around the magnetic field line with no effective bounce between conjugate points. The particle would, however, drift on that magnetic field line. As has been shown, the drifting particle's mirror point would change in altitude as a function of longitude. The result is that for the conditions of Figure 4.1.10, all of the electrons have a lowest mirroring altitude below the altitude of injection.

4.2. DESCRIPTION OF THE ATMOSPHERIC/SPACE MODEL

The atmospheric model used in the simulation and in the dissertation is a model used by the NASA Goddard Space Flight Center in Greenbelt, Maryland and was

developed by A.E. Hedin. The Mass Spectrometer and Incoherent Scatter (MSIS) empirical models of Hedin[48,49,50] provide thermospheric temperature and density based on in-situ data from seven satellites and numerous rocket probes. These models provide estimates of temperature and the densities of N_2, O, O_2, He, Ar, and H up to altitudes of 1,000 km. Low-order spherical harmonics are used to describe the major variations through out the atmosphere including latitude, annual, semiannual, and simplified local time and longitude variations. The model provides a useful format for organizing and making widely available the results of satellite missions which provide large amounts of data, but with limited coverage of relevant geophysical conditions by an individual mission. These models facilitate data comparisons and theoretical calculations requiring a background atmosphere, as well as providing a convenient engineering solution.

The MSIS models use a Bates-Walker temperature profile as a function of geo-potential height for the upper thermosphere and an inverse polynomial in geo-potential height for the lower thermosphere. Exospheric temperature and other atmospheric quantities are expressed as functions of geographical and solar/magnetic parameters. The temperature profiles allow for exact integration of the hydrostatic equation for a constant mass to determine the density profile based on a density specified at 120 km as a function of geographic and solar/magnetic parameters. The model is available for download at http://uap-www.nrl.navy.mil/models_web/msis/msis_home.htm.[51] Table 4.2.1 shows some of the data from the MSIS model.

---

[48] A. E. Hedin, "A Revised Thermospheric Model Based on Mass Spectrometer and Incoherent Scatter Data: MSIS-83," *J. Geophys. Res.,* Vol. 88, 1983: 10170.

[49] A. E. Hedin, "MSIS-86 Thermospheric Model," *J. Geophys. Res.,* Vol. 92, 1987: 4649.

[50] A. E. Hedin, "Extension of the MSIS Thermosphere Model into the Middle and Lower Atmosphere," *J. Geophys. Res.,* Vol. 96, 1991: 1159.

[51] NRL Mass Spectrometer, Incoherent Scatter Radar Extended Model: NRLMSISE-00, http://uap-www.nrl.navy.mil/models_web/msis/msis_home.htm (accessed on 17 April 2007).

height (km)	# O/cm^{-3}	# N2/cm^{-3}	# O2/cm^{-3}	Day (g*cm^{-3})	Night (g*cm^{-3})	Average density (g*cm^{-3})
0	0.0	1.94×10^{19}	5.20×10^{18}	1.19×10^{-03}	1.19×10^{-03}	1.19×10^{-03}
5	0.0	1.17×10^{19}	3.14×10^{18}	7.19×10^{-04}	7.18×10^{-04}	7.18×10^{-04}
10	0.0	6.79×10^{18}	1.82×10^{18}	4.18×10^{-04}	4.17×10^{-04}	4.17×10^{-04}
30	0.0	3.14×10^{17}	8.42×10^{16}	1.93×10^{-05}	1.93×10^{-05}	1.93×10^{-05}
50	0.0	1.92×10^{16}	5.16×10^{15}	1.18×10^{-06}	1.18×10^{-06}	1.18×10^{-06}
80	4.21×10^{09}	3.12×10^{14}	8.29×10^{13}	1.92×10^{-08}	1.92×10^{-08}	1.92×10^{-08}
100	2.68×10^{11}	7.35×10^{12}	1.68×10^{12}	4.43×10^{-10}	4.58×10^{-10}	4.50×10^{-10}
200	2.47×10^{09}	2.61×10^{09}	1.63×10^{08}	1.96×10^{-13}	1.57×10^{-13}	1.77×10^{-13}
300	2.64×10^{08}	6.24×10^{07}	2.31×10^{06}	1.02×10^{-14}	5.30×10^{-15}	7.73×10^{-15}
400	3.47×10^{07}	1.84×10^{06}	4.12×10^{04}	1.03×10^{-15}	3.85×10^{-16}	7.10×10^{-16}
500	4.92×10^{06}	6.05×10^{04}	830	1.41×10^{-16}	3.89×10^{-17}	8.98×10^{-17}
600	7.39×10^{05}	2.19×10^{03}	18.7	2.30×10^{-17}	5.66×10^{-18}	1.43×10^{-17}
700	1.17×10^{05}	87.4	0.471	4.98×10^{-18}	1.63×10^{-18}	3.31×10^{-18}
800	1.96×10^{04}	3.81	0.0131	1.71×10^{-18}	8.50×10^{-19}	1.28×10^{-18}
900	3.43×10^{03}	0.181	4.03×10^{-04}	8.90×10^{-19}	5.60×10^{-19}	7.25×10^{-19}
1000	6.31×10^{02}	0.00934	1.36×10^{-05}	5.72×10^{-19}	4.02×10^{-19}	4.87×10^{-19}

Table 4.2.1:   This is data from the MSIS atmospheric density code developed by Hedin. This set of data was collected for 6 August 1965, but data is available for any specific date or time or day. An average day/night mass density was used to build the lookup tables used in the simulation.

Instead of running the model (over 2,000 lines of code) to determine the atmosphere for each density calculation, a look-up table was developed with 1 km increments to call the density values based on the altitude of the particle. The date of 6 August, 1965 was input into the model for date of the density profile calculations. (If specific dates are of interest then the code can easily generate a complete set of data for a given date and time of day.) The values in Table 4.2.1 for the specific date were calculated for 1200 local and 2400 local and an average of the day and a night density value was used as the input for the lookup table. The density can vary by as much as an order of magnitude between day and night, depending on the altitude, so an average was selected as a fair representation of the atmosphere. Figure 4.2.1 presents the day and night mass density of air for different altitudes.
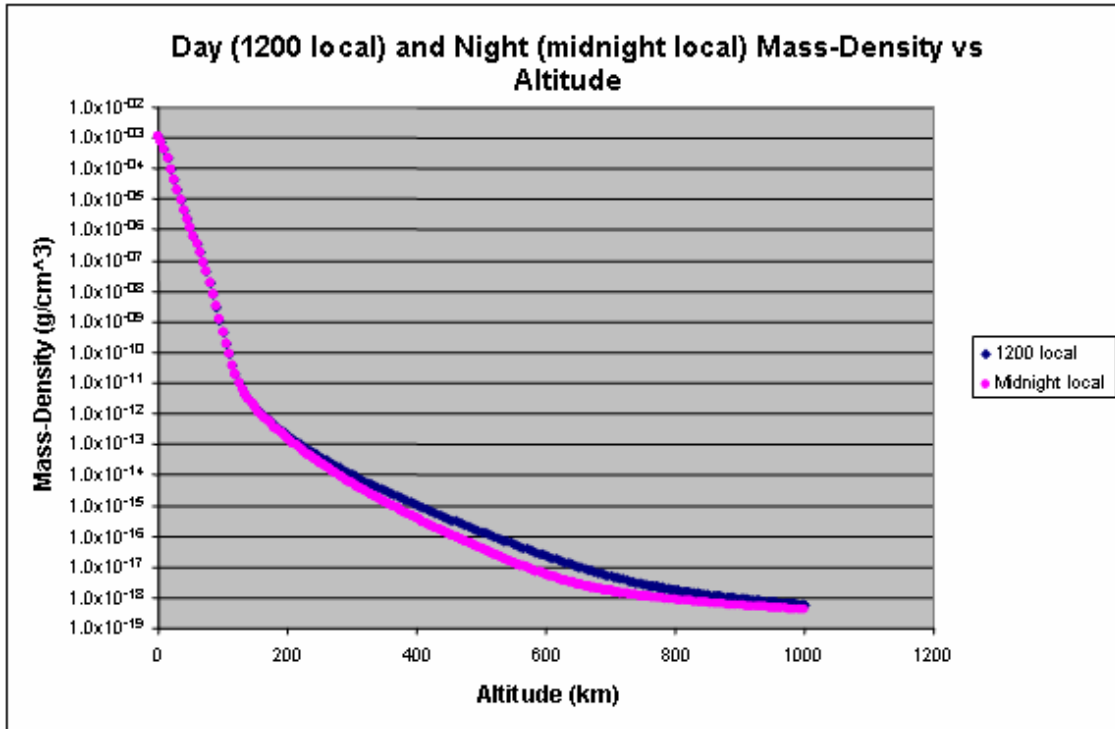
Figure 4.2.1: **The semi-log plot of the mass density vs. altitude is shown for values from the MSIS code for 6 August 1965. The purple (lowest dipping curve) represents the midnight density and the blue represents the midday density. The density can vary up to an order of magnitude between day and night. For the computer simulation, an average of the day and night densities is used.**

The data was analyzed for a fit to an equation or set of equations. In order to best fit the data, two regimes were established, 0 to 125 km, and 126 km to 1,000 km. Figure 4.2.2 show the fit for the density from 0 to 125 km. An exponential fit was found for the lower atmosphere. The least-squares best-fit equation was calculated using Excel.

(4.2.1) $\qquad \text{density}\left(\frac{\text{g}}{\text{cm}^3}\right) = 0.002 \times e^{-0.151 \times (\text{altitude[km]})}$
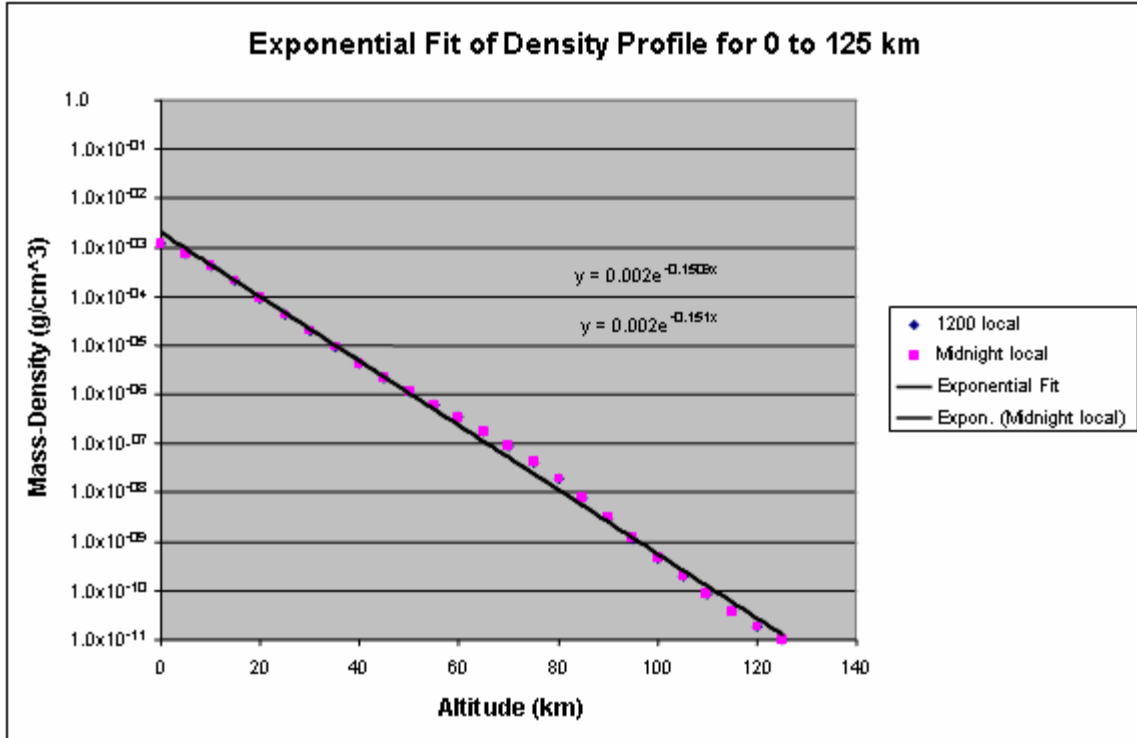
Figure 4.2.2: The semi-log plot of the mass density vs. altitude is shown for values from the MSIS code for 6 August 1965 for altitudes from 0 to 125 km. Within the resolution of the plot, there is little difference between the day and night density data. The best fit equation for each set of data is shown on the plot with virtually identical exponential best-fit equations.

Figure 4.2.3 shows the density plot for altitudes ranging from 126 km to 1,000 km. There is a noticeable, but relatively small difference between the day and night data. In order to generate the best fit equation a power law was developed to fit the average of the day and night data using Excel. The power law for the average density is

(4.2.2) $\text{density}\left(\frac{g}{cm^3}\right) = 4\text{x}10^6 \times \text{altitude}[km]^{-8.4079}$

The density profile in the lookup table was developed using equations 4.2.1 and 4.2.2. Equation 4.2.2 was used to create the table from 126 km up to 2,000 km. Above 2,000 km the density was considered to be zero. Using equation 4.2.2, the density at 2,000 km is on the order of $1\text{x}10^{-22}$ g/cm^3 which is 12 orders of magnitude down from the mass density at 100 km.

94
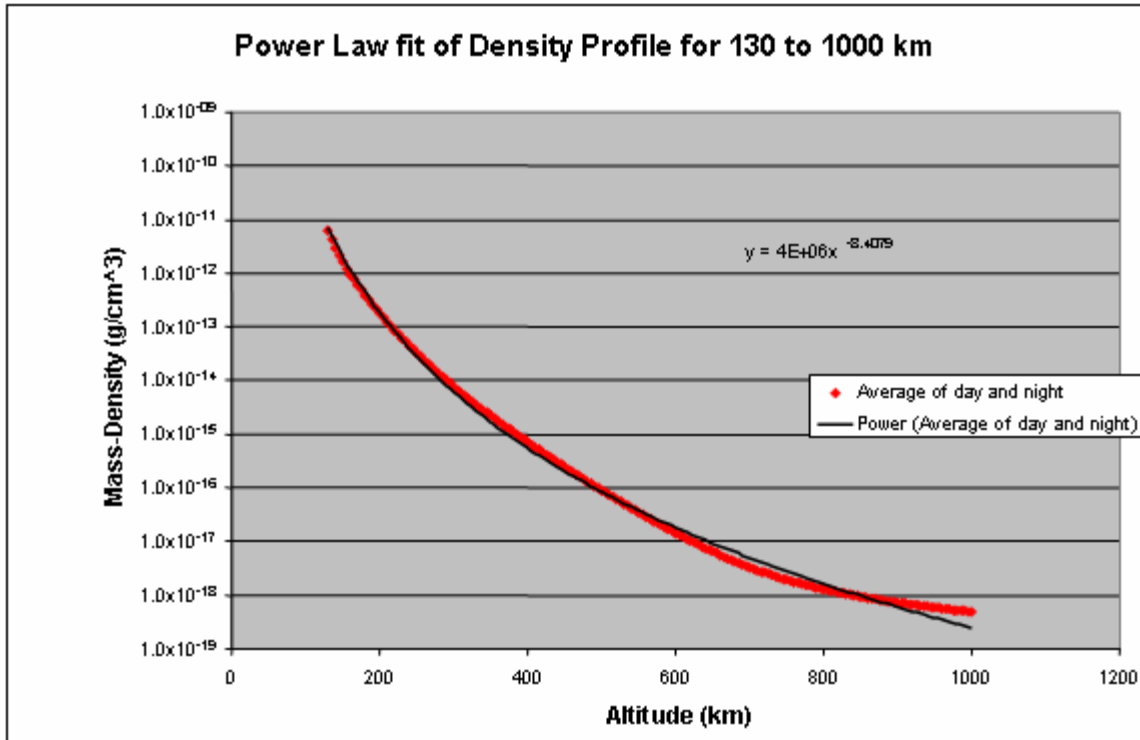
Figure 4.2.3: The semi-log plot of the average of day and night mass density vs. altitude is shown for values from the MSIS code for 6 August 1965 for altitudes from 126 to 100 km. The best fit equation for the data is shown on the plot. The best fit power-law equation was used to develop lookup tables used in the simulations.

There are many references and text that discuss the atmosphere of the earth in much greater detail,[52] but for the purposes of demonstrating the modeling capability, the MSIS model is more than adequate. If specific dates and times are of interest then the simulation can easily accommodate the unique atmospheres or atmospheric conditions.

4.3. ENERGY LOSS OF THE ELECTRONS AND THE IONS

Energetic electrons and ions passing through a matter are involved in elastic and inelastic collisions with the nuclei and the atomic electrons of the stopping medium. The massive nuclei absorb very little of the energy of the electrons and the collisions with the nuclei are almost entirely elastic. The collision with the electrons of the medium causes

---

[52] *US Standard Atmosphere 1976*, (Washington, D.C.: National Oceanic and Atmospheric Administration, National Aeronautics and Space Administration, United States Air Force, 1976).

most all of the energy loss of the charged particles moving through material. Depending on the density of the stopping medium, Cherenkov radiation may also account for some of the energy loss of the electron but, in general for kinetic energies less than 10 MeV, the radiation losses are neglected.[53]

Fermi,[54] Jackson,[55] Starodubtsev and Romanov,[56] and Balashov[57] all develop the expression for energy loss in the frame of a charged particle with charge Ze and mass M colliding with an atomic electron of charge –e and mass m. In this chapter, two different expressions are developed for incident particles that depend on the relative velocity of the incident particle; the first is developed for relativistic electrons and the second expression is developed for much slower ions. Each of the expressions has a wider range of application for different energies of particles than developed here (see Fermi, Jackson, Starodubtsev and Romanov, and Balashov), but for simplicity the energy loss of electrons and ions is treated with separate expressions. Work has been done on the transition region between the two models for charged particle. If necessary, mid-range energies of ions and electrons could be added. Given that the energy threshold of concern for electrons is greater than 40 keV and the ions are all known to have velocities around the Bohr velocity (~ 2000 km/s) the expressions and equations developed below are valid for use in the code to account for the energy loss of ions and electrons as the particles move through the atmosphere of the earth.

---

[53] S.V. Starodubtsev and A.M. Romanov, *The Passage of Charged Particles through Matter*, trans. and ed. Israel Program for Scientific Translation staff for U.S. Energy Commission and the National Science Foundation, (Jerusalem: Israel Program for Scientific Translation, 1965), 158.

[54] E. Fermi, *Nuclear Physics*, Rev. ed., A course given by Enrico Fermi at the University of Chicago with notes compiled by J. Orear, A.H. Rosenfeld, and R.A. Schluter, (Chicago: The University of Chicago Press, 1950) 27 – 33.

[55] Jackson, 625 – 631.

[56] Starodubtsev and Romanov, 175 – 183.

[57] V. V. Balashov, *Interaction of Particles and Radiation with Matter*, trans. G. Pontecorvo, (New York: Springer, 1997), 81 – 95.

4.3.1. Energy Loss of the Electrons

For the incident electron, both energy loss and scattering occur in collisions with atomic electrons. Consequently the electron path is not necessarily straight, and, depending on the density of the medium, the electrons tend to diffuse into the material, rather than go in a straight line.[58] If an elastic collision occurs with the nucleus, almost no energy is lost by the incident electron because of the relatively large mass of the nucleus. The energy losses are primarily from ionization or excitation of electrons in the medium. Following Fermi,[59] it is shown that a charged particle moving through matter loses energy through electromagnetic interactions which cause electrons of the matter to move to higher energy states. The electron of the medium is either left in an excited bound state or is ionized. In either case, the increment of energy is taken from the kinetic energy of the incident particle.

Fermi's derivation (in Gaussian units for the sake of history) considers a cylinder centered on the path of the electron along the x-axis as shown in Figure 4.3.1.1.
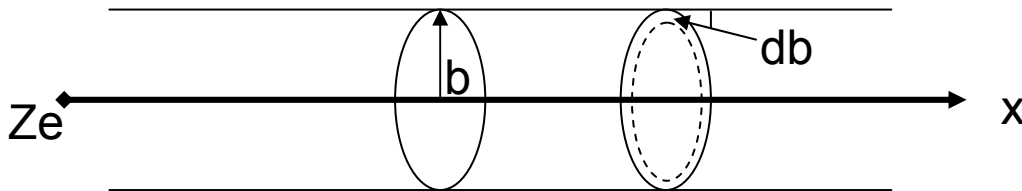
Figure 4.3.1.1: **The path of a particle of charge Ze moving along the x-axis through a cylinder with radius b. The cylinder is centered on the path of the particle. [from Fermi]**

An electric field $\vec{E}$ is caused by the particle with charge Ze. The electric flux is

$$(4.3.1.1) \qquad \Phi_E = \int_{-\infty}^{\infty} \vec{E} \bullet \hat{n} dA = 4\pi Ze$$

$$\Phi_E = \int_{-\infty}^{\infty} E_\perp 2\pi b dx = 4\pi Ze$$

[58] Jackson, 624.

[59] E. Fermi, 27.

where $E_\perp$ is the electric field perpendicular to the path of motion.

Equation 4.3.1.1 becomes

(4.1.1.2) $$\int_{-\infty}^{\infty} E_\perp dx = \frac{2Ze}{b} .$$

The variation of $E_\perp$ with time is assumed to be the same as if the charge, Ze, were kept fixed and observing at a point moving with velocity, v, along the cylinder surface. Therefore

$$\int_{-\infty}^{\infty} E_\perp(t)dt = \int_{-\infty}^{\infty} E_\perp(x)\frac{dx}{v} = \frac{1}{v}\int_{-\infty}^{\infty} E_\perp(x)dx = \frac{2Ze}{vb}$$

The impulse is then given by the expression

(4.3.1.3) $$I_\perp = \int_{-\infty}^{\infty} E_\perp e\, dt = \frac{2Ze^2}{vb} = \Delta p_\perp$$

Therefore, the momentum gain by one electron is, $p = \dfrac{2Ze^2}{vb}$ and the kinetic energy, T, gained by one electron is then

(4.3.1.4) $$T = \frac{p^2}{2m} = \frac{2Z^2e^4}{mv^2b^2} .$$

The number of collisions per unit length such that b lies in the range of b + db is equal to the number of electrons per unit length in the shell bounded by the cylinders of radii b and b + db as shown in Figure 4.3.1.1. The density, n, is the number of electrons per unit volume. The number of collisions per unit path length is then given by

(4.3.1.5) $$\frac{\#\text{collisions}}{\text{path length}} = 2\pi nb\, db .$$

The energy loss per length (centimeter) is

(4.3.1.6) $$\frac{dT(b)}{dx} = \frac{4\pi Z^2 e^4 n}{mv^2}\frac{db}{b} .$$

The total kinetic energy lost to all shells in the range of b_{min} to b_{max} is

(4.3.1.7) $$-\frac{dT}{dx} = \frac{4\pi Z^2 e^4 n}{mv^2}\ln\left(\frac{b_{max}}{b_{min}}\right) .$$

98

There is a necessary relativistic correction due to the contraction of the electric field in the direction of motion and as a result, the $E_\perp$ is decreased by a factor of γ. Fermi describes this as sharpening the pulse given to the electron and as a result, b_{max} has a limit of

$$b_{max} = \frac{v\gamma}{\bar{v}},$$

where $\bar{v}$ is the average frequency for electrons in the medium. The value for b_{min} is given by[60]

$$b_{min} \approx \frac{\hbar}{\gamma mv}.$$

Replacing b_{max} and b_{min} in equation 4.3.1.7, the equation for energy loss per length is

(4.3.1.8) $\qquad -\frac{dT}{dx} = \frac{4\pi Z^2 e^4 n}{v^2 m} \ln\left(\frac{\gamma^2 mv^2}{\hbar \bar{v}}\right)$ [erg cm^{-1}]

A more detailed and precise calculation by Starodbtsev and Romanov[61], and Bethe[62] for energy loss of a relativistic electron gives what is known as the Bethe-Bloch equation

(4.3.1.9) $\qquad -\left(\frac{dT}{dX}\right) = 0.153\rho\left(\frac{Z}{A}\right)\beta^{-2}\left[\ln\frac{T^2(\gamma+1)}{2I^2} + (1-\beta^2) - \frac{2\gamma-1}{\gamma^2}\ln 2 + \frac{1}{8}\left(\frac{\gamma-1}{\gamma}\right)^2\right].$

The value of dT/dx in equation 4.3.1.9 is measured in MeV/cm. The density is measured in gm/cm^3. I (capital I) is the mean excitation potential of the stopping medium and has units of eV. The mean excitation potential is determined using an expression

$$Z\ln(I) = \sum f_{nk} \ln(I_{nk}),$$

where f_{nk} are the oscillator strengths for transitions between the optical levels n and k. I_{nk} are the corresponding energies of these transitions.[63]

---

[60] E. Fermi, 28 - 30.

[61] Starodubtsev and Romanov, 178.

[62] Fermi, 30.

[63] Starodubtsev and Romanov, 45.

In text *The Passage of Charged Particles Through Matter* by Starodubstev and Romanov, the recommended value is for the excitation potential of air is 94 eV. Figure 4.3.1.2 show the affect of the excitation potential of air on the ionization energy losses of an electron passing through air with $\gamma = 3.9$.

The Effect of the Excitation Potential on Ionization Energy Losses
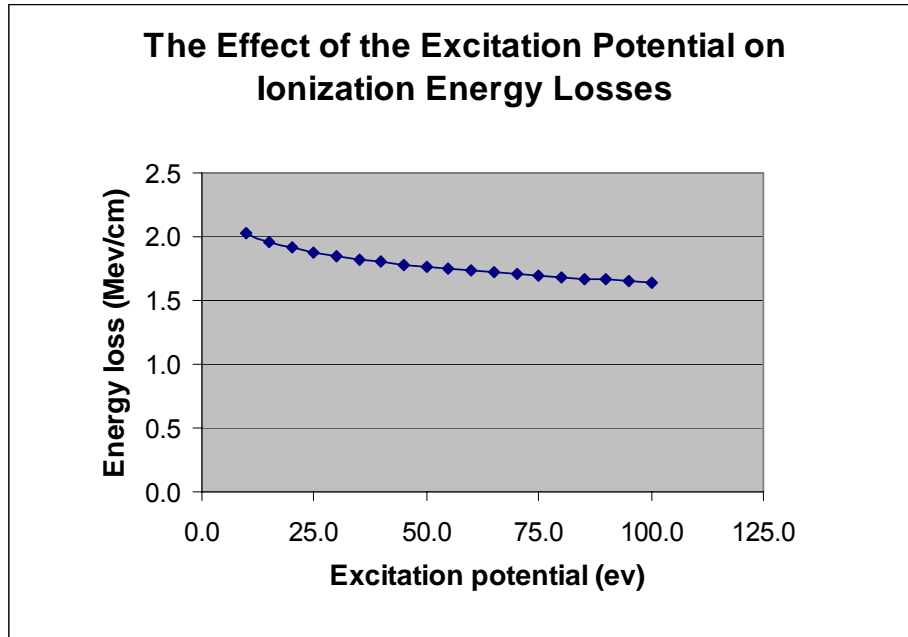
Figure 4.3.1.2: **The ionization energy losses of an electron with a speed of 2.9 x 108 m/s and $\gamma = 3.9$ are plotted as a function of the excitation potential (I) of air. Using equation 4.3.1.9 the ionization energy losses have a logarithmic dependence on I and decrease with an increase in the value of I. The code developed uses a value of 94 eV for the excitation potential.**

In Figure 4.3.1.3, a typical relativistic electron energy loss curve is plotted. Although the plot seems to suggest that as the kinetic energies approach zero the energy loss increases to large values, one would suspect that this is not the case for in the limit that the kinetic energy approaches zero, there would be no possible mechanism for ionization energy loss since the kinetic energy of the particle becomes zero.

The Bethe-Bloch formula described above is valid when the particles velocity exceeds the mean-free velocity of the electrons in the atom.[64] The Bohr velocity of an

---

[64] Balashov, 80.

electron in a hydrogen atom is on the order of 2,000 km/s. In general, electrons below 40 keV, with speeds less than 1.12×10^8 m/s, present little threat to satellites and are ignored. The Bethe-Bloch formula is used for all electron energy loss calculations.

de/dx vs Mev Energy of Particle
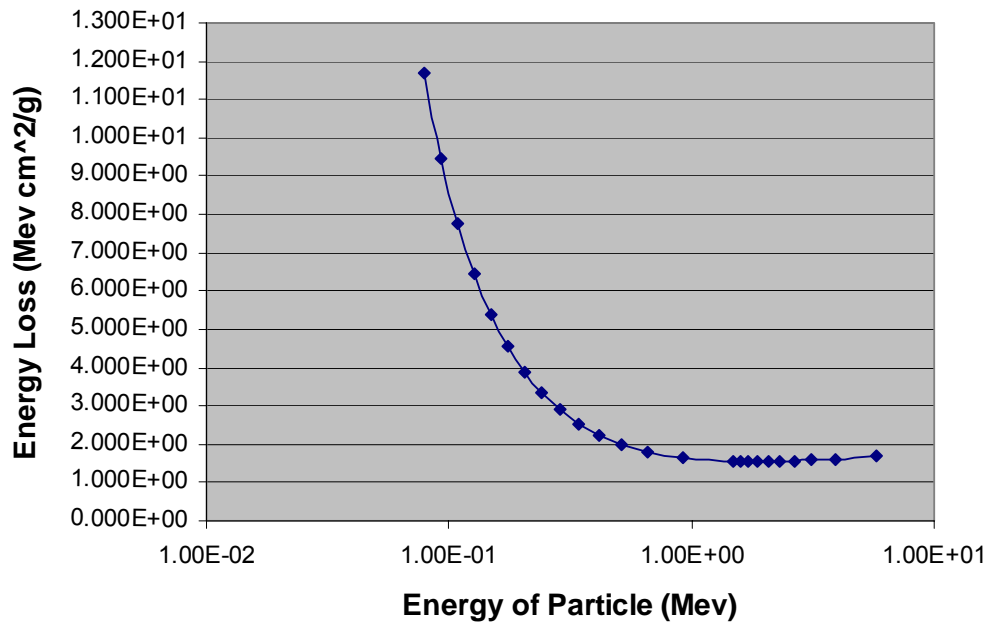
Figure 4.3.1.3: **This is a typical dE/dx curve for relativistic electrons moving through a stopping medium. Note that the energy loss decreases as the kinetic energy increases and the basically levels off around energies above 1 MeV. The energy loss does increase slightly above 1 MeV.**

4.3.2. Energy Loss of the Ions

The fission fragments and bomb debris have speeds around 2,000 km/s (this is about the same value of the Bohr velocity). The kinetic energy (T) used in equation 4.3.1.9 is the relativistic kinetic energy of the electron. If the relative electron velocity is 2,000 km/s then the kinetic energy of the electron is ~11 eV. The 11 eV kinetic energy is well below the ionization potential for air resulting in a positive gain in kinetic energy if the Bethe-Bloch formulation for dE/dxing is applied (non-physical). A positive energy gain due to ionization energy losses is non sensible and demonstrates the limit of the Bethe-Bloch equation. However, the positively charged fission fragments traveling at

speeds near 2,000 km/s have kinetic energies around 2,000 keV (~ 20 keV per nucleon) and are capable of causing ionization of the stopping medium. The early theoretical work on the passage of slowly moving charged particles (velocities less than the Bohr velocity) was done by Fermi and Teller. They were able to show the dependence of the stopping power of a medium on the velocity of a particle. Balashov presents two expressions for the kinetic energy loss per unit length, dT/dx.[65] For calculations in the computational code equation 4.3.2.1, based on the Thomas-Fermi atomic model, is used for all ions.

$$(4.3.2.1) \qquad -\left(\frac{dT}{dX}\right)_{ion} = 8\pi e^2 a_0 Z_{ion}^{1/6} \frac{Z_{ion} Z_{air}}{\left(Z_{ion}^{2/3} + Z_{air}^{2/3}\right)^{3/2}} n_0 \frac{v}{\varepsilon_0 v_{Bohr}} \quad [J/m]$$

In equation 4.3.2.1, v is the velocity of the slow ion (m/s), a_0 is the Bohr radius, V_{Bohr} is the Bohr velocity (2,000 km/s), ε_0 is the permittivity of free space, and n_0 is the number density of air. Coincidentally, the typical speed of a fission fragment produced in a nuclear explosion is around 2,000 km/s.

From equation 4.3.2.1 it is clear the energy loss per unit length is linear with the velocity of the ion and with the number density of the medium (in this case the medium is the air). If all variables are held constant, but the $\overline{Z}$ of air is increased the plot is shown in Figure 4.3.2.1.

---

[65] Balashov, 80.
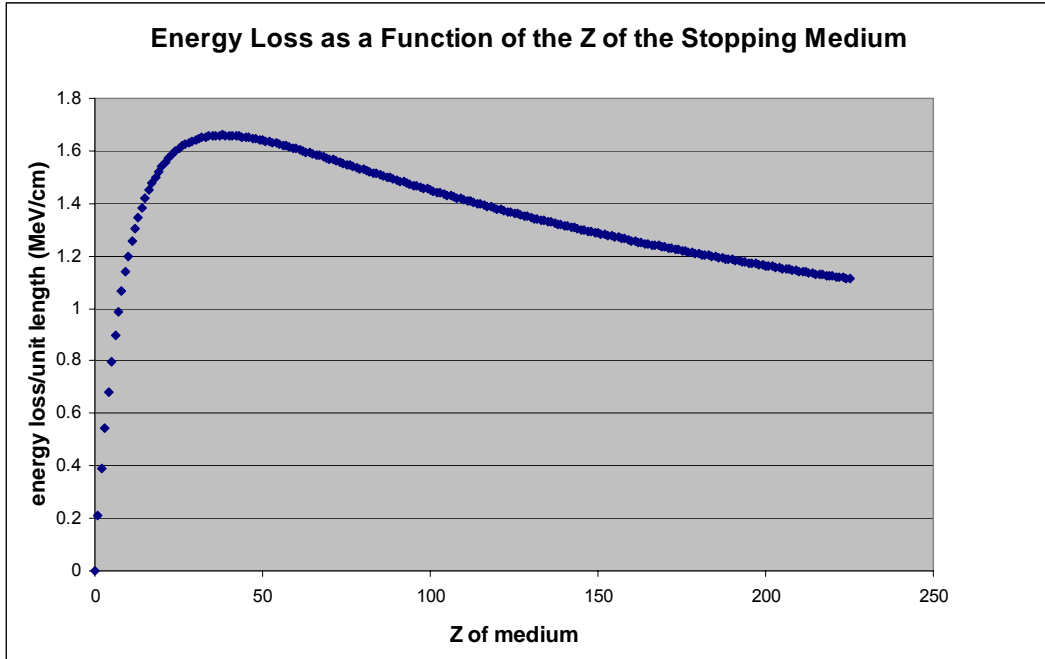
Figure 4.3.2.1: The energy loss per unit length is plotted as a function of the $\overline{Z}$ of the stopping medium. The ion was rhodium ($Z = 45$) with a speed of 1,000 km/s. The air had a density of $1x10^{18}$ atoms/m^3. The values on the y-axis are less important than an appreciation for the dependence on the Z of the stopping medium.

Similarly, if all of the variables of equation 4.3.2.1 are held constant and the Z of the ion is varied then the results are shown in Figure 4.3.2.2.
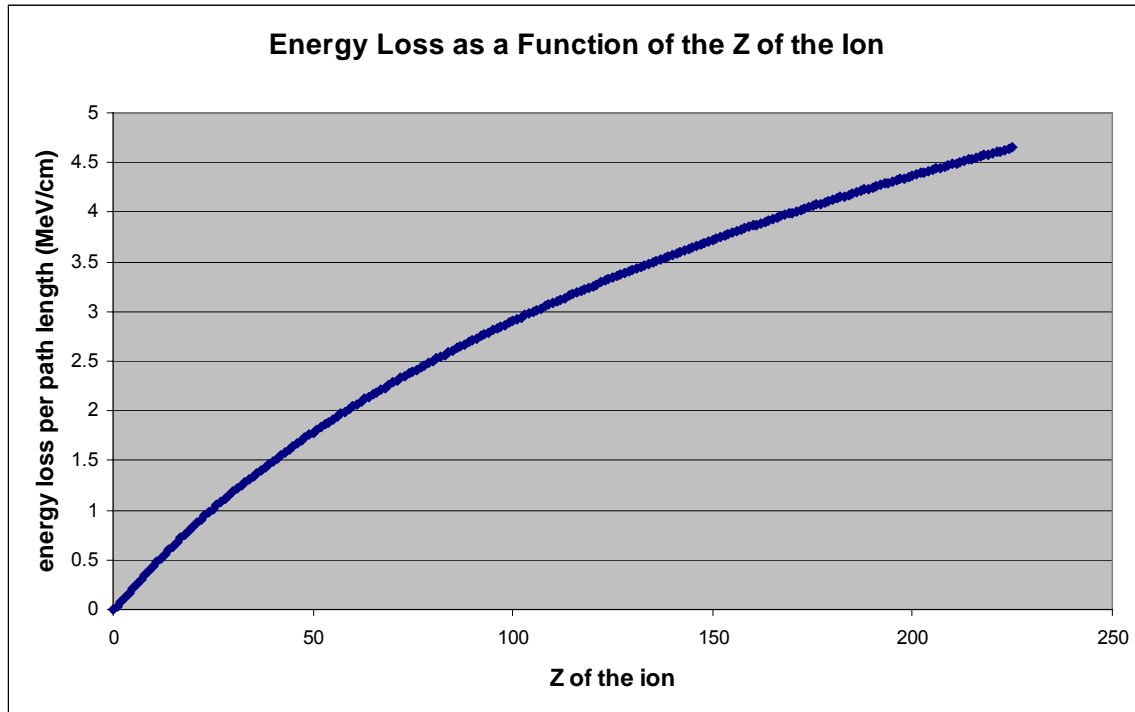
Figure 4.3.2.2: The energy loss per unit length is plotted as a function of the Z of the ion. The medium was given a Z value of 30 and the ions had a speed of 1,000 km/s. The medium had a density of 1e18 atoms/m^3. The values on the y-axis are less important than an appreciation for the dependence on the Z of the ion. Most of the ions tracked in the code have values of Z around 40 and 60.

Given the scope of the dissertation, there is a need to limit complexity of the energy loss of the charged particles as they pass through the atmosphere. The two models are well supported and agree with available data.[66,67]

Most of the ions of consideration are well suited for the Thompson-Fermi model because of the low velocities. The electrons with kinetic energies above 40 keV are well suited for the Bethe-Bloch model. As mentioned, the lower energy electrons are of little interest. The software path is built in this dissertation using equations 4.3.2.1 and 4.3.1.9.

[66] Starodubtsev and Romanov, 158 – 206.

[67] Balashov, 80 – 87.

4.3.3. Other Energy Loss Mechanisms

Radiation energy losses can be significant for electrons in circular accelerators like the synchrotron or betatron, but is not significant for electrons from beta decay trapped in the earth's magnetic field. Jackson[68] develops an expression for radiative energy loss per revolution for this synchrotron radiation

$$(4.3.3.11) \qquad \delta\varepsilon[\text{MeV}] = 8.85\text{x}10^{-2}\,\frac{(\varepsilon[\text{GeV}])^4}{r_c[\text{meteres}]}.$$

The energy loss from synchrotron radiation is not significant until the electron energies approach the GeV range and this is well beyond the energies of any of the electrons injected due to a nuclear detonation. Table 4.3.3.1 shows the energy loss per revolution and energy loss per day (assuming that the particle is in a vacuum) of electron beta decay energies and demonstrates why synchrotron energy losses are ignored in the modeling.

Gamma	Orbit Radius (m)	Orbit Period (s)	T (MeV)	Energy loss/revolution (MeV)	Energy Loss/Day (MeV)
2.294	117.56	$2.734\text{x}10^{-06}$	$6.613\text{x}10^{-01}$	$1.440\text{x}10^{-16}$	$1.896\text{x}10^{-07}$
2.502	130.60	$2.982\text{x}10^{-06}$	$7.676\text{x}10^{-01}$	$2.353\text{x}10^{-16}$	$2.840\text{x}10^{-07}$
2.785	148.02	$3.320\text{x}10^{-06}$	$9.124\text{x}10^{-01}$	$4.143\text{x}10^{-16}$	$4.492\text{x}10^{-07}$
3.203	173.23	$3.817\text{x}10^{-06}$	1.126	$8.198\text{x}10^{-16}$	$7.732\text{x}10^{-07}$
3.906	214.97	$4.655\text{x}10^{-06}$	1.485	$2.001\text{x}10^{-15}$	$1.547\text{x}10^{-06}$
5.500	307.95	$6.556\text{x}10^{-06}$	2.300	$8.037\text{x}10^{-15}$	$4.413\text{x}10^{-06}$
12.258	695.59	$1.461\text{x}10^{-05}$	5.753	$1.393\text{x}10^{-13}$	$3.433\text{x}10^{-05}$
17.328	984.95	$2.065\text{x}10^{-05}$	8.343	$4.354\text{x}10^{-13}$	$7.590\text{x}10^{-05}$
38.733	2204.63	$4.617\text{x}10^{-05}$	19.28	$5.549\text{x}10^{-12}$	$4.327\text{x}10^{-04}$
122.476	6973.22	$1.460\text{x}10^{-04}$	62.07	$1.884\text{x}10^{-10}$	$4.647\text{x}10^{-03}$
387.299	22051.74	$4.616\text{x}10^{-04}$	197.4	$6.094\text{x}10^{-09}$	$4.752\text{x}10^{-02}$
1224.745	69733.89	$1.460\text{x}10^{-03}$	625.3	$1.941\text{x}10^{-07}$	$4.786\text{x}10^{-01}$
3872.983	220517.98	$4.616\text{x}10^{-03}$	1979	$6.151\text{x}10^{-06}$	4.797
12247.449	697339.11	$1.460\text{x}10^{-02}$	$6.258\text{x}10+03$	$1.946\text{x}10\text{-}04$	$4.800\text{x}10+01$

Table 4.3.3.1: This table shows the synchrotron radiation losses of different energy electrons in a .3 T magnetic field. The end point energies of the beta decay electrons from fission fragments rarely exceed 10 MeV. Synchrotron radiation losses are not significant within the scope of the problem and are ignored for the energy loss modeling.

---

[68] Jackson, 667.

Charge exchange and Cherenkov radiation were also identified as mechanisms for potential energy loss. Cherenkov radiation would not significantly contribute to the scope of the study and is not included in the model. Given the current state of the model, charge exchange is not included and would not contribute to significant energy loss or trapping of charged particles. However, the addition of charge exchange should be considered as an area of future study, especially when modeling the effect of the neutral fragments.

4.4.   SCATTERING

When charged particles pass through matter there are several scattering processes that cause the particle to alter its velocity and path through the medium. For the charged particles trapped in the earth's dipole field, the atmospheric scattering may cause a change in the direction of the particle resulting from a change in the velocity components of the particle and therefore changing the pitch angle at a given location. The continuous and accumulated change in pitch angle is called "pitch angle diffusion". Pitch angle diffusion changes the parallel and perpendicular components of the velocity and therefore changes the location and altitude of the mirror point of the particle. As the pitch angle and mirror point changes so does the expected trapping lifetime of the particle. As shown, the probability of trapping decreases with an increase in the particles parallel component of velocity. A sudden increase in the parallel component of velocity, coupled with a decrease in the perpendicular component of velocity causes the particle to reach a mirror point lower in the atmosphere. (The extreme case is when the particle has no perpendicular component of velocity and tends to follow the field lines until all of the kinetic energy is lost due to ionization of the atmosphere.) The atmospheric scattering may also cause a significant change in the trajectory of the particle resulting in a change in L-shells. [As a particle bounces from conjugate point to conjugate, the L-shell of the particle is defined as the guiding distance in earth radii that the particle is away from the center of the axis of the earth. For example, a particle at the surface of the earth an with a latitude of 0° has an L-shell value of 1. If the particle is ½ the radius of the earth (3187 km) above the surface of the earth at the geographic equator then the L-shell is 1.5. Gyro-synchronous orbit is at L-shell ~ 6.6 and GPS orbits at a L-shell ~ 4.1] The maximum change in L-shell for a single, large angle scatter is one gyro-radius. The changing of L-

shells is called radial dispersion. Particles that diffuse inward are often lost due to ionization energy losses resulting from a larger loss cone. For low earth orbits (L < 1.3) and the focus of this study, atmospheric scattering is the primary mechanism for both pitch angle and radial diffusion.[69, 70]

A quick review of scattering from Jackson[71] or Starodubtsev and Romanov[72] introduces a swift particle of charge, Ze, mass, M, and momentum, γMv, colliding with an atomic electron of charge –e and mass m. For the energetic collisions, the binding energy of the electron is neglected and the electron is considered a free electron. The atomic electron is also considered at rest in lab frame. Rutherford viewed the collision as an elastic Coulomb scattering in the rest frame of the incident particle. Rutherford's famous scattering formula is

$$(4.4.1) \qquad \frac{d\sigma}{d\Omega} = \left(\frac{Ze^2}{2\gamma mv^2} \right) CSC^4 \left(\frac{\theta}{2} \right).$$

Often, for small angle scattering, Rutherford's equation is written as

$$(4.4.2) \qquad \frac{d\sigma}{d\Omega} = \left(\frac{Ze^2}{2\gamma mv^2} \right) \frac{1}{\theta^4}$$

This Coulombic collision with the electrons of the medium causes the excitation or ionization energy losses as described in Section 4.3. Although the Rutherford scattering formula was developed for heavy particles moving through a medium, with a change of reference frame, the same expression can also be applied to electrons moving through a medium. The $\frac{1}{\theta^4}$ singularity of equation 4.4.2 is discussed by Jackson[73] where he shows that the singularity is eliminated by both classical and quantum mechanical corrections.

---

[69] M. Walt and W. McDonald, "The Influence of the Earth's Atmosphere on Geomagnetically Trapped Particles," *Rev. Geophys.,* Vol. 2, 1964: 543.

[70] B. Able and R.M. Thorne, "Electron Scattering Loss in Earth's Inner Magnetosphere," *J. Geophys. Res.,* Vol. 103, 1998: 2385-2392.

[71] Jackson, 624.

[72] Starodubtsev and Romanov, 159.

[73] Jackson, 625 – 627.

$$(4.4.3) \qquad \frac{d\sigma}{d\Omega} = \left(\frac{ze^2}{2\gamma mv^2} \right) \frac{1}{\left(\theta^2 + \theta_{min}^2 \right)^2}$$

The total scattering cross-section can be obtained by integrating over the total solid angle.[74]

$$(4.4.4) \qquad \sigma = 2\pi \left(\frac{2zZe^2}{\gamma mv^2} \right)^2 \int_0^\infty \frac{\theta d\theta}{\left(\theta^2 + \theta_{min}^2 \right)^2} = \pi \left(\frac{2zZe^2}{\gamma mv^2} \right)^2 \frac{1}{\theta_{min}^2}$$

There are two values typically used for θ_{min} based on a classical approach and a quantum mechanical approach

$$\theta_{min}^{classical} = \frac{2zZe^2}{\gamma Mv^2 (1.4 a_0 Z^{-\frac{1}{3}})} \text{ and}$$

$$\theta_{min}^{QM} = \frac{Z^{\frac{1}{3}} mc}{192 \gamma Mv}$$

One of the constraints of Rutherford scattering is that it is generally limited to small angles for the fast particles. When the ion or electron passes through matter, the particle experiences many small angle deflections, and occasionally, due to elastic collisions with the nucleus, the particle may experience a single large angle deflection. Jackson and others treat the scattering in two regimes: multiple small angle scattering or a single large angle scattering. Experimental results presented by Starodubtsev and Romanov support the assertion that there is multiple scattering (caused by the Coulomb field) and single large angle scattering. The multiple-scattering and single-scattering probability distributions were derived by Rossi.[75]

$$(4.4.5) \qquad P_{Multiple}(\alpha)d\alpha = \frac{1}{\sqrt{\pi}} e^{-\alpha^2} d\alpha$$

$$(4.4.6) \qquad P_{Single}(\alpha)d\alpha = \frac{1}{8\ln(204 Z^{-\frac{1}{3}})} \frac{d\alpha}{\alpha^3}$$

---

[74] Jackson, 642.

[75] B. Rossi, *High-Energy Particles*, (New Jersey: Prentice-Hall, 1952).

In equations 4.4.5 and 4.4.6 α is the relative projected angle and is given by

$$(4.4.7) \qquad \alpha = \frac{\theta'}{<\Theta^2>^{\frac{1}{2}}} = \frac{\theta'}{\sqrt{4\pi N \left(\frac{2zZe^2}{\gamma Mv}\right)^2 \ln(204Z^{-\frac{1}{3}})t}},$$

where t is the thickness of the medium and θ' is the projected scattering angle, and $<\Theta^2>$ is the then square angle of the Gaussian dispersion. It is worth noting that different authors use different values for the numerical coefficient in the logarithm in equation 4.4.7 and 4.4.7.[76] Because the small angle scattering is similar to a random walk, one would expect, for large numbers of scattering, that the distribution of small angle scattering would resemble a Gaussian and that is shown when the multiple small angle scattering (equation 4.4.5) equation is plotted in Figure 4.4.1. Figure 4.4.2 shows a plot of single large-angle scattering distribution using equation 4.4.6.
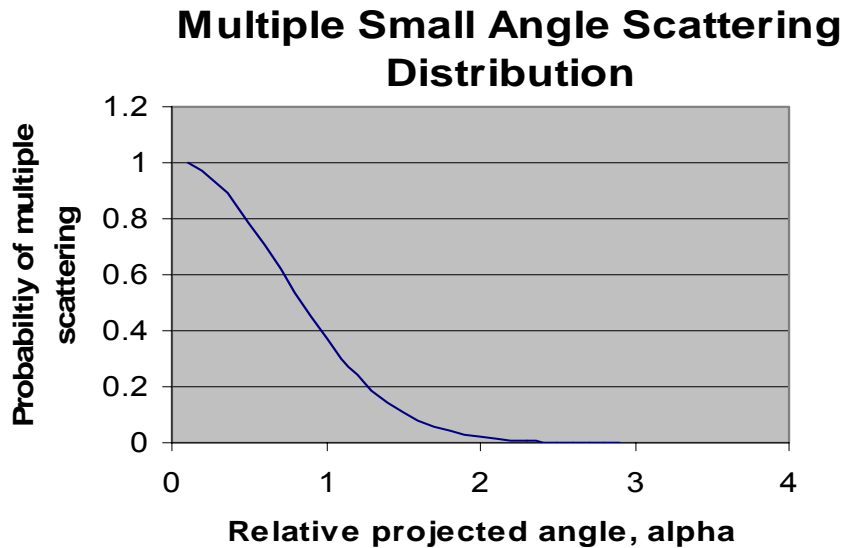
Figure 4.4.1: The equation for small angle scattering, $P_{\text{Multiple}}(\alpha) = \frac{1}{\sqrt{\pi}}e^{-\alpha^2}$, is plotted. The results produce the expected Gaussian distribution. The multiple small-angle scattering equation accounts for most of the scattering of a particle through a medium. The primary source of the small-angle scattering of particles through a medium is Coulomb field. Coulombic scattering does not typically cause large angle scattering.

---

[76] Jackson, 644 – 645.
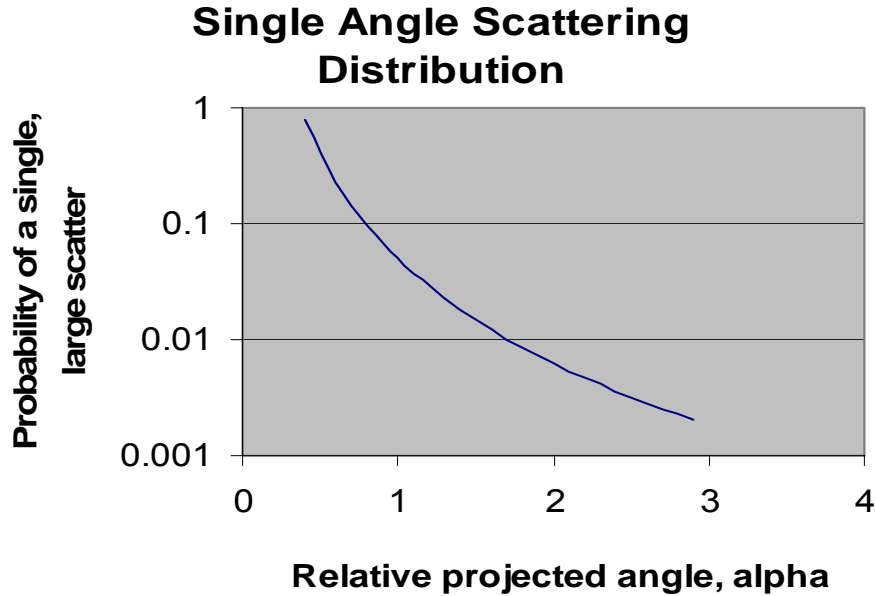
Figure 4.4.2: The equation for single, large-angle scattering,

$$P_{Single}(\alpha) = \frac{1}{8\ln(204Z^{-\frac{1}{3}})}\frac{1}{\alpha^3} \text{ , is plotted. The single, large-angle scattering equation}$$

accounts the large angle scattering as the particle passes through a medium. The primary cause of this single scattering is elastic collisions with the nucleus.

The challenge is to apply the appropriate single or multiple angle scattering equation during the Monte Carlo simulation. Neither equation alone provides adequate coverage of the full range of scattering angles. Figure 4.4.3 shows both equations plotted together. The two equations are normalized by equation 4.4.5 evaluated at $\alpha = 0$. What is suggested by Jackson and done in this project is to use the multiple-scattering equation for normalized probabilities greater than 0.003 and to use the single large-angle scattering equation when the normalized probabilities are less than 0.003. The 0.003 value is taken from the location of the crossing of the two curves on Figure 4.4.3. As Figure 4.4.3 shows, this allows the inclusion of the expected small angle scattering in the majority of the Gaussian, but introduces large angle scattering into the tail of the distribution. The expectation is that most of the scattering is multiple and small-angle with a bias toward the forward direction, but there is the possibility of large angle scattering as the particles pass through the atmosphere and collide with a nucleus. More elaborate scattering schemes are certainly available and will be considered for future work.
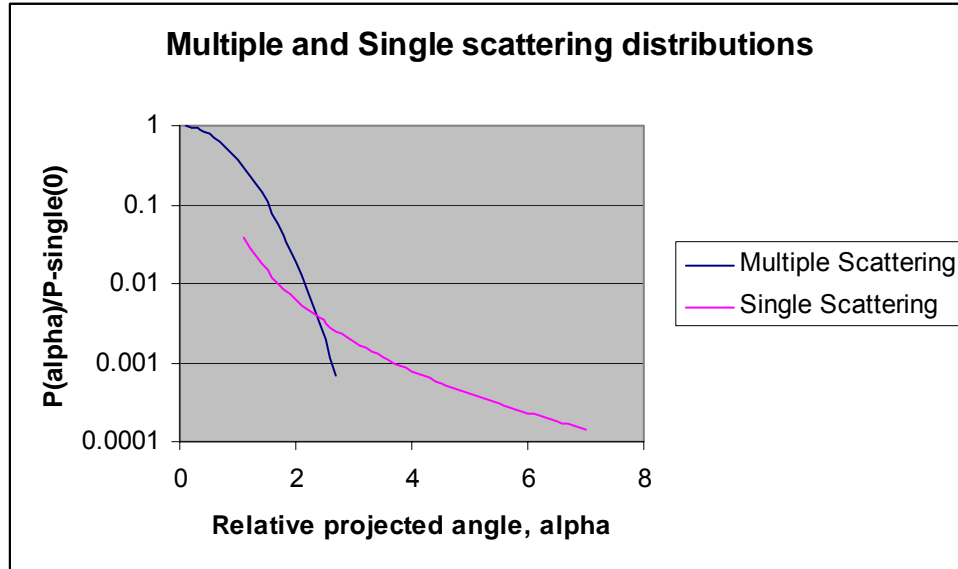
Figure 4.4.3: Multiple scattering and single scattering distributions are plotted against the projected angle, α. The distributions are normalized on the y-axis with the probability of small angle scattering evaluated at α = 0. The distributions are combined to allow for the expected multiple, small-angle scattering in the majority of the distribution and the possibility of large angle scattering in the tail of the distribution. The transition between multiple and single scattering occurs between $\alpha \approx 2-3$.

4.4.1. Pitch-Angle and Radial Diffusion Caused by Scattering

Recall that in Chapter II, the pitch angle was defined by equation (1.1.28)

$$\alpha = \text{Tan}^{-1}\left(\frac{v_\perp}{v_\parallel}\right).$$

When a particle scatters in the atmosphere, a principal effect is that the particle changes direction resulting in a change in the particles velocity. This means that the parallel and perpendicular components of the velocity are changed, while the speed remains the same. As the pitch angle changes, so does the location of the mirror point. If the parallel component of the velocity is increased then the particle will mirror at a location with a lower altitude. If the scattering causes the perpendicular component of the velocity to increase then the particle will mirror at a location higher in the atmosphere. The result is that a particle experiencing pitch angle diffusion will generally have a different mirror

point for each bounce. Figure 4.4.1.1 shows two different results from pitch angle scattering of an electron interacting with the atmosphere. Because the electrons are tracked using the guiding center approximation and the Larmor radius is relatively small, the atmospheric scattering causes very little radial dispersion, but can significantly affect the pitch angle, mirror point, and trapping lifetime of the electron.
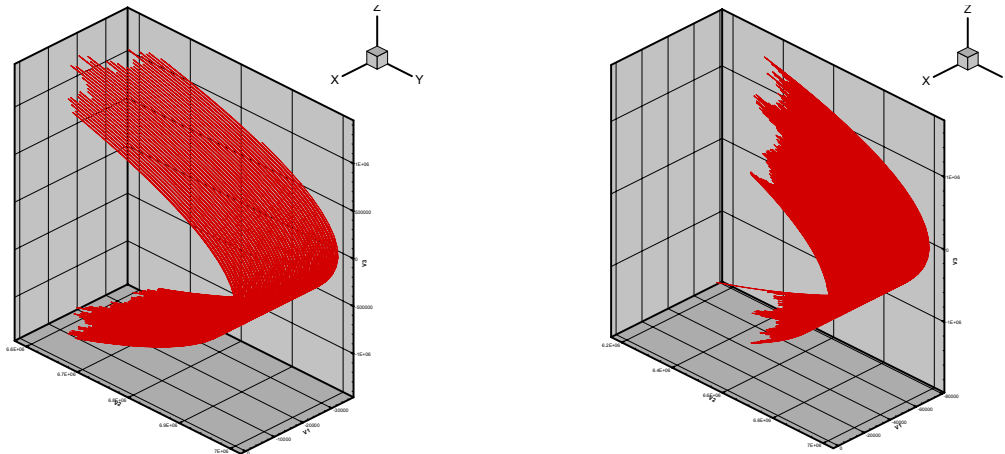
Figure 4.4.1.1: **Two examples of pitch angle diffusion caused by an electron scattering in the atmosphere of the earth. The pitch angle diffusion may cause the particle to reach a mirror point deeper in the atmosphere or the particle may mirror at higher altitudes**

As shown in Chapter II, the Larmor radius of the ion is much larger than the electron and can be on the order of 200 km. The pitch angle diffusion of the ion causes a change in the mirror location and can cause a radial dispersion of the ion, depending on where the particle scatters, as it spirals around the magnetic field lines of the earth. As the particle spirals around the magnetic field line along a particular L-shell, it undergoes scattering at different locations along the gyro-orbit. The effect of the pitch angle diffusion of ion on the mirror point location is shown in Figure 4.4.1.2. The ion's pitch angle continues to change as the particle interacts with and scatters in the atmosphere.

The details of the change of pitch angle scattering are shown in Figure 4.4.4.3 where the orbit is shown to clearly change due to scattering.
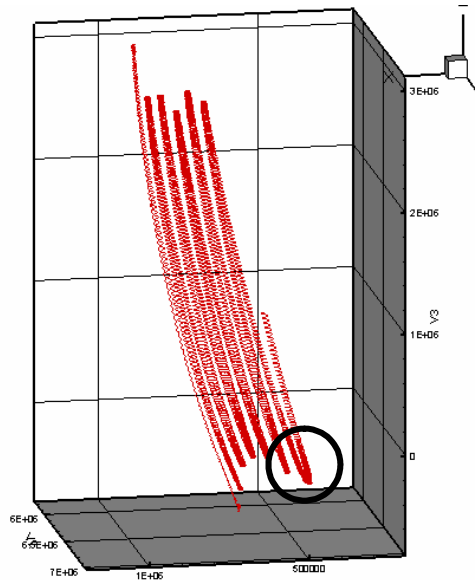
Figure 4.4.1.2: An ion released at an altitude of 670 km with a speed of 2300 km/s is shown to drift to the west and pitch angle scatter due to interactions with the atmosphere. In this particular case, the ion eventually looses all of its kinetic energy due to the collisions in the atmosphere. A close-up of the circled region is shown in Figure 4.4.1.3 and represents the details of the pitch angle diffusion.
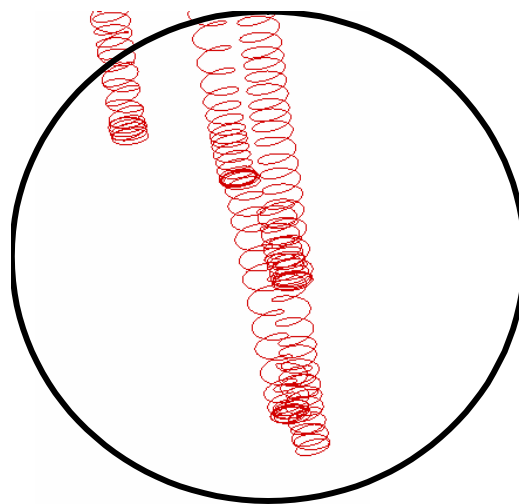
Figure 4.4.1.3: The circled region from Figure 4.4.1.2 is shown above. The effects of pitch angle change and diffusion are shown as the ion's pitch angle and orbit change as the particle interacts and scatters in the atmosphere. Most of the interaction with the atmosphere and scattering occurs near the conjugate point where the atmosphere is the densest.

If the scattering occurs radially outward (inward) from the guiding center of the ions trajectory, the ion will begin to spiral along an L-shell that is larger (smaller) than the previous guiding center L-shell of the ion. Figure 4.4.1.4 shows an example of radial diffusion caused by pitch angle change.
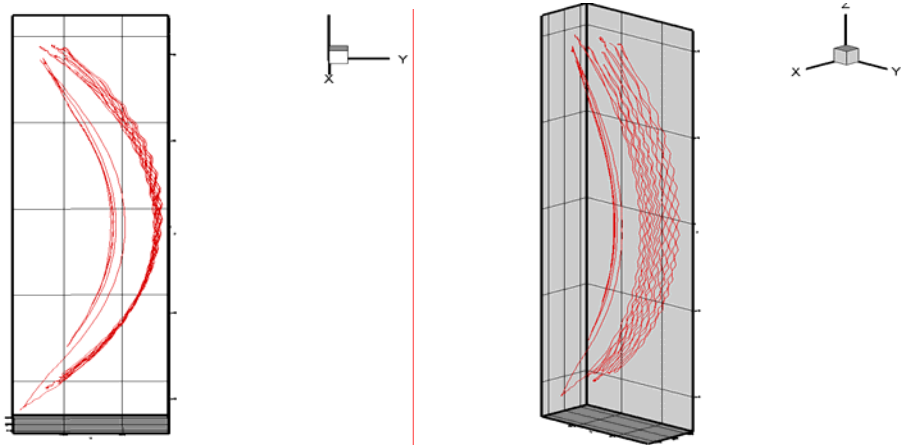
Figure 4.4.1.4: **Radial dispersion is shown above. The ion's L-shell changes due to scattering, radial dispersion, and pitch angle diffusion all of which are caused by an interaction with the atmosphere.**

In general, the atmospheric scattering of the electron only causes the pitch angle to change with no significant radial dispersion. The scattering of an ion may cause both pitch angle diffusion and radial dispersion of the ion. In both cases, the scattering is directly dependent on the density of the atmosphere and most of the scattering occurs near the conjugate point of the particle because this is where the atmosphere is the most dense. For particles trapped in such a way that they mirror at high altitudes (where the density is relatively low), scattering does not cause significant pitch angle diffusion or radial dispersion. The pitch angle and radial dispersion of particles trapped in high L-shells is caused by a number of factors briefly discussed below to include wave-particle interaction.

4.4.2. Other Sources of Pitch-Angle and Radial Diffusion

One of the "boundary conditions" for the initial application of this dissertation is that the code was developed to track the particles trapped in the magnetic fields where Coulombic forces are responsible for most of the energy loss and scattering. This application is valid for particles trapped in L-shells less than $L \approx 1.25 - 1.3$ This region is of interest because most of the low earth orbit satellites either reside in or pass through the region below $L = 1.3$. By examining the data from the Starfish test, Van Allen[77] concluded that the expected decay rate of trapped electrons was consistent with atmospheric losses up to an L-value of around 1.25. Other authors[78] report that the electron loss rate in the region below $L \approx 1.3$ is dominated by Coulombic collisions. Regardless of the selected L-shell cut off below which atmospheric interaction is the dominate mechanism for pitch angel and radial diffusion, the data appears to suggest that above $L = 1.3$ other mechanisms cause the trapped particles to radially disperse and pitch angle scatter. Figure 4.4.2.1 was produced by Van Allan[79] using the sparse data from the Starfish test.

---

[77] J.A. Van Allen, "Spatial Distribution and Time Decay of the Intensities of Geomagnetically Trapped Electrons from the High Altitude Nuclear Burst of 1962," published in *Radiation Trapped in the Earth's Magnetic Field*, edited by Billy M. McCormac, (Dordretch, Holland: D. Reidel Publishing Company, 1966), 591.

[78] B. Able and R.M. Thorne, "Electron Scattering loss in Earth's Inner Magnetosphere 2. Sensitivity to Model Parameters," *J. Geophys. Res.,* Vol. 103, 1998: 2397.

[79] Van Allen, "Spatial Distribution and Time Decay of the Intensities of Geomagnetically Trapped Electrons from the High Altitude Nuclear Burst of 1962," 591.
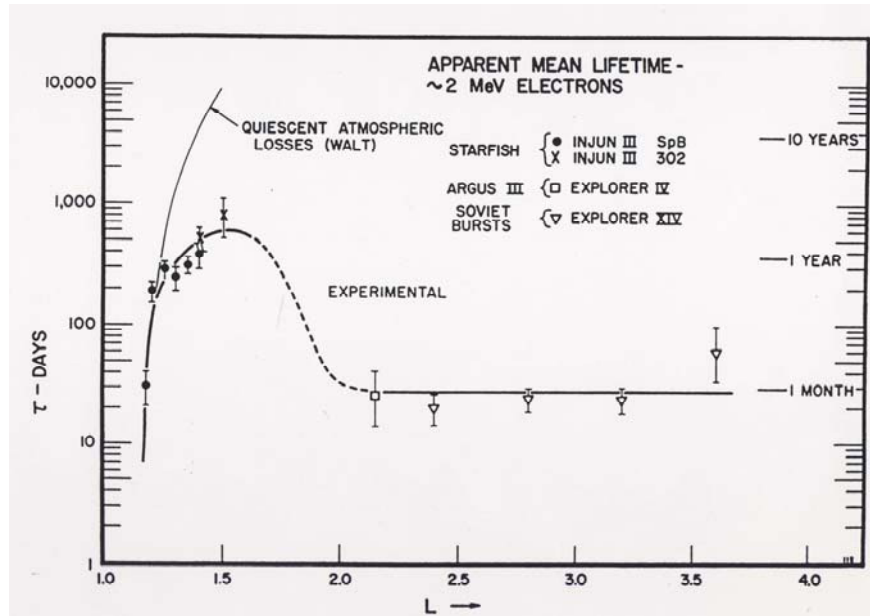
Figure 4.4.2.1: **The data from the Starfish nuclear test is presented from Van Allen's paper, "Spatial Distribution and Time Decay of the Intensities of Geomagnetically Trapped Electrons from the High Altitude Nuclear Burst of 1962." The figure compares the expected decay rate of electrons due to atmospheric loses to the measured decay rate of electrons. Above L ≈ 1.25 - 1.3 the decay rate of electrons exceeds rate expected from atmospheric loses. The increase in the rate of decay is thought to be caused by wave-particle interactions.[from Van Allen]**

One mechanism causing a more rapid decay rate from higher L-shells is wave-particle interaction. The plasma waves causing the wave-particle interaction are known as whistler waves. The whistler waves are known to be caused by lightening strikes[80], VLF transmissions[81], and plasmaspheric hiss[82], and other possible electro-magnetic sources. Although no significant attempt is made here to explain the details of the nature or physics of the wave-particle interactions, Shultz and Lanzerotti[83] offer the curious reader an introduction to exciting physics of wave-particle interaction. The interaction of the

---

[80] Clilverd et al., "Determining the Size of Lightening-Induced Electron Precipitation Patches," *J. Geophys. Res.,* Vol. 107, 2002: 1168.

[81] Inan et al., "Geographic Distribution of Lightening-Induced Electron Precipitation Observed as VLF/LF Perturbation Events," *J. Geophys. Res.,* Vol. 93, 1988: 9841.

[82] Draganov et al., "Magnetosperically Reflected Whistlers as a Source of Plasmaspheric Hiss," *Geophys. Res. Lett., 19,* 1992: 233.

[83] M. Schultz and L.J. Lanzerotti, *Particle Diffusion in the Radiation Belts*, (New York: Springer-Verlag, 1974), 60 - 62.

whistler waves with the trapped particles is known to cause both pitch angle and radial diffusion. The interaction is caused from a coupling of the plasma wave to the cyclotron and/or bounce resonance of the trapped particle. Not all whistler waves interact with a particle trapped in the magnetic field, but the result of the interaction is an increase in the decay rate and radial dispersion of the trapped particle.

Because a complete particle tracking model is needed for all L-shells and all altitudes, the effect of wave-particle interaction on trapped particles is certainly an area of future work necessary to expand the capability of the model. The most likely approach would be to develop a set of diffusion equations to account for the whistler-induced effects of pitch angle change and radial diffusion. The diffusion approach would need to account for the early time effects of the burst induced whistler waves as well as the late time coefficients of the "ambient" whistler modes. The development of the early-time coefficients would be challenging at best and possibly limited by the sparse data from the high-altitude nuclear tests. The late-time "ambient" diffusion coefficients have been studied by numerous groups and a group at Los Alamos National Laboratory is currently working on modeling trapped radiation for L-shells above L = 4. The author has met with the group and they are working hard to determine the appropriate diffusion equations and diffusion coefficients to account for wave-particle interaction at select altitudes of interest. The results of their work, and the work of others, may have direct application to the expansion of our current model to include charged particles trapped in L-shells above 1.3.

4.5.   SUMMARY OF ADDITIONAL PHYSICS

In Chapter IV, with the introduction of the altered magnetic field of the earth and the effects of the atmosphere on the energy loss and pitch-angle scattering of charged particles, we are able to expand the physics in the model from that of charged particles trapped in a perfect dipole in a vacuum to the realistic environment of particles trapped in the earth's magnetic field. The advantage of the "ideal environment" model of Chapter II and 3 was that the results of the model were successfully compared to analytic solutions. There are no analytical solutions that include the physics introduced in Chapter IV and there is only a limited set of data (Chapter VI) against which to compare the results of the

complete model. However, the addition of the real environment is absolutely necessary for useful application of the model. The results presented in Chapter VII are consistent with limited data from the atmospheric tests. Before providing the results of the model, Chapter V will introduce the source of the fission fragments and explain the spectrum of fission fragments and beta particles used to produce the results of Chapter VII.

V.   BRIEF DESCRIPTION OF THE SOURCE OF INJECTION OF PARTICLES

What possible man-made source could populate the space environment in such a way that the injected ions and electrons present a significant threat to satellites and other space-based assets? Today we know that energetic particles from the sun can become trapped in the earth's magnetic field and can cause damage to space based assets. In fact much of our knowledge about trapped radiation comes from the study of solar particles trapped in the earth's magnetic field. However, in order to answer the question about man-made sources of charged particles we recall that in 1959, N. C. Christofilos, the test director for the Argus atmospheric test series wrote:

> These results pointed toward a convenient source of large quantity of electrons, namely, to an A-bomb. This source is so plentiful that even 1 megaton of fission would create an electron layer so dense as to constitute a radiation hazard in outer space. To illustrate this I cite the following example: 1 megaton of fission yields 10^{26} fissions, approximately. If we assume that 4 electrons per fission are above 1 MeV energy and that half will be trapped in the earth's field we derive a number of trapped electrons, namely, 2 x 10^{26}. Then let us assume that these will spread in a volume in outer space equal to the earth's volume, or 10^{27} cm^3. The resulting electron density is 0.2 electrons/cm^3. The flux against any surface exposed to the electrons is 1.5 electrons/(cm^2-sec).[84]

Throughout the remainder of the dissertation, nuclear fission is assumed as the source for ions injected into the magnetic field of the earth. From the data, it will be shown that nuclear detonations in space can increase the density of charged particles by several orders of magnitude; and, depending on the initial condition of the release of particles, the trapped particles may remain trapped for years. All of the source information used in this dissertation is unclassified and available in the open literature.

In a nuclear explosion there are two basic processes for prompt energy release: fission and fusion. Fission is generally described as the splitting of a heavy isotope of uranium or plutonium into fission fragments, neutrons, and gammas. The complete fission of one pound of uranium or plutonium releases an amount of energy equivalent to

---

[84] N.C. Christofilos, "The Argus Experiment," *J. Geophys. Res.,* Vol. 64, 1959: 870.

8 kT of TNT. Fusion is associated with uniting or fusing of a pair of lighter nuclei (like deuterium or tritium) into a heavier element like helium. A complete fusion of all of the nuclei present in one pound of deuterium would release as much energy as 26 kT of TNT.[85]

What is important for this dissertation is that the fragments from fission are a significant source of ions injected into the magnetic field resulting from a nuclear explosion. The energetic electrons injected into the magnetic field are from the beta decay of the fission fragments. The fusion process does not directly add fission fragments to the environment; however, the neutrons released from the fusion process do cause additional fissions of the some fissile material. The energy released from fusion may also cause a change in charge state of the fission fragments and other bomb debris, but the initial charge state of the fragments is not calculated in the code or the dissertation. The charge state of the debris is either assumed or provided as an initial condition when the simulation is started.

5.1.   BASIC DESCRIPTION OF NUCLEAR FISSION

The fission process involves the breakup of heavy and unstable nuclei into lighter fission fragments. Although nuclear fission can be introduced by the absorption of neutrons, gamma quanta, or energetic charged particles into the nuclei, for practical purposes, the most important catalyst for the breakup of the nucleus is a neutron capture.[86] After the neutron capture, the heavy and unstable nucleus fissions, releasing additional neutrons and energy, and creating two new daughter products. An example of the fission process is

$$(5.1.1) \qquad {}_{0}^{1}\text{n} + {}_{92}^{235}\text{U} = {}_{57}^{144}\text{La} + {}_{35}^{90}\text{Br} + {}_{0}^{2}\text{n} .$$
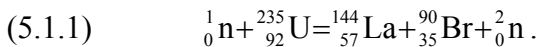
In equation 5.1.1, the upper number associated with each element is the number of nucleons and the lower number is the number of protons. The process in equation 5.1.1 not only produces two different fission fragments (also called daughter products), but it

[85] S. Glasstone and P. Dolan, *The Effects of Nuclear Weapons*, 3rd ed., (prepared and published by the United States Department of Defense and the United States Department of Energy, 1977), 5.

[86] G.R.Keepin, *Physics of Nuclear Kinetics*, (Reading, Ma: Addison-Wesley Publishing Co., Reading, 1965), 1.

also produces two more neutrons that may cause additional fissions in remaining atoms of $^{235}_{92}U$ or other fissionable material. The average number of neutrons produced by fission depends on the energy of the neutron causing the fission.[87] Figure 5.1.1 presents the average number of neutrons (nu-bar) emitted during the fission process as a function of the energy of the captured neutron.[88] For our purposes, the typical fission produces between two and three neutrons for each fission. One can conservatively approximate that a single fission produces two additional neutrons when calculating the energy released by the cascading of the fissile material.
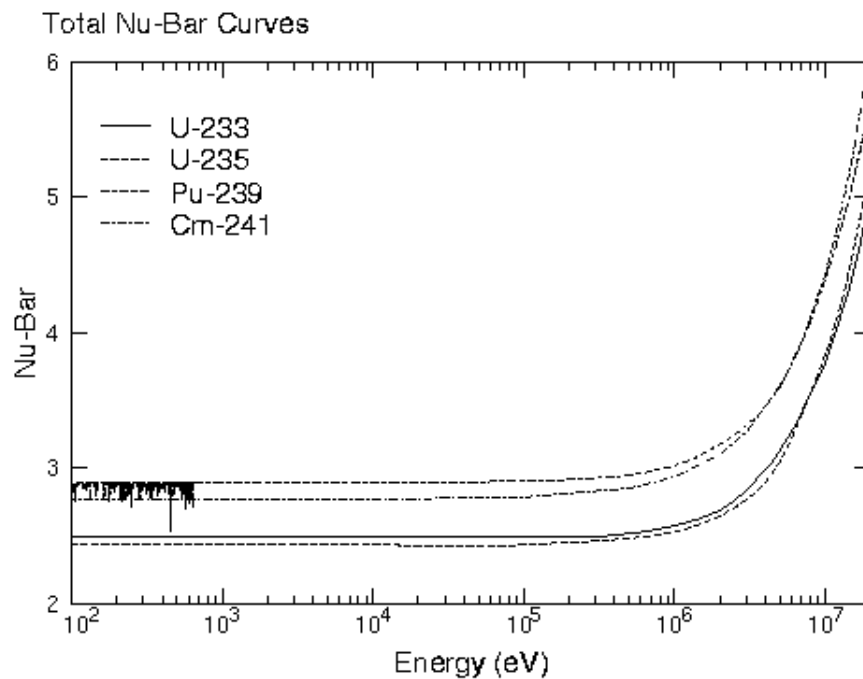
Figure 5.1.1: The number of neutrons produced during fission as a function of the fissioning neutron energy. [from http://t2.lanl.gov/endf/intro22.html Accessed 27 April 2007]

When each fission releases sufficient neutrons to cause one more fission, the assembly is called critical. If there is an excess number of effective neutrons (e.g., 2), then not only is the chain reaction sustained, the energy release grows exponentially in time. If such an

---

[87] Keepin, 4.

[88] Fission Neutron Yield, http://t2.lanl.gov/endf/intro22.html , (accessed on 27 April 2007).

exponentially growing chain reaction is contained and allowed to continue, and if it is further assumed that each fission results in two subsequent fissions, then the number of fissions resulting from a single fission initiation is

(5.1.2) $\quad\quad \#\text{fissions} = 2^f$

where f is the number of fission generations in the entire process. If f = 10 then there are 1,024 neutrons following 512 fissions. If f = 20 then there are 1,048,576 neutrons. If f = 40 then there are 1.1 x 10^{12} neutrons. If f = 60 then there are 1.2 x 10^{18} neutrons. If, as Christofolis suggested, there are 10^{26} fission fragments from a 1 MT fission weapon, then there would be on the order of 86 complete fission generations. In general, the number of possible fissions is limited by the difficulty of containing the fissile material during the chain reaction.

The distribution of energy released during fission is shown in Table 5.1.1. It is often convenient to think of around 200 MeV of energy released per fission. Table 5.1.2 offers a reference to other units of energy.[89]

Energy Released per Fission	U-235 (MeV)	Pu-239 (MeV)
Fission Fragment Kinetic energy	168	172
Neutron Kinetic Energy	5	6
Prompt Gamma Energy	7	7
Beta Decay from Fragments	8	8
Delayed Gamma Energy	7	7
Anti-neutrino Energy	12	12
Total Energy	207	212

Table 5.1.1: Fission energy breakdown.

[89] Glasstone and Dolan, 13.

Equivalents of 1 kiloton (kT) of TNT
Complete fission of 0.057 kg of fissionable material
Fission of 1.45×10^{23} nuclei
1×10^{12} calories
2.6×10^{31} electron volts (eV)
4.18×10^{12} joules (J)
1.16×10^{6} kilowatt-hours
3.97×10^{9} British thermal units (BTU)

Table 5.1.2: Equivalent units of energy.

The number of fission fragments produced is proportional to the fission yield of the weapon. Often the stated yield of a weapon includes the combined fission and fusion contributions and should not be confused with the fission yield in terms of contribution of total number of fission fragments. For the purposes of this dissertation, the yield of the weapon is not a concern and will not be discussed further. A reasonable source of fission fragments is assumed as part of the initial conditions for the computational analysis demonstrated as part of this dissertation.[90]

In the fission of typical heavy isotopes there may be at least 750 isotopically different fission fragments produced. Of these only about 250 occur with a frequency of more than 1 in 10^4 fissions. These more common isotopes are distributed with atomic weights from 76 to 155.[91,92] The distribution of the fission fragments tends to vary depending on the fissile material and the energy of the neutrons causing the fissions.[93]

When the fission occurs in $^{235}_{92}U$, the 92 protons and the remaining neutrons (those not released) are split between the two fission fragments. One of the daughter products has mass number (number of nucleons) around 100 atomic mass units (amu) and

---

[90] Tom Thomson (LLNL), private conversation with author, 11 October 2006.

[91] Memorandum from D. Nethaway and M. Mustafa, Memorandum to Thomas Thomson at Lawrence Livermore National Laboratory, Subject; The Addition of Prompt Fission Product Data to Explosion Eodes, March 23, 1998.

[92] T.R. England, B.F. Rider, *LA-UR-94-3106; ENDF-349*, Los Alamos National Laboratory, 1993.

[93] Glasstone and Dolan, 18.

the other fragment has a mass number around 130 amu. Figure 5.1.2 shows the distribution of atoms per fission for thermal neutrons, fission (pool) spectrum neutrons, and fusion spectrum neutrons.[94]
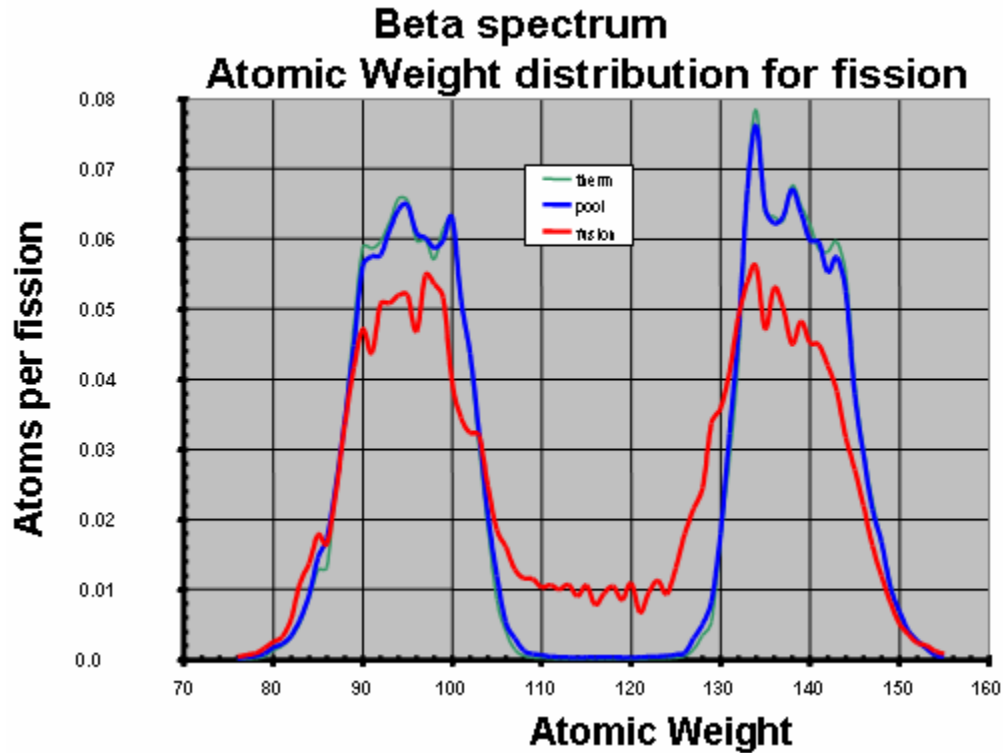
Figure 5.1.2: The distribution of atoms per fission. [after Thomson]

Although much is known about the distribution of fission fragments from all different fission sources, this dissertation does not try to incorporate every possible fragment species into the spectrum injected into the magnetic field. A reasonable representation of the fission fragment spectrum was selected for the project. An internal memorandum at Lawrence Livermore National Laboratory (LLNL)[95] lists an appropriate fission fragment distribution for thermal fissions, fission spectrum fission, and 14-MeV fissions of $^{235}_{92}$U and $^{238}_{92}$U. This list and internal discussions at LLNL[96] were used for the

---

[94] England and Rider, "LA-UR-94-3106; ENDF-349."

[95] Nethaway and Mustafa.

[96] Tom Thomson (LLNL), private conversation with author, 18 October 2006.

selection of fission fragments for the computational studies. Table 5.1.3 provides a list of the fission fragments used for most of the modeling. Although this list serves as the basis for the initial fission fragment selection in the dissertation, other sources are available for more fission spectrum information[97,98] and can be used as additional sources for fission fragment selection.

Code Fragment #	Element	# of Protons	# of Neutrons	Half-life (s)
1	Zirconium	40	52	Stable
2	Yttrium	39	53	12744
3	Strontium	38	54	9756
4	Rubidium	37	55	4.492
5	Krypton	36	56	1.84
6	Bromine	35	57	0.365

Table 5.1.3: The table presents the fission fragments used for most of the computations. The code fragment number is an identifier used to keep track of the fission fragment during the simulations.

An important reminder is that although fission fragments are a contributor to the debris trapped in the magnetic field, most of the bomb materials are also ionized and can become trapped in the magnetic field of the earth. For the 1 MT fission weapon there would also be 1×10^{28} bomb debris fragments from the materials of the weapon injected into the radiation belts. Most of these other bomb debris fragments do not contribute electrons from beta decay, but all of the ionized particles pose a threat to satellites similar to the solar protons already trapped in the earth's magnetic field.

5.2. BETA DECAY

The primary source of energetic electrons released following a nuclear detonation is from the beta decay of the fission fragments. Although there may be a small number of ionized electrons shock accelerated to MeV energies those electrons are not currently

---

[97] T. R. England and B. F. Rider, "Evaluation and Compilation of Fission Product Yields," Preliminary Report for the National Nuclear Data Center's Evaluated Nuclear Data File, Los Alamos National Laboratory Repot ENDF-349, LA-XXXX-MS, 1993.

[98] G. Audi, O. Bersillon, J. Blachot, and A. H. Wapstra, "The NUBase evaluation of nuclear and decay properties," *Nuclear Physics A 729*, (2003): 3-128.

included in the source term for electrons used in the model. Of the over 750 possible fission fragments resulting from the different fission processes, only those fission fragments that contribute at least one percent of the fragment population are currently included.[99]

By way of background, beta decay is a type of radioactive decay where an electron or a positron is emitted from the nucleus. (This dissertation will only address electron producing beta decay, but the code could also be used to model positrons from beta decay.) No one who has followed the development of the theory of beta decay could fail to appreciate the great importance that beta decay has played in the understanding of nuclear physics. As is well known and documented, beta decay is full of many surprises, subtleties, and fascinating physics. The continuous beta energy spectrum was the most illuminating clue revealing the existence of the neutrino.[100] When the neutron-heavy nucleus of uranium or plutonium splits into fission fragments, the resulting isotopes are generally neutron rich, i.e., there are more neutrons in the fragment nuclei than the stable isotope of the same element. Although the details and science of beta decay are fascinating, a simple model and understanding is developed for application in the simulation.

For the beta decay, the weak interaction converts one of the neutrons into a proton while emitting an electron and an anti-neutrino.

(5.2.1) $\qquad n^0 \rightarrow p^+ + e^- + \overline{v}_e$
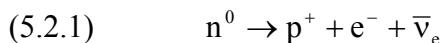
The electron-proton combination maintains charge conservation and the electron-anti-neutrino combination maintain lepton conservation. The continuous energy spectrum of the electron results from the splitting of the energy between the electron and the anti-neutrino. The average beta energy is around 1/3 of E_{max} where E_{max} is the end point energy of the spectrum. The result of the beta decay is a new elemental species that may also be radioactive plus a free and energetic electron. The chain of beta decay emissions continues until the final beta decay results in a stable isotope. The total beta decay energy

---

[99] Nethaway and Mustafa.

[100] C.S. Wu, and S.A. Moszkowski, *Monographs and Texts in Physics and Astronomy: Beta Decay,* (New York: Interscience Publishers, John Wiley and Sons, Inc., 1966), 1.

spectrum for all possible fission fragments was first reported by Carter-Reines[101] and is shown below in Figure 5.2.2. The significance of the spectrum is that the beta decay of the fission fragments may result in the release of energetic electrons that may become trapped and are hazardous to satellites.
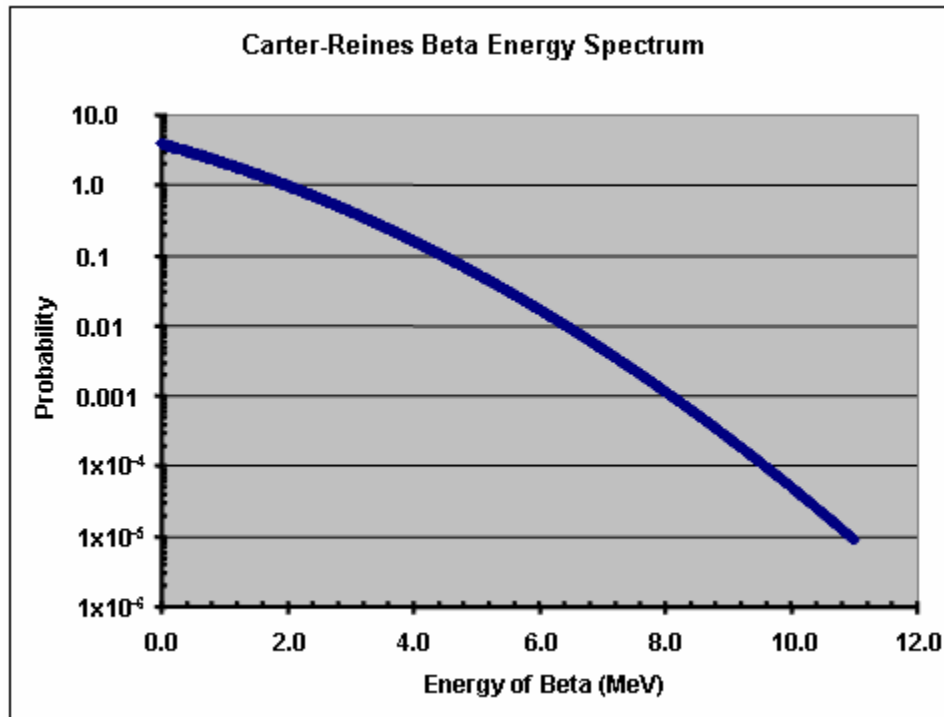
Figure 5.2.1: The Carter-Reines equilibrium beta decay energy spectrum from 1959. This spectrum represents the total energy of the beta decay particles for U-235 integrated over all time

Each fission fragment has a different half-life and associated beta energy spectrum.[102] Most of the late-time (after 1 s) energy spectrum is well known and documented from nuclear reactor research in text such as Browne and Firestone, but the early-time (fission fragments with a half-life less than one second) energy spectrum is not

---

[101] R.E. Carter, F. Reines, J.J. Wagner, and M.E. Wyman, "Free Antineutrino Absorption Cross Section II. Expected Cross Section from Measurements of Fission Fragments Electron Spectrum," *Phys. Rev.,* Vol. 113, 1959: 280.

[102] F. Browne and R.B. Firestone, *Table of Radioactive Isotopes*, (New York: John Wiley and Sons, 1986).

well documented or even completely understood. Tom Thomson at LLNL is currently compiling the best known data on the half-lives of fission fragments and the associated beta decay spectrum to include the early time fission fragments.[103]

The early-time decay spectrum is of particular interest in modeling the trapped radiation from a nuclear detonation. Generally, the beta particle from a radioactive isotope with a short half-life has a higher end point energy than radioactive isotopes with longer half-lives. Figure 5.2.2 shows the end point energies of the possible beta particles for the beta decay of the fission fragments of U-235.

End Point Energies of Betas from Fission Fragments
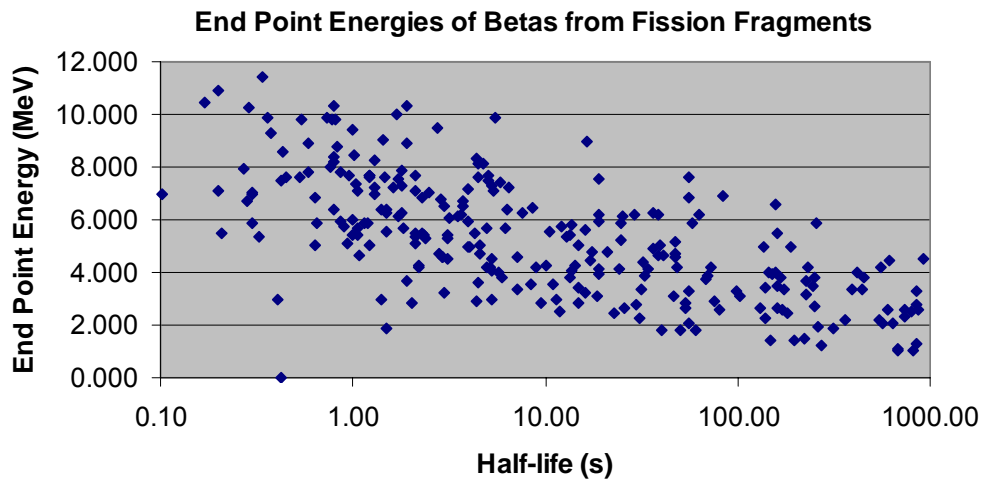
Figure 5.2.2: The end point energies of the beta spectrum is shown for most the possible fission fragments as a function of half-life. [after Thomson]

The fission fragments that decay quickly tend to produce the most energetic electrons. Figure 5.2.3 shows the number of each fragment per fission and the associated half-lives for the U-235 pool reactor fission spectrum. Fission fragments with long half-lives that are released into the magnetic field may become "lost" deep in the atmosphere before the fragment beta decays. The electrons released from beta decay when the ions are low in the atmosphere quickly lose most kinetic energy in the atmosphere and are not generally hazardous to satellites. Finally, the fission fragments with short half-lives will

---

[103] Tom Thomson (LLNL), private conversation with author, 17 January 2007.

not only produce an electron near the location of the burst, often well above the atmosphere, but the electrons from short half-life fragments may also have the highest energies.
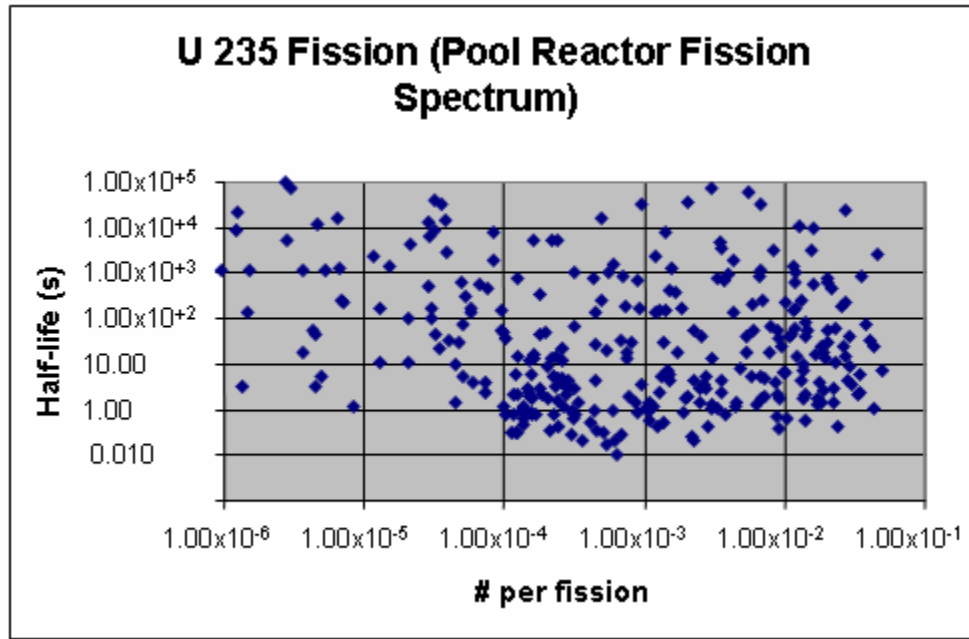
Figure 5.2.3:   This figure shows the number of fission fragments with different half-lives per fission of U-235 for the pool reactor fission spectrum. [from Thomson]

Because of the large number of fission products decaying in various decay chains it has proved expedient to treat the complex of all fission products as a statistical ensemble and to describe the gross radioactive decay from an average fission.[104] Way and Wigner developed a rule-of-thumb expression for the time dependence of β- energy released from fission products.[105,106] The rule-of-thumb expression for the energy released from beta decay as a function of time (t) for times from 1 second to 10^5 seconds and is

---

[104] Keepin, 14.

[105] K. Way and E.P. Wigner, "The Rate of Decay of Fission Products," *Phys. Rev, 73*, 1948: 1318.

[106] A.M. Weinberg and E.P. Wigner, *The Physical Theory of Neutron Chain Reactors*, (Chicago: University of Chicago Press, 1958), 133.

(5.2.2) $\beta(t) = 1.26t^{-1.2} (MeV/s)$.

Figure 5.2.4 shows the energy released from the beta decay of the fission fragments as a function of time using the Wigner rule of thumb. All of the very short half-life beta energy spectrum was provided by Tom Thomson.[107]
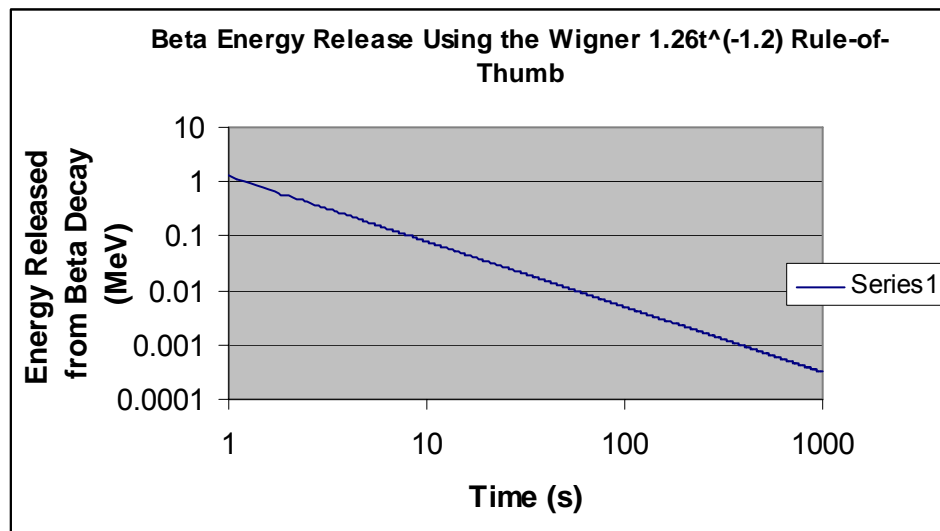
Figure 5.2.4: The Wigner rule-of-thumb for beta energy release.

After a fission fragment beta decays, the new isotope may still be radioactive and contribute another electron through beta decay. The beta decay chain for the selected fission fragments of Table 5.1.3 is shown in Figure 5.2.5.[108] As shown in Figure 5.2.5, some initial fission fragments will progress down the decay chain as many as eight times before the finally reaching a stable isotope. For the purpose of this dissertation, each beta decay changes the charge state of the fission fragment by plus one and produces an energetic electron that may become trapped in the magnetic field.

---

[107] Tom Thomson, e-mail message to author, 18 April 2007.

[108] LBNL Isotopes Project - LUNDS Universitet: WWW Table of Radioactive Isotopes, Version 2.1, January 2004, http://ie.lbl.gov/toi (accessed on 14 May 2007).
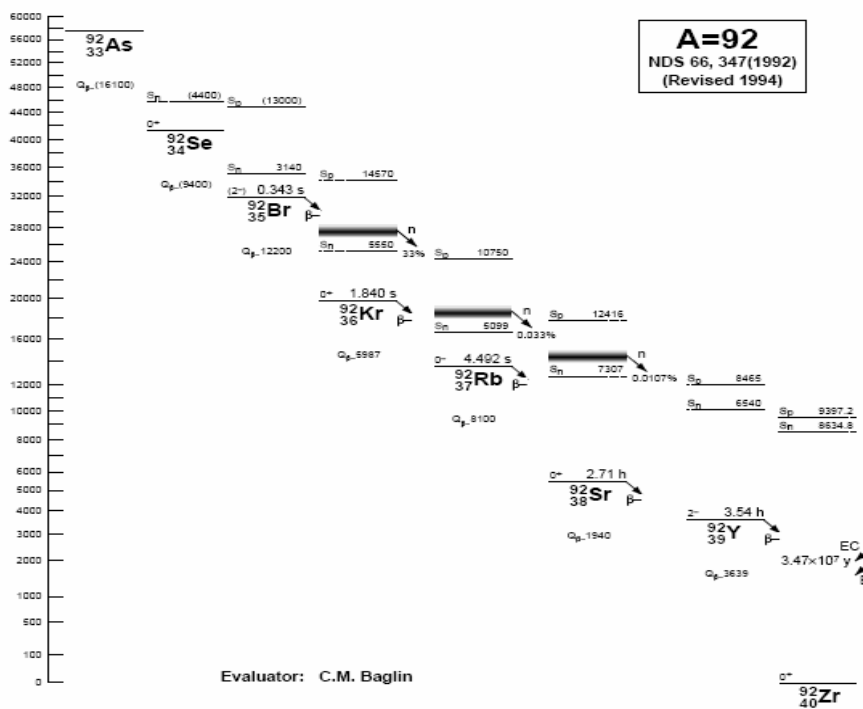
Figure 5.2.5: The fission fragment decay chain used in most of the simulation results presented in this dissertation. The decay chain is similar to the decay chain of most fission fragments. [from http://ie.lbl.gov/toi/sumsrame.htm Accessed 14 May 2007].

Another example of a fission and then the subsequent beta decay chain is shown in Figures 5.2.6 and 5.2.7 for the fission process[109]

$$\,_{0}^{1}n+\,_{92}^{235}U=\,_{57}^{144}La+\,_{35}^{90}Br+\,_{0}^{2}n\,.$$
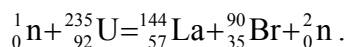
The "sliding down" the chain occurs for all processes until the beta decay results in a stable isotope like $\,_{60}^{144}Nd$ or $\,_{40}^{90}Zr$.

---

[109] LBNL Isotopes Project - LUNDS Universitet: WWW Table of Radioactive Isotopes, Version 2.1, January 2004, http://ie.lbl.gov/toi (accessed on 14 May 2007).
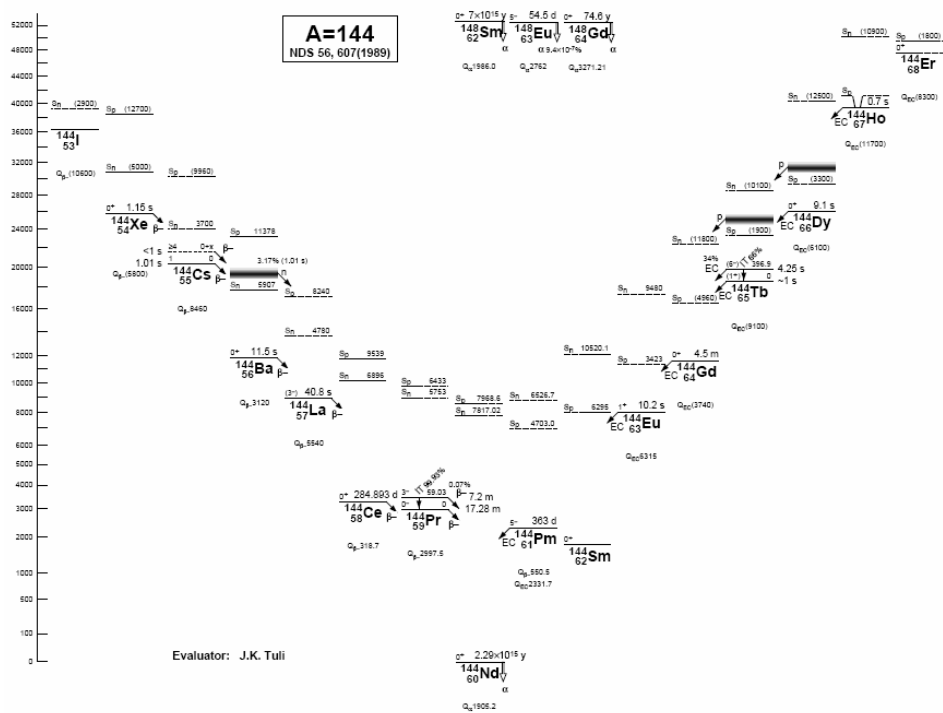
Figure 5.2.6: The decay chain of $^{144}_{57}\text{La}$. [from http://ie.lbl.gov/toi/sumsrame.htm Accessed 14 May 2007].
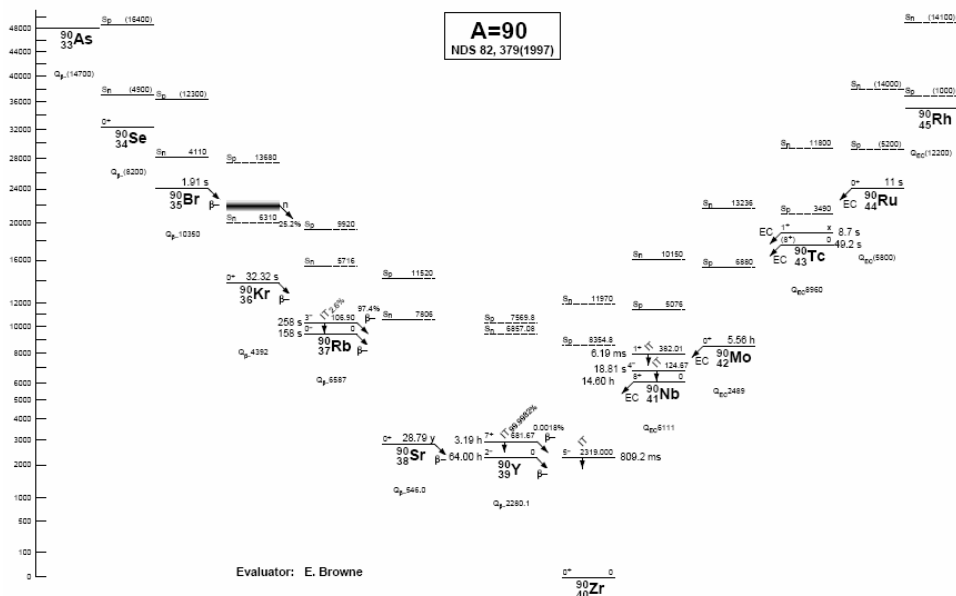
Figure 5.2.7: The decay chain of $^{90}_{35}\text{Br}$. [from http://ie.lbl.gov/toi/sumsrame.htm Accessed 14 May 2007].

Although the nuclear decay does not always produce an electron and may sometimes produce a positron (actually considered an isomeric transition), gamma, or neutron[110], the model developed for this dissertation only accounts for β^- decay of the nucleus. More elaborate models and physics exists to account for the different types of decay and could be added in the future, but given the scope of this dissertation, the modeling of beta decay is adequate for accounting for the injection of energetic electrons into the magnetic fields. A more sophisticated approach is certainly plausible, to include the emission of positrons, and should be considered for future work. The addition of a more complete model of the full spectrum of fission fragments and beta particles is "work in progress" but is not critical to this dissertation. Regardless of the potential addition of more elaborate fission fragment options and beta decay schemes, the fragments and beta electrons remain the most significant threat from trapped radiation.

---

[110] K.S. Krane, *Introductory Nuclear Physics*, (New York: John Wiley and Sons, 1988), 272.

THIS PAGE INTENTIONALLY LEFT BLANK

VI.   A QUICK LOOK AT HIGH-ALTITUDE NUCLEAR TEST DATA

Before presenting the complete computational model developed for this dissertation, as well as the results of the model, a quick look of the existing high-altitude nuclear explosion data is presented. The purpose of the quick look is to review the limited information and data available about each high altitude nuclear event. This chapter does not represent a complete description of all of the papers, books, and articles on high altitude nuclear tests and data, but only serves as a guide for the curious reader. The available data is actually quite sparse by no means represents an ideal collection of data. Very little early-time information is available and there was a small [the number of atoms in the universe is finite] number of satellites and sounding rockets used for the collection of the data. Nevertheless, the data reviewed in this chapter is most likely the only data that will ever exist from a high altitude nuclear detonation. An examination of the data, although guaranteed to introduce questions and concerns, is useful for providing some insight into the complicated physics of nuclear detonations in space. The data may eventually serve as a useful benchmark for comparisons to the computational output.

All of the high altitude nuclear tests data is from the late 1950s and early 1960s. Most of the effort committed by the DoD, DoE, and space physics community to understand the physics of and data from high altitude nuclear detonations was during the 1960s and early 1970s as an effort to understand the results of nine nuclear tests. One is allowed to stand on the shoulders of giants (Van Allen, Northrup, Cladis, Hess, Walt, Zinn, Dyal, and many others) of the space physics community while reviewing the data and knowledge of nuclear weapons effects in space. The works of the space physics pioneers allow the student to witness the unfolding of much of the theory introduced in Chapter II as well as motivate the need for the computational capability introduced in this dissertation. Additionally, a review of the data also helps explain why 45 years after the last high-altitude nuclear test, no complete model exists to predict the environment caused by a nuclear detonation in space. The National Labs, Defense Threat Reduction

Agency,[111] and other government organizations still maintain small programs working to better understand the nuclear induced environment and the effect of the possible environment on space-based systems. This dissertation is in fact sponsored by a high-altitude nuclear environments program at LLNL.

Although the data may eventually provide an opportunity to validate the environment predicted by the model, a lot of work is necessary (and beyond the scope of this dissertation) in order to understand the initial conditions of the weapons debris and perturbed magnetic field. As is shown in Chapter VII, the initial condition of the debris is critical if one hopes to confidently match the data from the nuclear test. The current position of the author is that if the model was able to correctly match the available data then the results should be considered suspect unless we confidently understand and predict the initial condition information about the debris. In the same manner, if the model developed for this dissertation was "perfect", but the initial conditions used to run the simulation were wrong then matching the data would be almost impossible. Nevertheless, a quick review of the data is presented to help the reader understand some of what is known from the results of a nuclear detonation in space.

There were eleven high-altitude "shots" from 1958 to 1962 and some data was collected after each detonation. Table 6.1 provides a summary of nine of the events.[112,113,114] The two of the eleven "shots" not included in Table 6.1 were small (~1.5 kt and the size of the Argus devices) Soviet tests in 1961 that apparently provided the U.S. with very little additional data as there is nothing reported in the open literature. With the exception of the name and date of the "shot", there is still uncertainty associated with most of the information reported in Table 6.1 so none of the values reported here should be considered exact.

---

[111] C. Allen, B. Roth, "Final Report Summarizing Blue Ribbon Panel and Support Work Assessing the Status of the High Altitude Nuclear Explosion (HANE) Trapped Radiation Belt Database," Final report to Air Force Research Laboratory, June 2006.

[112] Van Allen, "Spatial Distribution and Time Decay of the Intensities of Geomagnetically Trapped Electrons from the High Altitude Nuclear Burst of 1962," 577.

[113] Cladis et al., 6-2.

[114] Y.I. Zester, B.G. Gavrilov, V.A. Zhmailo, K.G. Gainullin, V.I. Selin, "Geomagnetic Effects from Expanding Plasma Formation of a High-Altitude Nuclear Explosion," *Combustion, Explosion, and Shock Waves,* Vol. 60, No. 6, (2004), 638 - 648.

Event	Date	Altitude (km)	Latitude	Longitude	L-shell of detonation	Yield	Approx. Decay Time of Betas
Teak	1-Aug-58	~77	17 N	169 W	1.12	~4 Mt	Few days
Orange	12-Aug-58	~43	17 N	169 W	1.12	~4 Mt	Few days
Argus I	27-Aug-58	~200	38 S	12 W	1.7	~1.4 kt	0-20 days
Argus II	30-Aug-58	~250	50 S	8 W	2.1	~1.4 kt	10-20 days
Argus III	6-Sep-58	~500	50 S	10 W	2	~1.4 kt	10-20 days
Starfish	9-Jul-62	~400	16.7 N	190.5 E	1.12	~1.4 Mt	1-2 years
USSR I	22-Oct-62	300	50 N	70 E	1.8	300 kt	~30 days
USSR II	28-Oct-62	150	50 N	70 E	1.8	300 kt	~30 days
USSR III	1-Nov-62	60	50 N	70 E	1.75	300 kt	~30 days

Table 6.1: **General information on nine high altitude nuclear detonations. Although Teak was ~35 km higher than Orange, the L-shells for Teak and Orange are shown in the table as identical. Teak was in a slightly higher L-shell, but to the degree of accuracy reported in the Trapped Radiation Handbook, they are listed as having the same L-shell for detonation. The approximate decay time of the betas is the time required for the number of electrons to return to the pre-shot ambient number of electrons**

During the 1960s, teams of scientist were assembled in an effort to compile and hopefully explain the results of the test shown in Table 6.1. A large portion of the Journal of Geophysical Research, Volume 64, August 1959, was devoted to the result of the Argus test series. Several articles were published in the Journal of Geophysical Research, Volume 68, February 1963, on the Starfish test. The proceedings of the Advanced Study Institute Held at Chr. Michelsen Institute, Bergen, Norway from August 16 – September 3, 1965 were published in Radiation Trapped in the Earth's Magnetic Field edited by Billy McCormac provide multiple reports and technical analysis on most of the high altitude tests, theory, and data. Another large source of information is found in the Trapped Radiation Handbook which was a Technical Report distributed by the Defense Technical Information Center in 1971. The four references listed above offer thousands of pages of data, theory, and descriptions from the atmospheric test. There are also many additional references not listed here.

Teak and Orange were the first tests conducted that provided data on the environment created by a nuclear detonation is space. They were both large-yield weapons, detonated 130 degrees west of the SAA, at relatively low altitudes. The data collection was limited to a single satellite. The Trapped Radiation Handbook[115] provides the summary of the results of the data collected from both shots. The data was collected by the Explorer IV satellite[116] and suggest a short duration increase in the fission spectrum electrons trapped in L-shells ranging from 1.1 up to 1.22. Of the two bursts, Teak had the most notable effect most likely due to the higher height of burst of the two weapons. Only the electron data is reported in the literature so no knowledge exists for the trapping of the ionized debris or the extent of the magnetic bubble.

The fission spectrum electrons detected as trapped from Teak remained trapped for only a few days. The electrons injected into $L = 1.1$ (the burst L-shell of the weapon) increased the density of electrons by five orders of magnitude for the first hours after the burst, but the electron density returned to the background levels in approximately 24 hours. Explorer IV also measured a five orders of magnitude increase in the electron density at $L = 1.2$ that was not detected until 24 hours after the detonation. This delay in increase is still not explained. In the $L \approx 2$ region, the time for 1/e decay was found to be approximately four days.[117]

After Orange, Explore IV recorded a three orders of magnitude increase in $L = 1.1$ (L-shell of burst) within the first few hours, but like Teak, the decay of electrons was rapid and the electron density returned to ambient levels within 24 hours. There was no significant increase in the electron density in L-shells higher than the burst L-shell for Orange.

Both Teak and Orange were large, ~ 4 Mt, tests at altitudes well below 100 km height of burst. The measured belt pumping from these large weapons was generally limited to 24 hours after the burst, with some noticeable increases in fission spectrum

---

[115] Cladis et al., 6-2 – 6-13.

[116] J.A. Van Allen, C.E. McIlwain, and G.H. Ludwig, "Satellite Observations of Electrons Artificially Injected into the Geomagnetic Field," J. Geophys. Res., 64, (1959), 877 - 891.

[117] Cladis et al., 6-12.

electrons of the L = 2 for a few days after Teak. A majority of the decay was most likely caused by Coulombic scattering and energy losses in the atmosphere enhanced by the effect of the SAA.

The next set of available data is from the Argus test series of late August and early September 1958. N.C. Christofilos proposed the experiment in October 1957 as a way to measure the natural environment, verify the trapping of charged particles in the earth's magnetic field, and conduct an experiment in the region of the earth's upper atmosphere.[118] The location for the three Argus shots was selected near the SAA and the L-shells of detonation ranged from 1.17 to 1.21. The altitudes of the three shots were all well above the altitudes of Teak and Orange. The yields of all three tests were around 1 – 2 kt and significantly smaller than Teak or Orange. The data from the Argus tests was collected by Explorer IV and by sounding rockets.[119] There were also optical and electromagnetic observations made of each test.[120,121] The Trapped Radiation Hand Book[122] proclaims that the Argus experiments demonstrated that electrons could be injected into the magnetic field and seemed to behave, at least for a while, as predicted by adiabatic theory. The narrow bands of electrons that formed on the L-shells were stable and exhibited some widening with time. The majority of electrons that were recorded as trapped due the nuclear explosions were trapped in the respective L-shells of each detonation. Virtually no radial dispersion was noted in the data. The density of electrons was reported to have increased by a factor of 1,000 above the ambient levels by 3 ½ hours after the Argus I. Argus II and III recorded a factor of 100 increases in the density of electrons on the L-shell of injection.[123] The effective lifetime of the electrons was reported to be on the order of a week. The time rate of decay was more rapid than

---

[118] N.C. Christofilos, 869-875.

[119] L. Allen, Jr., J.L. Beavers, II, W.A. Whitaker, J.A. Welch, Jr., R.B. Walton, "Project Jason Measurement of Trapped Electrons from a Nuclear Device by Sounding Rockets," *J. Geophys. Res.,* Vol. 64, (1959), 893 - 90.

[120] P. Newman, "Optical, Electromagnetic, and Satellite Observations of High-Altitude Nuclear Detonations, Part I," *J. Geophys. Res.,* Vol. 64, (1959), 923 - 932.

[121] A. M. Peterson, "Optical, Electromagnetic, and Satellite Observations of High-Altitude Nuclear Detonations, Part II," *J. Geophys. Res.,* Vol. 64, (1959), 933 - 938.

[122] Cladis et al., 6-29.

[123] Van Allen, McIlwain, and Ludwig, 882 - 883.

expected from just atmospheric loses. The Trapped Radiation Handbook concludes that because the decay was more rapid than expected, the increased decay rate must be caused by some other phenomena, like wave-particle interaction. Like Teak and Orange, most of the data was provided by a single satellite and there seems to be no data on the increase in the density of the ionized debris. The Argus tests were small, but they provide data for injection into higher L-shells.

The final US test from which data is available was called Starfish Prime detonated on 9 July, 1962. The yield was around 1.4 Mt and the height of burst was 400 km. The geographical coordinate location was almost identical to Teak and Orange, although the height of burst was much higher. Of all the high altitude tests, Starfish Prime resulted in the most significant trapping of energetic electrons and clearly demonstrated the vulnerability of satellites to the trapped radiation resulting from a nuclear explosion (several of the satellites failed unexpectedly after Starfish Prime.) There were a number of satellites in orbit to collect data and sounding rockets were used to collect data immediately after the burst. This data, coupled with the exact knowledge of the nuclear device, provides the best set of conditions and results available for analysis and potential model comparisons.

The Starfish Prime event clearly produced the most extensive and longest lived artificial radiation belts. Starfish not only resulted in the trapping of large number of energetic electrons, but the electrons also dispersed over much wider L-shells than any previously recorded tests. The data certainly suggest that fission spectrum electrons were injected at least as high as L ≈ 2 and radiation effects were noted considerably beyond this value[124] with some enhancements of the radiation belts seen out to L ≈ 6.[125,126]

In an abstract by J.A. Van Allen, he summarizes the satellite data from Starfish Prime:

---

[124] M. Walt, "Overall Analysis of Experiments on Artificial Radiation belts," published in *Radiation Trapped in the Earth's Magnetic Field*, edited by Billy M. McCormac, (Dordretch, Holland: D. Reidel Publishing Company, 1966), 667.

[125] W.N. Hess, "Project the Artificial Radiation Belt Made on July 9, 1962," *J. Geophys. Res.,* Vol. 68, (1963), 672.

[126] C. Allen, P. McDaniel, "Fission Spectra Electron Artificial Belt Widths and Error Analysis," published for Air Force Research Laboratory, Kirtland AFN, NM under Subcontract BOAS007-3011-7.

A one-year observational study of the artificial radiation belt produced by the nuclear burst Starfish on 9 July 1962 is reported. It is estimated that 1.3×10^{25} electrons from radioactive fission products, or some 2.6 % of the total yield, were present in geomagnetically trapped orbits at 10 hours after the burst. These electrons disappeared in the manner expected from the atmospheric loss theory of Walt for values of the magnetic shell parameter L<1.25 earth radii. At increasing values of L the rate of disappearance was progressively more rapid than expected by this theory. The maximum observed value of the apparent mean lifetime of ~2 MeV electrons in the range of $4,000 < \Delta t < 10,000$ hours was 2 years at L = 1.5. About 15% of the initially injected electrons (or 0.4 of 1% of the total) survived the first 5 ½ months, about 10% the first year.[127]

A summary of the data and satellite description is also provided in the Trapped Radiation Handbook.[128] Figure 6.1 presents some of the data available for Starfish. The apparent dispersion of the electrons away from the L-shell of the detonation is evident in Figure 6.1 and has been an issue of mystery for many years.

Also worthy of mention is recent work by Palmer Dyal.[129] Palmer's work is an effort to characterize the early-time magnetic bubble created by Starfish prime. He has also presented the data on the initial distribution of the electrons and weapons debris. Palmer's work is best summarized by an abstract from his most recent paper:

Recently analyzed beta particle and magnetic field measurements obtained from five spacecraft located 100 km to 1000 km around Starfish nuclear burst are used to describe the expansion and collapse of the diamagnetic cavity produced in the geomagnetic field. This unique data set shows the bubble evolved into an elongated shape 2,400 km along the magnetic field lines and 700 km across in 1.2 seconds and required approximately 15 seconds to collapse. Continued expanding debris from plasma instabilities injected a flux measuring 2.5×10^{10} betas/cm^2-s at H + 34 seconds into the most intense region of the artificial belt. This flux was measured at H + 10 hours later by Injun spacecraft to be 1×10^9 betas/cm^2-s.

---

[127] J.A. Van Allen, "Spatial Distribution and Time Decay of the Intensities of Geomagnetically Trapped Electrons from the High Altitude Nuclear Burst of 1962," published in *Radiation Trapped in the Earth's Magnetic Field*, edited by Billy M. McCormac, (Dordretch, Holland: D. Reidel Publishing Company, 1966), 575.

[128] Cladis et al., 6-31 – 6-46.

[129] P. Dyal, "Particle and Field Measurements of the Starfish Diamagnetic Cavity," J. Geophys. Res. Vol. 111 (2006), A12211, 1 – 23.

The results of this work by Palmer Dyal provide Hewett et al at LLNL a possible set of data against which they can verify their current work on characterization of the magnetic bubble from Starfish and expansion of the ionized debris. Understanding the correct initial conditions of the ionized fission fragments and eventually the beta particles is essential if the code developed in this dissertation is to be used successfully in an attempt to match the best set of high altitude data from Starfish Prime.
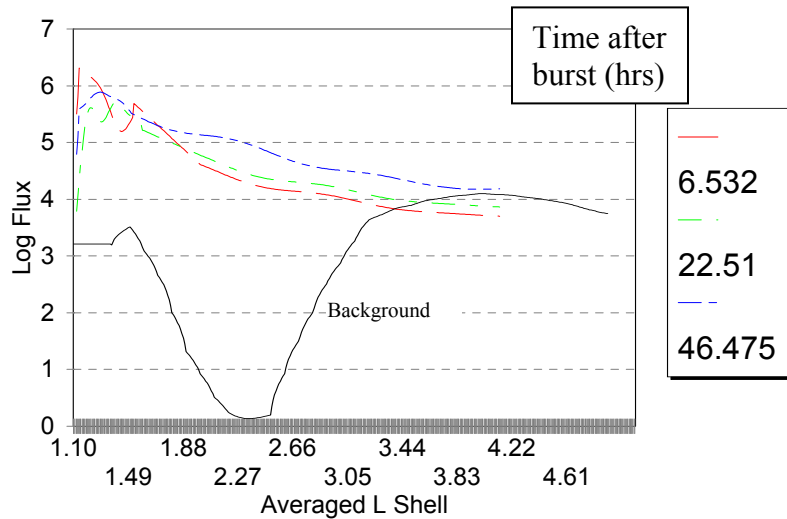
Figure 6.1: **Injun 1 satellite data for electron energies greater than 2.5 MeV processed for electron flux values for various times after Starfish and background.[130] The Starfish burst center was at L = 1.12 and the figure shows the "shoulder" of dispersion of the electrons possibly caused by the magnetic bubble effect on the electrons and fission fragments. [from C. Allen]**

Overall, the data from Starfish is the most complete (considering we know the source of the debris) of all the tests. There are inconsistencies between the data collected by the different satellites (specifically Injun I and Telstar) and recent work by Charles

---

[130] C. Allen, P. McDaniel, "Fission Spectra Electron Artificial Belt Widths and Error Analysis," published for Air Force Research Laboratory, Kirtland AFN, NM under Subcontract BOAS007-3011-7.

Allen suggests that a re-look at the data from Starfish is warranted and necessary.[131] The results from the Starfish event, although still riddled with questions, continue to serve as the baseline for predicting the effects of a nuclear detonation in space.

The final three high altitude nuclear events are often called Russian I, II, and III. All three shots had nominal yields of ~ 300 kt and the heights of the bursts are reported as 300 km, 150 km, and 60 km respectively. Although there are still significant questions and uncertainties about the yield and weapon design of the three events, significant numbers of fission spectrum electrons were trapped[132] and measured in L-shells ranging from 1.8 – 2.5. Table 6.2 presents the number of electrons measured by different satellites from the 1962 U.S.S.R. tests as published in The Trapped Radiation Handbook.[133]

Date	Satellite	Measured Value of Numbers of Electrons	Energy Level (MeV)
10/22/1962	Explorer XIV	$1.80 \times 10^{+24}$	E >0 .230
10/22/1962	Alouette	$1.15 \times 10^{+23}$	E > 3.9
10/28/1962	Explorer XIV	$1.50 \times 10^{+24}$	E >0 .230
10/28/1962	Alouette	$3.50 \times 10^{+22}$	E > 3.9
10/28/1962	Starad	$5.00 \times 10^{+24}$	E > 1.2
10/28/1962	Starad	$2.00 \times 10^{+25}$	E > 0.200
10/28/1962	Starad	$1.20 \times 10^{+25}$	E > 0.500
10/28/1962	Starad	$5.90 \times 10^{+24}$	E > 1.0
11/1/1962	Explorer XV	$5.60 \times 10^{+23}$	E > 0.500
11/1/1962	Explorer XV	$2.80 \times 10^{+23}$	E > 1.9
11/1/1962	Explorer XV	$8.50 \times 10^{+22}$	E > 2.9

Table 6.2:   The electron inventories of the last three U.S.S.R. tests as measured by the U.S. satellites. [from Cladis et al.]

---

[131] C. Allen, B. Roth, "Final Report Summarizing Blue Ribbon Panel and Support Work Assessing the Status of the High Altitude Nuclear Explosion (HANE) Trapped Radiation Belt Database," Final report to Air Force Research Laboratory, June 2006.

[132] H.I. West, Jr., "Some Observations of the Trapped Electrons Produced by the Russian High-Altitude Nuclear Detonation of October 28, 1962," published in *Radiation Trapped in the Earth's Magnetic Field*, edited by Billy M. McCormac, (Dordretch, Holland: D. Reidel Publishing Company, 1966), 634-662.

[133] Cladis et al., 6-53.

The Russian I increased the number of electrons in L = 2.2 by a factor of 100, but these electrons experienced a very rapid decay back to the post shot levels on the order of three days.[134]

Because of the location of the large number of radiation measuring satellites in orbit at the time of the Russian II detonation, the trapped radiation data is better known than that of any other high-altitude nuclear explosions.[135] What is unknown, at least by the scientists of the United States, is the exact yield and design of the Russian II device.

The Russian III shot, at a relatively low altitude, created a very narrow band of electrons on an L-shell of approximately 1.76. One of the perplexing results of the data from Russian III shot is that it apparently caused noticeable and significant trapping of electrons even though the detonation was at 60 km. The decay of the electrons was rapid, but belt pumping did occur. The observed belt-pumping of the Russian III event was much greater than either Teak or Orange which is surprising because Teak and Orange were both an order of magnitude larger in yield and Teak was ~ 15 km higher in altitude. There has been much speculation about why the Russian III caused belt-pumping and Teak or Orange did not. To date, no one has been able to offer a reasonable explanation for the belt pumping caused by Russian III. I will not attempt to explain the observation, but it is possible that the satellite used to collect data from the Russian III (the satellite was Explorer XV) was much improved over Explorer IV used to collect data from Teak and Orange.

Years have been spent by many great scientists trying to understand the data from the high altitude nuclear tests. There are still an abundance of questions and concerns about all of the results of the events. The data reviewed above most likely holds the keys that will unlock an improved understanding of the environments generated by a HANE. Eventually, the code developed in this dissertation can be applied to several of the events in an effort to compare with the existing data.

---

[134] W.L. Brown, "Observations of the Transient Behavior of Electrons," published in *Radiation Trapped in the Earth's Magnetic Field*, edited by Billy M. McCormac, (Dordretch, Holland: D. Reidel Publishing Company, 1966), 617.

[135] Cladis et al., 6-49.

VII. RESULTS AND FINDINGS

From the beginning the principal objective of this dissertation was to develop a particle tracking code capable of tracking very large numbers of ionized fission fragments and beta-decay electrons injected into the magnetic field of the earth. No known code existed for this explicit purpose. The code development was intended to provide a realistic computational capability to predict the environment produced by the injection of large numbers of ionized fission fragments (most likely due to a nuclear detonation at high altitudes) and/or the subsequent beta decay energetic electrons. Chapters I through V include the physics and computational proof of the ability to model the trajectory of individual charged particles released into and trapped in the earth's magnetic field. The model now has a multitude of applications at the classified and unclassified level. Using the model, several of the free parameters are examined and reported to highlight the sensitivity of the results to the initial conditions of the release of the fission fragments. The parameters examined and reported here include the effects of ion release location (longitude, latitude, and altitude), the charge state of the fission fragments, the beta decay half-life, and the initial pitch angle of the fission fragments. Additionally, the effects of the magnetic bubble on the dispersion and trapping efficiency of the particles is studied and reported.

7.1. BRIEF DESCRIPTION OF THE CODE

This section presents an overview of Fortran 95 computer code developed for and used in this dissertation. A line-by-line detailed description with comments is not presented but is available from the author or Dennis Hewett at LLNL. The purpose of this section is to describe the flow of the code without the specific details of the coding. The description of the how the physics is integrated into the code and verified is presented in the Chapters I – V.

The intent of the first five chapters was to describe the essential physics required to model the persistent radiation environment created when fission fragments and subsequent beta decay particles are released into the magnetic fields of the earth. Chapter

II presented and described the physics of charged particles moving in a perfect dipole vacuum magnetic field. Chapter III described the development of the numerical models used to track the charged particles as they moved in the magnetic field. The results of the two primary models selected and used in the simulation were compared to the analytic solutions of Chapter II and both models were shown to closely agree with the expected values for the bounce period, drift period and the constraint of conservation of energy. After validating the code for particles moving in a perfect vacuum, the effects of the "true" dipole field of the earth and charged particle interactions with air are presented in Chapter IV. Validation in modeling the trajectory of a charged particle in a perfect dipole was useful to establish confidence in the basis of the code, but in order to properly model the conditions experienced by a charged particle trapped in the earth's magnetic fields, the physics of Chapter IV must be included in the model. The addition of the detailed physics of particle interaction with air is absent from all other known "belt pumping" codes. Finally, in Chapter V, a description of the source of fission fragments and energetic betas is presented.

Each segment of the code was then developed in order to model the necessary physics of Chapter II – V. By segments, the physics modeled is well established, verified, and accepted, but the integration of each element (and necessary physics), coupled with the non-linear nature of the problem, makes the code unique. With the code, the debris of a nuclear weapon and the fission spectrum betas can be tracked as the debris interacts with the magnetic field thus providing a model capable of providing the space environment resulting from a nuclear detonation in space. The code also is well suited to provide a source term of the debris for after the burst for other similar codes that might be developed for predicting the environment days, weeks, and months after a nuclear detonation.

In order to run the model, an input file for the fission fragments is either provided to or created by the user. The initial condition of the fission fragments used in the code must include the location, velocity, isotope (atomic mass and number of protons), charge state, daughter products, and beta decay energy spectrum for each fission fragment. It is also possible to input the location of non-decaying particles (like the weapons debris and

debris electrons) in order to track all of the ionized debris. The code is designed to receive the output from other models in order to properly initialize the particles input into the code in order to match the best modeled conditions of the fission fragments resulting from a nuclear detonation or other event. The location and velocity of the fragments are either provided for a given scenario or selected with a defined distribution of particle locations and a Maxwell-Boltzman velocity distribution. The isotope for each particle is either defined or is randomly selected from a current list of six isotopes shown in Table 5.1.3 (generally representative of the possible fission fragments). The half-life and daughter product of each fragment is defined based on available information and can be adapted based on the interest of the user. The charge state is selected by the user and can vary from fragment to fragment.

Given the initial conditions of the fission fragments, the Boris push is used to model the trajectory of the ions as they move in the magnetic field. The size of the time step is determined by the code or the user and has a default setting of $1/100^{th}$ of the initial gyro-period of the ion in the ambient field. This small time step provides satisfactory energy conservation, in most cases, and also adequately matches the analytical solutions of the bounce and drift periods. Larger time steps can be applied, but caution should be exercised by checking for conservation of energy and a match to the analytic solutions of Chapter II if one chooses to use a larger time set in a attempt to reduce the computational time of the simulation. Typically, the time step size used in the simulation for an ion is on the order of $1x10^{-3}$ or $1x10^{-4}$ s. The ions (fission fragments) are tracked using the Boris method until they beta decay or until they lose most of the initial kinetic energy due ionization energy losses. At this point, there are two options. 1) If the kinetic energy is lower than a user selected kinetic energy cutoff, the simulation stops tracking the ion and the next fragment from the input deck is initialized. 2) If the fission fragment beta decays, the new daughter of the fragment is given the velocity and location of the old fragment with a single increase in charge state. Eventually, the decay chain produces a daughter product that is a stable isotope and the simulation stops tracking the stable fragment because it will not contribute another beta particle (within reasonable time limits) and the next fragment from the input deck is initialized.

With each time step, the ion travels through a density of air that causes ionization energy losses and scattering described in Chapter IV. The energy loss is first calculated in order to determine the new velocity and energy of the fission fragment. After determining the energy loss, Monte-Carlo methods are applied to calculate the pitch angle scattering of the particle. The scattering routine causes a change in the velocity components, but does not change magnitude of the velocity.

The new pitch angle from scattering and the new energy from ionization energy losses are used to move the particle in the magnetic field by applying the Boris Push for the next time step. In this way, the particle is tracked in the magnetic field; the kinetic energy is reduced as the particle moves through the atmosphere; and the particles pitch angle changes due to either a large-angle scatter or multiple small-angle scatterings. This particle tracking methodology continues until all ion kinetic energy is lost, the tracking time exceeds some defined limit of time, a daughter of decay is stable, or the fission fragment beta decays.

When a beta decay occurs, we insert that beta into the list of fragments to be tracked. The beta decay electrons trajectories are primarily modeled using the guiding center approximation. As described in Chapter III, this method reduces the size of the time step for each calculation by three to five orders of magnitude. The typical time step used with the guiding center for the relativistic electrons is 1×10^{-3} or 1×10^{-4} s and is generally close to the time step used for the ions with the Boris push. Like the ions, the electrons experience energy loss and scattering with each time step. The method used to calculate the energy loss is similar to that of the ions and the pitch-angle scattering is almost identical to that of the ions. A new pitch angle is calculated using multiple small-angle scattering after each step and the energy of the electron is reduced as described in Chapter IV. The electrons can be tracked in the code until they reach some cut-off energy level below which they are no longer hazardous to satellites or of concern to the simulation. The default energy cut-off for the electrons is 40 keV, but can be set at any value. The iteration for tracking the electron continues for a length of time defined by the user or until the electron's kinetic energy falls below the cut-off value.

In some cases the Boris push is necessary to model the trajectory of the electrons. Typically this is done when the adiabatic invariants fail due to significant, rapid perturbations of the magnetic field used in the simulation. In the results presented here, the Boris push is only used when the electron is interacting with the detonation-perturbed magnetic field or magnetic bubble. When the magnetic bubble is included in the code, all three adiabatic invariants are violated and the Boris push is necessary for accurate tracking of the electrons. The typical time step used by the Boris push to track relativistic electrons is on the order of 1×10^{-7} or 1×10^{-8} s.

The ambient magnetic field used for the Boris push and guiding center approximation is described in Chapter V. The code determines a new magnetic field at each location for each time step by either interpolation or evaluation of the specified magnetic field. Changes to this specified magnetic field or time dependent perturbations to the magnetic field are easily included in the magnetic field subroutine. If more sophisticated magnetic fields were necessary or desirable then adding them would be quite simple.

The time at which the fission fragments beta decay and the energy of the beta is determined based on half-life probabilities and Monte Carlo methods. The half-lives of the fission fragments are generally well know and included in an input file for the simulation. The energy spectrum used for the beta decay is described in Chapter V.

The code is well suited for running on multiple processors. Each fission fragment and beta particle is tracked until the kinetic energy is reduced to a determined value, the fragment beta decays, or for a determined length of time. Once the model is completed for a fission fragment, decay daughters, and associated beta particles, the code advances to the next fission fragment from the input deck. For larger runs, the input deck for the fission fragments is divided into as many sub-decks as there are computers or processors available. The code can be run separately for each input file in order to model multiple charged particles. There is no requirement to exchange information between the different computers/processors so parallel processing is trivial.

7.2.   THE IMPORTANCE OF LONGITUDE AND LATITUDE

Does the longitude of the release of the fission fragments effect the trapping efficiency of the ions and electrons?

The "short answer" is that the proximity of the injection of particles to the South Atlantic Anomaly (SAA) has a significant effect on the number of ions and electrons that become trapped in low L-shell magnetic fields. In order to verify the "short answer" to the question, 10,000 fission fragments were released at four different longitudes with identical magnetic latitudes. The fission fragments and electrons were tracked for up to 3,000 seconds after the initial injection of fission fragments to insure that the average particle in the distribution could complete one orbit around the earth. A 2 MeV beta at L = 1.1 has a drift period of 2,100 s and a fission fragment of charge state +1 from Table 5.1.3 with a speed of 2,000 km/s has a drift period of 2,500 s. The four locations of release are shown in Figure 7.2.1 and include one near the SAA, one on the opposite side of the earth from the SAA, and then two 90 degrees away from the SAA generally along the magnetic equator.
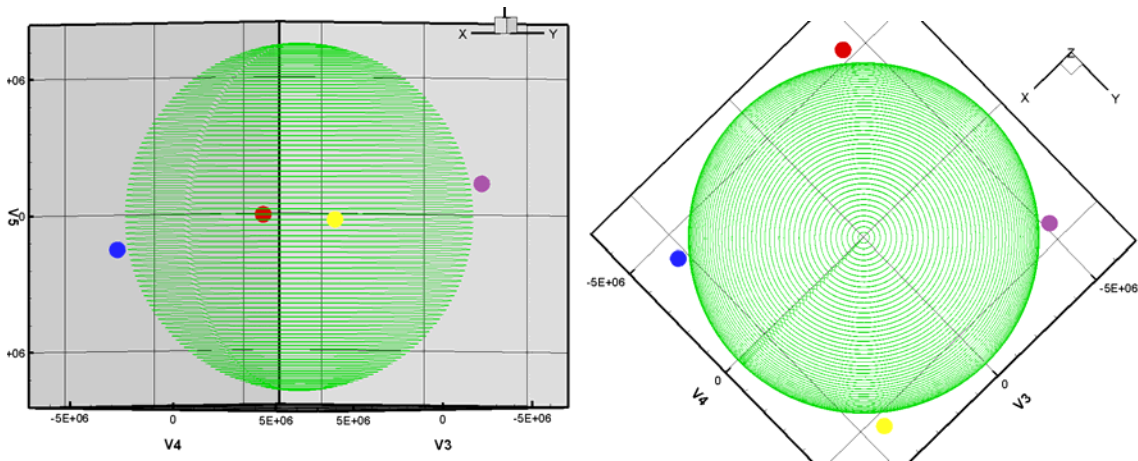
Figure 7.2.1: The blue dot, point 1, represents the location of the release of the fission fragments near the SAA. The purple dot, point 3, is the location opposite of the SAA. The yellow and red dots, point 2 and point 4, respectively, represent the release locations 90° away from the SAA. All release locations are in the vicinity of the magnetic equator.

150

The center of mass altitude of the particles release was 500 km above the surface of the earth. The particles were uniformly distributed in a sphere of radius 300 km. The velocity distribution was a Maxwell-Boltzman distribution with an average speed of 1,830 km/s as shown is Figure 7.2.2. Note, the Maxwell-Boltzmann distribution had some particles in the low speed tail of the distribution. These slow particles were not eliminated from the distribution, but because they have very low drift speeds and, reduced ionization energy losses, they are mentioned several times throughout the discussions as a source of an increase in the number of trapped particles as a function of time. This selected distribution is representative of an unclassified fission fragment velocity distribution. The fission fragments were given no initial preferred velocity and the average x, y, and z-components of the velocity was less than 10 m/s (center of mass velocity is basically zero.) The initial charge state of all of the fission fragments was selected as plus 2.

Maxwell-Boltzman Distribution of Initial Fission Fragment Speeds
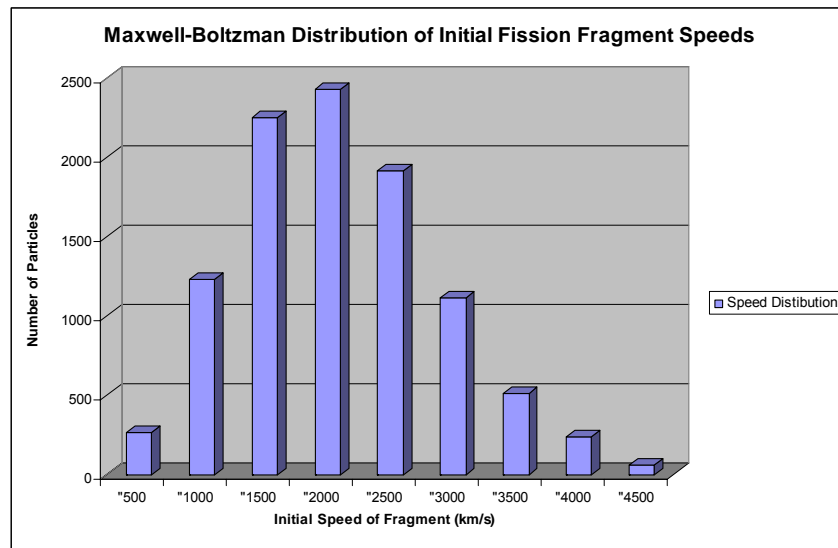
Figure 7.2.2: The Maxwell-Boltzman speed distribution of the fission fragments used to compare the trapping efficiency of fission fragments and beta-decay electrons. The low energy ions were kept in the simulation.

The fission fragment information for the simulations is shown in Table 5.1.3 and Table 7.2.1 presents the energy spectrum associated with the beta decay of the isotope. Recall that the actual beta energy spectrum is continuous, but for simplicity in modeling

the beta particles are given defined values for kinetic energy with an equal probability of a beta particle having one of the energies listed in Table 7.2.1. The fission fragments released at the beginning of each simulation have equal numbers of each of the six fission fragments.

As discussed in Chapter V, the typical end-point energy of the beta decay electrons is highest when the half-life is the shortest. The significance of the short half-lives of Rubidium-92, Krypton-92, and Bromine-92 is an early release of energetic betas. The ions with longer half-lives typically disperse away from the burst location before beta decay. Recall also the drift velocity of the guiding center of a charged particle, as shown in equation 1.2.3.1, $\vec{W}_{Drift} = \dfrac{m}{qB^2}\left(v_{\parallel}^2 + \dfrac{v_{\perp}^2}{2}\right)\vec{B} \times \nabla\left(\dfrac{B^2}{2}\right)$, is dependent on the kinetic energy of the particle. The most energetic betas injected soon after the release of the fission fragments will also disperse quickly away from the burst location and drift rapidly around the earth in an eastward direction. Additionally, as shown in the 10,000 particle summary in Table 7.2.2, for an initial distribution of ions (half of the ions are released at altitudes less than 500 km), only 60% of the fragments remain trapped after the first second and less than 25% remain trapped after the first 10 seconds. The primary cause of this rapid loss of ions is a large loss cone and the resulting interaction with the atmosphere causing significant ionization energy losses of the ion. The effect of the initial pitch angle and loss cone will be discussed in detail in Section 7.6.

If the fission fragment is an isotope with a short half-life, there is a high probability that the fission fragment will beta decay before the fragment's kinetic energy is lost in the atmosphere. Although the beta particle has no preferred direction, the initial electron velocity and location of the beta decay are factors in the probability of trapping of the released beta particle. The specific effect of the decay lifetimes are discussed in Section 7.4, but one expects that the number of trapped electron will increase with the number of injected electrons from beta decay.

Element	Simulation #	Half-life (s)	Beta Decay Daughter	Beta Energy Spectrum (eV)
Zr-92	1	1.00E+20	Stable	N/A
Y-92	2	12744	Zr-92	249.35, 401.97, 487.87, 661.41
				782.27, 903.24, 1012.1, 1145.64
				1154.27, 1366.46, 1530.27, 1656.4
				1789.67, 1939.69, 2090.27, 2251.26
				2413.27, 2608.1, 2880.79
Sr-92	3	9756	Y-92	19.606, 35.65, 51.70, 67.76, 83.81
				99.86, 115.91, 131.96, 148.82
				166.07, 183.35, 192.79, 220.38
				240.56, 257.33, 285.32, 315.29
				347.79, 392.08, 1025.2
Rb-92	4	4.492	Sr-92	1900, 3000, 4000, 5000,7500
Kr-92	5	1.84	Rb-92	1200, 1800, 2400, 3600, 5000
Br-92	6	0.365	Kr-92	2480, 3420, 4050, 4700, 5300
				6000, 6600, 7500, 8400, 11205

Table 7.2.1:   The fission fragment beta decay information used in the simulation is shown above. For each of the isotopes, the beta has an equal probability of one of the listed energies.[136] The energy spectrum shown is described in Chapter V and represents the beta energies of the decay of the fission fragments.

The location of the release of the fission fragments clearly affects the number of ions and electrons that become trapped as a function of time. Table 7.2.2 suggest that as the fission fragments drift toward the SAA and the conjugate points become lower in altitude, many of the fragments are lost due to increased interactions with the atmosphere. Likewise, fewer fission fragments are lost as the particles drift away from the SAA. The results presented in Table 7.2.2 show that ions and electrons, while moving away from the SAA, generally have a higher trapping initial efficiency than those particles that moving toward the SAA. At the altitudes of release of the particles represented above, particles released very near to the SAA have the highest probability of remaining trapped after one complete orbit around the earth. Particles, both ions and betas, released opposite the SAA have an extremely low probability of remaining trapped after one complete orbit around the earth unless the particle has very low speeds. From equation 4.3.2.1, the energy lost per distance traveled is shown to be proportional to the speed of the particle. If the speed is low then the fission fragment will not only drift slowly, but the energy loss will be significantly reduced due to the reduced interactivity with the atmosphere at low

---

[136] Tom Thomson (LLNL), private conversation with author, 11 October 2006.

speeds. At very low speeds, the energy loss per unit length traveled becomes exceedingly small and the particle still requires multiple interactions with the atmosphere before all of the kinetic energy is lost. Generally, ions that remain trapped as they pass the SAA will continue to remain trapped as they move away from the SAA. Therefore ions injected near the SAA with pitch angles outside the loss cone remain trapped in the radiation belts as they drift around the earth.

	Point 1: Long 38W and Lat 9S (Near SAA)			point 3: Long 142E and Lat 9N (opposite SAA)	
Time (s)	# of betas trapped	# of ions trapped		# of betas trapped	# of ions trapped
1	482	6156		495	5998
10	1359	2326		1384	2107
100	519	820		507	752
500	458	328		12	84
1000	402	273		4	24
3000	227	179		0	18
	Point 2: Long 52E and Lat 0 (East of SAA)			point 4: Long 232E and Lat 0 (West of SAA)	
Time (s)	# of betas trapped	# of ions trapped		# of betas trapped	# of ions trapped
1	470	6002		476	5945
10	1558	2241		1456	2217
100	908	779		205	1186
500	693	52		7	686
1000	216	19		13	438
3000	4	5		1	48

Table 7.2.2: The results from the release of 10,000 fission fragments at four different locations are shown above. Point 1 represents a location near the SAA. Point 3 represents a point on the opposite side of the earth from the SAA. Points 2 and 4, respectively, represent locations 90 degrees to the east and west of the SAA.

Likewise, betas that are trapped away from the SAA and then drift back toward the SAA are generally lost as the betas approach the SAA. Figures 7.2.3 through 7.2.10 present the location of fission fragments and beta particles 500 s after the fission fragments were released. Figures 7.2.3 and 7.2.4 show the location of the ions and beta decay electrons 500 s after the release of the fission fragments near the SAA. Even

though the altitude is relatively low, many of the ions remain trapped after 500 s because the release location is near the South Atlantic Anomaly (SAA) and they are drifting away from the SAA. Additionally, the electrons also have a higher trapping efficiency when the fission fragments are released near the SAA, especially the early-time decay betas, because they quickly drift away from the SAA and their orbits move away from the atmosphere. The optimal location of release for long-term trapping of ions and electrons is shown to be near the SAA.
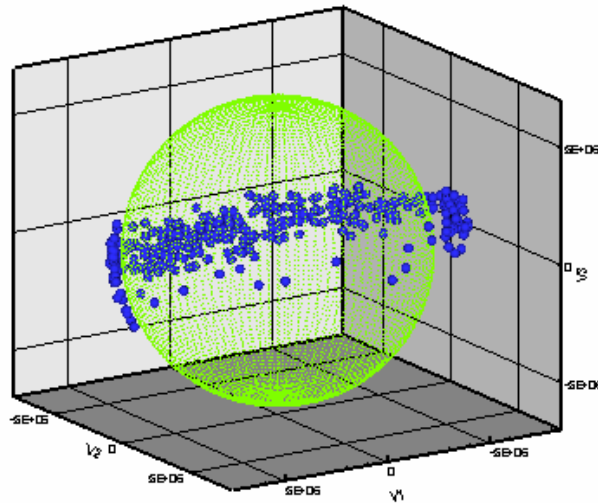
Figure 7.2.3: This plot presents the location of the ions at 500 s after release from point 1, near the SAA. All of the ions are initially moving away from the SAA and the conjugate points are generally increasing in altitude so the energy loss rate of the ions is decreasing as the ion drifts toward the opposite side of the earth.
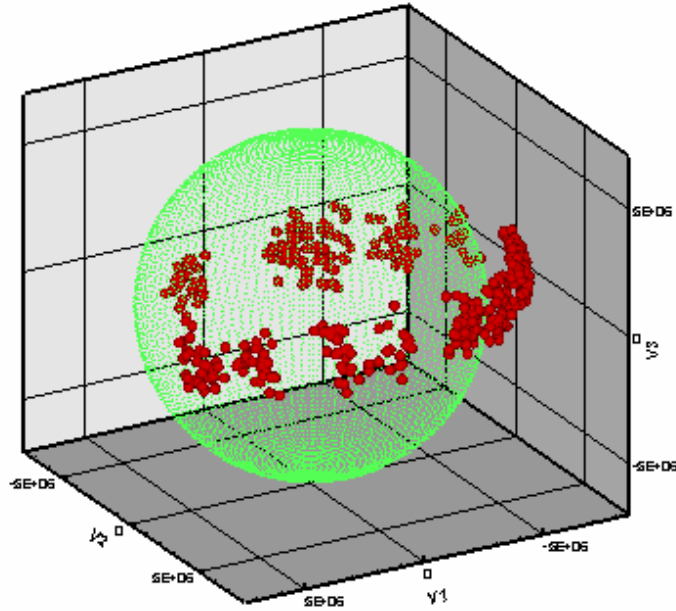
Figure 7.2.4: This plot presents the location of betas at 500 s after the ions are released from point 1, near the SAA. The betas are from the beta decay of the fission fragments. The beta decay spectrum used is shown in Table 7.2.1. The bunching of the betas is a result of the discrete energies of the electron resulting from beta decay spectrum used in the simulation. If a continuous spectrum were used then the betas would be more dispersed in space.

Figures 7.2.5 and 7.2.6 present the location of ions and electrons 500 s after a release of fission fragments 90° east of the SAA. Except for the ions with very low drift velocities and pitch angles near 90°, most of the ions are lost in the atmosphere as they drift toward the SAA because they mirror lower in the atmosphere as they approach the SAA. The electrons in Figure 7.2.6 drift away from the SAA and remain trapped until they approach the SAA from the west where most are "scrapped off" near the SAA.

156
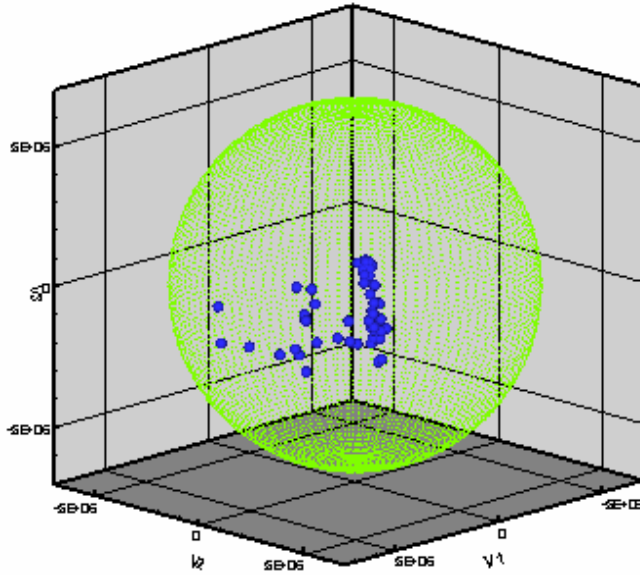
Figure 7.2.5: This plot presents the location of ions at 500 s after release from point 2, 90 degrees east of the SAA. The ions are drifting toward the SAA and the conjugate point is decreasing in altitude. As the atmospheric density increases with a decrease in altitude, the energy loss increases and the ions eventually lose all kinetic energy.
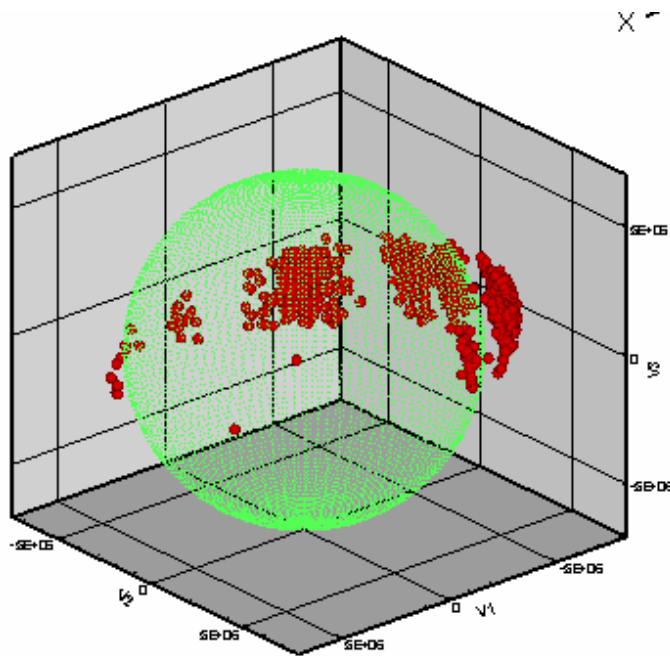
Figure 7.2.6: This plot presents the location of betas at 500 s after release from point 2, 90 degrees east of the SAA. The early-time betas drift away from the SAA and many remain trapped after 500 s, but are generally "lost" as they approach the SAA.

Figures 7.2.7 and 7.2.8 present the location of the ions and electrons 500 s after release at a point 180^0 away from the SAA. The ions and electrons are quickly lost in the atmosphere as they both quickly drift toward the SAA. Only the ions with low drift velocities and steep pitch angles remain after 500 s. Very few of the electrons remain trapped after 500 s. The optimal location for minimizing the trapping of charged particles is 180° away from the SAA.
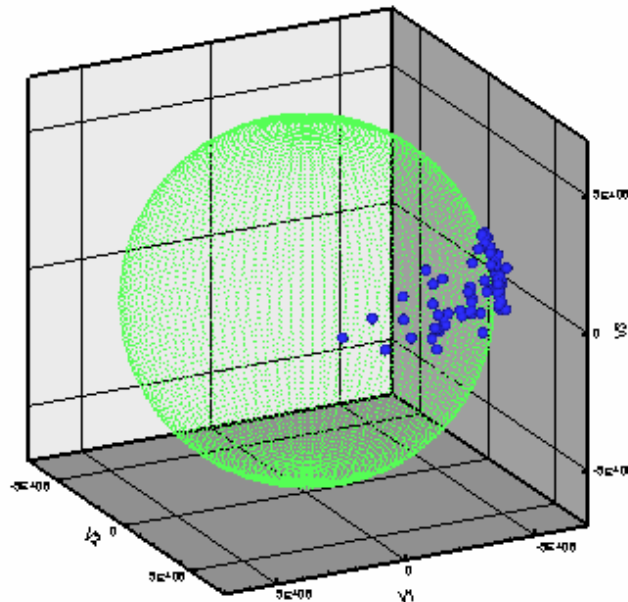
Figure 7.2.7: This plot presents the location of ions at 500 s after release from point 3, opposite of the SAA. The ions drift toward the SAA resulting in the loss of many of the ions.
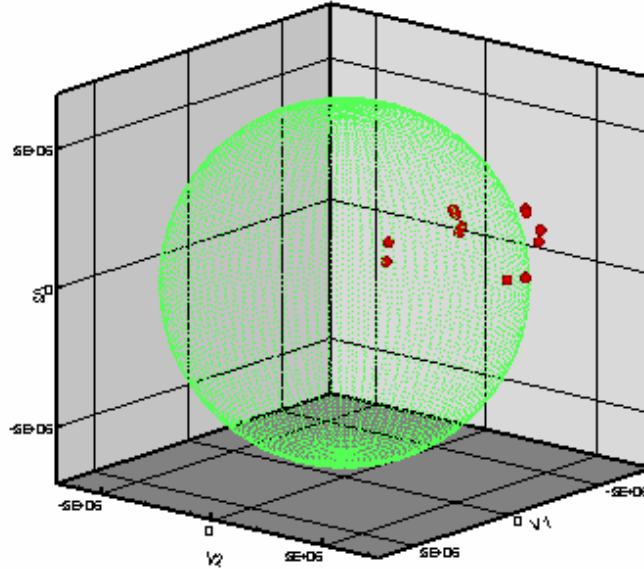
Figure 7.2.8: **This plot presents the location of betas at 500 s after release from point 3, opposite of the SAA. There are clearly not many betas remaining trapped after 500 s. Although, the data from Table 7.2.2 indicates that at 100 s there are roughly as many betas remaining released from point 3 as there were from those released at the other points, by 500 seconds most of the betas are lost because they are drifting toward the SAA and mirroring lower into the atmosphere.**

Finally, Figures 7.2.9 and 7.2.10 present the location of ions and electrons from a release of fission fragments 90° to the west of the SAA. The ions, because they drift immediately away from the SAA, have a higher trapping efficiency, until they approach the SAA from the east. The electrons, especially those from early-time beta decay, are quickly lost as they drift back toward the SAA. The only betas remaining trapped at 500 s are those released from late-time beta decay hundreds of seconds after the release. For the beta to remain trapped at 500 s, the ion has drifted away from the SAA and the beta decay electrons have not yet been lost at 500 s because they are still far away from the SAA.
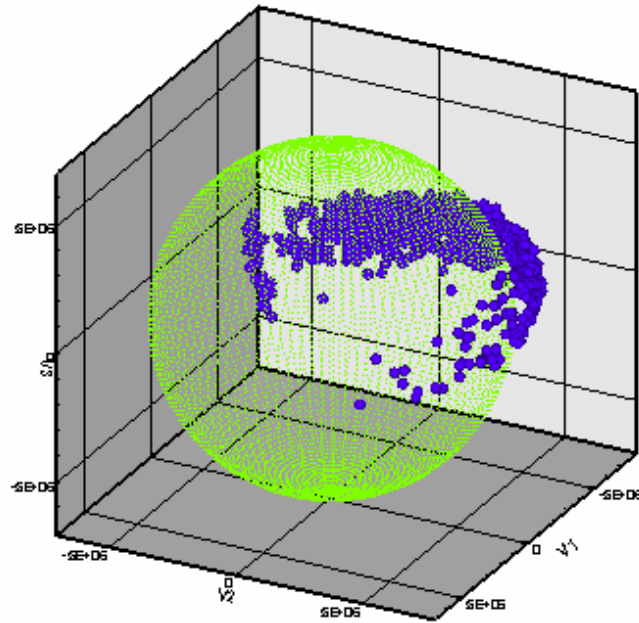
Figure 7.2.9: This plot presents the location of ions at 500 s after release from point 4, 90 degrees west of the SAA. Because the ions initially drifted away from the SAA, many of the ions are still trapped at 500 s. However, as the ions begin to drift back toward the SAA most of the ions are lost.
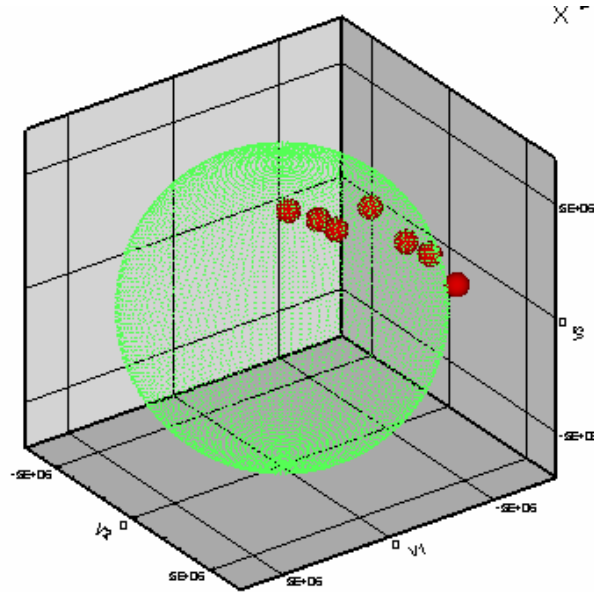
Figure 7.2.10: This plot presents the location of betas at 500 s after release from point 4, 90 degrees west of the SAA. The early-time decay betas were all lost as they drifted toward the SAA and the late-time betas eventually drifted back toward the SAA resulting in few trapped betas.

160

The optimal location of release in order to minimize the long-term trapping of particles is 180 degrees away from the SAA. For a given L-shell, the long-term trapping efficiency of ions and electrons increases as the location of release of particles becomes closer to the SAA. The particles that remain trapped after one complete orbit continue to lose kinetic energy and scatter due to atmospheric interaction during each approach to the SAA, but have pitch angles such that the atmospheric interaction is minimized. If the particles are tracked long enough then all would eventually lose kinetic energy due to the atmospheric interactions.

Further evidence of the significance of the proximity of the initial release to the SAA is shown in Figures 7.2.11 through 7.2.14. In these plots, the only initial release location that allows for a dispersion of the ions around the entire earth is the point near the SAA as shown in Figure 7.2.11. In Figure 7.2.11, the ions are injected into orbits that allow the particles to survive near the SAA and mirror at higher altitudes away from the SAA. The electrons from beta decay are released into similar orbits. In the other three plots (7.2.12, 7.2.13, and 7.2.14) at the other three points, the only ions remaining trapped after 3,000 seconds are those ions with very low initial kinetic energies and low drift velocities. The electrons from beta decay released at points 2, 3, and 4 will also lose a substantial amount of kinetic energy as they pass near the SAA. Eventually, the slower ions of point 2, 3, and 4 will pass near the SAA and will most likely be lost in the atmosphere.
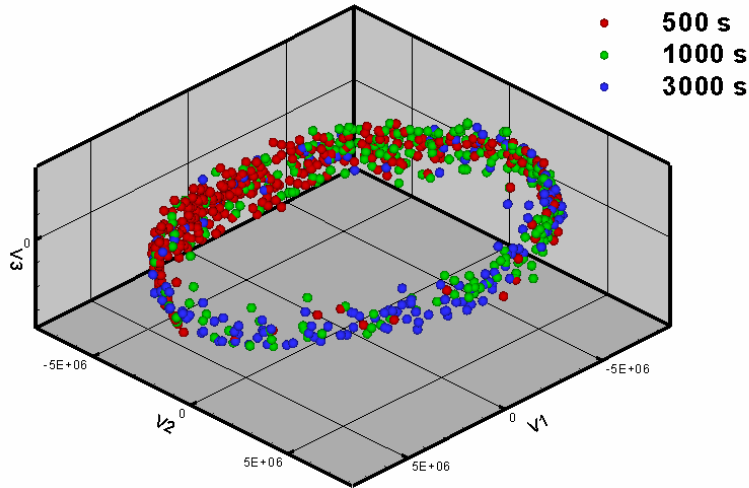
Figure 7.2.11: This presents the location of the fission fragments at 500 s, 1,000 s, and 3,000 s after release at point 1, near the SAA. The plot shows the fission fragments dispersed around the earth.
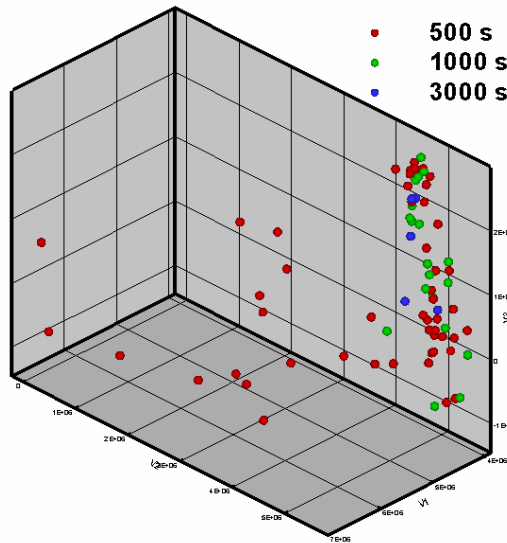
Figure 7.2.12: This presents the location of the fission fragments at 500 s, 1,000 s, and 3,000 s after release at point 2, 90 degrees east of the SAA. The plot shows that only the very low energy fragments with very small drift speeds survive, again due to the reduced interactivity with the atmosphere at low speed. These fragments are lost when they drift near the SAA. Note that the only fragments remaining trapped after 1,000 s and 3,000 s are those fragments with minimal drift velocities and kinetic energies.

162
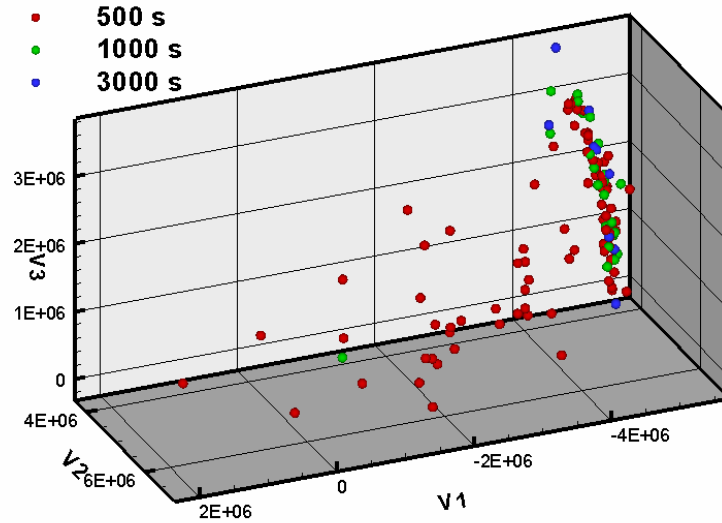
Figure 7.2.13: This presents the location of the fission fragments at 500 s, 1,000 s, and 3,000 s after release at point 3, opposite of the SAA. The plot shows that only the very low energy fragments with very little dE/dx interaction survive after 1,000 seconds. These fragments are lost only when they drift near the SAA and mirror much lower in the atmosphere.
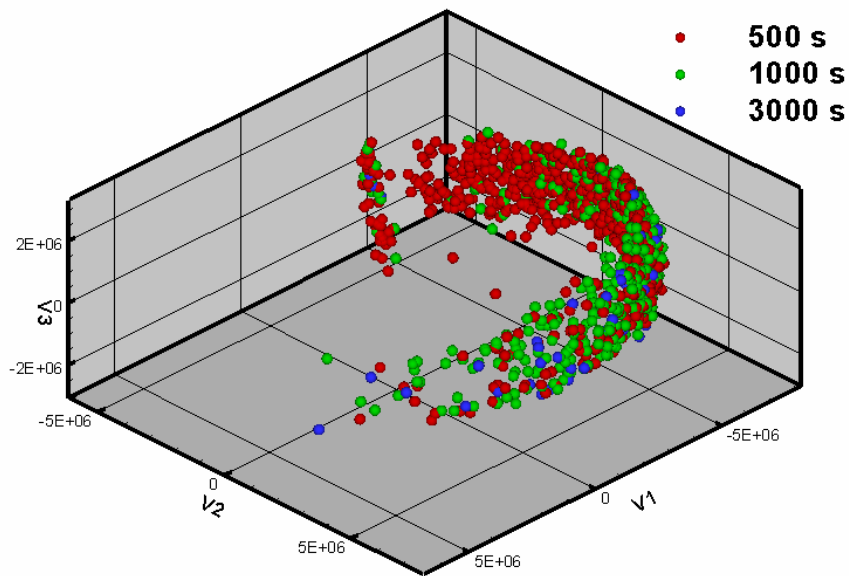
Figure 7.2.14: This plot presents the location of the fission fragments at 500 s, 1,000 s, and 3,000 s after release at point 4, 90 degrees west of the SAA. Here the fragments remain trapped until they approach the SAA from the east

163

Given the altitude distribution of the fission fragments released at the four locations described above, the optimal release location for increasing the trapping efficiency of the fission fragments and electrons is near the SAA. The charged particle's mirroring altitude is always lowest at the SAA. An important observation is that, without significant pitch angle scattering, particles trapped in the vicinity of the SAA will remain trapped as they move away from the SAA.

What affect does latitude have on the trapping efficiency?

Table 7.2.3 shows the data from the release of 2,500 fission fragment at a longitude of 232E and at two different latitudes separated by 16°. The initial conditions of the particles (altitude, velocity, isotope, and position distribution) are identical to the distribution and altitude described above for the longitude comparison. The first latitude is at geomagnetic equator (0°) and the second latitude is 16N. The results show that at a given longitude, the number of fission fragments and betas trapped increase with the latitude of the injection. At one second, the number of trapped particles is generally the same for each location, but as time increases fewer of the particles released at the geographic equator remain trapped. The fragments from the 16N release spend less time in the atmosphere because their orbit is in a higher L-shell (L = 1.07 vs. L = 1.11). The reduced amount of time interacting with the atmosphere minimizes the ionization energy loss and pitch angle scattering of the fission fragment and increases the trapping lifetime of the particle. In addition to spending more time at higher altitudes, the particles in the higher L-shell also have a smaller loss cone.

Time (s)	Long 232E and Lat 0			Long 232E and Lat 16N	
	# of betas trapped	# of ions trapped		# of betas trapped	# of ions trapped
1	126	1472		154	1451
10	381	540		639	688
100	56	269		465	384
500	5	158		279	279
1000	2	101		262	192
3000	1	11		238	48

Table 7.2.3:   The table presents the results of the release of 2,500 fission fragments at a center of mass altitude of 500 km at a longitude of 232E and two different latitudes. There is a noticeable increase in the trapping of the fission fragments and a significant increase in the number of trapped betas for the injection at higher latitudes.

Recall that the magnetic field at the mirror point is related to the pitch angle and magnetic field by equation 1.1.33

$$B_{mirror} = \frac{B_0}{Sin^2(\alpha_0)}.$$

The values for the components of the magnetic field, in spherical coordinates are:

(7.2.1) $$B_r = -\frac{\mu_0 M}{2\pi} \frac{Sin(\lambda)}{r^3}$$

(7.2.2) $$B_\lambda = -\frac{\mu_0 M}{4\pi} \frac{Cos(\lambda)}{r^3}$$

(7.2.3) $$B_\varphi = 0$$

where λ is the angle above the magnetic equator. The value of the magnitude of the magnetic field at the equator, $B_{0\text{-mag}}$, is given by

(7.2.4) $$B_{0-mag} = \sqrt{B_\lambda^2 + B_r^2} = \frac{\mu_0 M}{4\pi r_0^{\,3}}.$$

By selecting the minimum value of B_{mirror} as the lowest point at which the particle can mirror without quickly losing all kinetic energy (generally around 100 km in altitude), the value of the critical angle of the loss cone below which all particles are lost in the atmosphere becomes

(7.2.5) $$\alpha_{0-min} = ArcSin(\sqrt{\frac{\mu_0 M}{4\pi r_0^{\,3} B_{mirror}}})$$

Figure 7.2.13 shows the loss cone angle as a function of L-shell. The loss cone becomes smaller as the L-shell increases and therefore, the more of the particles injected at the higher latitude will become trapped.
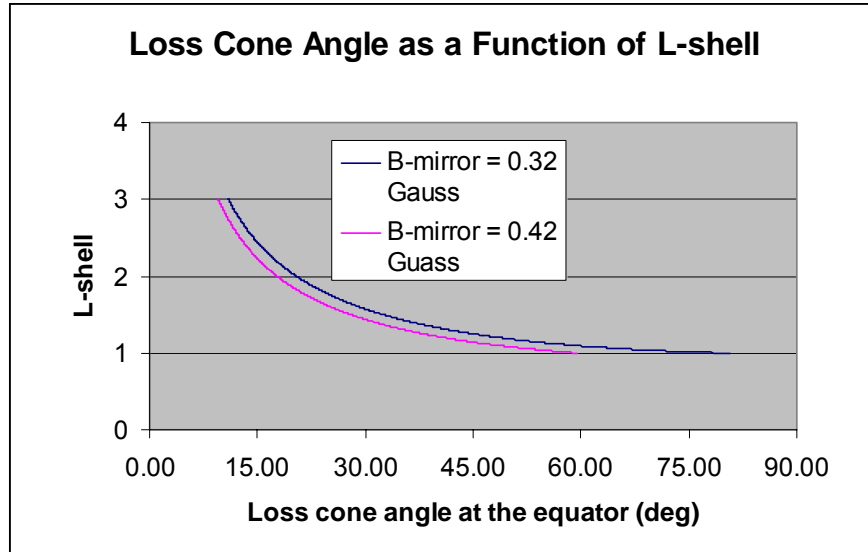
Figure 7.2.13: The loss cone becomes smaller as the L-shell of the trapped particle increases. Particles injected into higher L-shells have smaller loss cones resulting in an increase in trapping efficiency of the particles.

The release of fission fragments into a higher L-shell leads to an increase in the trapping efficiency of the electrons. For the most part, all of the fission fragments with relatively small pitch angles and with velocities directed generally along the magnetic field lines are lost in the atmosphere soon after the release. However, a fission fragment that moves toward higher altitudes may beta decay along the field line path between the two conjugate points. Although the initial velocity of the beta particle has no preferred direction, the altitude and L-shell of the electron do affect the probability of trapping of the electron.

Recall from equation 1.3.1.9 that the expression for the loss cone was

$\alpha_{0-min} = Sin^{-1}(\sqrt{\frac{B_0}{B_{max}}})$ where B_{max} is the magnitude of the magnetic field at the

conjugate point. For a particle trapped on an L-shell, the value of B_{max} remains constant. As the L-shell and altitude at the equator increases B_0 decreases $\sim 1/r^3$ so the loss cone angle α_{0-min} also decreases as shown in Figure 7.2.13. The result of a smaller loss cone is that more of the beta decay electrons are trapped in the magnetic field. Therefore, in general, the number of beta particles trapped increases with an increase in the L-shell.

(Recall that the focus of this study is on particles trapped in L-shells less than 1.5 so applying this statement to higher L-shells is may not valid for late time analysis due to other scattering and loss mechanisms.)

Figure 7.2.14 shows the location of the latitude 16N electrons 3,000 s after the initial release of 2,500 ions. Many of these electrons drifted past the SAA without loss because they were trapped at higher L-shells and altitudes. Figure 7.2.14 also shows that the electrons are dispersed around the earth. Only one of the zero latitude electrons remains in orbit after 3,000 s. As shown in Figure 7.2.15, after 100 s, there are roughly nine times as many electrons from the higher latitude release when compared with the zero latitude release. The electrons released at the higher latitude have a higher trapping efficiency, they are more dispersed, and they will survive much longer in the radiation belts.

The longitude and latitude of the fission fragment release are both key parameters when determining the trapping efficiency and "belt-pumping" environment caused by a release of fission fragments. A general rule of thumb is that to increase the trapping efficiency of ions and the beta decay electron, the fission fragments should be injected close to the SAA and at higher L-shells. Knowing the location of the burst does not completely specify the problem but, clearly, locations matters.
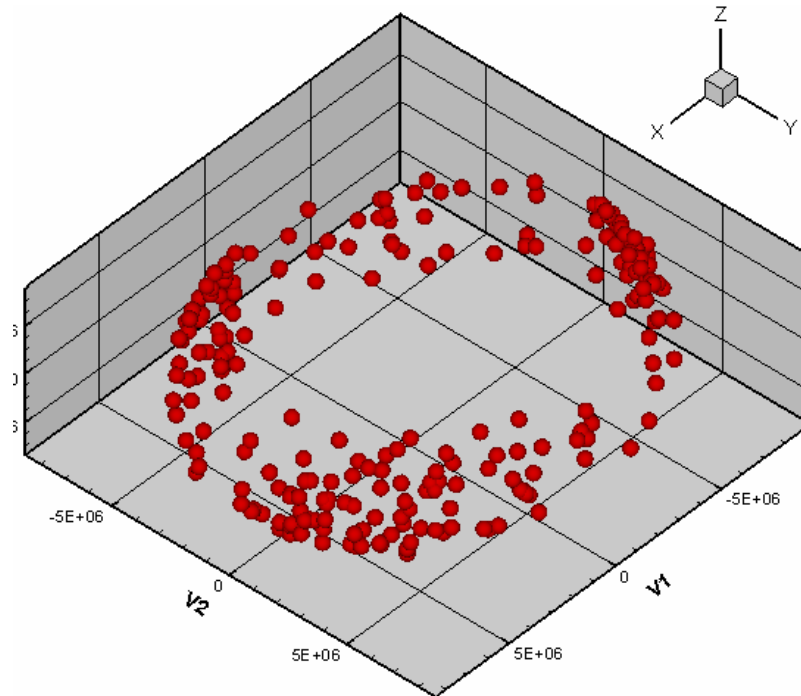
Figure 7.2.14: This figure presents the location of 238 beta decay electrons 3,000 seconds after the fission fragments were injected at a longitude of 232E and latitude of 16N. After 3,000 seconds there is only about 10% of the initial number of ions.
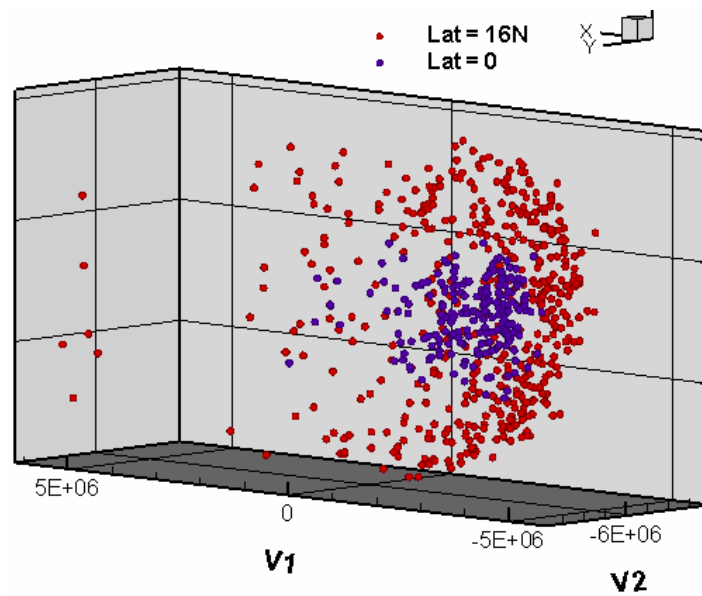
Figure 7.2.15: The figure presents the location of the beta decay electrons 100 s after the fission fragments were released at a longitude of 232E and the two different latitudes as shown in the figure. Because of the different latitudes of injection there were almost nine times as many electrons from the release at higher latitude. Not only are there more of the 16N electrons, but the higher latitude electrons are more widely dispersed.

7.3. THE IMPORTANCE OF ALTITUDE

Does altitude matter?

From the argument presented in Section 7.2 about the loss cone angle dependence on L-shell one would expect that if particles were injected into the magnetic field at identical longitudes and latitudes, but at different altitudes (L-shells) then the particles injected at the highest altitude would have the highest trapping efficiencies for ions and beta electrons. In order to validate the analytic prediction of the effect of the initial L-shell on the release presented in Section 7.2, 10,000 particles with initial conditions identical to those presented in Section 7.2 were released at a longitude of 142E and latitude of 9N (opposite of the SAA) at 500 km, 1,000 km, 1,500 km, and 2,000 km (recall that the radius of the earth is 6375 km). The location of injection was chosen because the results of the effect of longitude from Section 7.2 suggest that the long-time trapping efficiency for electrons and fission fragments is lowest at locations opposite of the SAA and particles released at an altitude of 500 km are lost before one orbit around the earth. The ions were tracked for 3,000 s and the electrons were tracked for 1,000 s of the simulation time. Table 7.2.1 presents the results of the simulation. The data confirms that the trapping efficiency increases with altitude. The loss cone is smaller for the particles in higher L-shells and the sheer number of trapped ions increases the number of betas injected into the field.

Figures 7.3.1 and 7.3.2 present the location of the ions released from the four different release altitudes at 1,000 s after injection. None of the ions released at 500 km or 1,000 km make it past the SAA, but large numbers of the ions from 1,500 km and 2,000 km drift past the SAA and remain trapped. Figure 7.3.3 shows the location of the electrons from 1,000, 1,500, and 2,000 km release altitudes at 1,000 s after injection. The number of electrons trapped increases, like the ions, as the altitude of release increases (and the loss cone becomes smaller.)

169

	500 km HOB			1000 km HOB	
Time (s)	# of betas trapped	# of ions trapped		# of betas trapped	# of ions trapped
1	495	5998		732	6204
10	1384	2107		2223	2544
100	469	752		1834	1966
500	4	84		476	1711
1000	2	24		34	961
3000	na	9		na	135
	1500 km HOB			2000 km HOB	
Time (s)	# of betas trapped	# of ions trapped			
1	783	6265		987	6129
10	2708	2672		3182	2670
100	2437	2239		3143	2352
500	1605	2170		2476	2266
1000	987	1946		2138	2118
3000	na	1011		na	1984

Table 7.3.1: The results are shown from releasing 10,000 particles at 142E and 9N and four different altitudes. The data indicates that ions injected into higher L-shells have higher trapping efficiencies for the fission fragments and larger numbers of electrons trapped in the magnetic field. The loss cone is smaller for higher L-shells and the atmospheric interactions are reduced.
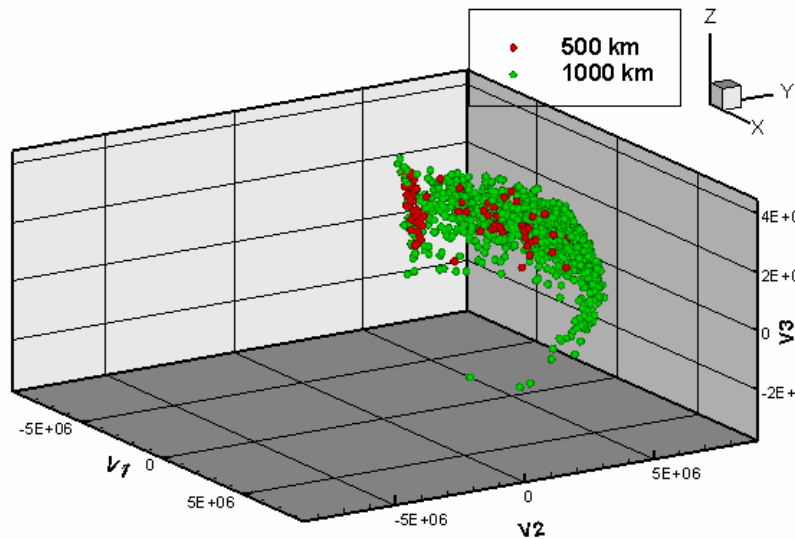
Figure 7.3.1: The locations of the ions 1,000 s after injection are plotted for injection altitudes centered on 500 km and 1,000 km. After 1,000 s none of the ions have been able to drift past the SAA.
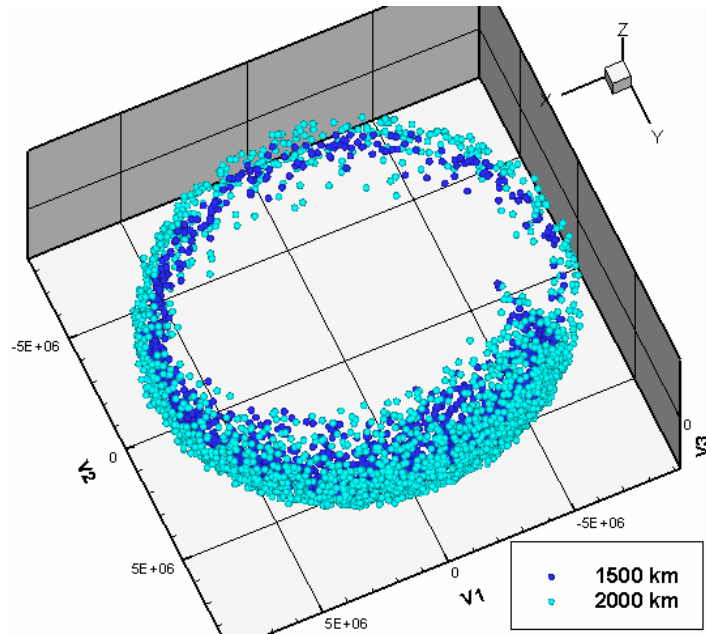
Figure 7.3.2: **The locations of the ions 1,000 s after injection are plotted for injection altitudes centered on 1,500 km and 2,000 km. After 1,000 the ions are dispersed around the earth and many drift past the SAA and remain trapped.**
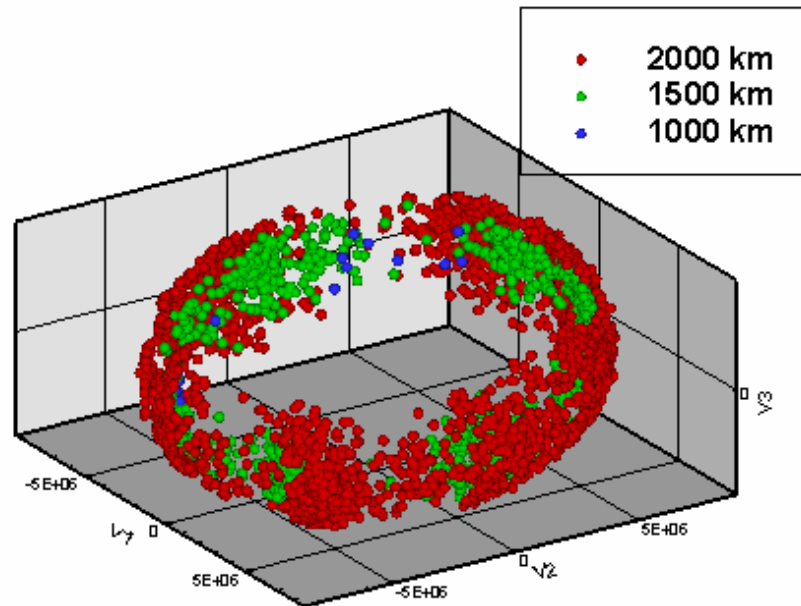
Figure 7.3.3: **The location of the electrons 1,000 s after the release of the ions at three of the four different altitudes. There were only two electrons remaining from the release of fission fragments at 500 km. Like the ions, the electrons from the 1,500-km and 2,000-km release altitude are dispersed around the earth and not experiencing major losses at the SAA.**

171

7.4. CHARGE STATE MATTERS

Another parameter that affects the trapping of the fission fragments, and eventually, the number of trapped electrons is the initial charge state of the fission fragments. Estimates on the charge state of the debris normally range from +1 up to complete ionization of the fission fragment. Although there are most likely also some neutral fragments, a majority of the fission fragments are ionized. The charge state associated with an atomic mass, normally referred to as the total charge divided by the mass, (q/m), is inversely proportional to the gyro-radius of the charged particle spiraling around the direction of the magnetic field. The q/m also affects the drift velocity of the fission fragment. Both the gyro-radius and drift velocity of the fission fragment matter when predicting the trapping of ions and subsequent electrons.

7.4.1. Charge State Affects the Gyro-Radius of the Ions and Trapping Efficiency

Recall from equation 1.1.19 that the gyro-radius, r_c, of a charged particle in a magnetic field is $r_c = \dfrac{\gamma m}{q} \dfrac{v_\perp}{B}$. The value for q for the ion is defined as the total charge of the ion. If the ion is neutral then $q = 0$ and if the ion has 15 more protons than electrons then the total charge is 15 times the charge of a single proton. For a fission fragment with a given mass, the value for r_c decreases as the charge state of the fragment increase. For example, a Xe^{140} atom with a speed of 2,000 km/s and charge state of +1 located 400 km above the earth's equator has a gyro-radius of 150 km. If the charge state of the Xe^{140} atom is +10 then the gyro-radius is 15 km. The gyro-radius of a 2-MeV electron, with a mass that is on the order of $2.6x10^5$ smaller than the mass of Xe^{140}, is around 200 m. As a trapped, charged particle spirals around the magnetic field lines and travels from conjugate point to conjugate point, a particle with a large gyro-radius will travel deeper into the atmosphere, because of the large gyro-radius, and through an atmosphere with a higher density. The energy loss and the scattering are both proportional to the density of the air. The difference in the density of air at 400 km compared to 250 km is almost two-orders of magnitude so the fission fragment would lose 100 times more energy in atmosphere at 250 km than it would in atmosphere at 400 km for identical particles and

distances traveled. Additionally, from Section 4.4, the probability of a large angle scatter and significant pitch angle change of the fragment is also proportional to the density of the air.

The data in Table 7.4.1.1 suggest that the charge state of the fission fragment does make a difference in the trapping efficiency of the electrons and fission fragments. The data in Table 7.4.1.1 might convince one that when two fragments have identical initial conditions (mass, location, and velocity), but different charge states, the fragments with the lowest charge state have the lowest trapping efficiency because of an increase in ionization energy loss. The fission fragments with a larger gyro-radius and lower charge state appear from the data to lose the kinetic energy the quickest. However, as is shown in Section 7.4.2, the charge state of the ions also affects the drift velocity of the charged particle which also has a competing effect on the trapping efficiency of the ions.

Time after release (s)	Particle	# of particles remaining for initial CS1	# of particles remaining for initial CS3	# of particles remaining for initial CS8	# of particles remaining for initial CS15
1	Beta	2868	3006	2944	2837
10	Beta	8396	9389	10674	11916
100	Beta	5196	5546	5996	6396
500	Beta	3981	4199	4523	4909
1000	Beta	1345	1278	1384	1532
1	Fission Frag	33811	36013	37601	38619
10	Fission Frag	12321	14645	17417	20183
100	Fission Frag	4679	4476	4334	5277
500	Fission Frag	295	355	665	1114
1000	Fission Frag	93	146	335	643
3000	Fission Frag	20	33	87	211

Table 7.4.1.1: This table presents the results of 60,000 fission fragments injected at a longitude of 52E and 0N with the velocity, position, and fragment distribution described in Section 7.2. The data represents the number of each of the particles remaining trapped at different times. The fission fragments with a higher charge state have a higher trapping efficiency. The number of trapped betas also increases with an increase in the charges state of the fission fragment. CS is charge state of the particle.

7.4.2. Charge State Affects the Drift Velocity and Trapping Efficiency

The drift velocity of the guiding center of the particle was derived in Section 1.2.3. An expression for the drift velocity of the guiding center, equation 1.2.3.1, is $\vec{W}_{Drift} = \dfrac{m}{qB^2}\left(v_{\parallel}^2 + \dfrac{v_{\perp}^2}{2}\right)\vec{B} \times \nabla\left(\dfrac{B^2}{2}\right)$. The magnitude of the drift velocity is dependent on the ratio of m/q. As the charge state of the particle increases the drift speed decreases. As the guiding center speed decreases, the particles disperse less rapidly from the initial release location and take longer to orbit the earth. If, as is shown in the data in Table 7.4.2.1, the charged particles are injected into the belts near the SAA, the fission fragments with a higher charge state have a lower trapping efficiency. This is not consistent with the results presented in Table 7.4.1.1, where particles with higher charge states had higher trapping efficiencies and the release was away from the SAA.

The difference in trapping efficiency of the two different locations is partially a result of the release proximity to the SAA. For the particles released near the SAA, the ones with lower charge states drift rapidly away from the SAA. As the particle drifts away from the SAA, the mirror point increases in altitude. As discussed, a higher altitude for the mirror point results in less atmospheric interaction and less corresponding ionization energy losses and scattering. On the other hand, the ions with a higher charge state drift less rapidly away from the SAA and spend more time mirroring near the SAA where the mirror point is the lowest. The actual difference in the drift velocity is related by a ratio of the charges of the ions. For example, a charge state 15 would have 1/15th of the drift velocity of an identical charge state 1 particle. The mirror point is lowest in altitude near the SAA and therefore the particles with a low drift speed spend more time mirroring at lower altitudes resulting in rapid ionization energy losses.

Time after release (s)	Particle	# of particles remaining for initial CS1	# of particles remaining for initial CS3	# of particles remaining for initial CS8	# of particles remaining for initial CS15
1	Beta	513	492	504	533
10	Beta	1316	1499	1673	1899
100	Beta	521	493	570	603
500	Beta	484	433	510	527
1000	Beta	417	364	437	446
1	Fission Fragment	5489	6277	6453	6436
10	Fission Fragment	1988	2385	2990	3224
100	Fission Fragment	944	771	706	856
500	Fission Fragment	516	232	125	141
1000	Fission Fragment	465	171	63	64
3000	Fission Fragment	299	104	28	14

Table 7.4.2.1: This table presents the results of 10,000 fission fragments injected at a longitude of 38E and 9S with the velocity, position, and fragment distribution described in Section 7.2. The data represents the number of each of the particles remaining trapped at different times. Unlike the Table 7.4.1.1, the fission fragments with a lower charge state have a higher trapping efficiency at later times.

The fission fragment data of Table 7.4.2.1 is similar to the data in Table 7.4.1.1 for the first 10 seconds. In both cases the trapping efficiency of the higher charge state is greatest for the largest charge state due to a smaller gyro-radius as explained in Section 7.4.1. However, for times greater than 100 s, the trapping efficiency of the smaller charge state particles (released near the SAA) becomes greatest because the particles are rapidly drifting away from the SAA and mirroring at higher altitudes. This observation was not obvious from the data in Table 7.4.1.1 because as the ions drifted toward the SAA they were lost due to an increased interaction with the atmosphere near the SAA.

A conclusion from a first look at the data is charge state clearly matters, but the effect of charge state also depends on the location of the release of the ions. There is a significant difference in the trapping efficiency of particles at the selected altitude of release with initial charge state 1 and charge state 15 at each of the release locations. The data alone from Section 7.4.1 and 7.4.2 is not enough to appreciate the complexity of the

result. Figures 7.4.2.1 through 7.4.2.4 present the location of the ions 1,000 s and 3,000 after release from the two locations. Figures 7.4.2.1 and 7.4.2.2 show that particles with a higher charge state will have reduced drift velocities and move less quickly away from the burst location. One of the results of the reduced drift velocity is that when the particle passes near the SAA it will spend more time near the SAA and at a lower mirroring altitude thus interacting with the more dense atmosphere for longer periods of time. If the particle remains in the vicinity of the SAA (and at relatively low altitudes) long enough then it will lose all kinetic energy and will be considered lost. If the charge state were smaller then the particle would pass by the SAA quickly and continue to disperse around the earth. This is most evident in Figure 7.4.2.2 where the only particles dispersed around the earth at 3,000 s are the charge state 1 particles.
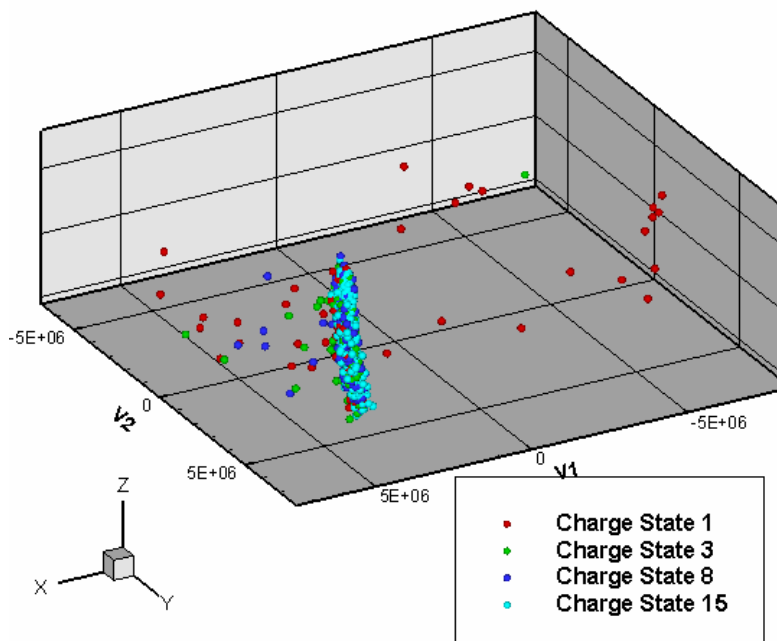
Figure 7.4.2.1: **This plot is the result of 60,000 ions released at a location centered at 500-km altitude at 52E and 0N. The plot shows the location of the remaining fission fragments 1,000 s after the particles were released. Although more of the charge state 15 particles remain than the other charge states, the lower charge state ions are the only ones to make it past the SAA and disperse around the earth.**
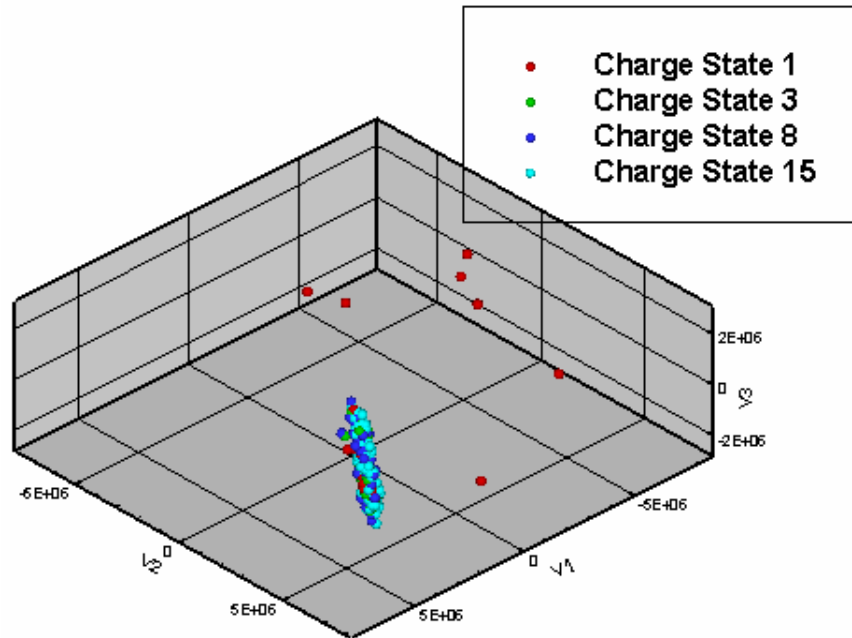
Figure 7.4.2.2: This plot is the result of 60,000 ions released at a location centered at 500-km altitude at 52E and 0N. The plot shows the location of the remaining fission fragments 3,000 s after the particles were released. Although more of the charge state 15 particles remain than the other charge states, only the charge state 1 ions make it past the SAA and disperse around the earth. The high charge state particles, due to low drift velocities, do no move far from the injection location.

The results shown in Figures 7.4.2.3 and 7.4.2.4 are slightly different from Figures 7.4.2.1 and 7.4.2.2 because the release location is near the SAA. Here the particles with a low drift velocity (high charge state) remain near the burst location and the SAA thus quickly losing kinetic energy so fewer of the high charge state particles remain trapped. The lower charge state particles, with a higher drift velocity, move away from the SAA and are able to disperse around the earth. Figure 7.4.2.4 shows that after 3,000 s, many of the lower charge state particles have dispersed around the earth and only a few charge state 15 particles remain trapped.
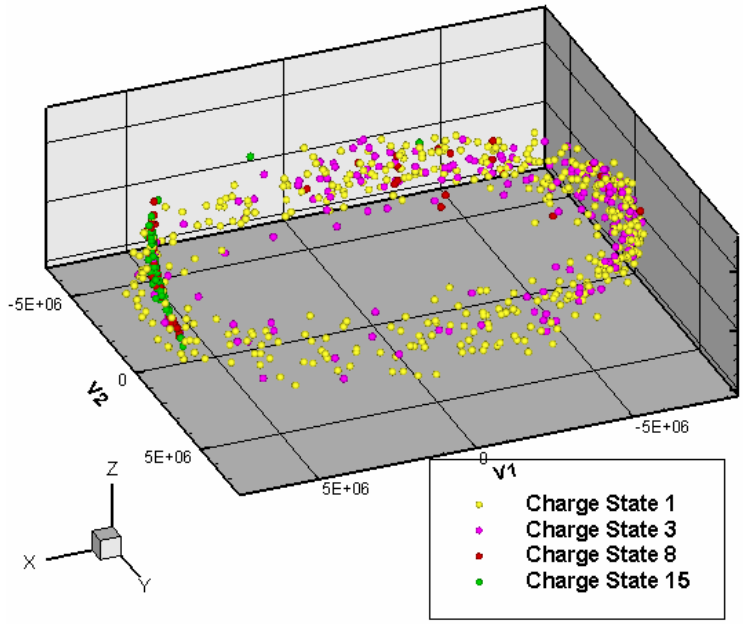
Figure 7.4.2.3: This plot is a result of 10,000 ions released centered at 500-km altitude near the SAA and the locations are shown 1,000 s after release. The low charge state particles drift quickly away from the SAA and disperse around the earth. The high charge state particles remain near the SAA longer and tend to lose most of the kinetic energy due to atmospheric interactions.
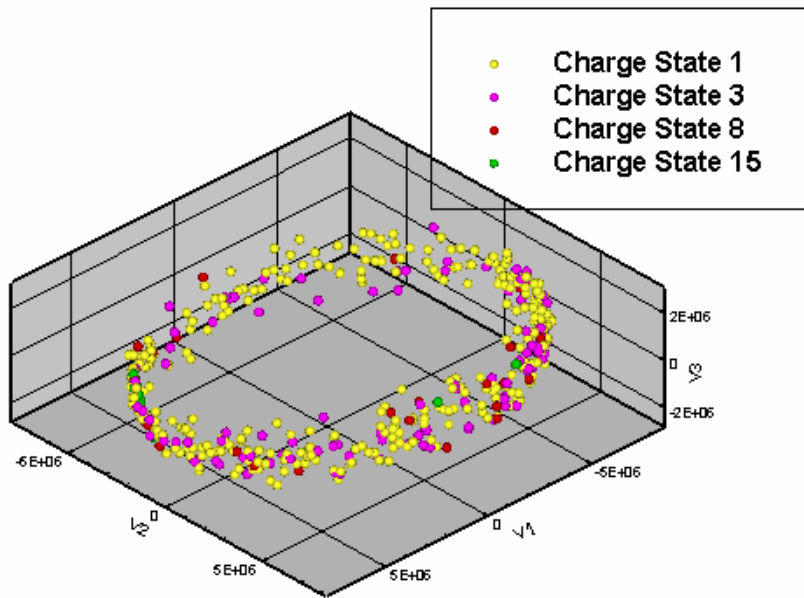
Figure 7.4.2.4: This plot is the result of 10,000 ions released centered at 500-km altitude near the SAA and the locations are shown 3,000 s after release. The low charge state particles drift quickly away from the SAA and disperse around the earth. The high charge state particles remain near the SAA longer and tend to lose most of the kinetic energy due to increased numbers of atmospheric interactions.

178

Figures 7.4.2.1 and 7.4.2.2 reveal that although there are more of the high charge state particles remaining after 1,000 s and 3,000 s from a release away from the SAA, most of the remaining, high charge state particles have not drifted far from the release location and have not passed the SAA. The drift speed is 15 times less for the charges state 15 ions than the charge state 1 ions. Additionally, only the charge state 1 ions manage to drift past the SAA and disperse completely around the earth. Because the charge state 1 ions have the largest drift velocity the ions spend the least amount of time in the vicinity of the SAA where the energy losses are the greatest. The ions are therefore able to drift past the SAA and continue to orbit the earth. Similarly, Figures 7.4.2.3 and 7.4.2.4 also demonstrate that the ions with the largest drift velocity (smallest charge state) are most likely to pass the SAA without loosing all of their kinetic energy.

As can be seen in equation 1.1.19, $r_c = \dfrac{m}{q}\dfrac{v_\perp}{B}$ and equation 1.2.3.1,

$$\vec{W}_{Drift} = \frac{m}{qB^2}\left(v_\parallel^2 + \frac{v_\perp^2}{2}\right)\vec{B} \times \nabla\left(\frac{B^2}{2}\right),$$ charge state affects both the gyro-radius and drift

velocity. The charge state effect on the gyro-radius appears most significant at early times for contributing to the initial ionization energy losses because of increased atmospheric interaction. As suggested in the data from the nuclear tests and the results of many simulations, most of the charged particles lose kinetic energy because they are in or near the loss cone. The large gyro-radius increases the loss rate for those particles near the loss cone. But for long time, global effects, the charge state influenced drift speed dominates the impact of charge state on the trapping efficiency. An ion with a small charge state and a larger drift velocity spends less time near the SAA and therefore is not necessarily "lost" at the SAA. (Future work could include additional efforts to establish a complete understanding of the effect to charge state on belt-pumping.) The effect of charge state is clearly coupled with location and altitude and provides an interesting example of the challenges of predicting the environment caused by a nuclear detonation is space.

To summarize our understanding at this point, lower charge state gives bigger gyro-radii and thus more interaction with the lower, denser region of the atmosphere at the conjugate points. The larger gyro-radii tends to increase the early-time losses of those

particles mirroring at lower altitudes. However, lower charge states give rise to more rapid drifts and thus the particle moves past the SAA much quicker where the likelihood having a significant interaction with the atmosphere is enhanced. The result is that particles with lower charge states tend to disperse completely around the earth and pass by the SAA with less probability of loss when compared to the higher charge state particles. We are currently unable to predict, without running the code, which effects is more dominant in general—it depends on the details of the burst point location. We do know that the higher charge state particles have reduced drift speeds and this may increase losses near the SAA. This is a complex problem; it is highly non-linear and begs for a computational approach. The code developed for the work reported here has laid most of the ground work for a more thorough investigation to determine the trapping efficiency of the ions and beta decay electrons.

7.4.3. The Effect of Neutral Fission Fragments on Trapped Radiation

Thus far, the focus of the study has been on the effect of the release of charged fission fragments and beta particles into the magnetic field of the earth. However, a small fraction of the fission fragments are neutral.[137] While the number of neutral fission fragments is not well known, even a small percentage of neutral fragments can effect the persistent radiation environment caused by a nuclear explosion in space. Recall that a 1-kt weapon produces 2.9×10^{23} fission fragments and if only 1 in 10,000 of the fission fragments is neutral then a 1-kt device produces $\sim 3 \times 10^{19}$ neutral fission fragments. The neutral fission fragments would not interact with the magnetic field of the earth or the magnetic bubble created by the explosion and would freely cross magnetic field lines. Some of the neutral fragments would interact with the high-density atmosphere causing collisions, ionization, energy exchange and eventual loss of kinetic energy. The neutral fission fragments stopped in the atmosphere would eventually beta decay, but the beta particles would then quickly lose all kinetic energy due to ionization energy losses. The

---

[137] Todd Hoover (LLNL), private conversation with author, 7 November 2006.

neutral fission fragments moving away from the burst and not lost into the atmosphere would continue to move with the fragment's initial velocity until it collides with another particle or beta decays.

Once the neutral fragment beta decays, the charge state increases to +1 and the ionized fragment becomes trapped in the earth's magnetic field. Additionally, the beta particle also becomes trapped in the magnetic field. Both particles contribute to the radiation environment caused by a nuclear detonation.

In order to examine the effect of the neutral fission fragments on the trapped radiation environment, 10,000 neutral fission fragments were released at the nominal 500-km altitude distributed over a bubble with a 300-km radius at longitude 191E and latitude 16N. The velocity distribution was the Maxwell-Boltzman shown in Figure 7.2.2 with randomly selected directions. There is currently no physics within the code to account for neutral scattering and energy exchange. Instead, all fission fragments reaching altitudes below 75 km were treated as though they lost all kinetic energy due to collisions and were eliminated from the simulation. Previous runs also indicate that beta particles emitted below 75 km quickly lose all kinetic energy due to ionization energy losses. The half-lives associated with the fission fragments were the short half-life set from Table 7.5.1. Neutral fission fragments with long half-lives (greater than 10 s) either move well beyond 10 earth radii away from the earth or are lost inside the dense atmosphere of the earth. The fast half-life chain was selected in order to increase the number of beta decays from the neutral fragments and is consistent with many of the half-lives of the fission fragments. Any fragment located beyond 10 earth radii was also eliminated from the simulation because this is well beyond the geosynchronous orbit and of little current interest to the results of the dissertation.

Table 7.4.3.1 presents the number of electrons remaining trapped at different times after the beta decay from the release of the neutral fission fragments. The average L-shell of the initial release location for the neutral fission fragments was 1.176. One of the interesting results of the data in Table 7.4.3.1 is the large number of electrons trapped after 500 s. Compared to all of the data in the previous sections, there are more electrons

trapped at 500 s than all others. There are even more electrons trapped at 500 s than were trapped at 500 s when the ionized debris was released at an average altitude of 2,000 km as shown in Table 7.4.1.

Time (s)		# of trapped electrons	Average L-shell of trapped particle
1		761	1.181
10		3732	1.936
100		3491	2.201
500		2733	2.471

Table 7.4.3.1: The number of trapped beta decay electrons is shown. The source of the electrons was the beta decay of 10,000 neutral fission fragments released at an average altitude of 500 km. The neutral fragments all had short half-lives. Electrons trapped in L-shells greater than 10 are not included in the data.

Additionally, the spread of the electrons was over L-shells from 1 to 10. The increase in the number of trapped electrons was due to the L-shell location of the beta decay that produced the electron. As was shown in Section 7.3, the trapping efficiency increases with altitude and L-shell. The neutral fragments cross the magnetic field unimpeded until the first beta decay. Figure 7.4.3.1 shows the volumetric spread of the electrons over a region in space at 100 s and 500 s after release. The neutral fission fragments are certainly a potential source of fission spectrum electrons injected into L-shells well above the burst location and into virtually any L-shell.
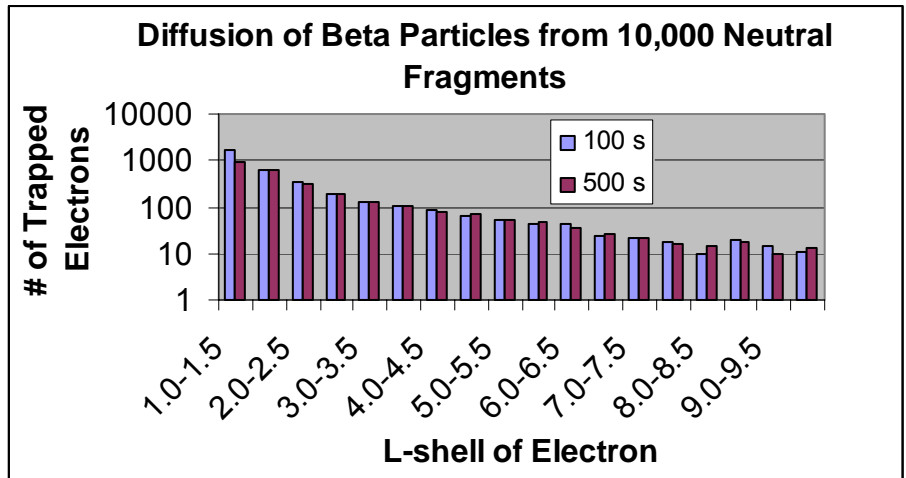
Figure 7.4.3.1: **The spread of the electrons is shown resulting from a release of 10,000 neutral fission fragments at an L-shell value of 1.176. The neutral fragments move away from the injection location and some beta decay before penetrating the earth's atmosphere or traveling off into space.**

One of the historic and unexplained questions about the data collected from the high-altitude nuclear test is how did fission spectrum electrons become trapped in L-shells much greater than the burst location (out to L ~ 6). The electron dispersion evident in the data is still a wonderful scientific mystery from which legends are made and friendships have been torn to shreds. The data presented above clearly suggest that neutral fission fragments were a source for the electrons injected into all L-shells as measured after the nuclear tests. This source of high L-shell electrons should help explain some of the data from the test. Even if the number of neutral fission fragments is a small percentage of total number of fragments, the contribution would be detectable and is significant.

7.5.   THE EFFECT OF HALF-LIFE ON TRAPPING EFFICIENCY

There are over 800 fission fragments possible from different types of fission and each of the fission fragments have a different half-life.[138] The half lives of the daughter products of fission range from tens of milliseconds to years. As discussed in Section 4.2, high energy betas are associated with short half-lives. When the high energy beta particles become trapped they present the most significant risk to satellites from trapped radiation. In order to examine the effect that the variance of half lives might have on the trapping of the betas and ions, 10,000 of the standard particles were released centered on an altitude of 500 km at 232E and 0N with three different sets of half lives associated with the beta decay. The beta decay chain and beta energy spectrum of Table 7.2.1 was applied to all three comparisons, but the half lives of the fission fragments were varied as shown in Table 7.5.1. One would expect that more beta particles would be released if the isotopes in the decay chain had shorter half lives because more of the total beta decays would occur before the ion's kinetic energy was lost due to atmospheric interaction. Once the particles lose all kinetic energy, the simulation no longer considers the particle trapped or a threat to space systems.

---

[138] Nethaway and Mustafa.

Isotope	Actual 1/2 life (s)	Short 1/2 life (s)	Long 1/2 life (s)
Zr-92	Stable	Stable	Stable
Y-92	12744	1.2744	12744
Sr-92	9756	9.756	9756
Rb-92	4.492	1.492	44.92
Kr-92	1.94	1.84	18.4
Br-92	0.365	0.365	3.65

Table 7.5.1:   The different half lives associated with each of the three comparisons of the effects of half life on trapping efficiency.

As expected, the isotopes with the shortest half lives injected the largest number of total betas as is evident in the data of Table 7.5.2. The release location of the ions was to the west of the SAA and the beta decay electrons drifted back toward the SAA and were mostly lost in the atmosphere in the vicinity of the SAA. After the daughter products became Zirconium-92, the stable isotope in the decay chain, the simulations quit tracking the fragments. That is why there are no trapped ions shown the Table 7.5.2 after 100 s for the fast decay chain.

	Standard Decay Chain			Slow Decay Chain	
Time (s)	# of betas trapped	# of radioactive ions trapped		# of betas trapped	# of radioactive ions trapped
1	476	5945		90	6764
10	1456	2217		705	2717
100	205	1186		921	884
500	7	686		590	451
1000	13	438		79	357
3000	1	48		4	100
	Fast Decay Chain				
Time (s)	# of betas trapped	# of radioactive ions trapped			
1	702	5465			
10	2280	1249			
100	594	4			
500	2	0			
1000	0	0			
3000	0	0			

Table 7.5.2:   The number of trapped electrons and ions varies for different half-life isotopes and decay chains. Isotopes with short half lives inject more betas into the magnetic field because they have a higher probability of beta decay before they lose all kinetic energy.

Because one expects that the set of injected ions with the shortest half-lives would contribute the greatest number of betas from early time beta decay, the data presented in Table 7.5.2 is of little surprise. Typically (for particles in low L-shells), given a homogeneous distribution of initial ion velocities, between 50% and 90% of the injected ions are lost in the first 10 seconds. If the ions that become lost do not beta decay before loosing all kinetic energy in the atmosphere then they do not contribute to the source of betas. For this reason, appropriate modeling of the fission fragments with the shortest half-lives (less than 10 seconds) is important for predicting the number of beta particles injected into the magnetic field. One must be careful about reaching conclusions when using the model unless a reasonable representation of fission fragments is used in the calculation. As mentioned, Tom Thomson at LLNL is currently working to provide an appropriate set of fission fragments representative of the over 800 possible fission fragments. In this dissertation, we have used only 6 of the fission fragments in order to demonstrate the capability of the code. One could clearly include all of the possible fission fragments (with appropriate decay and half-life), but a computationally more efficient approach is to include the minimum number of fission fragments that represent the range of half-lives of the fission fragments and the energy spectrum of the beta particles.

7.6.   THE INITIAL PITCH ANGLE MATTERS

The initial pitch angle of the particle determines if the ion or electron is within the loss cone. In the purest sense, the loss cone is not an absolute for predicting the likelihood of trapping because the pitch angle can and does change as the particles interact with the atmosphere. However, the data in Table 7.6.1 confirm that the initial pitch angle is critical for properly modeling the trapping of particles. The data in Table 7.6.1 was generated from the release of 10,000 particles spread with a spherical distribution over a radius of 100 km at an altitude of 500 km. The velocity was identical to the Maxwell-Boltzman distribution of Figure 7.2.2. The simulation was run with four different ranges of pitch angles shown in Table 7.6.1.

	Long 190.5E and Lat 16.7N		Long 190.5E and Lat 16.7N	
	pitch angle > 67.5		45 < pitch angle < 67.5	
Time (s)	# of betas trapped	# of ions trapped	# of betas trapped	# of ions trapped
1	574	6473	541	6123
10	2910	4718	1986	2565
100	1618	3800	971	526
500	80	2030	33	133
1000	37	703	2	65
3000	na	99	na	23
	Long 190.5E and Lat 16.7N		Long 190.5E and Lat 16.7N	
	22.5 < pitch angle < 45		0 < pitch angle < 22.5	
Time (s)	# of betas trapped	# of ions trapped	# of betas trapped	# of ions trapped
1	522	5211	440	4698
10	1199	891	915	480
100	609	237	500	146
500	15	73	23	52
1000	2	34	1	24
3000	na	11	na	8

Table 7.6.1:   The results of 10,000 particles released at identical locations, but with different pitch angles are presented. The initial pitch angle plays an important role in particle trapping. The only reason that there are any particles with initial pitch angles less than 60 degrees trapped after 1,000 s is because of the very low speed of the particles at the tail of the velocity distribution.

What is not obvious from Table 7.6.1, but is obvious in Figures 7.6.1 and 7.6.2, is that for the particles inside the loss cone, only those with a very low velocity remain trapped after 1,000 s. The average loss cone for a particle centered on this initial distribution of particles is 63 degrees. The low speed particles lose less kinetic energy per unit time and therefore remain trapped (for identical pitch angles) longer than the high velocity particles. For the particles with initial pitch angles inside the loss cone, as shown in Figure 7.6.1, the only particles remaining after 1,000 seconds are particles with low initial velocities clearly identified because the particles have not drifted far from the release location. All of the more energetic particles, inside the loss cone, are quickly lost in the atmosphere. In contrast to Figure 7.6.1 where most of the particles are inside the loss cone and lost in the atmosphere, Figure 7.6.2 presents the location of particles with

pitch angles outside the loss cone. As expected, many more of the particles outside the loss cone remain trapped after 1,000 s even though the fission fragments are drifting around the earth.
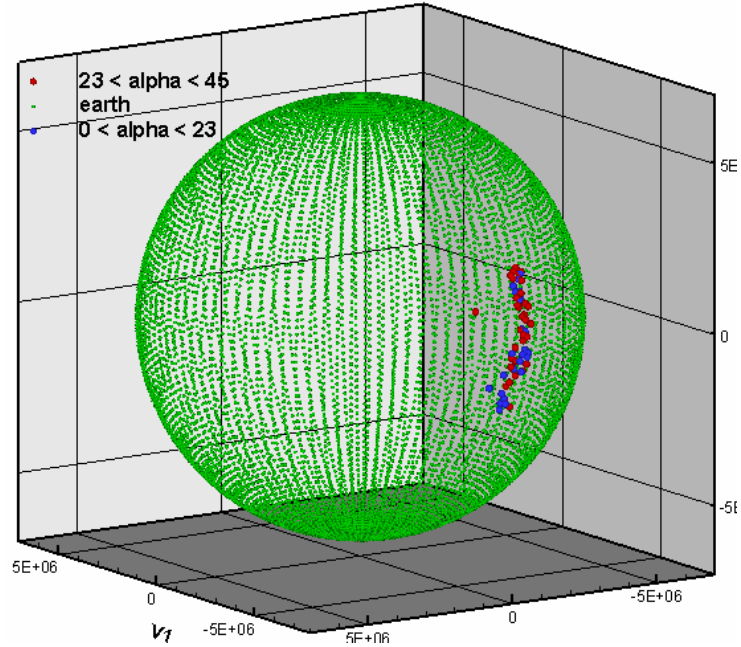
Figure 7.6.1: The remaining ions with initial pitch angles less than 45 degrees are shown 1,000 s after release. Only the particles with very low speeds remain. The energy loss is proportional to the velocity so slow particles lose less energy as a function of time. The faster particles penetrated the atmosphere and lost all of the kinetic energy.
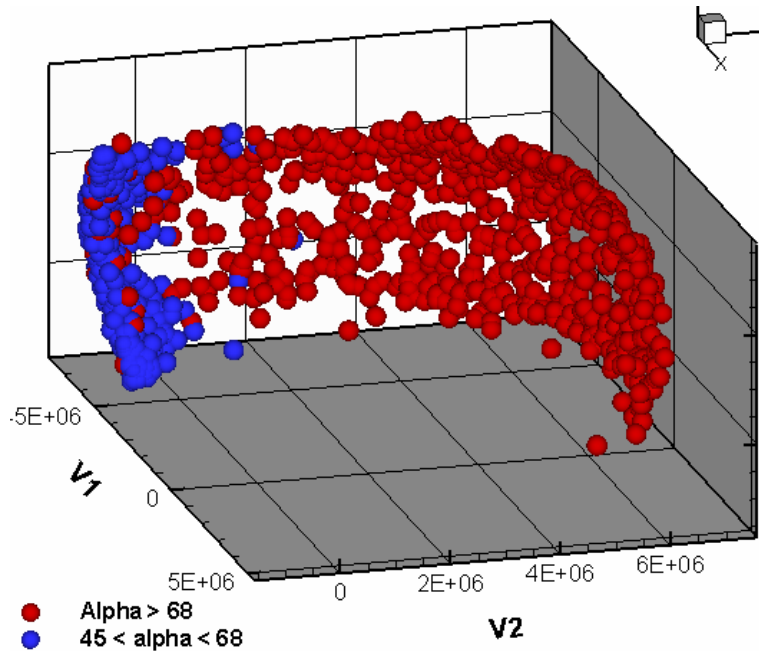
Figure 7.6.2: The loss cone for the particles released is 63 degrees. Many of the ions with initial pitch angles outside the loss cone (red dots) remain trapped after 1,000 s. The blue dots represent ions with initial pitch angles generally inside the loss cone. With few exceptions, only those particles with reduced speeds remain after 1,000 s.

The data of Table 7.6.1 and Figures 7.6.1 and 7.6.2 leave little doubt that the initial pitch angle is a critical parameter in trapping particles in the magnetic field. If one could inject all of the ions with pitch angles close to 90^0 then the trapping efficiency of the ions would be extremely high and the total number of trapped beta particles would also be significantly increased. Conversely, if the initial pitch angle of the ions was close to 0^0 then the number of trapped ions would be significantly reduced and the number of trapped betas would be minimized.

The remaining portion of the dissertation offers insight into other parameters that contribute to the trapped radiation environment. One of the difficulties of explaining the sparse data from the high-altitude nuclear test is the radial dispersion of the fission fragments and beta electrons. Sections 7.8 present the effects of a magnetic bubble on the dispersion and trapping of ions and electrons.

188

7.7.   THE EFFECT OF A MAGNETIC BUBBLE ON PARTICLE DISPERSION

The data from Starfish Prime presented in Chapter VI indicates a significant perturbation to the magnetic field surrounding the nuclear detonation. The extent of the magnetic perturbation is not completely clear due to a limited number of sounding rockets and satellites in the vicinity of the burst. However, based on lengthy discussions with Palmer Dyal[139] and the data presented in his recent paper there appears to have been a "magnetic bubble" generated by the explosion. Although the data clearly indicates the formation of a magnetic bubble after the Starfish detonation, there is less understanding about exactly what causes the magnetic bubble. There is currently a significant effort at LLNL to model the formation of the magnetic bubble. Magnetic "bubbles" may form because of the combination of large ion gyro-orbits and the long ion mean free path leads to the ions basically free-streaming away from the burst. The ions are impeded by very strong E fields that arise because the electrons associated with these ions are themselves strongly magnetized and are thus prevented from following and neutralizing "their" ions. Thus the electrons effectively couple the radial ion momentum from the explosion to the magnetic field. This momentum then pulls the magnetic field away from the burst point. Once the bubble forms it provides a new, additional scattering center for the trapped debris.[140] The effect of the magnetic bubble on the dispersion of the debris has not been previously reported. In order to study the dispersive effect of a magnetic bubble, two simple models of a magnetic bubble are included in the simulations and the results are reported. We show here that the magnetic bubble may cause significant pitch angle scattering and radial dispersion of the weapon debris and subsequent beta particles and the dispersion resembles the Starfish data. As more sophisticated bubble configurations are developed, we can continue to analyze the possible effect of the magnetic bubble on the dispersion of the debris. The inclusion of a magnetic bubble offers hope to finally understand the cause of the significant fragment dispersion noted from Starfish.

---

[139] Palmer Dyal (at LLNL), private conversation with author, 15 November 2005.

[140] Dennis Hewett (at LLNL), private conversation with author, 15 November 2005.

7.7.1. Description of the Debris without Any Magnetic Perturbation

In order to demonstrate the significance of the magnetic bubble on the pitch angle and radial dispersion of fission fragments and betas, a base line was established using 10,000 particles released 500-km altitude at 192E and 16N with no magnetic bubble. The particles were all given a speed of 2,000 km/s with a random distribution of directions. The 10,000 particles were homogenously distributed in a 100-m sphere (essentially a delta function in both energy and position). In order to isolate and identify the effects of a magnetic bubble on the charged particles, a perfect dipole field centered on the geographic axis of the earth was used for all computational comparisons. Additionally, effects of the air were removed from the simulation so that the only cause of pitch angle scattering or radial dispersion would be the magnetic bubble. Any particle mirroring at an altitude below 75 km was not considered in the results of the simulations and considered "lost" in the atmosphere and subsequently removed. The physics is complicated enough without adding the effects of the atmosphere or the actual magnetic field.

Table 7.7.1.1 and Figure 7.7.1.1 present the results of the simulation used for the base line of comparison. All of the particles were from the list of six fragments described earlier. The initial charge state of the ions was +2. The gyro-radius of the ions at the location of release was approximately 65 km in the unperturbed ambient field. The particles were only tracked up to 100 s in all simulation. The loss cone of the particles at the release point is 62°. (Incidentally, the loss cone for these particles at the equator (α_0) in L = 1.176 is 46.5^o.) With the given distribution of particles, slightly less than 1/3 of the initial release of particles were outside the loss cone and remained trapped after one complete bounce (as seen in the number of remaining ions trapped at 10 s and 100 s). Without the scattering and energy loss due to air and the scraping off effect of the SAA, particles that are trapped at 100 s would remain trapped. Both Table 7.7.1.1 and Figure 7.7.1.1 show that the number and location of particles trapped at 10 s is almost identical to the results at 100s. Once the particle is trapped and without the effects air and the shift-tilt of the magnetic field, there is not loss mechanism.

Time after release (s)	# of particles remaining trapped	Average alpha-0	Average L-shell
1	5774	na	na
10	3092	53.17	1.176
100	3088	53.17	1.176

Table 7.7.1.1: The number of remaining fission fragments of the 10,000 released at 500-km altitude at 192E and 16N. The loss cone at the release location is 62° so slightly less than 1/3 of the ions remain trapped after one complete bounce.

Distribution of Debris 10 s after Release without a Magnetic Bubble
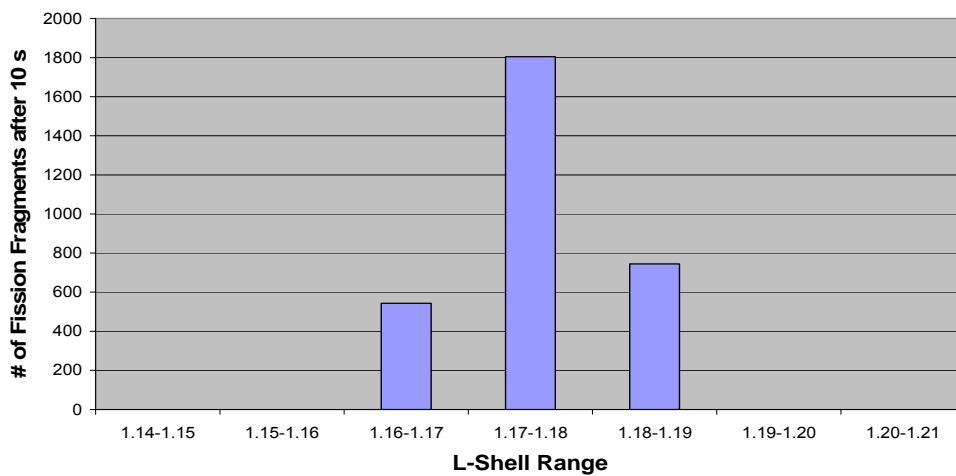
Figure 7.7.1.1:   The distribution of fission fragments 10 s after the release without the effects of a magnetic bubble. Because there are no loss mechanisms other than the loss cone, the location of the particles is identical for 10 s and 100 s. The distribution of particles is a result of the gyro-radius of the ions. The L-shell represents the altitude of the particle at the equator. The average L-shell is 1.176 at the equator.

This example and data will serve as the baseline against which we compare the effects of different bubbles. Of particular interest is the change of pitch angle at the equator (α_0), the average L-shell change of the particles, and the percentage of trapped particles.

7.7.2. Description of the Effect of a Hollow Bubble

The nuclear test data presented in Chapter VI, especially the recent work by Palmer Dyal,[141] suggest that the nuclear explosion causes a region in space temporarily void of any magnetic field or at least a region with a significantly reduced magnetic field. With this magnetically disturbed region in mind, we will now examine the effects of the magnetic perturbation on the trapping efficiency and dispersion of ionized fission fragments and beta decay particles. A simple first approximation to the localized change in the magnetic field is to consider a region in space without any magnetic field. The area without a magnetic field will be referred to as a hollow magnetic bubble.

In order to study the effects of a hollow magnetic bubble on the trapping and dispersion of ionized fission fragments, an identical set of fission fragments from Section 7.7.1 was released at the center of a hollow magnetic bubble centered on the release location of the particles. The hollow bubble was given a finite life of 10 s. Like before, the trajectory of the fission fragments was determined using the Boris push. The results of the effect of two different sizes of hollow bubbles, one with a radius of 300 km and the other with a radius of 500 km, were compared to the results of Section 7.7.1 (no magnetic bubble). Table 7.7.2.1 shows a comparison of the data for 1 s, 10 s, and 100 s.

---

[141] P. Dyal, "Particle and Field Measurements of the Starfish Diamagnetic Cavity," J. Geophys. Res. Vol. 111 (2006), A12211, 1 – 23.

	No Bubble		
Time after release (s)	**# of particles remaining trapped**	**Average alpha-0**	**Average L-shell**
1	5774	na	na
10	3092	53.17	1.176
100	3088	53.17	1.176
	Hollow 300-km Bubble		
Time after release (s)	**# of particles remaining trapped**	**Average alpha-0**	**Average L-shell**
1	6173	na	na
10	2700	53.52	1.18
100	2690	53.41	1.182
	Hollow 500-km Bubble		
Time after release (s)	**# of particles remaining trapped**	**Average alpha-0**	**Average L-shell**
1	6250	na	na
10	2653	53.35	1.182
100	2653	53.32	1.185

Table 7.7.1.2: The data is from the release of 10,000 fission fragments at the center of two different hollow bubbles. The bubble "collapsed" at 10 s and the particles were tracked for 100 total seconds.

The data in Table 7.7.1.2 indicates that the bubble acts as a scattering source for the ions. The typical bounce period of an ion with these initial conditions is around 12 s so the ions will have at least two significant interactions with the bubble before the bubble collapses at 10 s. The interaction of the fission fragment with the hollow bubble causes the ions to disperse radially inward and outward. When the ion moves through the bubble there are no magnetic forces acting on the particle. The particle moves in a straight line through the magnetic bubble until the particle reaches the other side of the bubble and resumes the interaction with the ambient magnetic field. When the ions move out of the hollow bubble, depending on the gyro-radius and pitch angle, it may either follow the ambient magnetic field lines or the ion may loop back into the bubble for another pass across the bubble. Eventually the ion passes out of the bubble or the bubble collapse and the interaction with the bubble is complete.

The interaction with the bubble also causes the particles to disperse away from the initial injection location. The average value of the L-shell location of the ions interacting with the bubble was between 1.182 and 1.185. This is compared to the average L-shell of 1.76 for the ions not interacting with the bubble (Section 7.7.1). The average value of the

L-shell location of the particles increased by 0.06 of an L-shell or 38 km indicating that more of the ions scattering to higher L-shells remained trapped than those ions scattering to lower L-shells. The diffusive effect of the bubble is more clearly identified in a plot comparing the locations of the particles with and without the bubble. Figures 7.7.2.2 and 7.7.2.3 show the diffusive effect of the bubble on the location of the ions resulting from an interaction with the hollow bubble. The magnetic bubble causes the ions to disperse away from the initial L-shell of injection. More of the particles appear to disperse outward than inward because some of the particles that disperse inward are lost below 75 km altitude (the loss cone increases with the a decreasing L-shell). This fission fragment dispersion caused by the magnetic bubble is strikingly similar to the debris "shoulder" described in Chapter VI in the work by and C. Allen[142] and shown in Figure 6.1 for Starfish and in Figure 7.7.2.1 for the Russian II shot. The debris shoulder is a way of describing the dispersion of the debris away from the L-shell of detonation.

---

[142] C. Allen and P. McDaniel, "Review of the High Altitude Nuclear Burst 1958 and 1962 Satellite Data." published for Air Force Research Laboratory, Kirtland AFN, NM under contract DTRA-01-00-C-0088, 20.
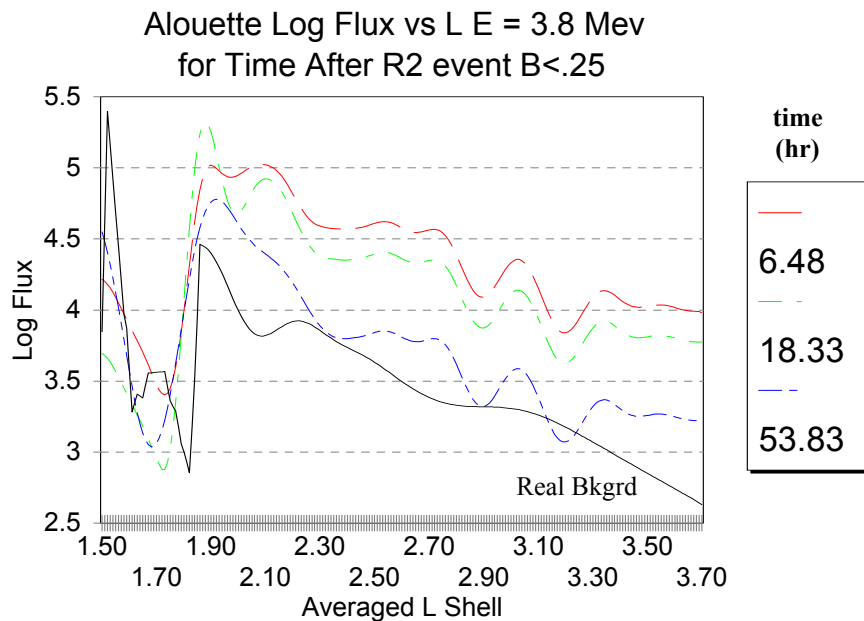
Figure 7.7.2.1: Aloett satellite data for electron energies greater than 3.8 MeV processed for electron flux values for various times after the Russian II test and background. The Russian II burst center was at L = 1.86 and the figure shows the "shoulders" of dispersion of the electrons possibly caused by the magnetic bubble effect on the electrons and fission fragments.[from C. Allen]
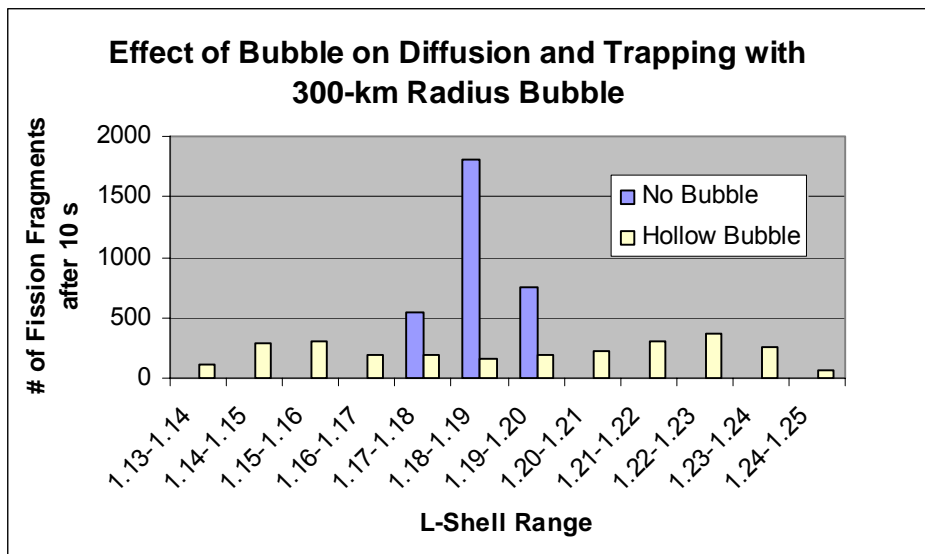
Figure 7.7.2.2: The effect of the 300-km hollow bubble on the radial dispersion of fission fragments. After 10 s, the bubble was removed from the simulation and the magnetic field return to the ambient field.
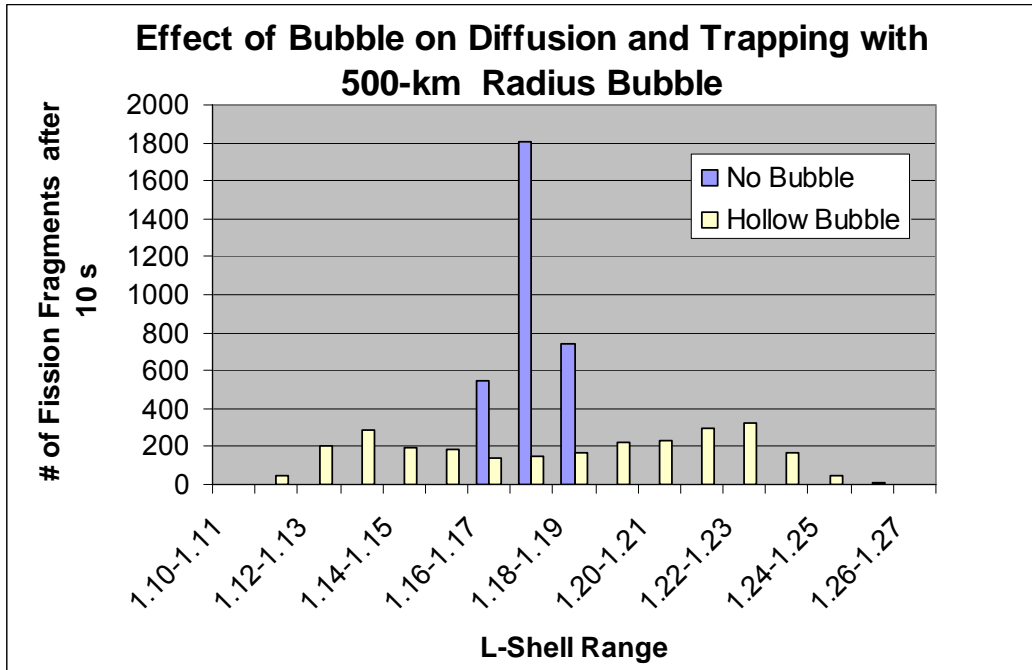
Figure 7.7.2.3: The effect of the 500-km hollow bubble on the radial dispersion of fission fragments. After 10 s, the bubble was removed from the simulation and the magnetic field return to the ambient field.

The general dispersion effect was noted with both bubble diameters. The limitation of the radial dispersion caused by a hollow bubble is set by the size of the bubble. The guiding center of the particle does not disperse more than a bubble radius away from the bubble center, but the guiding center does tend to disperse away from the release location. Figure 7.7.2.4 shows the location of the particles at the time of the bubble collapse. More of the particles are bunched near the location of the bubble because when the fission fragment interacts with the bubble, it may bounce around several times inside the bubble, temporarily trapped inside the magnetic bubble, before exiting the bubble into the ambient field. The particle's velocity does not change while inside the bubble. Depending on where the particle leaves the bubble and the velocity components of the particle, the fragment will either follow the direction of the magnetic field lines or it may enter back into the bubble and move across to another location on the edge of the bubble.
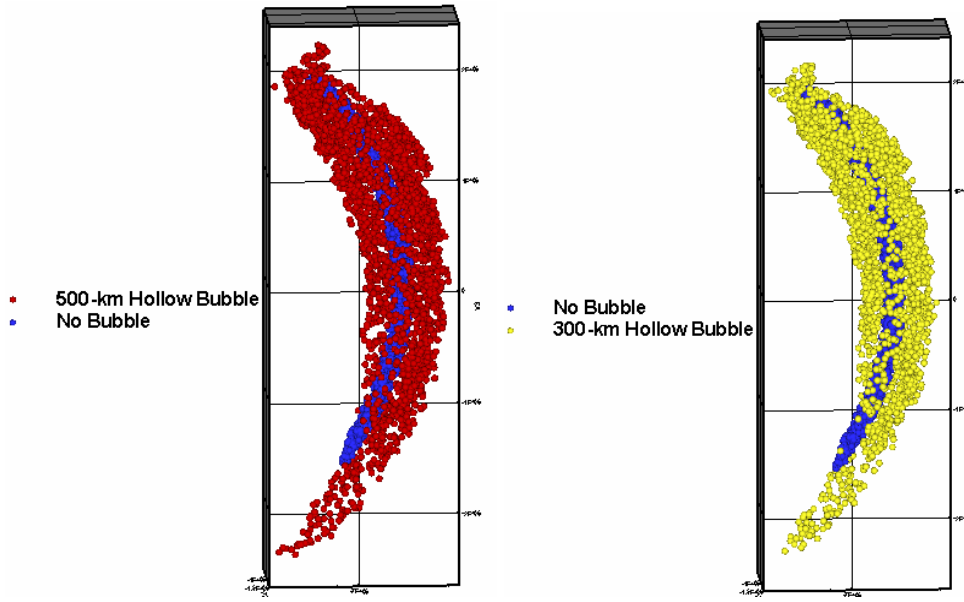
Figure 7.7.2.4: The location of the ions 10 seconds after release with and without the effects of a bubble. The blue represents the case with no bubble, the red represents the case with a 500-km bubble, and the yellow represents the case with a 300-km bubble. The bubble acts as a scattering source and the particles disperse out to the edge of the bubble. More of the particles are near the location of the bubble because the bubble can act as a temporary trap for particles.

In addition to causing a radial dispersion of the fission fragments, the bubble also reduces the number of particles trapped compared to simulations without the hollow magnetic bubbles. Every time the ion interacts with the hollow bubble, there is an opportunity for the fragment to exit the bubble inside the loss cone. Once a particle is inside the loss cone, especially without any columbic scattering (recall atmospheric interaction is turned off for these results) then the particle is lost below the selected cutoff off altitude 75 km. Even particles initially outside the loss cone may enter the loss cone after interacting with the hollow bubble. As was shown in Section 7.2, the loss cone becomes larger as the particle moves to lower L-shells. For the case with no magnetic bubble, 3,088 fission fragments remain trapped after 100 s compared to 2,690 for the 300-km bubble and 2,653 for the 500-km bubble. This is a reduction of 13% and 14% in the total number of trapped fission fragments caused by interaction with the hollow bubble.

The hollow magnetic bubble causes both dispersion of the fission fragments and a decrease in the number trapped. The reduction in the number of the fragments affects the trapping of the beta particles by reducing the number of fission fragments available for beta decay. Although not shown, the dispersion of the trapped fission fragments results in a larger volume populated by the beta particles from the late time beta decay. The trapping efficiency of the betas increases with the increase in the L-shell of the fragment.

An additional source of volumetric spread of the beta particles is the hollow bubble induced dispersion of the electrons from the very rapid beta decay of the fission fragments while the fragments are still inside the bubble and before the bubble collapses. As discussed in Section 5.2, many of the most energetic betas are a result of short half-life fission fragments and many beta particles would be injected into the bubble before the bubble collapsed and/or the ions leave the bubble. The data presented in Chapter VI indicates that there were many fission spectrum electrons moving omni-directionally inside the bubble well before the bubble collapsed[143] indicative of either the absence of a magnetic field or a omni-directional magnetic field. After the bubble collapsed, the trapped electrons were measure in a trapped distribution.

In order to demonstrate the effect a hollow magnetic bubble would have on fission spectrum electrons released inside of a hollow bubble imbedded in the earth's magnetic field, 10,000 electrons were released at the center of hollow magnetic bubbles identical to the bubbles described for the release of the fission fragments. The 2.04 MeV (kinetic energy) electrons ($\gamma = 5$) with δ-function in energy were given random velocities. The bubble collapsed after 3 seconds instead of the 10 seconds used for the ions. The bounce period of the electrons is approximately 0.1 s resulting in up to 60 interactions with the hollow bubble before collapse. The Boris push was used to track the electrons for the first 3 seconds while the electrons were interacting with the bubble. After the bubble collapsed the guiding center method was used to track the electrons up to 100 s after the initial release. Table 7.7.2.3 shows the results of the electron data comparing no

---

[143] P. Dyal, A12211, 6.

bubble, a 300-km hollow bubble, and a 500-km hollow bubble. There is a significant decrease in the number of trapped electrons and the pitch angle increases for the electrons interacting with the different bubbles.

Time after release (s)	No Bubble # of particles remaining trapped	Average alpha-0	Average L-shell
1	4237	52.48	1.176
3	4237	52.48	1.176
100	4236	52.48	1.176
Time after release (s)	Hollow 300-km Bubble # of particles remaining trapped	Average alpha-0	Average L-shell
1	2125	54.88	1.172
3	1352	55.48	1.174
100	1351	55.48	1.174
Time after release (s)	Hollow 500-km Bubble # of particles remaining trapped	Average alpha-0	Average L-shell
1	329	57.93	1.175
3	126	59.34	1.169
100	126	59.34	1.169

Table 7.7.2.3: The data is from the release of 10,000 2-MeV electrons at the center of two different hollow bubbles. The bubble "collapsed" at 3 s and the electrons were tracked for 100 total seconds.

Even though the hollow magnetic bubble collapsed after 3 s, it caused a significant reduction in the number of trapped electrons at 1 s, 3 s, and 100 s. The 300-km bubble caused a 68% reduction in the number of trapped electrons when compared to the number trapped after 100 s in the normal ambient field. The 500-km bubble caused a 97% reduction in the number of trapped electrons. Similar to the ions, each time an electron interacted with the bubble, there was a chance that the electron would travel out of the bubble at an altitude and with a pitch angle such that the electron mirrored below the 75-km cutoff. Because the electrons had multiple interactions with the bubble during the 3 s lifespan of the bubble, many of the electrons were lost below 75 km. The 500-km bubble amplified the effect because the bubble actually extended well below the 75-km

cutoff resulting in the loss of most of the electrons. The same trend was observed with the ions, but was minimized due to at least a factor of 10 or 20 reduction in the number of bubble interactions because the ion bounce period is so much longer.

One of the differences in the effect of the bubble on the electrons when compared to the effect on the fragments was that the average L-shell value decreased for the electrons. The decrease was not significant, but as shown in Table 7.7.1.3, the decrease was noticeable with all bubbles and at all three times. Because the gyro-radius is on the order of 200 m, all of the electrons trapped in the ambient field have an L-shell of 1.176. This result for the electrons is not yet understood, but was consistent with all of the runs. This seemingly inward dispersion of electrons should be considered for additional future work.

Another difference in the effect of the bubble on the electrons was that the average pitch angle of the trapped electrons increased. This is not only evident in Table 7.7.2.3 where the average pitch angle is shown to increase with the magnetic bubble size, but in Figures 7.7.2.5 through 7.7.2.7 the electrons that interacted with the bubbles clearly have mirror points that are higher in altitude consistent with larger pitch angles at the equator. Figure 7.7.2.5 presents the location of the electrons 1 s after release inside the two bubbles compared with the location of the electrons in the absence of a magnetic bubble. At 1 s after release, the bubbles have clearly cause dispersion of the electrons away from the release location. Figure 7.7.2.6 shows the location of the electrons immediately after the bubble collapses at 3 s. In addition to causing dispersion, this figure also suggest that the bubble acts as a pitch angle selector such that only electrons with large pitch angles remain trapped after the bubble collapse. If the pitch angle is large enough then the electron will not enter the bubble and therefore remain trapped with no additional scattering or energy loss mechanism. Figure 7.7.2.7 shows the location of the electrons 100 s after release and 97 s after the bubble collapse. Similar to Figure 7.7.2.6, the size of the bubble is shown to increase the dispersion and increase the average pitch angle of the trapped electrons. The figures generally show that as the bubble size increases, the average pitch angle increases and the electrons mirror at higher altitudes. As discussed, each time an electron interacts with the magnetic bubble there is a chance

that the electron will mirror below the 75-km cutoff. Therefore, the electrons leaving the bubble with larger pitch angles may not interact with the bubble when they return to a similar mirror point because they mirror before reaching the bubble and remain trapped. The bubble, therefore, seems to act like a pitch angle cut-off selector or screener and causes the average pitch angle of the trapped electrons to increase. If the electrons interact often enough without increasing in pitch angle, they will eventually become lost below the 75-km cutoff.
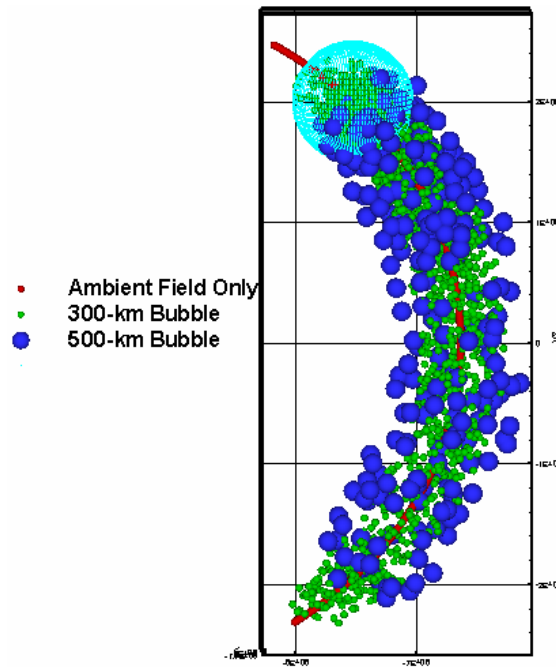
Figure 7.7.2.5: **The location of the remaining electrons for the three different cases is shown after 1 s. The electrons released in the ambient field do not disperse from the original L-shell and the electrons interacting with the bubble disperse away from the location of injection. The location of the 500-km bubble is also shown at the top of the figure. Notice that the altitude of the mirror location of electrons tends to increase with the size of the hollow bubble. The bubble seems to act like a pitch angle selector for the remaining electrons.**
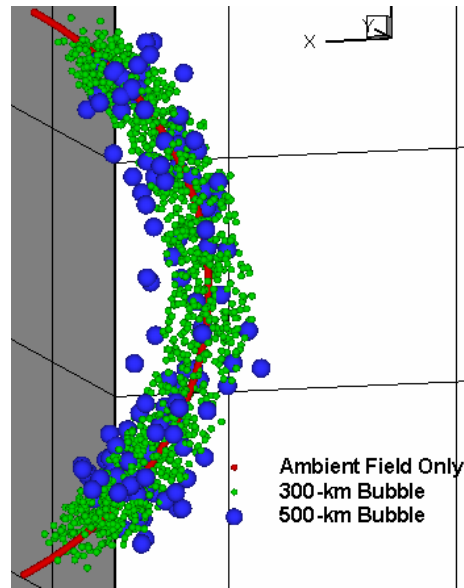
Figure 7.7.2.6: The location of the remaining electrons for the three different cases is shown after 3 s. As in Figure 7.7.2.5, the electrons interacting with the bubble have increasingly larger pitch angles at the equator and do not mirror as close to the earth. The bubbles seem to be screening out the pitch angles of the electrons.
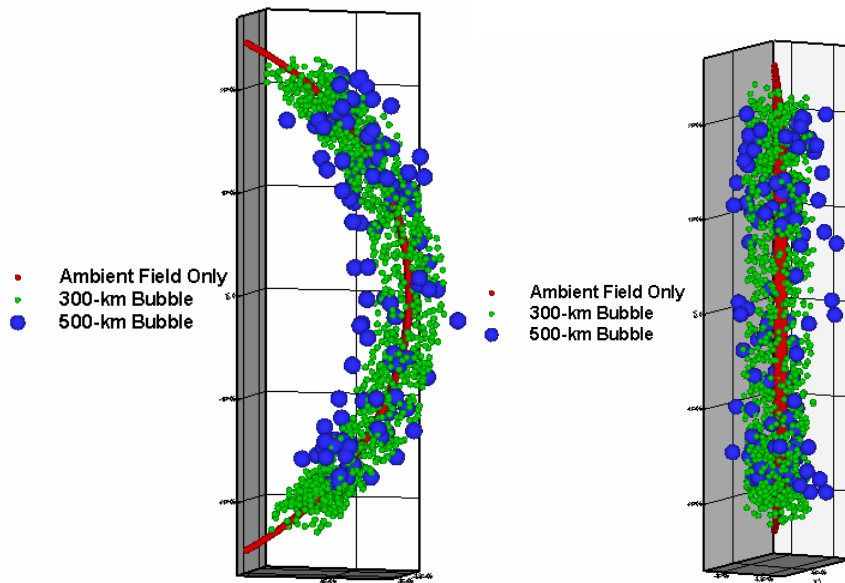
**Figure 7.7.2.7:** The location of the remaining electrons for the three different cases is shown after 100 s. The electrons released in the ambient field do not disperse from the original L-shell and the electrons interacting with the bubble disperse away from the location of injection. As in Figure 7.7.2.4, the electrons that interacted with the bubbles have pitch angles that cause the electrons to mirror at higher altitudes.

202

Also evident in Figures 7.7.2.5 through 7.7.2.6 is the eventual dispersion of the electrons that interact with the hollow bubble. The dispersion of the electrons is similar to the dispersion of the fission fragments. Figures 7.7.2.8 and 7.7.2.9 compare the location of the electrons after interacting with the two different bubbles. Both bubbles cause dispersion out to the edge of the bubble and the distribution appears less symmetric than was observed for the ions.
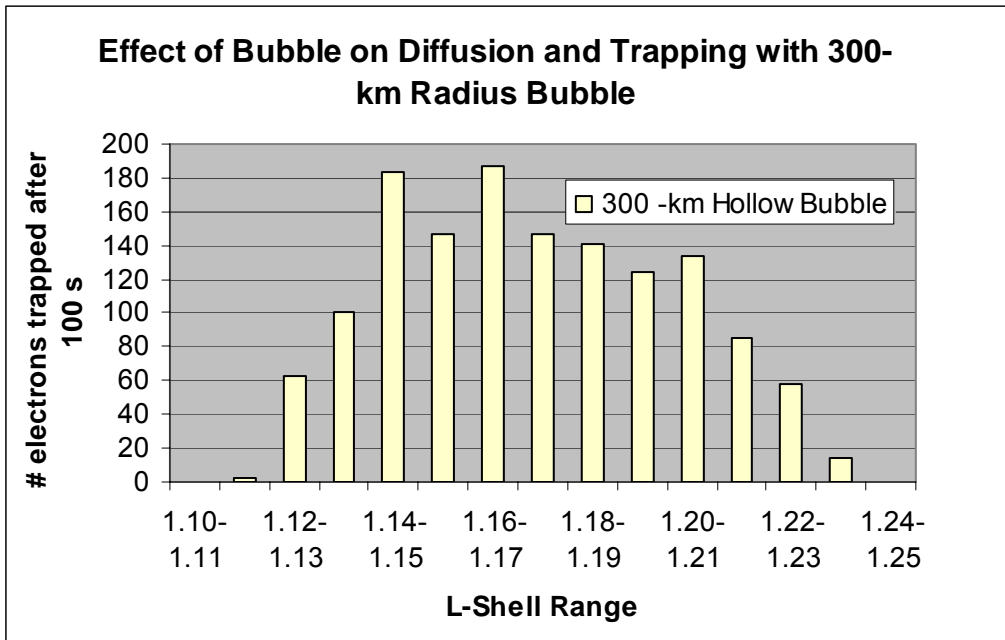
Figure 7.7.2.8: The distribution of locations of the remaining electrons is shown for those interacting with the 300-km bubble. The L-shell of injection and location of all of the remaining electrons not interacting with a bubble is 1.176. The remaining trapped electrons are widely dispersed over the radius of the bubble.
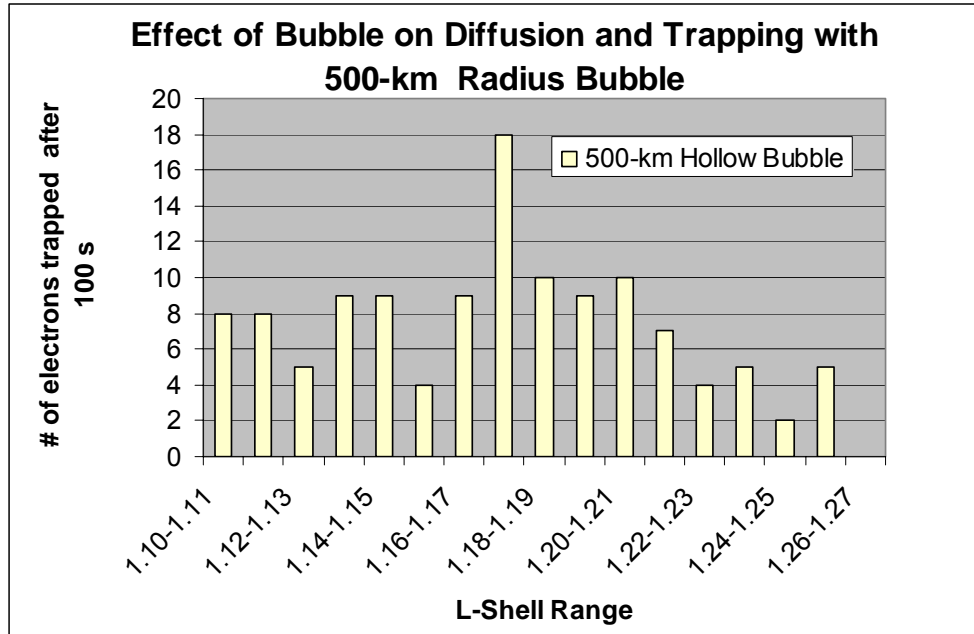
Figure 7.7.2.9: The distribution of locations of the remaining electrons is shown for those interacting with the 500-km bubble. The L-shell of injection and location of all of the remaining electrons not interacting with a bubble is 1.176. The remaining trapped electrons are widely dispersed over the radius of the bubble.

7.7.3. Description of the Effect of a Dipole-Like Bubble

There are some who believe that the magnetic field of the bubble is caused by a current ring of charged particles from the background atmosphere and the weapon debris. This current ring of charged particles resembles a current loop and generates a magnetic field opposing the direction of the ambient field in the center of the loop causing the magnetic field of the loop to cancel the ambient field. Jackson[144] develops the analytic expression for the magnetic field of a current loop both on and off axis. If the current ring had a radius of 500 m then the current would need to be ~ 20 kA in order to cancel the magnetic field at the center of the loop if the ambient field at the center of the loop was ~ 2.5×10^{-5} T. To generate this current loop one would need ~ 5×10^{20} 10 eV electrons. If the bubble was created by singly ionized debris (2,000 km/s) forming a current loop of 400-km radius then one would need ~1×10^{26} ions to generate the necessary 15 MA. Nuclear explosion could easily provide the necessary charge to generate the current ring

---

[144] Jackson, 181.

speculated as the cause of the dipole like field. The actual geometry of the current loop may even resemble that of a solenoid. For the dissertation, a simpler model of this dipole-like magnetic field was applied in much the same fashion as the hollow magnetic bubble of Section 7.7.2 and the results are reported below.

This configuration was selected because it resembles (at least in the magnitude of the magnetic field) magnetometer data from the Starfish Prime nuclear test presented in Chapter VI and reported recently by Palmer Dyal.[145] The dipole-like magnetic bubble applied to the code did not change the direction of the ambient field, but did change the magnitude of the field as a function of the distance from the center of the bubble. The actual data from Palmer indicates that during the bubble expansion and collapse, the magnetic field inside the bubble had no preferred direction, but at the edge of the bubble, the magnetic field did increase well above the ambient magnitude. Figure 7.7.3.1 and 7.7.3.2 show the change in the ambient field magnitude as a function of distance away from the bubble center. The characteristics of the bubble were also based on recommendations from Stephen Brecht[146] and Bernie Roth,[147] both experts in high-altitude physics. Undoubtedly, more complicated magnetic configurations could or should be investigated, but one must understand the effect of the simplest magnetic perturbation before complicating the problem. The work to understand the complicated structure of the magnetic field caused by a high altitude nuclear explosion is currently being investigated by Hewett et al at LLNL.[148] Once a better understanding and model of the magnetic bubble is available then the "improved" field should be added to the simulation if one ever hopes to match the data from the nuclear test.

---

[145] P. Dyal, A12211, 7.

[146] S. Brecht (at LLNL), private conversation with author, 14 December 2006.

[147] B. Roth (at LLNL), private conversation with author, 29 November 2006.

[148] D. Hewett (LLNL), private conversation with author, 5 October 2006.
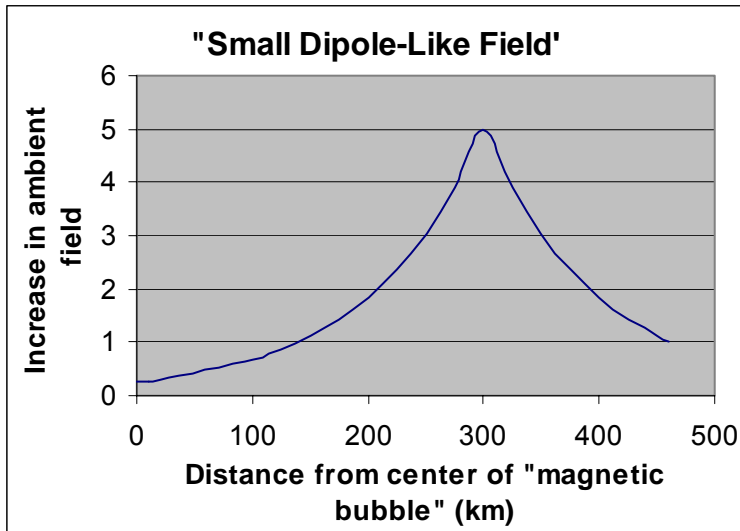
Figure 7.7.3.1:   The small dipole-like field is shown. The magnetic field is significantly reduced near the center of the bubble and eventually increases to five times ambient at 300 km away from the center. The bubble then decays back to the ambient field at 460 km from the center.
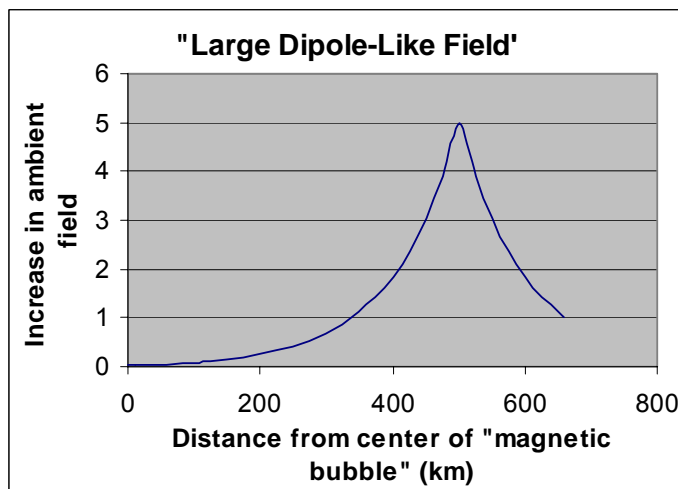
Figure 7.7.3.2:   The large dipole-like field is shown. The magnetic field is significantly reduced near the center of the bubble and eventually increases to five times ambient at 500 km away from the center. The bubble then decays back to the ambient field at 660 km from the center.

In order to study the effects of a dipole-like magnetic bubble on the dispersion and pitch angle scattering of fission fragments, an identical set of fission fragments like those described in Section 7.7.2 was released at the center of the bubble. The dipole-like bubble had a lifetime of 10 s. Two sizes of dipole-like bubbles, one with a peak field at a

206

radius of 300 km (small dipole-like bubble) and the other with a peak field at a radius of 500 km (large dipole-like bubble) were analyzed and compared to the results of Section 7.7.1. Table 7.7.3.1 shows a comparison of the data for 1 s, 10 s, and 100 s. The average L-shell of the fragments and the pitch angle at the equator did not change significantly due to interactions with either bubble. The number of particles trapped at 100 s after interacting with the small bubble was almost identical to the number of particles remaining trapped after 100 s with no magnetic bubble interaction. The larger bubble did cause a decrease of 8% in the number of trapped particles at 100 s. The most significant effect was the dispersion of the fragments from their initial release location.

No Bubble			
Time after release (s)	**# of particles remaining trapped**	**Average alpha-0**	**Average L-shell**
1	5774	na	na
10	3092	53.17	1.176
100	3088	53.17	1.176
Dipole-like 300-km Bubble			
Time after release (s)	**# of particles remaining trapped**	**Average alpha-0**	**Average L-shell**
1	5795	na	na
10	3096	53.13	1.177
100	3081	53.16	1.177
Dipole-like 500-km Bubble			
Time after release (s)	**# of particles remaining trapped**	**Average alpha-0**	**Average L-shell**
1	5978	na	na
10	2871	53.4	1.177
100	2854	53.41	1.178

Table 7.7.3.1: The results of the release of 10,000 fission fragments at the center of the dipole-like bubble are compared to an identical release of fission fragments in the ambient field of the earth. The number of particles trapped decreases and the dipole-like bubble causes dispersion of the fragments.

Both dipole-like bubbles caused radial dispersion of the fission fragments. Based on the results of Section 7.7.2, most of the observed dispersion was caused by the significantly reduced field near the center of the bubble. The decrease in magnetic field near the center of the bubble caused the ion's gyro-radius to increase near the center of the bubble and the particles move away from the injection location as part of the normal

Lorentz force motion, but when the magnetic field increased further away from the center of the bubble, the gyro-radius of the fragment became smaller and the particle becomes trapped on the new magnetic field line L-shell. Figures 7.7.3.3 and 7.7.3.4 show the dispersion of the ions as well as a comparison to the results from no bubble and the hollow bubble. The larger bubble allows for more dispersion primarily resulting from the a larger size of the volume of the decreased magnetic field near the center of the bubble as shown in Figures 7.7.2.1 and 7.7.3.2. The magnitude of the magnetic field near the center of the larger bubble is less than the ambient field out to 350 km from the center. The field near the center of the smaller bubble is less than the ambient out to only 150 km from the center. Particles that move away from the center and become trapped in higher or lower L-shells may not ever again interact with the center of the bubble where the field strength is reduced and gyro-radius is large. The dispersion is caused by the interaction with the weak magnetic field. The double-hump distribution is similar to the distribution of the ions from Section 7.7.2.
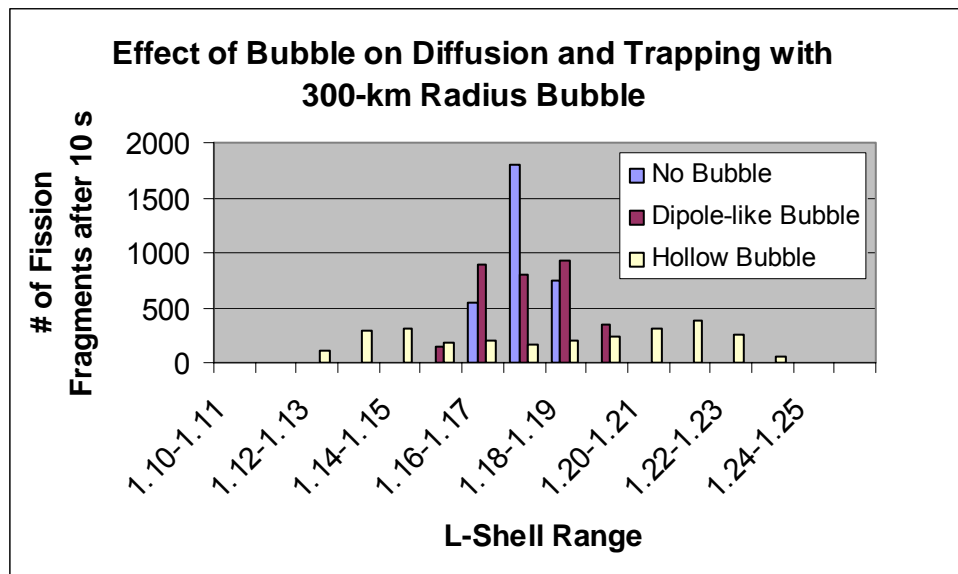
Figure 7.7.3.3: Shows the distribution of L-shell value of the fission fragments interacting with different magnetic field configurations at 10 s. The dipole-like bubble causes significantly less dispersion than the hollow bubble, but the dipole-like bubble does cause a redistribution of the particles.
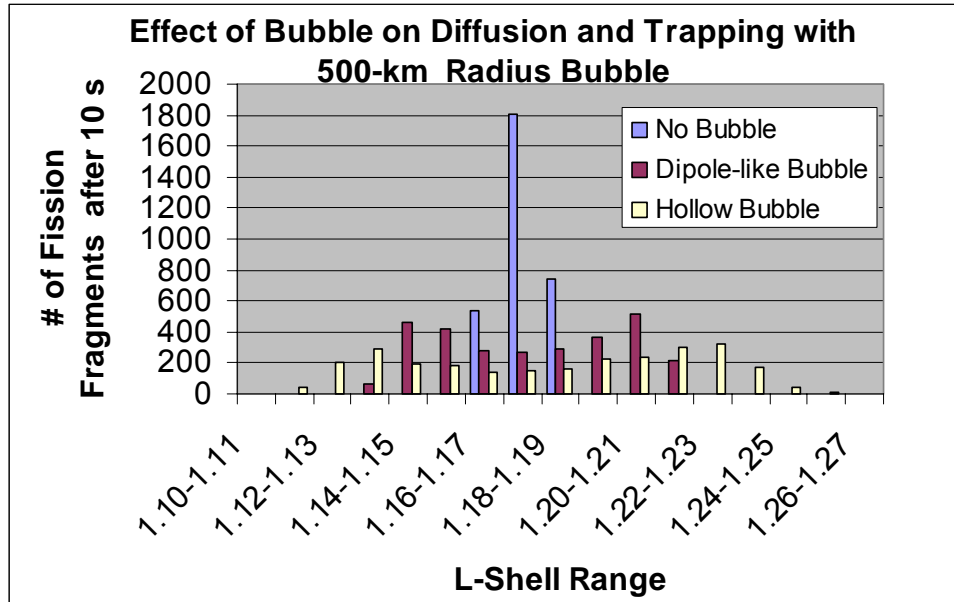
Figure 7.7.3.4: Shows the distribution of L-shell value of the fission fragments interacting with different magnetic field configurations at 10 s and larger bubbles than are compared in Figure 7.7.3.3. Because the field inside the dipole-like bubble increases to five times the ambient field, the fission fragments do not spread out as much when compared to the hollow bubble.

The location of each of the trapped particles is shown in Figure 7.7.3.5 one second after the particles are released inside the larger bubble. The bubble has already caused the dispersion of the particles, but unlike the hollow bubble, the particles only disperse out to a region where the field becomes large enough for the gyro-radius to become comparable or smaller than the gyro-radius in the ambient magnetic field. For the larger dipole-like bubble, the particles, based on the results in Figure 7.7.3.4, disperse up to 350 km away from the initial L-shell, which happens to be where the magnitude of the field in the bubble is equal to the ambient field without the bubble. Similarly, the ions only disperse up to 130 km away from the initial L-shell for the small bubble and this is again where the field inside the bubble is equal to the magnitude of the ambient field without the bubble. Figure 7.7.3.6 presents the location of the fragments 100 s after the release. At 100 s the spread is still obvious and is a result of the initial interaction with the bubble.

209
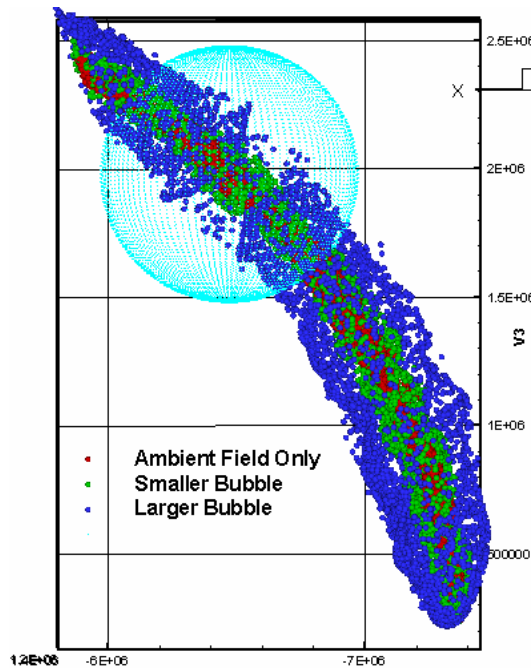
Figure 7.7.3.5: The location of the fission fragments is shown 1 s after the release of fragments moving at 2,000 km/s with a random distribution of initial pitch angles. The spherical light-blue bubble represents a sphere of 500-km radius from the release location. The dipole like bubble causes the fission fragments to disperse out to 350 km away from the release location for the larger bubble and 130 km away from release in the smaller bubble.
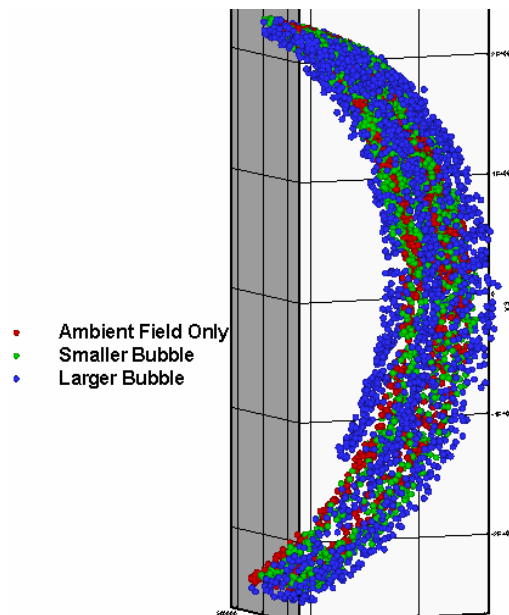

Figure 7.7.3.6: The location of the fission fragments is shown 100 s after the release of fragments moving at 2,000 km/s with a random distribution of initial pitch angles. Both bubbles cause dispersion of the fragments and tend to move the particles out to an edge of the field and away from the burst location.

210

Ultimately, the dipole-like bubble modeled here did not have a significant impact on the trapping, radial dispersion, or pitch-angle diffusion of the fission fragments. However, what is clear from the investigation is that the area of the bubble with a magnetic field less than the ambient field certainly causes dispersion and a decrease in trapping efficiency. If the magnetic void is large enough then the effects of the bubble on the trapping of the particles will increase. Additionally, the field produced by a current loop or solenoid would not only decrease the magnetic field at the center of the bubble, but it would also change the direction of the magnetic field. The ions would follow the direction of the "new" magnetic field and additional dispersion would be expected.

In order to study the effect the dipole-like bubble would have on energetic betas released in the center of the bubble, a source of 10,000 electrons, (2.04 MeV electrons (γ = 5) with δ-function in energy were given random velocities identical to the source used to examine the effects of the hollow bubble of Section 7.7, was released at the center of the dipole-like magnetic bubbles. The bubble instantaneously collapsed after 10 s. The bounce period of the electrons is approximately 0.1 s resulting in up to 200 interactions with the bubble before collapse. The Boris push was used to track the electrons for the first 10 seconds while the electrons were interacting with the bubble and after the bubble collapsed the guiding center method was used to track the electrons up to 100 s after the initial release. Table 7.7.3.2 shows the results of the electron data comparing no bubble, a 300-km dipole-like bubble, and a 500-km dipole-like bubble.

	No Bubble		
Time after release (s)	# of electrons remaining trapped	Average alpha-0	Average L-shell
1	4237	52.48	1.176
10	4237	52.48	1.176
100	4236	52.48	1.176
	Dipole-like 300-km Bubble		
Time after release (s)	# of electrons remaining trapped	Average alpha-0	Average L-shell
1	3922	52.96	1.77
10	3920	52.96	1.177
100	3920	52.96	1.177
	Dipole-like 500-km Bubble		
Time after release (s)	# of particles remaining trapped	Average alpha-0	Average L-shell
1	3921	52.96	1.78
10	3920	52.96	1.178
100	3918	52.96	1.178

Table 7.7.3.2: This table compares the number of remaining electrons after interacting with the dipole bubble to the results of the same release of electrons into the ambient dipole field of the earth. The dipole-like bubble causes some radial and pitch angle diffusion as seen by a slight increase in the pitch angle at the equator and the average L-shell of the electrons. The bubble also causes an increase in the initial loss of electrons most likely resulting from an inward dispersion. After the initial losses, the bubble has no additional affect on the electrons. The electrons that are lost are lost before 1 s into the simulation.

The dipole-like bubble causes an early time, most likely during the first bounce period, loss of electrons. The decrease in the number of trapped electrons was 7.5 % for both bubble configurations. The radial dispersion was greater for the larger bubble because of a larger volume of reduced magnetic field allowing for the dispersion. The pitch angle change was virtually identical for both bubble sizes. Figure 7.7.3.7 presents the L-shell locations of the electrons after interacting with the 300-km dipole-like bubble. The figure suggest a more limited dispersion of electrons when compared to the hollow bubble. Figure 7.7.3.8 presents the L-shell locations of the electrons after interacting with the 500-km dipole-like bubble where once again the electrons are shown exhibit limited dispersion from the initial injection L-shell. What is evident in both figures is that there is some radial dispersion, but the number of electrons does not change by a significant amount, especially when compared to the effect of hollow bubble on the electron dispersion.
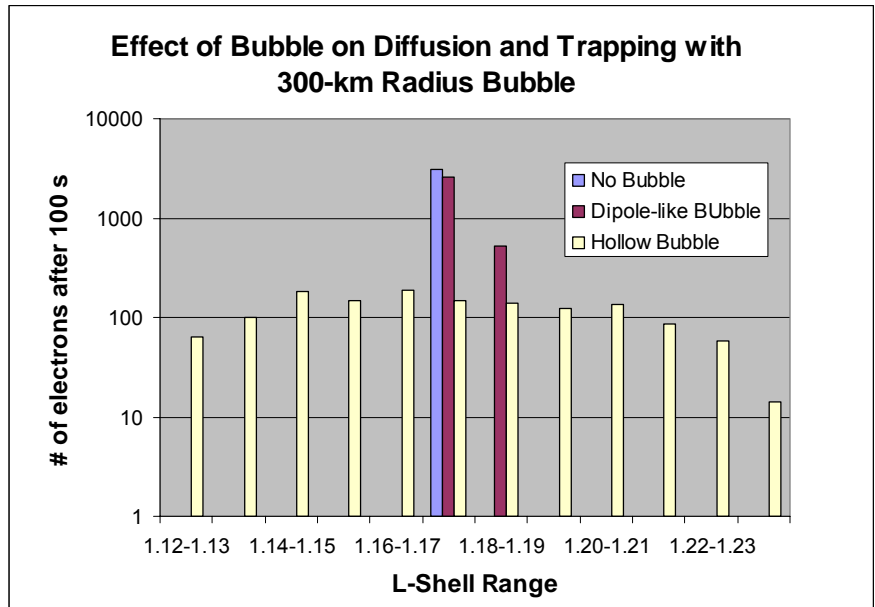
Figure 7.7.3.7: The semi-log plot shows the distribution of L-shell value of the electrons interacting with different magnetic bubbles at 100 s. The dipole-like bubble causes significantly less dispersion than the hollow bubble, but the dipole-like bubble does cause a redistribution of the particles.
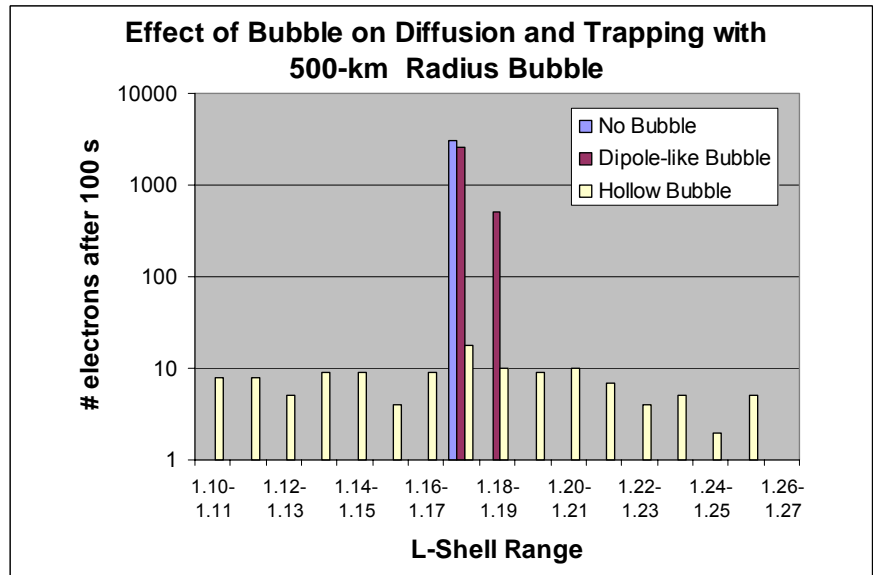
**Figure 7.7.3.8:** The semi-log plot shows the distribution of L-shell value of the electrons interacting with the large magnetic bubbles at 100 s. The dipole-like bubble causes significantly less dispersion than the hollow bubble, but the dipole-like bubble does cause a redistribution of the particles. The dipole-like bubble appears to cause dispersion away from the center of the dipole into higher L-shells.

213

Compared to the hollow bubble, the dipole-like bubble does not cause a significant change in the location of the electrons or the number of trapped electrons. This is most likely a result of not changing the direction of the ambient field, only the magnitude, with the dipole-like bubble. Electrons continue to follow the lines of force as they move through the bubble, even though the gyro-radius of the electron may change as the magnitude of the magnetic field changes. Recall that the gyro-radius of a 2 MeV electron at the location of release is on the order of a couple of hundred meters and a decrease in the gyro-radius due to an increase in the magnetic field does not significantly change the orbit or trajectory of the electron. With this magnetic field configuration, the only opportunity for dispersion occurs where the magnetic field is down by several orders of magnitude near the center of the bubble. When this occurs, the electron disperses away from the center as shown above in Figures 7.7.3.7 and 7.7.3.8.

What is clear is that the shape, size, and dynamics of the magnetic perturbations and bubble significantly affect the dispersion and trapping efficiency of the weapons debris and subsequent beta decay electrons. However, one should be reminded that there is still speculation about the characteristics of the magnetic perturbations caused by a nuclear explosion in space. We have shown the effect of four simple approximations (two sizes and two general shapes) to the bubble's characteristics. Ongoing work at LLNL may provide better insight into the formation and important characteristics of the bubble. So, although more effort is needed to appropriately model the conditions of the magnetic field to be applied to the model for analysis, the effects of any shape and magnetic structure can be investigated using this code.

7.8.   STATISTICAL CONFIDENCE IN THE RESULTS OF THE CODE

This is the last major effort of the written dissertation is a presentation of a set of statistics associated with the trapping efficiency of 10,000 fission fragments released at 1,500 km altitude spread out of in a spherical volume with a radius of 300 km. The fission fragments are initialized with a the Maxwell-Boltzman velocity distribution shown in Figure 7.2.2. The fission fragments are released and allowed to beta decay. No magnetic bubble is include, but the particles are allowed to scatter and dE/dx through interactions with the atmosphere, and interact with the SAA. The ions and betas are

tracked for up to 3,000 s after the initial release. In order to accumulate the statistics, five unique sets of 10,000 fission fragments are constructed and run in the code and the results are compared to demonstrate the consistent output of the code and examine the rapidity of convergence of the results. The initial random number is unique for each set of runs. The geographic release location of the fission fragments is at a longitude of 142E and a latitude of 9N.

The results of the computed trapping efficiency of the fission fragments for the 5 runs are shown in Figures 7.8.1 – 7.8. 7. The figures present the expected Monte Carlo induced random behavior for small numbers of particles and then the convergence of the computed trapping efficiency for larger numbers of particles. Although 10,000 particles were used to compile the data, the convergence of all of the data at around 5,000 particles suggest that the trapping efficiency could be determined with no more than ½ of the initial 10,000 particles. The reduction in the total number of particles could save at least half of the computer run time (about 45 hours for these runs) if the trapping efficiency is the only desired output from the code. Figures 7.8.1 and 7.8.2 offer a view of the data comparing a linear plot to a semi-log plot. In each case the trapping efficiency converges for all five sets of data and establishes confidence in the consistent output of the code.
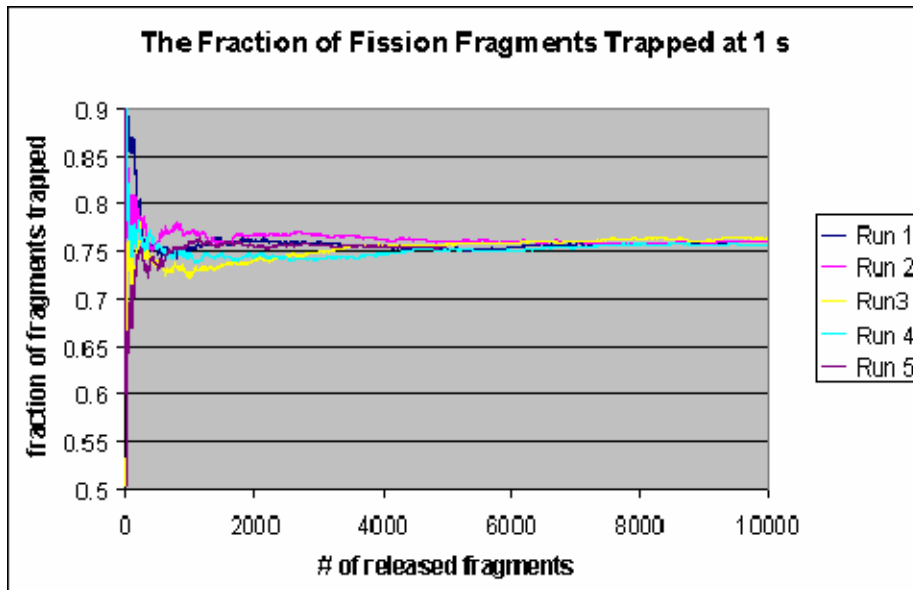
Figure 7.8.1: The trapping efficiency of fission fragments 1 s after the release of the fragments.

215
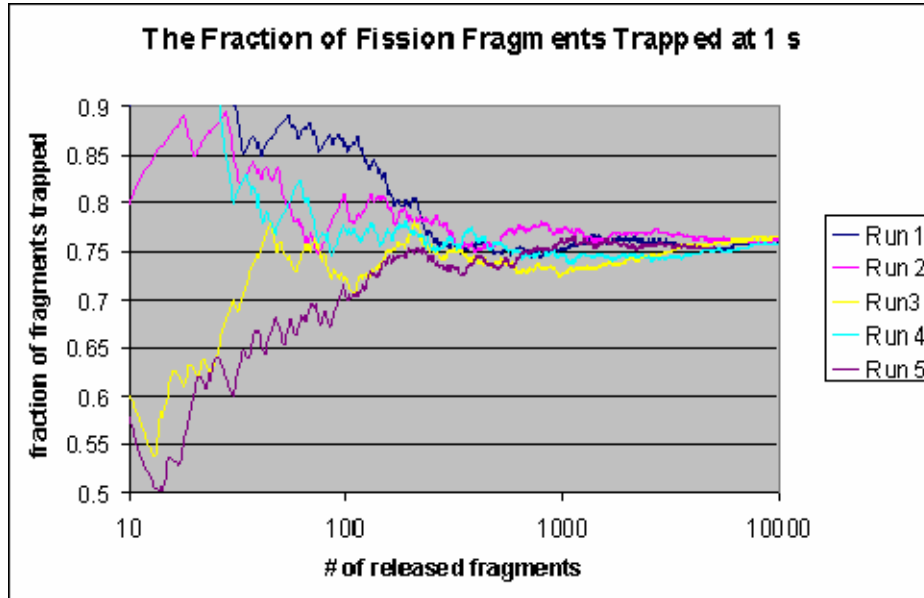
Figure 7.8.2: The trapping efficiency of fission fragments 1 s after the release of the fragments using a semi-log plot. This view provides more amplified detail of the data when compared to Figure 8.8.1.
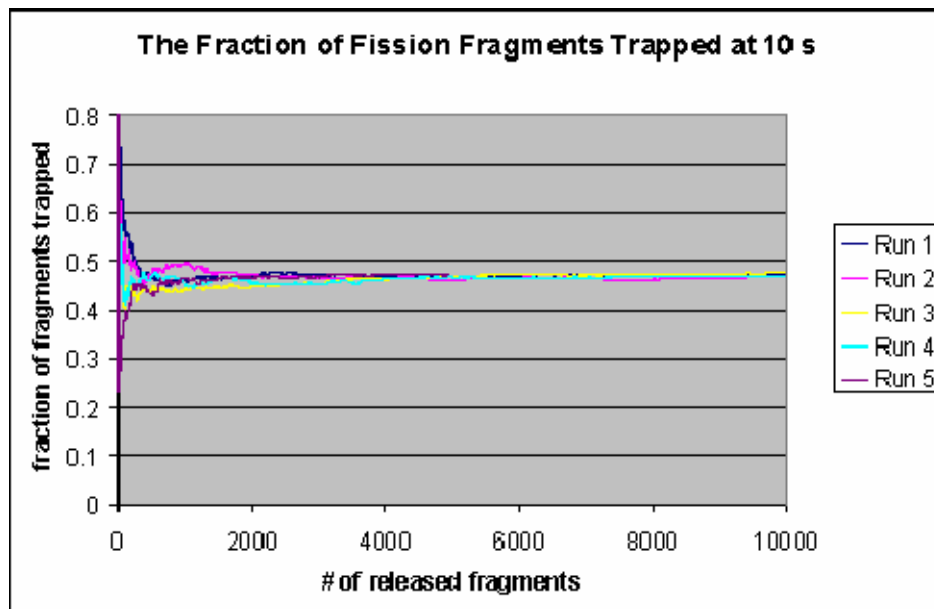
Figure 7.8.3: The trapping efficiency of fission fragments 10 s after the release of the fragments.

216
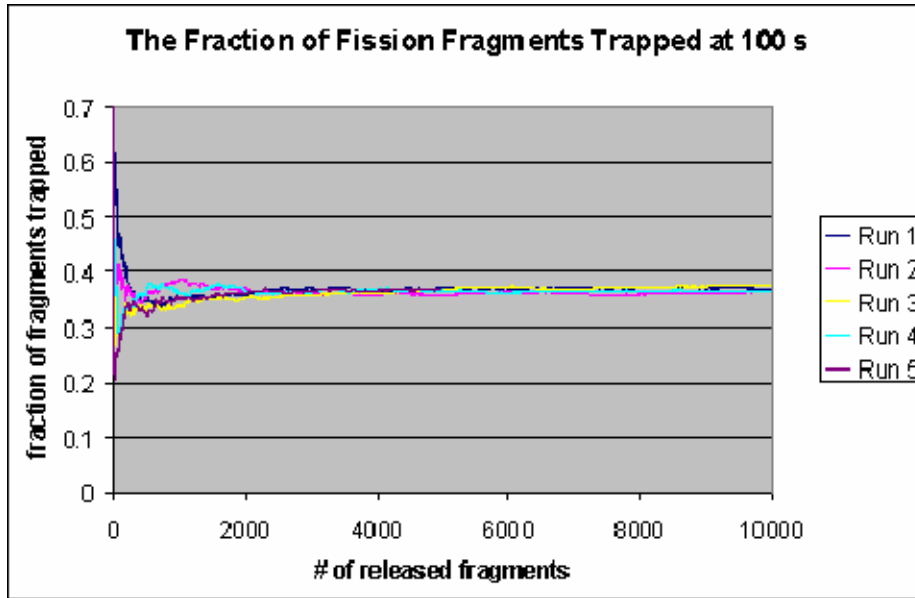
Figure 7.8.4: The trapping efficiency of fission fragments 100 s after the release of the fragments.
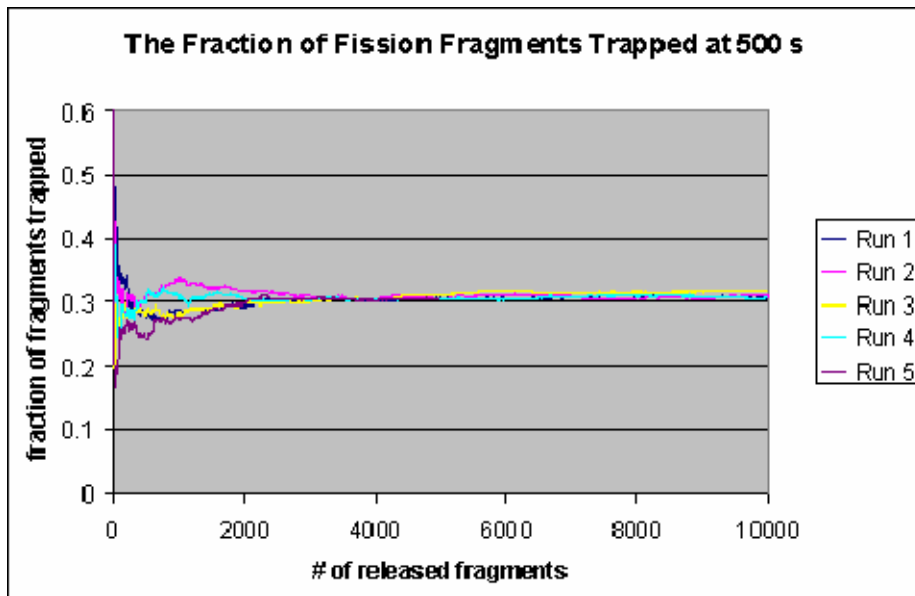
Figure 7.8.5: The trapping efficiency of fission fragments 500 s after the release of the fragments.
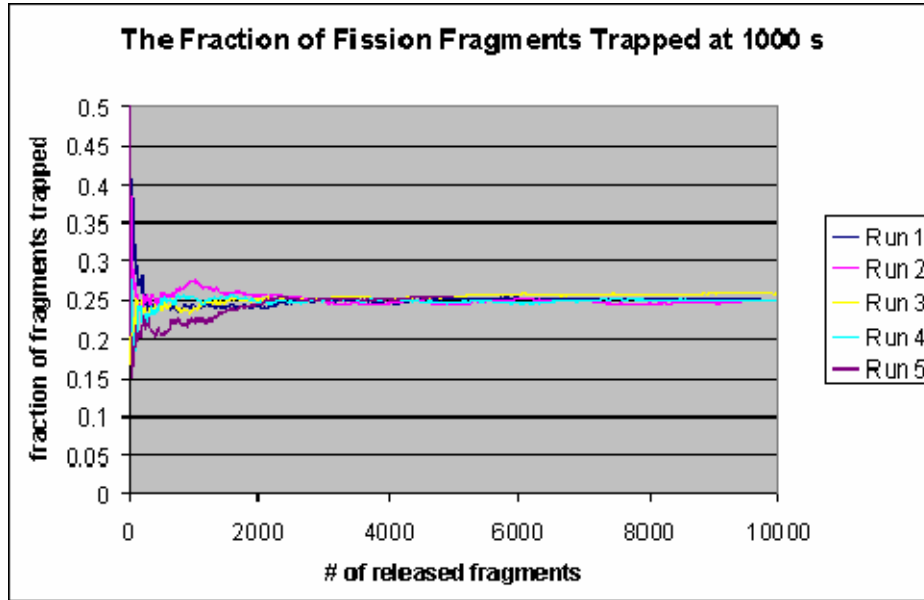
Figure 7.8.6: The trapping efficiency of fission fragments 1,000 s after the release of the fragments.
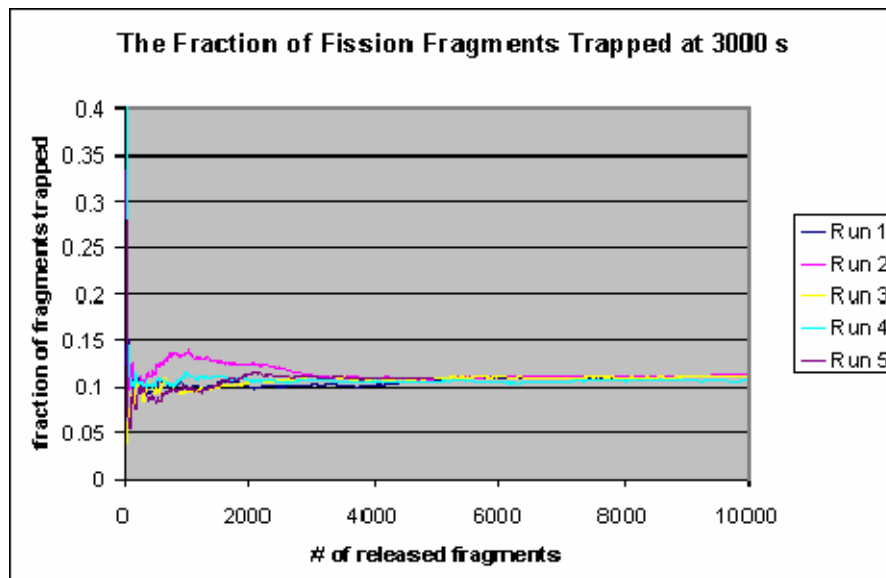
Figure 7.8.7: The trapping efficiency of fission fragments 3,000 s after the release of the fragments.

218

Similar electron data is shown in Figures 7.8.8 – 7.8.11. The source of the electrons is beta decay of fission fragments. The figures present the fraction of electrons trapped for different times. The fraction of electrons actually represents the number of trapped electrons divided by the number of released fission fragments. Like the fission fragments, the data converges around 5,000 particles.
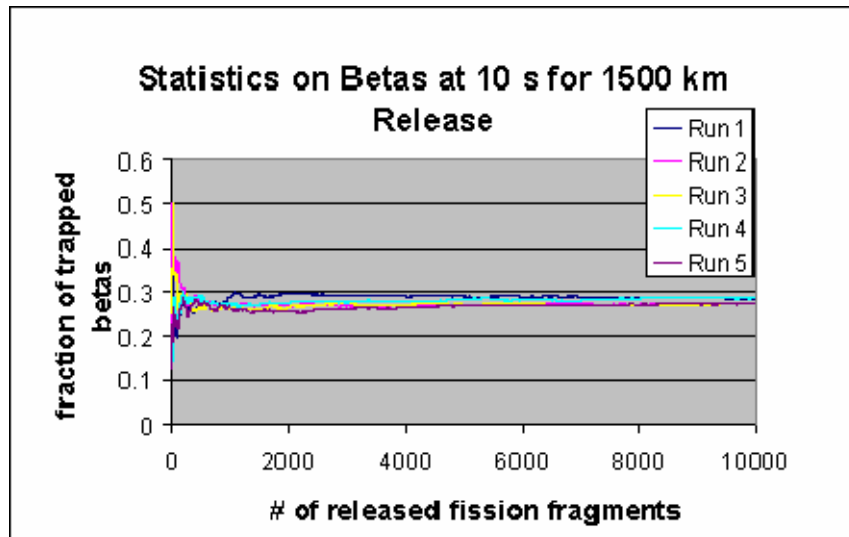
**Figure 7.8.8: The trapping efficiency of betas 10 s after the release of the fragments.**
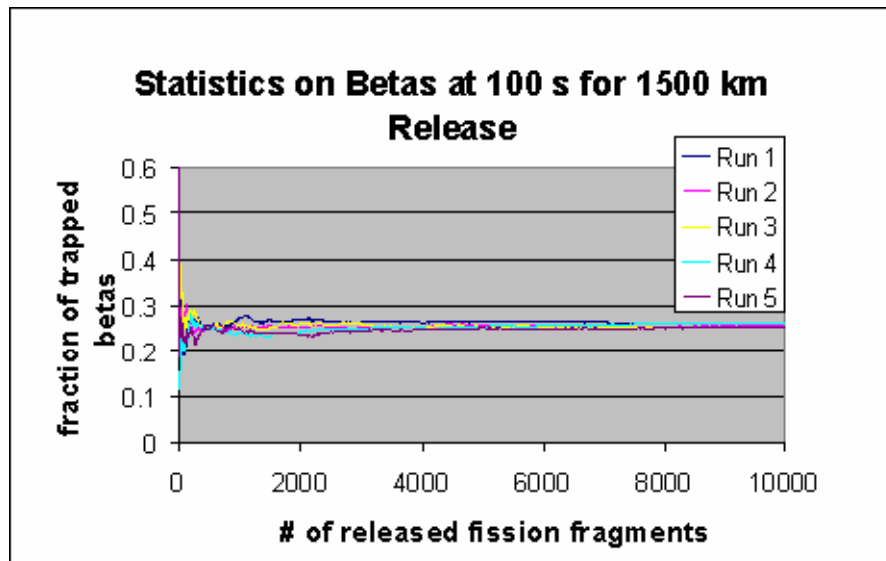
Figure 7.8.9: The trapping efficiency of betas 100 s after the release of the fragments.
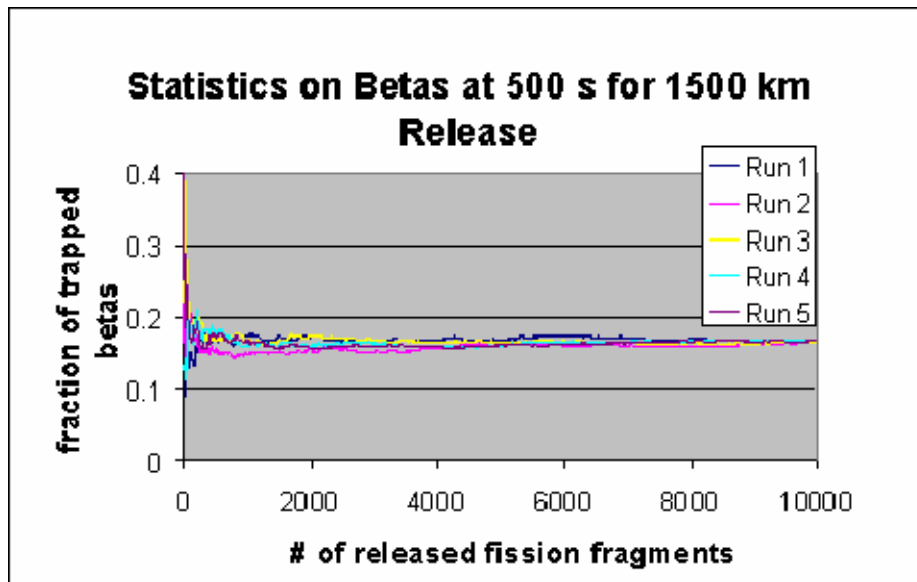
**Figure 7.8.10: The trapping efficiency of betas 500 s after the release of the fragments.**
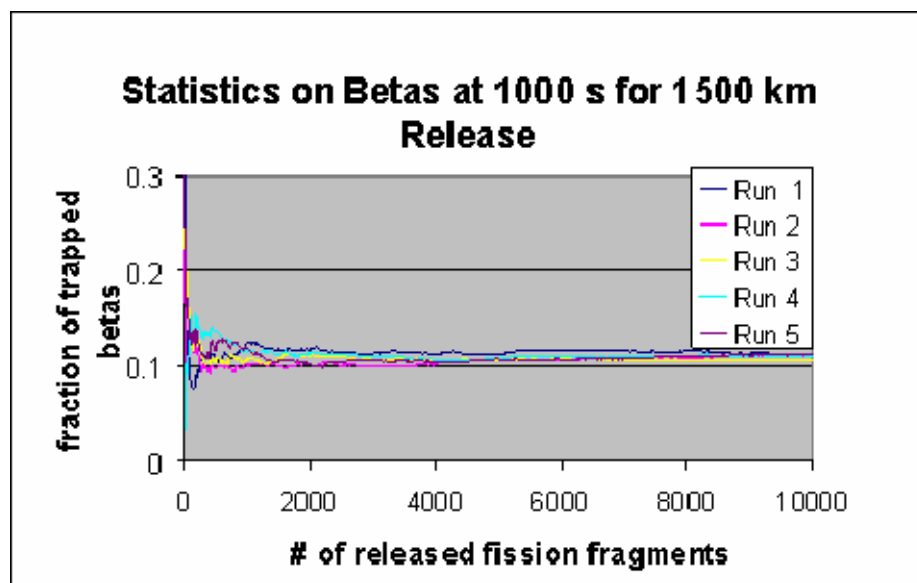

Figure 7.8.11: The trapping efficiency of betas 1,000 s after the release of the fragments.

The statistics presented above are representative of many computational trials. The output of the code is consistent and should be used with confidence, at least within the limits of the included physics.

7.9. SUMMARY OF INITIAL FINDINGS

The data and analysis presented in Sections 7.2 – 7.7 demonstrate the complicated, non-linear nature of the art and science of releasing, tracking, and trapping charged particles released from a nuclear explosion. Each of the key parameters studied affect the injection and trapping of the ions and energetic betas in different ways. The persistent radiation environment (belt pumping) involves many coupled parameters and complicated initial conditions. The complex nature of the problem begs for a computational approach. The solution to the problem quickly becomes impractical to solve without the aid of computation and this is most likely part of the reason for the current very limited status of our predictive capability for belt-pumping. As demonstrated, most of the critical physics required to model the trapped radiation environment is integrated into the code developed as part of the dissertation. For the first time, given a source term for injection, the trapped radiation environment can be adequately modeled for L-shells less than 1.5. Even for L-shells greater than 1.5 (altitudes greater than 3,200 km at the equator), the code can provide a reasonable source term for the location of ions and betas hours after the burst. The compilation of the required physics offers a unique and previously unavailable capability to help understand the persistent environment caused by a high-altitude nuclear event. Below is a brief summary of the effects of the parameters examined and discussed in Sections 7.2 – 7.6 and the summary of the effects of the magnetic bubble.

1. Longitude: In general, the trapping efficiency of particles increases as the detonation or release location approaches the location of the South Atlantic Anomaly.

2. Latitude: Because the loss cone is smaller for particles at higher latitudes, the trapping efficiency, especially for betas, increases with the latitude of release of the ions. The existing data supports that above $L \approx 1.3$ (altitudes greater than 2000 km at the equator), wave-particle interaction increases the radial dispersion and pitch angle change and the long-term trapping efficiency does not necessarily increase with latitude.

However, the code can still be used for the creation of a source term of debris for minutes to hours after the burst, the "rule of thumb" for latitude is reasonable.

3. Altitude: Similar to the effects of latitude, the loss cone is smaller for particles injected at higher altitudes. The short-term trapping efficiency increases with altitude. This statement does not account for the effects of wave-particle interaction that begin to appear around $L \approx 1.3$.

4. Charge State: The charge state affects the gyro-radius and drift velocity of the ions. A smaller charge state results in a larger gyro-radius and a larger drift velocity. For early time losses, especially for particles mirroring near altitudes of 100 km, the smaller charge state may cause a more rapid decay due to increased atmospheric interaction resulting from the larger gyro-radius. For long-term trapping (at least one complete earth orbit) the larger drift velocity associated with the low charge state minimizes the time the particle spends near the SAA where a trapped particle loses most of the kinetic energy during an orbit. Eventually, however, all of the particles trapped in low L-shells, lose their kinetic energy and most of the kinetic energy is lost in the vicinity of the SAA. Finally, neutral fission fragments that travel away from the burst location (and the earth) eventually beta decay and are a source of fission spectrum electrons injected into L-shells well above the burst.

5. Half-life of Fission Fragment: The daughter products with short half lives generally produce higher energy beta particles. Additionally, daughter products with short half lives are more likely to produce beta particles before all of the fission fragment's kinetic energy is lost in the atmosphere.

6. Initial Pitch Angle: The trapping efficiency of charged particles increases as the initial pitch angle approaches 900.

[Although the study of the key parameters certainly offers insight into the nature of trapped radiation, the complicated nature of the physics prevents the establishment of absolute "rules-of-thumb". The above summaries are observations from the computations and consistent with the data.]

7. The magnetic bubble: The effect of the magnetic bubble appears to cause significant radial dispersion of the debris. The presence of the magnetic bubble will cause

the debris to expand out to the edge of the bubble and clearly offers evidence that the shape and size of the magnetic bubble affects the dispersion and trapping of the debris. Like the other key initial condition parameters, the initial condition and perturbation of the magnetic field is critical for understanding, modeling, and predicting the environment caused by a nuclear detonation in space.

This dissertation has produced a computational capability and model that can be used to help predict the environment caused by a high-altitude nuclear explosion. There are, as expected, a number of areas for future work, but the unique capability developed here has advanced our computational capability and is better than anything that existed. If I had access to this code during my tenure at USSTRATCOM I would have provided the Nation's leadership with much better advice and answers to the questions about "belt-pumping" and the effects of a nuclear detonation is space.

THIS PAGE INTENTIONALLY LEFT BLANK

LIST OF REFERENCES

Able, B., and R.M. Thorne. "Electron Scattering Loss in Earth's Inner Magnetosphere." *J. Geophys. Res.*, Vol. 103, (1998).

Al'pert, Ya L. *Plasma: Volume 1: Theory and main properties*. Cambridge: Cambridge University Press, 1990.

Allen, C., and P. McDaniel. "Fission Spectra Electron Artificial Belt Widths and Error Analysis." published for Air Force Research Laboratory, Kirtland AFN, NM under Subcontract BOAS007-3011-7.

Allen, C., and P. McDaniel. "Review of the High Altitude Nuclear Burst 1958 and 1962 Satellite Data." published for Air Force Research Laboratory, Kirtland AFN, NM under contract DTRA-01-00-C-0088.

Allen, C., and B. Roth. "Final Report Summarizing Blue Ribbon Panel and Support Work Assessing the Status of the High Altitude Nuclear Explosion (HANE) Trapped Radiation Belt Database," final report to Air Force Research Laboratory, June 2006.

Allen, L. Jr., J.L. Beavers, II, W.A. Whitaker, J.A. Welch, Jr., R.B. Walton. "Project Jason Measurement of Trapped Electrons from a Nuclear Device by Sounding Rockets." *J. Geophys. Res.*, Vol. 64, (1959).

Audi, G., O. Bersillon, J. Blachot, and A. H. Wapstra. "The NUBase evaluation of nuclear and decay properties." *Nuclear Physics A 729*, (2003).

Balashov, Vsevolod V. *Interaction of Particles and Radiation with Matter*. Translated by G. Pontecorvo. New York: Springer, 1997.

Blau, Joe. Lecture Notes: Introduction to Numerical Modeling, SE2911, Winter Quarter 2005, Naval Postgraduate School.

Bloomfield, Louis A. *How Things Work: The Physics of Everyday Life*. New York: John Wiley and Sons, 1997.

Boyd, T.J.M., and J.J. Sanderson. *The Physics of Plasmas*. Cambridge: Cambridge University Press, 2003.

Brown, W.L. "Observations of the Transient Behavior of Electrons." published in *Radiation Trapped in the Earth's Magnetic Field*, edited by Billy M. McCormac. Dordretch, Holland: D. Reidel Publishing Company, 1966.

Browne, F., and R.B. Firestone. Table of Radioactive Isotopes. New York: John Wiley & Sons, 1986.

Carter, R.E., F. Reines, J.J. Wagner, and M.E. Wyman. "Free Antineutrino Absorption Cross Section II. Expected Cross Section from Measurements of Fission Fragments Electron Spectrum." Phys. Rev., Vol. 113, (1959).

Chen, Francis F. *Introduction To Plasma Physics And Controlled Fusion, Volume 1: Plasma Physics*, 2nd ed. New York: Plenum Press, 1984.

Christofilos, N.C. "The Argus Experiment." *J. Geophys. Res.*, Vol. 64, (1959).

Cladis, J.B. *The Trapped Radiation Handbook*. Palo Alto, CA: Lockheed Palo Alto Research Laboratory, published by General Electric Company, TEMPO DNA Information and Analysis Center, Santa Barbara, CA, for Defense Nuclear Agency, 1971.

Clilverd et al. "Determining the Size of Lightening-Induced Electron Precipitation Patches." *J. Geophys. Res.*, Vol. 107, (2002).

Crowley. Lecture Notes: Introduction to Finite Differences Methods: Lawrence Livermore Laboratory: provided by Tom Thomson at LLNL.

Draganov et al. "Magnetosperically Reflected Whistlers as a Source of Plasmaspheric Hiss." *Geophys. Res*. Lett., 19, (1992).

Dyal, P. "Particle and Field Measurements of the Starfish Diamagnetic Cavity," *J. Geophys. Res. Vol., 111,* A12211, (2006).

England, T.R., and B.F. Rider. "Evaluation and Compilation of Fission Product Yields." Preliminary Report for the National Nuclear Data Center's Evaluated Nuclear Data File, Los Alamos National Laboratory Repot ENDF-349, LA-XXXX-MS, 1993.

England, T.R., and B.F. Rider. LA-UR-94-3106; ENDF-349. Los Alamos National Laboratory, 1993.

Fermi, Enrico. *Nuclear Physics*, Rev. ed., A course given by Enrico Fermi at the University of Chicago with notes compiled by J. Orear, A.H. Rosenfeld, and R.A. Schluter. Chicago: The University of Chicago Press, 1950.

Fission Neutron Yield, http://t2.lanl.gov/endf/intro22.html , (accessed 27 April 2007).

Fong, P. *Statistical Theory of Nuclear Fission*., New York: Gordon and Breach, Science Publishers, 1969.

Giordano, Nicholas J. *Computational Physics*. Upper Saddle River, NJ: Prentice Hall, 1997.

Glasstone, S., and P. Dolan. *The Effects of Nuclear Weapons*, 3rd ed. prepared and published by the United States Department of Defense and the United States Department of Energy, 1977.

Griffiths, David J. *Introduction to Electrodynamics*, 2nd ed. Englewood Cliffs, NJ: Prentice Hall, 1989.

Hamlin, D.A., R. Karplus, R.C. Vik, and K.M. Watson. "Mirror and Azimuthal Drift Frequencies for Geomagnetically Trapped Particles." *J. Geophys. Res.*, Vol. 66 (1966).

Hedin, A.E. "Extension of the MSIS Thermosphere Model into the Middle and Lower Atmosphere." *J. Geophys. Res.*, Vol. 96, (1991).

Hedin, A.E. "MSIS-86 Thermospheric Model." *J. Geophys. Res.*, Vol. 92, (1987).

Hedin, A.E. "A Revised Thermospheric Model Based on Mass Spectrometer and Incoherent Scatter Data: MSIS-83." *J. Geophys. Res.*, Vol. 88, (1983).

Hendricsk, S.J., and J.C. Cain. "Magnetic Field Data for Trapped Particle Evaluations." *J. Geophys. Res.*, Vol. 71, (1963).

Hess, Wilmot N. "Project the Artificial Radiation Belt Made on 9 July 1962." *J. Geophys. Res.*, Vol. 68, (1963).

Hess, Wilmot N. *Introduction To Space Science*. New York: Gordon and Breach Science Publishers, 1965.

Hockney, R.W., and J.W. Eastwood. *Computer Simulation Using Particles*. Philadelphia, PA.: Institute of Physics Publishing, 1988.

Inan et al. "Geographic Distribution of Lightening-Induced Electron Precipitation Observed as VLF/LF Perturbation Events." *J. Geophys. Res.*, Vol. 93, (1988).

Jackson, John David. *Classical Electrodynamics*, 3rd ed. Hoboken, NJ: John Wiley and Sons, Inc., 1998.

Jakes, E.M., K.J. Daul, and R. Greaves. "PL-TR-1056: Exo-atmospheric Nuclear Radiation Environments Prediction and Shielding Codes, Final Report, "Report for Phillips Laboratory, Advance Weapons and Survivability Directorate, Air Force Material Command, Kirtland Air Force Base, NM, March 1993.

Jensen, D.C., and J.C. Cain. "An Interim Magnetic Field." *J. Geophys. Res.*, Vol. 67, (1962).

Jensen, D.C., and W.A. Whitaker. "A Spherical Harmonic Analysis of the Geomagnetic Field." *J. Geophys. Res.*, Vol. 65, (1960).

Keepin, G.R. *Physics of Nuclear Kinetics*. Reading, Ma: Addison-Wesley Publishing Co., Reading, 1965.

Krane, K.S. *Introductory Nuclear Physics*. New York: John Wiley and Sons, 1988.

LBNL Isotopes Project - LUNDS Universitet: WWW Table of Radioactive Isotopes, Version 2.1, January 2004, http://ie.lbl.gov/toi (accessed 14 May 2007).

Nethaway, D., and M. Mustafa. Memorandum to Thomas Thomson at Lawrence Livermore National Laboratory, Subject: The Addition of Prompt Fission Product Data to Explosion Eodes. 23 March 1998.

Newman, P. "Optical, Electromagnetic, and Satellite Observations of High-Altitude Nuclear Detonations, Part I." *J. Geophys. Res.*, Vol. 64, (1959).

Northrup, Theodore G. *The Adiabatic Motion of Charged Particles*. New York: Interscience Publishers, 1963.

NRL Mass Spectrometer, Incoherent Scatter Radar Extended Model: NRLMSISE-00, http://uap-www.nrl.navy.mil/models_web/msis/msis_home.htm (accessed 17 April 2007).

Parkinson, W.D., and J. Cleary. "The Eccentric Geomagnetic Dipole." *J. Geophys. Res.*, Vol. 1, (1958).

Parks, George K. *Physics of Space Plasmas: An Introduction*, 2nd ed. Bolder, CO.: Westview Press, 2004.

Peterson, A.M. "Optical, Electromagnetic, and Satellite Observations of High-Altitude Nuclear Detonations, Part II." *J. Geophys. Res.*, Vol. 64, (1959).

Rhodes, Richard. *The Making of the Atomic Bomb*. New York: Simon and Schuster, 1986.

Roederer, J.G. *Dynamics of Geomagnetically Trapped Radiation*. Heidelberg: Springer-Verlag Berlin, 1970.

Rossi, B. *High-Energy Particles*. New Jersey: Prentice-Hall, 1952.

Schulz, Mike, and L. J. Lanzerotti. *Particle Diffusion in the Radiation Belt*. New York: Springer-Verlag, 1974.

Serge, Emilo. *Nuclei and Particles: An Introduction to Nuclear and Subnuclear Physics*, 2nd ed. Reading, MA: W.A. Benjamin, Inc., 1977.

Starodubtsev, S.V., and A.M. Romanov. *The Passage of Charged Particles through Matter*. Translated and edited by Israel Program for Scientific Translation staff for U.S. Energy Commission and the National Science Foundation. Jerusalem: Israel Program for Scientific Translation, 1965.

United States Air Force. *Handbook of Geophysics*, Rev. ed., United States Air Force. New York: The Macmillan Co., 1960.

United States Air Force. *US Standard Atmosphere 1976*. Washington, D.C.: National Oceanic and Atmospheric Administration, National Aeronautics and Space Administration, United States Air Force, 1976.

Van Allen, J.A. "Spatial Distribution and Time Decay of the Intensities of Geomagnetically Trapped Electrons from the High Altitude Nuclear Burst of 1962." published in *Radiation Trapped in the Earth's Magnetic Field*, edited by Billy M. McCormac. Dordretch, Holland: D. Reidel Publishing Company, 1966.

Van Allen, J.A., C.E. McIlwain, and G.H. Ludwig. "Satellite Observations of Electrons Artificially Injected into the Geomagnetic Field." *J. Geophys. Res.*, 64, (1959).

Walt, M. "Overall Analysis of Experiments on Artificial Radiation belts," published in *Radiation Trapped in the Earth's Magnetic Field*, edited by Billy M. McCormac. Dordretch, Holland: D. Reidel Publishing Company, 1966.

Walt, M., and W. McDonald. "The Influence of the Earth's Atmosphere on Geomagnetically Trapped Particles." *Rev. Geophys.*, Vol. 2, (1964).

Way, K., and E.P. Wigner. "The Rate of Decay of Fission Products." *Phys. Rev, 73*, (1948).

Webb, R.C. "The Effects of a Nuclear Detonation in Space (with an Emphasis on Low Earth Orbit Satellites)," Briefing to Defense Science Research Meeting, Electronics Technology Division, Defense Special Weapons Agency. 6 July 1998.

Weinberg, A.M., and E.P. Wigner. *The Physical Theory of Neutron Chain Reactors*. Chicago: University of Chicago Press, 1958.

West, H.I. Jr. "Some Observations of the Trapped Electrons Produced by the Russian High-Altitude Nuclear Detonation of 28 October 1962." published in *Radiation Trapped in the Earth's Magnetic Field*, edited by Billy M. McCormac. Dordretch, Holland: D. Reidel Publishing Company, 1966.

Wu, C.S., and S.A.Moszkowski. *Monographs and Texts in Physics and Astronomy, Vol. XVI: Beta Decay*. New York: John Wiley & Sons, 1966.

Zester, Y.I., B.G. Gavrilov, V.A. Zhmailo, K.G. Gainullin, V.I. Selin. "Geomagnetic Effects from Expanding Plasma Formation of a High-Altitude Nuclear Explosion." *Combustion, Explosion, and Shock Waves, Vol. 60, No. 6*, (2004).

Zysin, Yu A., A.A. Lbov, and L.I. Sel'chenkov. *Fission Product Yields and their Mass Distribution*, (authorized translation from the Russian). New York: Consultants Bureau, 1964.

THIS PAGE INTENTIONALLY LEFT BLANK

INITIAL DISTRIBUTION LIST

1.   Defense Technical Information Center
        Ft. Belvoir, Virginia

2.   Dudley Knox Library
        Naval Postgraduate School
        Monterey, California

3.   LLNL
        Attn: Dennis Hewett
        Livermore, California

4.   LLNL
        Attn: Tom Thomson
        Livermore, California

5.   Department of Physics
        United States Military Academy
        West Point, New York